THESIS

SYNTHESIS, CHARACTERIZATION AND APPLICATION OF
RHODIUM(III) AND PLATINUM(IV) COMPLEXES WITH
2-(2′-THIAZOLYLAZO)-5-AMINOANISOLE AND
4-(2′-THIAZOLYLAZO)-3-AMINOANISOLE

BUSSABA BOONSENG

GRADUATE SCHOOL, KASETSART UNIVERSITY
2009

THESIS APPROVAL

GRADUATE SCHOOL, KASETSART UNIVERSITY

Master of Science (Chemistry)
DEGREE

Chemistry   Chemistry
FIELD   **DEPARTMENT**

TITLE: Synthesis, Characterization and Application of Rhodium(III) and
              Platinum(IV) Complexes with 2-(2´-thiazolylazo)-5-aminoanisole
              and 4-(2´-thiazolylazo)-3-aminoanisole

NAME: Miss Bussaba Boonseng

THIS THESIS HAS BEEN ACCEPTED BY

_____ **THESIS ADVISOR**
(Associate Professor Apisit Songsasen, Ph.D.   )

_____ **THESIS CO-ADVISOR**
(Assistant Professor Nattamon Koonsaeng, Ph.D.   )

_____ **THESIS CO-ADVISOR**
(Associate Professor Waraporn Parasuk, Dr.rer.nat   )

_____ **DEPARTMENT HEAD**
(Assistant Professor Noojaree Prasitpan, Ph.D.   )

APPROVED BY THE GRADUATE SCHOOL ON _____

_____ **DEAN**
(Associate Professor Gunjana Theeragool, D.Agr.   )

THESIS

SYNTHESIS, CHARACTRIZATION AND APPLICATON OF
RHODIUM(III) AND PLATINUM(IV) COMPLEXES
WITH 2-(2'-THIAZOLYLAZO)-5-AMINOANISOLE
AND 4-(2'- THIAZOLYLAZO)-3-AMINOANISOLE

BUSSABA BOONSENG

A Thesis Submitted in Partial Fulfillment of

The Requirements for the Degree of

Master of Science (Chemistry)

Graduate School, Kasetsart University

2009

Bussaba Boonseng 2009: Synthesis, Characterization and Application of Rhodium(III) and Platinum (IV) Complexes with 2-(2´-thiazolylazo)-5-aminoanisol and 4-(2´-thiazolylazo)-3-aminoanisole. Master of Science (Chemistry), Major Field: Chemistry, Department of Chemistry. Thesis Advisor: Associate Professor Apisit Songsasen, Ph.D. 235 pages.

2-(2´-thiazolylazo)-5-aminoanisole (*p*-amino TAA) and 4-(2´-thiazolylazo)-3-aminoanisole (*o*-amino TAA) was synthesized by diazotization of 2-aminothiazole and coupling with *m*-anisidine. FT-IR, ^{1}H-NMR, mass spectroscopy and elemental analysis were used to identify the structure of *p*-amino TAA and *o*-amino TAA. The acid dissociation constants (pK_a) of the two compounds determined by half-height method and limiting absorbance methods were 3.0 and 3.3, respectively. The stoichiometric studies showed that the ratio of rhodium(III) with both ligands and platinum(IV) with *o*-amino TAA were 1:2 with the stability constants in the range of 10^9 to 10^{10} while the ratio between platinum(IV) and *p*-amino TAA were 1:1 with the stability constant of 10^5. The complexes of rhodium(III) were prepared by refluxing. The structures of complexes were characterized by FT-IR and ^{1}H-NMR spectroscopy. The structures of complexes between rhodium(III) and *p*-amino TAA were also determined by quantum chemical calculations at B3LYP level of theory using 6-31G* basis set for all atoms and SDD basis set for rhodium atom. The results showed that *trans*-[Rh(*p*-TAA-n)$_2$(Cl)$_2$]$^+$ was the most stable complex with the stabilization energy of -1350.72 kcal/mol.

Binding of calf thymus DNA with rhodium(III) complexes was studied by UV-Vis spectroscopy. There was evidence from the experiment which showed the interaction between these complexes and CT DNA. The results from quantum chemical calculations indicated that this interaction did not occur via the dissociation reaction of chloride ion. So this interaction could be spontaneous reaction via other mechanisms or mode of binding.

		/ /
Student's signature	Thesis Advisor's signature	

ACKNOWLEDGEMENTS

Bussaba Boonseng

February, 2009

TABLE OF CONTENTS

Page

LIST OF TABLES

LIST OF TABLES (Continued)

LIST OF TABLES (Continued)

LIST OF TABLES (Continued)

LIST OF TABLES (Continued)

LIST OF FIGURES

LIST OF FIGURES (Continued)

LIST OF FIGURES (Continued)

LIST OF FIGURES (Continued)

LIST OF FIGURES (Continued)

LIST OF FIGURES (Continued)

LIST OF FIGURES (Continued)

LIST OF FIGURES (Continued)

LIST OF FIGURES (Continued)

LIST OF FIGURES (Continued)

LIST OF FIGURES (Continued)

LIST OF ABBREVIATIONS

p-amino TAA	=	2-(2′-thiazolylazo)-5-aminoanisole
o-amino TAA	=	4-(2′-thiazolylazo)-3-aminoanisole
B3LYP	=	Becke-Lee, Yang and Parr correlation functional
CT-DNA	=	Calf thymus DNA
DFT	=	Density Functional Theory
DMSO-d^6	=	Dimethylsulfoxide, D-6
ESI-MS	=	Electrospray Ionization Mass Spectroscopy
UV-Vis	=	Ultraviolet-visible spectroscopy
FT-IR	=	Fourier Transform Infrared Spectrophotometry
^{1}H NMR	=	Proton Nuclear Magnetic Resonance Spectroscopy
KHP	=	Potassium Hydrogen Phthalate
SDD	=	Stuttgart/Dresden basis set
Tris-HCl	=	Trishydroxymethylaminomethane hydrochloride
TLC	=	Thin Layer Chromatography
pK_a	=	Acid Dissociation Constant
ECP	=	Effective Core Potential
DNA	=	Deoxyribonucleic Aacid
RNA	=	Ribonucleic Acid

SYNTHESIS, CHARACTERIZATION AND APPLICATIONS OF RHODIUM(III) AND PLATINUM(IV) COMPLEXES WITH 2-(2′-THIAZOLYLAZO)-5-AMINOANISOLE AND 4-(2′-THIAZOLYLAZO)-3-AMINOANISOLE

INTRODUCTION

1. Rhodium

Rhodium is a metallic element of atomic number 45 and atomic weight 102.905 which was discovered in 1803 by W.H.Wollaston. The name rhodium, naming it after the Greek word for "rose" because of its rose-color (Hunt, 1987), commonly found in aqueous solutions of its salts. Rhodium is a member of platinum group metals, of which it is found the widest application due to its several properties. It is unaffected by air and water up to 875 K, and unaffected by acids, but is attached by molten alkalis (Emsley, 1998). Rhodium remains bright in all atmospheric exposures at room temperatures and is completely resistant to a variety of corrosives. These properties plus the high and relatively uniform reflectivity (75-80%) and the ease with which hard, bright electrodeposits can be produced have led to wide use of rhodium for jewelry, reflectors and electrical contacts. Rhodium has certain specific uses but the principle application of rhodium is an alloying element for platinum. The 10% -rhodium-platinum alloy is used in the oxidation of ammonia, for spinnerets, glass-fiber bushings, furnace windings and thermocouples. A trace of rhodium is requires in the liquid bright gold used for decorating glass and porcelain to achieve a very fine-grained, bright deposit. Rhodium has been used in large quantities as the reduction catalyst for NO_x in catalytic converters. Small amounts of rhodium plus indium or ruthenium are used in dental alloys to produce a very fine-grained casting (Sasomsap, 1989).

All the platinum metals are generally associated with each other including rhodium. However, the relative proportions of the individual metals are by no means constant and the more important sources of rhodium are the nickel-copper-sulfide ores found in South Africa and in Sudbury, Canada, which contain about 0.1% rhodium. The production methods of rhodium are used by the alternative solvent extraction processes and ion exchange techniques. These methods offer superior efficiency and they are increasingly replacing the classical process that is not high efficiency and costly recycling (Greenwood, 1997). The diagram for refining rhodium is shown in Figure 1.

2.   Properties of the rhodium

The oxidation states of rhodium are listed in Table 1. The oxidation state 1 and 3 are the most important, the other oxidation states are rare. The -1 and 0 states occur in carbonyls including clusters and in nitrosyls, the +2 state principally in the carboxylates, and the +4, +5 and +6 states mainly as fluorides. The geometry of rhodium(I), (d^8) is predominantly square planar, but a few five-coordinate species have been isolated. Many of the square planar complexes are of importance in catalysis, since the metal atom can increase its coordinate number by accepting ligands in the apical sites (Emsley, 1998).

The geometry of rhodium(III) (d^6) is almost invariable octahedral. The electronic (visible) spectra of rhodium(III) complexes display two bands toward the blue end of the spectrum, although in many instances only the first spin allowed ligand-field band ($^1T_{1g} \leftarrow {}^1A_{1g}$) is observed, since the second band is often obscured by charge transfer transitions which the band are responsible for the yellow, red or reddish-brown colors for the rhodium(III) compounds (Sasomsap, 1989).

```
                            ┌─────────────────────┐
                            │ Pt metal concentrates│
                            └─────────────────────┘
```

Dissolve in
aq HCl, Cl$_2$ → Distill off RuO$_4$, OsO$_4$

Extract in metal
Au, Fe, Te ← isobutyl ketone

Boil off HCl → AgCl

Extract with
Palladium extract ← hydroxyoxime

Extract with tributyl phosphate or amine → Platinum extract

Strip with aq HCl, add NH$_4$Cl

Pd(NH$_3$)$_2$Cl$_2$

(NH$_4$)$_2$IrCl$_6$ and [Rh(NH$_3$)$_5$Cl]C1 precipitated

Strip with aq HCl, adjust to pH 10

H$_2$PtCl$_6$

Ignite

Pd metal

Extract with amine

NH$_4$Cl, ignite

Pt metal

aqueous phase [Rh(NH$_3$)$_5$Cl]C1

organic phase [IrCl$_6$]$^{2-}$

precipitate, ignite in H$_2$

Rh metal

Figure 1 Flow diagram for refining of Platinum group metals by solvent extraction.

Source: Greenwood (1997)

Table 1 Some properties of an elemental rhodium

Properties	Value
Atomic symbol	Rh
Atomic number	45
Atomic weight/g mol^{-1}	102.90550
Electronic configuration	[Kr] $4d^8 5s^1$
Density(20°C)/g cm^{-3}	12.39
Melting point/°C	1,960
Boiling point/°C	3,760
ΔH_{fus}/ kJ mol^{-1}	21.6
ΔH_{vap}/ kJ mol^{-1}	494
ΔH_f (monoatomic gas)/ kJ mol^{-1}	556(±11)
Electronegativity (Pauling Scale)	2.2
Electrical resistivity (20°C)/µΩ cm	4.33
Number of naturally occurring isotopes	1
Metal radius (12-coordinate)/pm	134
Effective ionic radius (6-coordinate)/pm	
V	55
IV	60
III	66.5
II	-

Source: Greenwood (1997)

3. Compounds of rhodium

Heating rhodium metal or the trichloride in oxygen at 600°C, or simply heating the trinitrate, produces dark-grey Rh_2O_3; it is the only stable oxide formed by this metal. The yellow precipitate formed by the addition of alkali to aqueous solutions of rhodium(III) is actually $Rh_2O_3 \cdot 5H_2O$ rather than a genuine hydroxide. Electrolytic oxidation of Rh^{3+} solutions and addition of alkali gives a yellow precipitate of $RhO_2 \cdot 2H_2O$, but attempts to dehydrate this produce Rh_2O_3. Black anhydrous RhO_2 is obtained by heating Rh_2O_3 in oxygen under pressure.

The octahedral hexafluorides are obtained directly from the elements and both are volatile, extremely reactive and corrosive solids, RhF_6 being the least stable of the platinum metal hexafluorides. The pentafluorides of rhodium may be prepared by the thermal dissociation of the hexafluorides. It is also highly reactive and are respectively dark-red and yellow solids, RhF_4 is a purple-red solid, usually prepared by the reaction of the strong fluorinating agent BrF_3 on $RhBr_3$ (Bartlett, 1974).

The most familiar and most stable of the halides of rhodium is the trihalides. Those of rhodium range in color from the red RhF_3 to black RhI_3. The anhydrous trihalides are generally unreactive and insoluble in water but, excepting the triiodide which is only known in this form, water-soluble hydrates can be produced by wet methods. The dark-red $RhCl_3 \cdot 3H_2O$ is the most common compound of rhodium and the usual starting point for the preparation of other rhodium compounds, and is itself best prepared from the metal sponge. This is heated with KCl in a stream of Cl_2 and the product extracted with water. The solution contains $K_2[Rh(H_2O)Cl_5]$ and treatment with KOH precipitates the hydrous Rh_2O_3 which can be dissolved in hydrochloric acid and the solution evaporated to dryness. $RhBr_3 \cdot 2H_2O$ also is formed from the metal by treating it with hydrochloric acid and bromine.

4.   Complexes of rhodium

For rhodium element, oxidation +3 (d^6) is the most prolific oxidation state, providing a wide variety of kinetically inert complexes. All the compounds of Rh^{3+} are diamagnetic, low-spin and octahedral, a major stabilizing influence being the high CFSE associated with the $^6t_{2g}$ configuration ($^{12}/_5\Delta_o$, the maximum possible for any d^x configuration). Rhodium can form the stable aqua complex, $[Rh(H_2O)_6]^{3+}$ yellow ion when hydrous Rh_2O_3 is dissolved in mineral acid, and it occurs in the solid state in salts such as the perchlorate, sulfate and alums. There is also clear evidence from predominantly class-a to class-b metal that rhodium(III) coordinate readily with P-, As- and S- donor ligands (Al-Bubaie *et al*., 1990). Ternary hydrides of rhodium(III) containing the octahedral $[MH_6]^{3-}$ anions have been prepared (Bronger *et al*., 1994) by the reaction of LiH and the metal under a high pressure of H_2. It is however unusual for hydrides of metals in such a high formal oxidation state as +3 to be stable in the absence of π-acceptor ligands and in the presence of n-acceptor ligands such as tertiary phosphines and arsines, the stability of rhodium(III) hydrides is enhanced. Thus H_3PO_2 reduces $[RhCl_3L_3]$ to either $[RhHCl_2L_3]$ or $[RhH_2ClL_3]$, depending on L; and the action of H_2 on $[Rh^I(PPh_3)_3X]$ (X = Cl, Br, I) yields $[RhH_2(PPh_3)_3X]$ which is, formally at least, an oxidation by molecular hydrogen.

Furthermore, the oxidation state +1 with electronic configuration d^8, that normally require the stabilizing effect of π-acceptor ligands and some of these are appropriately considered along with organometallic compounds. These complexes are usually prepared by the reduction of compounds such as $RhCl_3 \cdot 3H_2O$ in the presence of the desired ligand. It is often unnecessary to use a specific reductant, the ligand itself or alcoholic solvent being adequate, and not infrequently leading to the presence of CO or H in the product. A considerable proportion of the complexes of Rh^I are phosphines and particular demand attention isWilkinson's catalyst, $[RhCl(PPh_3)_3]$, essentially square planar. $[RhCl(PPh_3)_3]$ is red-violet compound (Dunbar and Heafner, 1992), which is readily obtained by refluxing ethanolic $RhCl_3 \cdot 3H_2O$ with an excess of PPh_3, was discovered in 1965 (Young *et al*., 1965). It undergoes a variety of reactions, most of which involve either replacement of a phosphine ligand (e.g. with

CO, CS, C_2H_4, O_2 giving *trans* products) or oxidative addition (e.g. with H_2, MeI) to form rhodium(III), but its importance arises from its effectiveness as a catalyst (Dickson, 1985) for highly selective hydrogenations of complicated organic molecules. Its use allowed, for the first time, rapid homogeneous hydrogenation at ambient temperatures and pressures. The rhodium catalyst is able to fulfill its role because the metal is capable of changing its coordination number (loss of phosphine from the dihydro complex being encouraged by the large size of the ligand) and it possesses oxidation states (+1 and +3) which differ by 2 and are of comparable stability. The discovery of the catalytic properties of $[RhCl(PPh_3)_3]$ naturally brought about a widespread search for other rhodium phosphines with catalytic activity. In addition, its selectivity and the ability of rhodium to change its coordination number and oxidation state make the great advantage over the other conventional other catalysts.

5.   The biochemistry and organometallic compounds of rhodium

Transition-metal-based compounds constitute a class of chemotherapeutics, which are widely used in the clinic (Brabec and Nováková, 2006). Especially precious metals, for example, platinum compounds being used in the treatment of cancer, silver compounds being used for antimicrobial agents and gold compounds use in the treatment of rheumatoid arthritis (Allardyce and Dyson, 2001). The interaction between DNA molecules and heavy metal compounds has been studied by several researchers for nanoelectronics (Braunand *et al*., 1998), development of antitumor drugs (Takusagawa *et al.*, 2001) and tracing biological activity. In recent years, rhodium complexes have attracted in the interaction of complexes with biomolecules, for example, the binding effect of the antitumor complex rhodium(II) acetate $[Rh_2(O_2CCH_3)_4]$ to the plasmid DNA has been studied under different molar ratio of $[Rh_2(O_2CCH_3)_4]$ compound to base pair of DNA and reaction time. The structure of $[Rh_2(O_2CCH_3)_4]$ is shown in Figure 2.
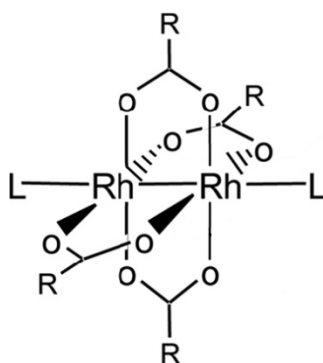
Figure 2 Structure of $[Rh_2(O_2CCH_3)_4]$, L, axial ligand; R, carbon chain of carboxylate groups; R = -CH$_3$, rhodium(II) acetate.

Source: Rahman *et al*. (2007)

For the organometallic compounds, carbonyl hydrides and carbonylate anions are obtained by reducing neutral carbonyls and in addition to mononuclear metal anions, anionic species of very high nuclearity have been obtained, often by thermolysis. These are especially numerous for rhodium and in certain Rh_{13}, Rh_{l4} and Rh_{15} anions have structures conveniently visualized either as polyhedra encapsulating further metal atoms, or alternatively as arrays of metal atoms forming portions of hexagonal close packed or body centred cubic lattices stabilized by CO ligands. $[Rh_{l3}H_3(CO)_{24}]^{2-}$ (Figure 3a) is typical.

The incorporation of interstitial or encapsulated heteroatoms is a common and stabilizing feature. Carbon is the most common and may originate from the solvent or from cleavage of a CO ligand. The carbido C contributes 4 electrons to the cluster bonding and in the 90-electron species $[Rh_6C(CO)_{15}]^{2-}$ features trigonal prismatic coordination of Rh_6 about the central C (Figure 3b). Even more complicated structures are found for the large rhodium clusters containing 2 carbido C atoms: $[Rh_{12}(C)_2(CO)_{25}]$ (Figure 3c); the cluster also has 14 pendant terminal CO groups, 10 μ-CO groups and one μ_3-CO. In contrast, $[Rh_{15}(C)_2(CO)_{28}]^-$ has individual 6-coordinate (octahedral) carbide C atoms symmetrically placed on each side of a central rhodium which itself has 12 rhodium nearest neighbours in addition to the 2 C atoms. Again, the approach to metal structures is notable and is one of the main

interests in constructing large clusters and studying their chemical and catalytic activity. The structures of compounds mentioned above are shown in Figure 3.

(a)   (b)   (c)
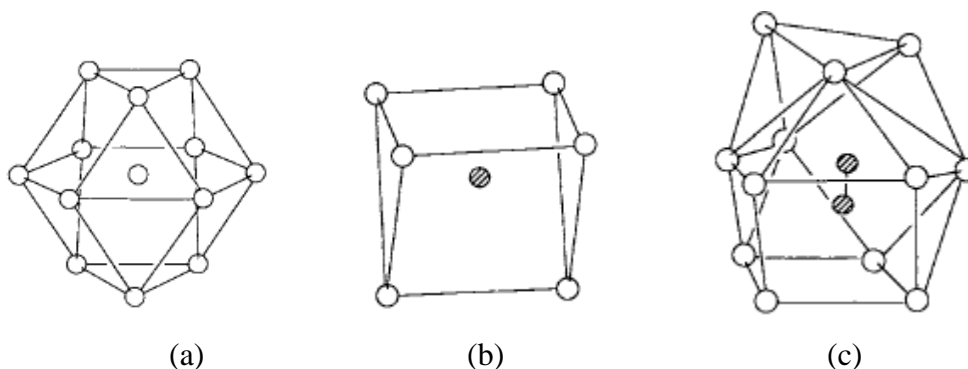
Figure 3 Schematic representations of the metal cores of some clusters;
(a) $[Rh_{13}H_3(CO)_{24}]^{2-}$, (b) $[Rh_6C(CO)_{15}]^{2-}$ and (c) $[Rh_{12}(C)_2(CO)_{25}]$.

Source: Martinengo *et al*. (1992)

H, P, As, S have also been encapsulated in ions such as [$Rh_{13}(H)_3(CO)_{24}]^{2-}$, $[Rh_9(P)(CO)_{21}]^{2-}$, $[Rh_{10}As(CO)_{22}]^{3-}$ and $[Rh_{17}(S)_2(CO)_{32}]^{3-}$. More recently N has been encapsulated in $[Rh_{14}(N)_2(CO)_{25}]^{2-}$ and $[Rh_{23}(N)_4(CO)_{38}]^{3-}$. The latter is the largest rhodium cluster so far characterized. It consists of an irregular polyhedron of 21 rhodium atoms encapsulating a pair of particularly close (257.1 pm) rhodium atoms as well as 4 N atoms each of which is located in a semi octahedral site.

Rhodocene, $[Rh(\eta^5\text{-}C_5H_5)_2]$, is also known but is unstable to oxidation and has a tendency to form dimeric species. However, the yellow rhodicenium cations are certainly known and are entirely analogous to the cobalticenium cation in their resistance to oxidation and susceptibility to nucleophilic attack.

6.   Platinum

Platinum was discovered by pre-Columbian South Americans and taken to Europe about 1750. Platinum is a metallic element of atomic number 78 and atomic weight 195.08. It is found the widest application due to its several properties. Platinum is a lustrous, silvery-white, malleable and ductile metal. It is unaffected by air and water, and will only dissolve in aqua regia (HCl/HNO_3) and molten alkali. Platinum is used in jewellery, anti-cancer drugs, catalysts and catalytic convertors. The properties of platinum are shown in Table 2.

The production methods of platinum are used by the alternative solvent extraction processes and ion exchange techniques as already shown in Figure 1.

7.   Properties of the platinum

Platinum is silvery-white and lustrous, and is both malleable and ductile. It is also readily obtained in finely divided forms which are catalytically very active. Platinum black is a velvety-black powder obtained by adding ethanol to a solution of $PtCl_2$ in aqueous KOH and warming. Another property of platinum which has led to numerous laboratory applications is its coefficient of expansion which is virtually the same as that of soda glass into which it can therefore be fused to give a permanent seal. Like rhodium and iridium, platinum has the fcc structure predicted by band theory calculations for elements with nearly filled d shells (Emsley, 1998).

The maximum oxidation state of platinum is +6 in PtF_6 and has no oxidation state below zero. For platinum, however, both +2 and +4 are prolific and form a vital part of early as well as more recent coordination chemistry. Platinum exhibits a strong preference for the square planar geometry. The kinetic inertness of platinum(II) complexes has led to their extensive use in studies of geometrical isomerism and reaction mechanisms. In the divalent state, platinum shows the class-b characteristic of preferring CN^- and ligands with nitrogen or heavy donor atoms rather than oxygen or fluorine. Platinum(IV) by contrast is more nearly class-a in character and is

frequently reduced to platinum(II) by P- and As-donor ligands. The organometallic chemistry of these metals is rich and varied and that involving unsaturated hydrocarbons is the most familiar of its type.

Table 2 Some properties of an elemental of platinum

Properties	Value
Atomic symbol	Pt
Atomic number	78
Atomic weight/g mol^{-1}	195.078
Electronic configuration	[Xe] $4f^8 5d^9 6s^1$
Density(20°C)/g cm^{-3}	21.45
Melting point/°C	1,769
Boiling point/°C	4,170
ΔH_{fus}/ kJ mol^{-1}	19.7($\pm$2.1)
ΔH_{vap}/ kJ mol^{-1}	469($\pm$25)
ΔH_f (monoatomic gas)/ kJ mol^{-1}	545($\pm$21)
Electronegativity (Pauling Scale)	2.2
Electrical resistivity (20°C)/$\mu\Omega$ cm	9.85
Metal radius (12-coordinate)/pm	138.5
Effective ionic radius (6-coordinate)/pm	
V	57
IV	62.5
III	-
II	80

Source: Greenwood (1997)

8.   Compounds of platinum

Platinum forms only one reasonably well-characterized oxide PtO_2, although the existence of many others has been made. The stable oxide of platinum is found, instead, in the higher oxidation state. Platinum can form a mono and a di-sulfide. Black PtS_2 is obtained when H_2S is passed through aqueous solution of platinum(IV) and green PtS are best obtained by heating $PtCl_2$, Na_2CO_3 and S. The only hexa- and penta-halides are the dark-red PtF_6 and $[PtF_5]_4$ which are both obtained by controlled heating of Pt and F_2. It is one of the strongest oxidizing agents known, oxidizing both O_2 (to O_2^+, $[PtF_6]^-$). Platinum alone forms all 4 tetrahalides and these vary in color. The diamagnetic "trichloride" and "tribromide" of platinum contain platinum(II) and platinum(IV) and the triiodide probably does also. Platinum dichlorides are less well-known (Krebs, 1988).

9.   Complexes of platinum

Apart from the few platinum(VI) and platinum(V) fluoro and oxofluoro compounds, there is no chemistry in oxidation states above +4. Platinum(II) and platinum(IV) are both thermodynamically stable and kinetically inert. The oxidation state +4 (d^6), K_2PtCl_6 is commercially the most common compound of platinum and the brownish-red, chloroplatinic acid, $H_2[PtCl_6]$(aq), is the usual starting material in platinum(IV) chemistry. It is prepared by dissolving platinum metal sponge in aqua regia, followed by one or more evaporations with hydrochloric acid. A route to chemistry is also provided by precipitation of the sparingly soluble K_2PtCl_6 followed by its reduction with hydrazine to K_2PtCl_4. The chloroammines were extensively used by Werner and other early coordination chemists in their studies on the nature of the coordinate bond in general and on the octahedral geometry of platinum(IV). In particular, O-donor ligands such as OH- and acetyl acetone also coordinate to platinum(IV), but S- and Se-, and more especially P- and As-donor ligands, tend to reduce it to platinum(II).

The oxidation state +2 (d^8), their complexes are diamagnetic and planar. Not many complexes are formed with O-donor ligands but, of the few that are, $[Pt(H_2O)_4]^{2+}$ ions, and the polymeric anhydrous acetates $[Pt(O_2CMe)_2]_4$ is the most important. Approximately square planar $[Pt(NO_3)_4]^{2-}$ anions containing the unusual unidentate nitrato ion are also known. Fluoro complexes are even less prevalent, the preference of these cations being for the other halides, cyanide, N- and heavy atom-donor ligands. The complexes $[PtX_4]^{2-}$ (X = C1, Br, I, SCN, CN) are all easily obtained and may be crystallized as salts of $[NH_4]^+$ and the alkali metals. Aqueous solutions of red $[PtC1_4]^{2-}$ are common starting materials for the preparation of other platinum(II) complexes by successive substitution of the chloride ligands. In both $[Pt(SCN)_4]^{2-}$ complexes the ligands bond through their π-acceptor (S) ends, though in the presence of stronger π-acceptor ligands such as PR_3 and AsR_3, they tend to bond through their N ends.

Complexes with ammonia and amines are among the first complexes of platinum to be prepared and interest in them. For example, the colorless $[Pt(NH_3)_4]C1_2 \cdot H_2O$ can be obtained by adding NH_3 to an aqueous solution of $PtCl_2$. Many substitution reactions are possible with these ammines. It is noticed that when there are alternative positions at which an incoming ligand might effect a substitution; the position chosen depends not so much on the substituting or substituted ligand as on the nature of the ligand *trans* to that position. This became known as the "*trans*-effect" and has had a considerable influence on the synthetic coordination chemistry of platinum(II). In 1969 B.Rosenberg and co-workers discovered the anti-tumour activity of *cis*-$[PtCl_2(NH_3)_2]$ (cisplatin). Binding of cisplatin to DNA appeared to be the central feature of the action and, since the *trans*-isomer is inactive, it was evident that chelation (or at least coordination to donor atoms in close proximity) is an essential part of the activity.

Stable complexes of platinum(II) are formed with a variety of S-donor ligands which includes the inorganic sulfite (SO^{3-}) and thiosulfate ($S_2O_3^{2-}$). The essentially class-b character of platinum(II) is further indicated by the ready formation of complexes with phosphines and arsines. $[Pt(PR_3)_2X_2]$ and the arsine analogues are

particularly well known. Zero dipole moment indicates that platinum complexes may be either *cis* or *trans*, the latter being much more soluble and having lower melting points.

10. Organometallic compounds of platinum

Platinum has played major roles in the development of organometallic chemistry. The first compound containing an unsaturated hydrocarbon attached to a metal was $[Pt(C_2H_4)Cl_2]_2$ and platinum methyls were among the first-known transition metal alkyls.

For σ-bonded compounds, platinum have been known since the beginning of this century and commonly involve the stable $(PtMe_3)$ group; and compounds of the divalent metals. In the platinum(II) compounds the metal is always octahedrally coordinated and this is frequently achieved in interesting ways. Moreover, platinum(II) are among the most stable σ-bonded organo-transition metal compounds.

On the basis of the 18-electron rule, the d^8s^2 configuration is expected to lead to carbonyls of formula $[M(CO)_4]$ and this is found for nickel. On the other hand, carbonyl complex of platinum is not stable. It may be added that the introduction of halides (which are σ-bonded) can reverse the situation: the colorless of $[PtX_3(CO)]^-$ are quite stable. Reductions of $[PtC1_6]^{2-}$ in an atmosphere of CO provide a series of clusters, $[Pt_3(CO)_6]_n^{2-}$ (n = 1-6, 10) consisting of stacks of Pt_3 triangles in slightly twisted columns; Pt-Pt = 266 pm in triangles, 303-309 pm between triangular planes. A feature of these and other platinum clusters is that they mostly have electron counts lower than predicted by the usual electron counting rules (Hao *et al*., 1995).

The cyclopentadienyls of platinum are less stable than those of nickel, and while the heavier pair of metals form some monocyclopentadienyl complexes, neither forms a metallocene. Alkene and alkyne complexes are important not only for their part in stimulating the development of bonding theory but also for their catalytic role in some important industrial processes (Albano *et al*., 1994). These are of the forms

[PtC1$_3$Alk]$^-$, [PtC1$_2$Alk]$_2$ and [PtC1$_2$Alk$_2$] which provide the most stable compound of this type. They are generally prepared by treating a platinum(II) salt with the hydrocarbon when a less strongly bonded anion is displaced. A common property of coordinated alkenes is their susceptibility to attack by nucleophiles such as OH$^-$, OMe$^-$, MeCO$_2^-$ and Cl$^-$.

11. Thiazolylazo dyes

Thiazolylazo dyes are organic compounds easily prepared by the diazotization of 2-aminothiazole and its derivatives. The intermediary diazotate form is highly reactive that it has to be coupled with aromatic substances in acidic solutions at low temperature (-5-0°C) to yield thiazolylazo dyes.

General appearances of thiazolylazo dyes are red, violet or brownish colors in their crystalline state. Most of these compounds are only partly soluble or water insoluble. Nevertheless, their solubility can be increased by the addition of organic (Bezerra, 2005) solvent such as chloroform, methanol, ethanol, dichloromethane, dimethylformamide, tetrahydrofuran and acetone. The general structure of thiazolylazo dyes is shown in Figure 4.

Azo dyes comprise the largest group of organic reagent used in spectrophotometric analysis. They are found in a variety of industrial applications because of their color fastness. These dyes are characterized by chromophoric azo group (-N=N-) offering a wide range spectrum of colors. They also used for coloring consumer goods such as leather, clothes, food, toys, plastic and cosmetics (Ahlstrom, 2005).
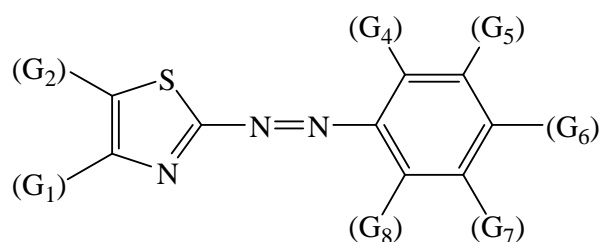
Figure 4 General structure of thiazolylazo dyes. G may be H, OH, NH_2, SO_3H, halogen atoms or other groups.

.

Source: Lemos (2007)

Thiazolylazo dyes are sensitive chromogenic reagents in addition to being interesting complexing agents, and have been used as reagents for spectrophotometry, solid phase extraction (Saeed, 2005) and liquid chromatography (Chen, 2005). The application in spectrophotometry is based on the colored compounds resulting from their reaction with most metals, especially some transition metals, usually stable chelate complexes are produced. They have been employed in separation procedures, because of their limited solubility in aqueous solution but greater in organic solvent. Some of them have also proved to be particularly useful as indicators in complexometric titrations.

The thiazolylazo dye derivatives chosen in this work are 2-(2'-thiazolylazo)-5-aminoanisole (*p*-amino TAA) and 4-(2'-thiazolylazo)-3-aminoanisole (*o*-amino TAA) which are structural isomers as shown in Figure 5. For *p*-amino TAA, it can form complex with paladium(II) (Songsasen, 1989) and for *o*-amino TAA, it is the new thiazolylazo compound that has been synthesized and studied in this work. Due to the platinum group metal relationship of rhodium(III) and platinum(IV) with palladium(II), *p*-amino TAA and *o*-amino TAA might act as a complexing agent with rhodium(III) and platinum(IV).

(a)

(b)
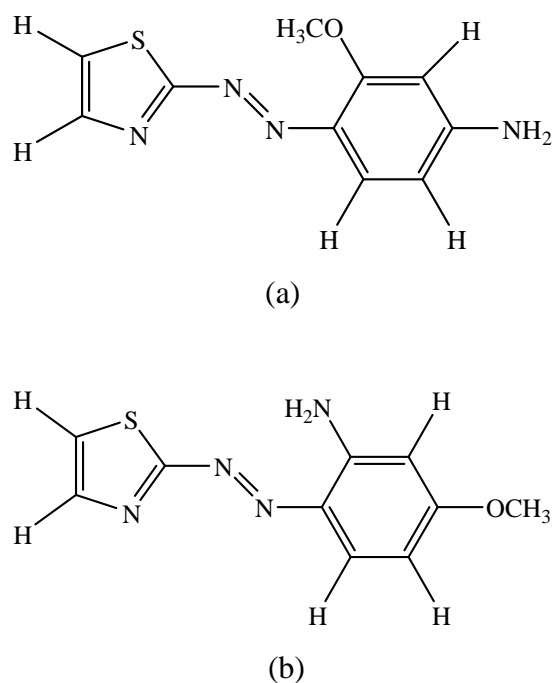
Figure 5 The structures of

    (a) 2-(2'-thiazolylazo)-5-aminoanisole (*p*-amino TAA) and

    (b) 4-(2'-thiazolylazo)-3-aminoanisole (*o*-amino TAA).

For the application, calf thymus DNA solution was prepared from DNA sodium salt from calf thymus. After that, the purity of DNA was studied by A260/A280 method (Warburg, 1942) and then DNA binding properties with the rhodium (III) complexes were investigated by experimental and theoretical study to calculate the energies and optimize the structures of nucleobases with rhodium(III)-(*p*-amino TAA) complex.

12. Complexation and stability constant

The complex formation between *p*-amino TAA and *o*-amino TAA with rhodium(III) and platinum(IV) are determined by using continuous variation method and mole ratio method for studying the ratio of metal ion and *p*-amino TAA and *o*-amino TAA in complex. The quantum chemical calculation is used to calculate the energy of complex formation between rhodium(III) and *p*-amino TAA for predicting the molecular geometry of the complex. Then, the possible structure and stability

constant of complex is studied. The determination of stability constant was performed by Benesi-Hildebrand's equation (Benesi, 1949) with continuous variation method (Connors, 1987).

12.1 Stability constant by Benesi-Hildebrand's equation

12.1.1 The stoichiometric ratio between metal and ligands is 1:2

The determination of equilibrium constant, K, the Benesi-Hildebrand's equation was applied from equilibrium reaction of complex.

$$M + 2L \xrightleftharpoons{K} ML_2 \qquad \text{------ (1)}$$

The equilibrium constant for the above reaction is defined by the equation

$$K = \frac{[ML_2]}{([M]-[ML_2])([L]-[ML_2])^2} \qquad \text{------ (2)}$$

Where $[ML_2]$ is molar concentration of the complex, $[M]-[ML_2]$ is molar concentration of free metal ion and $[L]-[ML_2]$ is molar concentration of free ligand.

From Beer's law, the true molar extinction coefficient, ε_0, of the complex at the wavelength of maximum absorption will then be given by the equation

$$\varepsilon_0 = \frac{A}{cb} = \frac{A}{[ML_2]b}$$

$$[ML_2] = \frac{A}{\varepsilon_0 b} \qquad \text{------ (3)}$$

In this reaction, ligand is added in excess. Therefore, $[L]$ is much more than $[ML_2]$. The $[ML_2]$ can be eliminated and the equation (2) can be rearranged and obtained as the relationship;

$$K = \frac{[ML_2]}{([M]-[ML_2])([L]-[ML_2])^2}$$

$$K = \frac{A/\varepsilon b}{([M]-A/\varepsilon b)(L)^2}$$

$$K = \frac{A}{\varepsilon b[M][L]^2-[L]^2A}$$

$$A = K\varepsilon b[M][L]^2 - K[L]^2A$$

$$K\varepsilon b[M][L]^2 = A + K[L]^2A$$

$$K\varepsilon b[M][L]^2 = A(1 + K[L]^2)$$

$$\frac{[M]b}{A} = \frac{1}{K\varepsilon[L]^2} + \frac{1}{\varepsilon} \qquad \text{------ (4)}$$

The equation (4) is "Benesi-Hildebrand's equation" which is in the form of the linear equation, $y = mx + c$.

12.1.2 The stoichiometric ratio between metal and ligand is 1:1

The determination of equilibrium constant, K, the Benesi-Hildebrand's equation was applied from equilibrium reaction of complex.

$$M + L \underset{\xleftarrow{\hspace{1cm}}}{\overset{K}{\xrightarrow{\hspace{1cm}}}} ML \qquad \text{------ (5)}$$

The equilibrium constant for the above reaction is defined by the equation

$$K = \frac{[ML]}{([M]-[ML])([L]-[ML])} \qquad \text{------ (6)}$$

Where [ML] is molar concentration of the complex, [M]-[ML] is molar concentration of free metal ion and [L]-[ML] is molar concentration of free ligand.

From Beer's law, the true molar extinction coefficient, ε_0, of the complex at the wavelength of maximum absorption will then be given by the equation

$$\varepsilon_0 = \frac{A}{cb} = \frac{A}{[ML]b}$$

$$[ML] = \frac{A}{\varepsilon_0 b} \qquad ------ (7)$$

In this reaction, ligand is added in excess. Therefore, [L] is much more than [ML]. The [ML] can be eliminated and the equation (6) can be rearranged and obtained as the relationship;

$$K = \frac{[ML]}{([M]-[ML])([L]-[\cancel{ML}])}$$

$$K = \frac{A/\varepsilon b}{([M]-A/\varepsilon b)[L]}$$

$$K = \frac{A}{\varepsilon b[M][L]-[L]A}$$

$$A = K\varepsilon b[M][L] - K[L]A$$

$$K\varepsilon b[M][L] = A + K[L]A$$

$$K\varepsilon b[M][L] = A(1 + K[L])$$

$$\frac{[M]b}{A} = \frac{1}{K\varepsilon[L]} + \frac{1}{\varepsilon} \qquad ------ (8)$$

The equation (8) is "Benesi-Hildebrand's equation" which is in the form of the linear equation, $y = mx + c$.

For the experiment, the concentration of rhodium(III) and platinum(IV) are fixed while the concentrations of ligands are varied. The equilibrium constant is obtained from the slope of the plotted between $[M]/A$ and $1/[L]$ or between $[M]/A$ and $1/[L]^2$.

12.2   Stability constant by continuous variation method

Another method for the determination of equilibrium constant is obtained from continuous variation method by using equation (2), where $[M]$ and $[L]$ are initial concentration of free metal ion and free ligand, respectively. $[ML]$ is equilibrium concentration of the optimum ratio of complex solution from continuous variation method which observed from equation (3). The extinction coefficient can obtained from linear calibration curve of complex solution.

12.2.1 The stoichiometric ratio between metal and ligands is 1:2

$$M + 2L \quad \underset{}{\overset{K_{stab}}{\rightleftharpoons}} \quad ML_2 \quad \text{------ (9)}$$
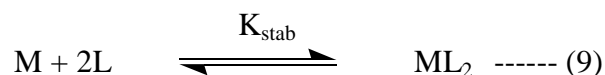
$$K_{stab} \; = \; \frac{[ML_2]}{[M][L]^2}$$

$$C_M = [M] + [ML_2]$$

$$[M] = C_M - [ML_2] = C_M - \frac{A}{A_{ex}} C_M \quad \text{when } [ML_2] = \frac{A}{A_{ex}} C_M$$

$$[L] = C_L - [ML_2] \; = C_L - \frac{A}{A_{ex}} C_L \quad \text{when } [ML_2] = \frac{A}{A_{ex}} C_L$$

$$ML_2]_{ex} \; = \; C_M$$

$$A_{ex} \; = \; \varepsilon b[ML_2]_{ex} \; = \; \varepsilon b C_M$$

$$A \; = \; \varepsilon b[ML_2]$$

$$\frac{A}{A_{ex}} = \frac{\varepsilon b[ML_2]}{\varepsilon b C_M}$$

$$[ML_2] = \frac{A}{A_{ex}} C_M$$

$$K_{stab} = \frac{\dfrac{A}{A_{ex}} C_M}{\dfrac{A}{A_{ex}}(C_M - \dfrac{A}{A_{ex}}C_M)(C_L - C_M)}$$

So, $$K_{stab} = \frac{\dfrac{A}{A_{ex}}}{\dfrac{A}{A_{ex}}(1 - \dfrac{A}{A_{ex}})(C_L - C_M)} \qquad \text{------ (10)}$$

12.2.2 The stoichiometric ratio between metal and ligand is 1:1

$$M + L \quad \xrightleftharpoons{K_{stab}} \quad ML \qquad \text{------ (11)}$$
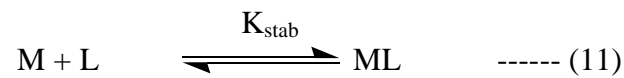
$$K_{stab} = \frac{[ML]}{[M][L]}$$

$$C_M = [M] + [ML]$$

$$[M] = C_M - [ML] = C_M - \frac{A}{A_{ex}} C_M \quad \text{when } [ML] = \frac{A}{A_{ex}} C_M$$

$$[L] = C_L - [ML] = C_L - \frac{A}{A_{ex}} C_L \quad \text{when } [ML] = \frac{A}{A_{ex}} C_L$$

$$[ML]_{ex} = C_M$$

$$A_{ex} = \varepsilon b[ML]_{ex} = \varepsilon b C_M$$

$$A = \varepsilon b[ML]$$

$$\frac{A}{A_{ex}} = \frac{\varepsilon b[ML]}{\varepsilon b C_M}$$

$$[ML] = \frac{A}{A_{ex}} C_M$$

$$K_{stab} = \frac{\dfrac{A}{A_{ex}} C_M}{\dfrac{A}{A_{ex}} (C_M - \dfrac{A}{A_{ex}} C_M)(C_L - C_M)}$$

So, $$K_{stab} = \frac{\dfrac{A}{A_{ex}}}{\dfrac{A}{A_{ex}} (1 - \dfrac{A}{A_{ex}})(C_L - C_M)} \qquad \text{------ (12)}$$

13. Quantum chemical calculation

The computational calculation has a potential role in the molecular modeling development. Molecular structure can be created in the virtual model on computer by bonding the elements into 3-dimension structure. The thermodynamic parameters and some physical properties can be calculated.

Ab initio was used as quantum chemistry method. This method indicates that the calculation is from first principles and that no empirical data is used. Each type of methods has several classes of electronic structure calculation. Density functional theory (DFT) is a quantum mechanical theory used in physics and chemistry to investigate the electronic structure of many-body systems, in particular atoms, molecules and the condensed phases. DFT is among the most popular and versatile methods available in condensed matter physics, computational physics, and computational chemistry. This theory uses the three parameter compound functions of Becke (B3LYP (Lee-Yang-Parr) correlation functional) as a hybrid functional with the 6-31G* basis set for all atoms except metal atom and electron core potential of

SDD which is mixed basis set for metal was used to calculate the energies of complexes between *p*-amino TAA and rhodium(III).

14. Calf thymus DNA (CT-DNA)

Calf thymus DNA is a deoxyribonucleotide polymer that is the primary genetic material of all cells. Eukaryotic and prokaryotic organisms normally contain DNA in a double-stranded state, yet several important biological processes transiently involve single-stranded regions. Calf thymus DNA usually used for a number of purposes, such as a substrate for DNA-modifying enzymes, in DNA-binding assays, as carrier DNA and a blocking agent in hybridization solutions (Sun, 2008). Calf thymus DNA has been used in many DNA researches and laboratories probably because it is available in large quantities, stable for long time and easy to handle.

Calf thymus nuclei are extracted from calf thymus cells by chopping up calf thymus tissue in a blender with a buffer containing a mild detergent to break the plasma membrane of the cells. The resulting mixture will be centrifuged in order to separate the large dense nuclei from organelles, fragments of membranes and soluble components. The centrifugal force developed the nuclei to collect at the bottom of the tube. Next, DNA will be liberated from the proteins found in chromatin. These nucleoprotein complexes will be dissociated using a detergent (sodium dodecyl sulfate) and the DNA will be precipitated in the form of long fibers using alcohol. In the presence of alcohol, DNA molecules precipitate as long fibers, whereas contaminating RNA molecules and proteins precipitate as finer particles (Anderson, 1987).

OBJECTIVES

The main objectives of this work are

1. To synthesize and characterize the ligands of 2-(2´-thiazolylazo)-5-aminoanisole (*p*-amino TAA) and 4-(2´-thiazolylazo)-3-aminoanisole (*o*-amino TAA).

2. To study the formation of rhodium(III) and platinum(IV) complexes with *p*-amino TAA and *o*-amino TAA.

3. To characterize the structures of the ligands and complexes by experimental methods and theoretical study via the calculation of stabilization energy of rhodium(III)-(*p*-amino TAA) complex.

4. To study the possibility in binding between rhodium(III)-(*p*-amino TAA) and rhodium(III)-(*o*-amino TAA) complexes and calf thymus DNA.

LITERATURE REVIEWS

The reviews studied the previous researches on synthesis of thiazolylazo dyes and their complex formation with various metal ions by several methods. The acid dissociation constants of organic compounds were studied to determine the dissociation constants of thiazolylazo dyes. Quantum chemical calculations of metal complexes including application in studying the interaction of their complexes with DNA are also reviewed.

1. Synthesis thiazolylazo dyes

Thiazolyl azo dyes have known and have been widely used in many analytical procedures for years. The main applications of thiazolylazo dyes in chemical operations include spectrophotometry, solid phase extraction, liquid chromatography, electrochemistry and liquid and cloud point extraction. The reviews have been focused on synthesis, characterization and application of new thiazolyl azo dyes in the pass 10 years.

Fan and Zhu (1998) synthesized three new thiazolylazo chromogenic reagents of the benzoic acid 2-[2-(6-methylbenzothiazolyl)azo]-5-(*N*-ethyl-*N*-carboxylmethyl) aminobenzoic acid (6-Me-BTAECB), 2-[2-(6-methylbenzothiazolyl)azo]-5-(*N*-methyl-*N* sulfomethyl) aminobenzoic acid (6-Me-BTAMSB) and 2-[2-(6 - methylbenzothiazolyl)azo]-5-(*N*-ethyl-*N*-sulfomethyl)aminobenzoic acid (6-Me-BTAESB). These compounds were synthesized by diazotization, coupling with 3-(*N*-ethyl-*N*-carboxylmethyl)aminobenzoic acid. For the application, these compounds were applied to the determination of nickel in aluminum alloy certified reference material and alloy steel certified reference materials. The results showed that 6-Me-BTAECB was one of the most sensitive reagents for the determination of nickel.

Matsui *et al.* (1998) synthesized bathochromic thiazolylazo having 2-hydroxyethyl group(s) in a molecule. These compounds were prepared by diazotization of 2-amino-5-chlorothiazole-4-carbaldehyde, coupling with anilines

which had different functional groups on nitrogen atom and then the mixture was refluxed with 3-cyano-6-hydroxy-2-pyridones for 30 minutes. All the compounds were studied in physical properties, absorption, decomposition temperatures and solubility. The films of these compounds were prepared and measured the relaxation behavior. The results indicated that tris(2-hydroxyethyl) derivatives gave the best relaxation behavior.

Georgiadou and Tsatsaroni (2001) synthesized and characterized four disperse dyes of amino-substituted thiazole and thiophene by diazotization of the heterocyclic amines followed by coupling with *N*-2-hydroxyethyl-1-naphthylamine. Diazo liquors of these compounds were slowly added into a solution containing *N*-2-hydroxyethyl-1-naphthylamine in a mixture of sulfuric acid, hydrochloric acid, or acetic acid-phosphoric acid (7:1), sulfamic acid and surfactant. The crude product was purified by recrystallization from ethanol which gave a solid violet to greenish-blue of azo dyes. The results from absorption spectra of benzoisothiazole and thiophene systems showed the significant bathochromic shifts compared to their phenyl analogues.

Maradiya and Patel (2001) synthesized a series of disperse dyes from 5-acetyl-2-amino-4-methylthiazole using various substituted *N*-alkyl-*N*-(2-hydroxyethyl) aniline derivatives as coupling components. The reaction took place readily on adding the diazonium salt to the solution of coupling component in acetic acid at 0-3°C. The purity of all the dyes were checked by TLC using methanol/ water/ acetic acid (12:3:7 v/v) as the solvent system and silica chromatography plates as the absorbent. The results from the absorption spectra indicated that the introduction of electron donating or electron withdrawing groups at suitable positions in the coupled ring affect the absorption characteristics of the dyes. The infrared spectra of dyes showed that bands at 820-830 cm^{-1} and 1515-1520 cm^{-1} corresponded to *para* disubstituted ring and azo group stretching, respectively.

Georgiadou and Tsatsaroni (2002) synthesized ruby-red to greenish-blue azo dyes by diazotization of heterocyclic amines, coupling with *N,N*-di-β-hydroxyethyl aniline and *N,N*-di-β-acetoxyethylaniline to study the effect of substituents in the

diazo component on the color shifts in these dyes by UV-Vis spectroscopy. The results showed that dyes derived from 2-methoxy-5-acetylamino-*N,N*-di-β-acetoxyethylaniline had absorption maxima at longer wavelengths than those of dyes derived from 3-acetylamino-*N,N*-di-β hydroxyethyl aniline. This result was caused by donor methoxy substituent in the coupling component of dyes which resulting in bathochromic shifts of these dyes.

Karet and Ertan (2002) synthesized hetarylazopyrazolone dyes by diazotization of five heterocyclic amines using nitrosyl sulphuric acid, coupling with 3-methyl-1-(3´,5´-dipiperidino-s-triazinyl)-5-pyrazolone. The infrared spectra of all the compounds showed carbonyl bands at 1651–1709 cm^{-1}. The visible absorption spectra of dyes showed the dyes spectra which depended on the types of solvents. The results indicated that the hetarylazopyrazolones existed in the tautomeric form in chloroform and acetonitrile, in the anion form in DMF and DMSO and in a partly dissociated form in methanol and acetic acid. The studies of substituent effects indicated that the electron-donor methyl and methoxy groups stabilized the excited state of the neutral form of the dyes whereas the strong electron-accepting nitro group stabilized the excited state of the common anion form of the dyes.

Wang *et al.* (2003) prepared bis(hetaryl)azo dyes by diazotization of hetarylamine and coupling with heteroaromatic. The compounds were characterized by UV-Vis spectroscopy. Thermo gravimetric differential thermal analysis (TG-DTA) which used to study the thermal stability of azo dyes showed an endothermic peak corresponding to melting at 161°C and then decomposed with exothermic peaks at 253 and 520°C, respectively. From the investigation, compounds having high melting point also have high decomposition temperature (T_d). The photostability study showed that the highly electron-withdrawing nature of the substituent gave the less stable of the dyes under UV irradiation.

Karet and Ertan (2005) synthesized some novel hetarylazocoumarin dyes by diazotization of nine heterocyclic amines using nitrosyl sulphuric acid, coupling with 4-hydroxy-2*H*-1-benzopyran-2-one (4-hydroxycoumarin). These dyes were

characterized by UV-Vis, FT-IR and ^{1}H NMR spectroscopic techniques and elemental analysis. The infrared spectra of all the compounds showed intense carbonyl bands at 1766-1678 cm^{-1} and broad hydroxy bands at 3536-3500 cm^{-1}. It can be suggested that these compounds existed as the azo-enol form in solid state. The ^{1}H NMR spectra measured in DMSO showed that the dyes existed as a mixture of several tautomeric forms in DMSO. The results from the study of solvent effects indicated that the hetarylazocoumarins existed in a dissociated state in methanol, DMSO and DMF.

Ren *et al.* (2005) synthesized two new fluorinated chromophores containing amino groups; 2,4-diamino-4′-fluoro-3′-nitroazobenzene (2R-4F-3N-DIAMINE) and 2,4-diamino-2′-fluoro-5′-nitroazobenzene (2R-2F-5N-DIAMINE), and a non-fluorinated analogue; 2,4-diamino-3′-nitroazobenzene (2R-3N-DIAMINE) as shown in Figure 6. Chromophores were synthesized through diazotization and coupling with 1,3-phenylenediamine and were characterized by ^{1}H NMR, ESI and elemental analysis. The theoretical calculations showed that fluorine in different positions in the structure can significantly influence the absorbance because the position of fluorine group affected the energy levels of the chromophores. The results from the decomposition temperatures study showed that the fluorinated chromophores had a higher thermal decomposition temperature than non-fluorinated analogues, possibly the presence of fluorine.
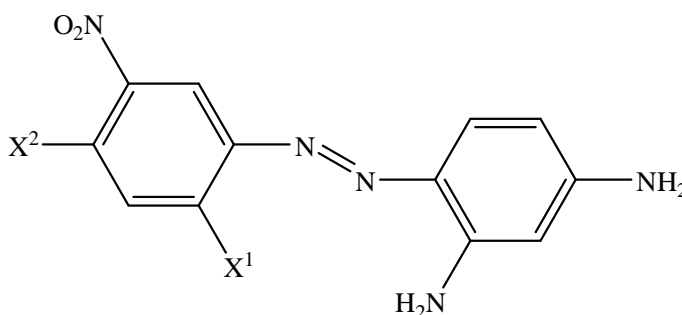
Figure 6 The structure of fluoronitroaryl azo diaminobenzene chromophores and non-fluorinated analogue.

Lui *et al.* (2007) synthesized the new azo-phophyrins, in which the azonaphthalene was in *para* position of the tetraphynylporphyrin and they were di- tri- and tetra- substituted. The compounds were synthesized by diazotization of amino-porphyrins and coupling with naphthol or naphthylamine. The azo-porphyrin dyes were characterized by FT-IR, ^{1}H NMR, ESI-MS and UV-Vis spectroscopic techniques. The IR spectra of chromophores showed a weak band within the range 3483-3395 cm^{-1} corresponding to υ_{OH} and υ_{NH} of each compound which corresponding to the intramolecular hydrogen bonding in compounds. The fluorescence peak intensity decreased significantly in the order of di-, tri- and tetra-azo group substituted compounds. These results indicated that substantial amount of electron transfer occurred from the azonaphthalene group to the porphyrin chromophore in the excited state. Owing to fluorescence quenching, they were potentially capable of molecular sensing or switching applications.

2.   The acid dissociation constants

Perigic-Janjic *et al.* (1973) studied the acid dissociation of arsenazo-*p*-NO$_2$, structure as shown in Figure 7, and reaction of lanthanum with this reagent. Arsenazo-*p*-NO$_2$ in slightly acidic solution (from 1N to pH 6) had an absorption spectrum with a maximum at 545 nm. Upon the increasing the pH from 1 to 6, dissociation of sulfo and arsono groups occured, but the absorption spectrum of the reagent remained unchanged. With further pH increase, dissociation of OH groups from the naphthalene ring took place and effected to the absorption spectrum. The result showed that the maximum absorption at pH 8 was shifted toward longer wavelength (580 nm). This can be attributed to the dissociation of the first OH group of the naphthalene ring. The dissociation constant (K_a) can be calculated by the relation pK_a = pH-log (R$^-$)/(HR) when (R$^-$) and (HR) were the concentration of reagent in ionic and neutral forms, respectively. The result showed that pK_a of arsenazo-*p*-NO$_2$ is 7.40. The reaction of lanthanum with this reagent was studied according to Beer's law. The results showed that Beer's law was valid from 5 to 50 μg of lanthanum per 25 ml. The molar absorptivity calculated from Beer's law was 6.2×10^4. All these indicated that

arsenazo-*p*-NO$_2$ was very sensitive reagent for spectrophotometric determination of lanthanum.
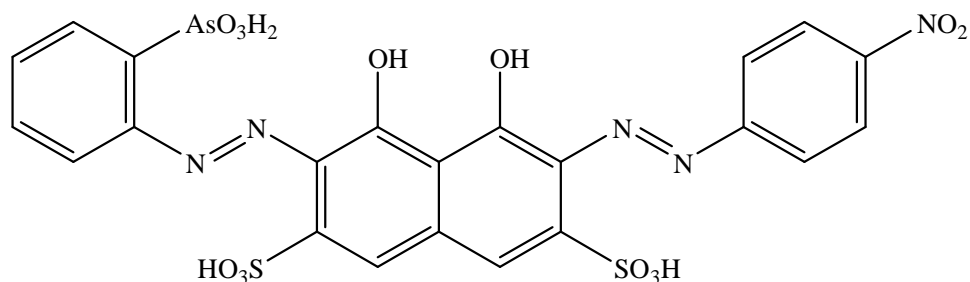
Figure 7 The structure of arsenazo-*p*-NO$_2$.

Ertan and Gürkan (1997) synthesized azo pyridone dyes by the coupling of 3-cyano-6 -hydroxy-4-methyl 2 (IH) pyridone with diazotized *para* and *meta* substituted anilines. The acid dissociation constants of the dyes were determined by measuring the pH and the absorbance by spectrophotometric technique of the dyes in either the ionic medium or 80% (v/v) ethanol as a blank. The pH of the sample solutions were increased by addition of small volume of concentrated carbonate-free potassium hydroxide. The value of the pK_a was calculated from the data and using the equation pK_a = pH$_i$ + log(A$_a$ - A$_i$)/(A$_i$ - A$_b$). The absorption spectra showed two maxima in the ranges of 416-430 nm and 445-494 nm for the anionic and molecular species, respectively. As the pH value of the solution increased, the height of the former band increased and the latter band decreased. Spectra recorded at different pH values in each case showed an isosbestic point. This indicated that two species were in equilibrium. The pK_a values of the dyes were found to be within the range of 6.98-8.57.

Mitchell *et al.* (1998) studied the acid dissociation constants (pK_a) of multi-protic histamine H$_2$-receptor, namely icotidine (SK&F 93319), lupitidine (SK&F 93479) and SK&F 93944 by a multiwavelength spectrophotometric (WApH) titration method over the pH range of 2–10. The result showed that the pK_a values as

determined using the WApH method were in agreement with those obtained from the pH-metric titration. Spectral data was recorded in the region of 210–350 nm and calculated by the SPOIL function. The concentration was related to the operational pH reading by a multi-parametric equation. These results showed that the WApH technique could determine the pK_a values in excellent agreement with those measured using a conventional pH-metric method.

Ibrahim *et al.* (1999) studied the electronic spectra of 5-amino-4-(arylazo)-3-methyl-1-phenylpyrazole derivatives in buffer solutions containing various organic solvents with different polarities. The acetate buffer solutions were used to control the pH and the spectra were measured in the wavelength range of 240-580 nm. The acid dissociation constants were determined from the variations of the absorbance with pH by using three different methods namely, half-curve height, isobestic point and limiting absorbance method. The results showed that pK_a values decreased within an increase of the organic cosolvent content. This was due to the high stability constants of the free base by hydrogen bonding in pure aqueous in comparison to that in the presence of organic solvents. From the investigation, the pK_a values increased according to the following sequence DMF< acetone< ethanol<methanol, respectively.

Bartak *et al.* (2000) studied the dissociation constant of 6-benzylaminopurine (BAP) by ultraviolet spectrometry. The relation of pK_a to absorbance was assigned as pK_a = pH – [log(A-A$_{BH}$$^+$)/(A$_B$-A)]+ logγBH. The equation of sigmoidal curve was obtained by mathematical transformation in form

$$A = \frac{A_{BH}}{1+10^{(pH-pKa+\log \gamma BH)}} + \frac{A_{BH}}{1+10^{(pKa-pH-\log \gamma BH)}}$$

The neutral molecule of BAP exhibited the absorption band at 270 nm and protonation of BAP shifted the maximum wavelength to 275 nm. The pH-absorbance curve at 280 nm was used to obtain the sigmoidal curve. The result from UV-spectrometry was corresponded with the result from computer fitting, so this method was used as a standard procedure for the measuring of pK_a values.

Perez-Urquiza and Beltran (2001) studied the dissociation constants of sulfonated azo dyes by two different systems, capillary electrophoresis (CE) and UV-Vis absorption spectrophotometry. For CE method, the electrophoresis buffers were used in the pH range between 5.6-12.0 and the absorbance from 275-550 nm. The pK_a determination was based on the principle that the total ionized form gave the highest electrophoretic mobility, the total protonated form gave the lowest mobility and in the pH region of its pK_a gave an intermediate mobility. The relationship between dissociation constant, pH and electrophoretic mobilities was $pK_a = -\log[H^+] - \log(m_e-m_a/m_b-m_e)$ (m_e = the electrophoretic mobility at the pH of the buffer in the capillary electrophoresis column, m_a = the electrophoretic mobility of the fully ionized acid and m_b = the electrophoretic mobility of the protonated species). The results from this method were corresponding to the result form UV-Vis spectrophotometry method. So, it was possible to determine the pK_a values by capillary electrophoresis.

Masoud *et al.* (2003) studied structures and chemical equilibria of 5-carboxy-2-thiouracil (**1**), 5,6-diphenyl-3-hydroxy-1,2,4-triazine (**2**), 1-phenyl-3-methyl-5-pyrazolone (**3**) and 2-mercapto-4,6-dimethylpyrimidine hydrochloride (**4**) by heating a mixture of all solutions under reflux for 3 hours. All compounds which formed in a solution of different pH were characterized by absorption spectroscopy to explain the mechanism of ionization of such compounds and to evaluate their dissociation constants (pK_a). The pK_a were obtained from the absorbance-pH curves by application of the half height method, the modified limiting absorption method and the colleter method. The results from the half height method showed that the dissociation constants of (**1**) were 4.7 and 7.7, (**2**) are 4.3 and 7.6, (**3**) is 8.1 and (**4**) are 3.6 and 8.1 at 335 nm, respectively. Besides, the results from the modified limiting absorption and the colleter methods also corresponded to the half height method.

Wojciechowska *et al.* (2003) synthesized the azo compound by diazotization and coupling of 8-amjno- naphthalene-2-sulfonic acid (CA-CA). The structure was characterized by NMR, FT-IR, UV-Vis which compared with the spectra from MM/PM5 followed by ZINDO calculation method. The first dissociation constant of the dye was also studied. The UV-Vis spectra showed a maximum absorption at 470

nm upon increasing of pH, the absorption band was shifted toward longer wavelength at 534 nm. The isobestic point at $\lambda = 499$ nm indicated the compound occurrence in two forms at equilibrium. The first constant of dissociation corresponding to the equilibrium of the azo compound was determined as 2.75×10^{-2}. The results from FT-IT can indicate the protonation in compound from the shift of wavenumber in IR spectra. The calculated structure of CA-CA showed a very good correlation between their azo bond lengths and torsion angles and also corresponded to the result from the experiment.

Yazdanbakhsh *et al.* (2007) synthesized a series of coumarin by diazotization of aniline and its derivatives, coupling with 4-hydroxy coumarin. The –OH group of coumarin in synthesized dyes was confirmed by IR spectra. The spectra also showed typical lactone carbonyl group at 1732-1745 cm^{-1} and azo group (-N=N-) at 1470-1508 cm^{-1}. The ^{1}H NMR spectra of the dyes, which have –CH$_3$ group on diazo component showed the different chemical shifts in the *ortho, meta* and *para* position of the substituent. ^{1}H NMR spectra were also exhibited a broad signal near 14.2-14.4 ppm, indicating a NH proton resonance of the hydrazone form. Electronic absorption properties of the dyes were also studied. The results showed that introduction of an electron donor substituent into diazo moiety produced bathochromic shift, whereas electron acceptor substitutent produced hypsochromic shift. The acid dissociation constants (pK_a) were determined by the spectrophotometric titration method. In basic solution, the spectra show lower absorption wavelength which assigned to anionic form. So, log (AH$_{In}$−A$_i$/A−A$_{In}^-$) at each λ_{max} against the pH of the solution were plotted. From the intercept, the pK_a values of the dyes were determined. The results showed that electron withdrawing groups can reduce the electron density on the aromatic rings resulting in the increasing of pK_a values. On the other hand, electron donating groups such as –OEt and –CH$_3$ can decrease the acidic character resulting in the decreasing of the pK_a values.

Razus *et al.* (2009) synthesized azo-benzene derivatives, substituted with (azulene-1-yl)-azo group and compared some properties of these compounds with those of the corresponding derivatives that contained only phenyl and phenylene

moieties. From the electronic spectra, the visible absorption maximum was well defined and had a high molar extinction coefficient. The substitution of azo-benzene with phenylazo moiety had a small influence on the electronic spectra. It was also observed that there was the change in color with the pH modification, so the acid dissociation constant (pK_a) values of their conjugated acids were determined. The pK_a values can be considered as equal to the pH value when the absorptions of the base and conjugated acid of the dyes are 50% of the maximum values of the bands. The results showed that the pK_a values increased smoothly with the azulenyl alkylation due to their inductive effect.

3.   The complexes between transition metal ions and thiazolylazo dyes

Lihong and Fulong (1996) synthesized 2-(2–thiazolylazo)-5-[(*N,N*-dicarboxymethyl) amino] benzoic acid (TADCAB), the newly water-soluble reagent, by introducing (*N,N*-dicarboxymethyl)amino into the benzene ring. TADCAB was characterized by elemental analysis and spectroscopy techniques. The acid dissociation constants K_{a1} and K_{a2} were 0.88 and 4.28, respectively. The complexes between TADCAB and the 29 kinds of the metal ions were synthesized and characterized to study their color reactions. The results showed that the sensitivities of TADCAB reacting with copper(II), nickel(II), cobalt(II), vanadium (V), and palladium(II) were relatively high. The reaction of palladium with TADCAB was further studied to determine the microamounts of palladium in Pt/Pd catalysts by the dual-wavelength method. The results indicated that this method agreed well with the data obtained by atomic absorption spectrophotometry with good results.

Nonoyama and Nakajima (1998) studied the interaction of 2-(2-pyridyl) benzeo[b]furan (Hbpf), 1-(2-pyridyl)indole (Hpyi) and 1-(2-pyrimidyl)indole (Hpmi) with palladium(II) acetate and trichlorobis(tri-*n* butylphosphine)rhodium(III). The complexes were synthesized by keeping a mixture of these ligands and $Pd(OAc)_2$ in acetronitrile solution under reflux giving the product of $[Pd(NO_2)(L)(CH_3CN)]$ (L = bpf, pyi or pmi). The formation of NO^{2-} was unexpected and was assuumed to result from the oxidation of CH_3CN catalyzed by metallic palladium by-produced during the

reaction. Rhodium complexes were also synthesized by mixing of these ligands with RhCl$_3$(PBu$_3$)$_2$ (PBu$_3$ = tri-*n*-butylphosphine) in toluene solution to give [RhCl$_2$(L)(PBu$_3$)$_2$]. These complexes were characterized by spectroscopic methods. The IR spectra showed two strong bands which assigned to v(Rh-Cl) indicating *cis* coordination of the two Cl donor atoms. The structures of these complexes were confirmed by X-ray analysis.

Alder *et al.* (1999) studied the reaction of Na[MCl$_4$] (M=Pd or Pt) with the azo-containing phosphines Ph$_2$P{1-(4-RC$_6$H$_4$N$_2$)-2-OR′-C$_{10}$H$_5$} {R=Me or NMe$_2$; R′=C(O)Me} which afforded the complexes in good yield. The complexes were characterized by elemental analysis, ^{1}H-, ^{13}C{^{1}H}-, and ^{31}P{^{1}H}-NMR spectroscopy and UV–Vis spectroscopy. The complexes were investigated in the Heck reaction, the reaction between unsaturated halide and alkene in the presence of catalysts. The palladium complexes were used as the catalysts in the coupling reaction. The results showed that the palladium complexes containing azo-functionalised phosphines can be prepared and were reasonably used as the catalysts for the Heck reaction.

Rauth *et al.* (2001) studied the reaction of 2-(arylazo)pyridines (aap) with K$_2$PtCl$_4$ which gave the product Pt(aap)Cl$_2$. The addition of catechols to a solution of Pt(aap)Cl$_2$ yielded complexes with the formula Pt(aap)(cat) (cat = catecholate). The complex of Pt(aap)Cl$_2$ was prepared by mixing of K$_2$PtCl$_4$ with 2-(arylazo)pyridines in CH$_3$CN under reflux for 24 hours. Pt(aap)Cl$_2$ was dissolved in CHCl$_3$ and the solution of catechols were slowly added followed by triethylamine under N$_2$. The absorption spectra of Pt(aap)(cat) complex was different from their parent complexes. The most significant difference of the spectra was the new band in near-IR region which assigned as a ligand to ligand charge transfer (LLCT) transition. In catecholato complexes Pt(aap)(cat), the ^{1}H NMR signals showed an upfield shift compared with the parent compound Pt(aap)Cl$_2$. This might be attributed to charge transfer from the catecholato group to platinum(II) ion. The redox properties of the complexes were also studied by cyclic voltammetry. Pt(aap)Cl$_2$ gave two responses and Pt(aap)(cat) gave four responses for redox processes at negative potential. The two couples were

due to the azo reduction and others due to the oxidation of catechol to be semiquinone and quinone, respectively.

Kaim *et al.* (2003) studied the oxidative coupling of of 2-aminopyrimidine (abpy) with LiOCl to produce 2,2′-azobis(5-chloropyrimidine) (abcp) which increase the π- acceptor capacity of abpy ligand. The abcp ligand was characterized and the results showed that abcp had a twisted conformation in the crystal, appproacing a *trans* configuration. The N=N double bonds had typical length 1.246 A^o for azoaromatics. The ligand abcp was reacted with complexes to give (μ-abcp) [Cu(PPh$_3$)$_3$]$_2$}(PF$_6$). The results from spectroscopy methods and structure analysis showed the radical nature of the isolated dicopper complex. The superior π-accepting capability of the abcp ligand was evident from the shift to more positive in reductive potentials of the ligand and its complexes from cyclic voltammetry. The complex of abcp radical showed decrease and hypsochromic shift in MLCT features which indicated the concept of stabilized π* orbital of abcp. The structure of complex was also confirmed by DFT calculations on the radical cation model which indicated that the experiment could be supported by DFT calculations. All these results indicated that the metal complex fragments showed the strong π-accepting bis(chelate) of abcp ligand.

Castro *et al.* (2004) studied the structure, stability and molar absorptivity of the complex between AlCl$_3$ and 5,7-dihydroxy-flavone (**1**) in methanol. The UV-Vis spectrum of (**1**) was shifted to the higher frequency after forming complex with AlCl$_3$. The stoichiometry of the complex was performed by molar ratio and continuous variation methods. The results showed the stoichiometric composition of the complex formed is 1:2. The stability constant (K_C) of the complex showed the high value of K_C 4.55×10^{11}. The structural properties of the complex were obtained by the quantum semi-empirical AM1 method. It was evident that the ligand sufferd some structural changes when it reacted with AlCl$_3$. From the quantum calculation, it was obvious that the simultaneous increased of a bond length and the charges of the implied atom can increase the polarization of the bond and dipole moment of the complex molecule. This explained the higher dipole moment of the complex than that of free ligand.

From the results, it can be concluded that two classes of metal-ligand interactions were involved in the formation of the complex, two covalent bonds between the aluminum atom and the oxygen atoms of *o*-hydroxyl groups of (**1**) and coulombic interactions between the aluminum atom and the carbonyl oxygen atoms of the ligand.

El-Shazly *et al.* (2004) prepared several ligands and complexes of thiosemicarbazone derivatives with Ni(II). Structures of the ligands and their complexes were characterized by using elemental analysis, magnetic moment, spectral and thermal studies. Most of these ligands had melting point below 245°C. The thermal decomposition of some ligands and complexes were recorded at temperature 30–1000°C. The TG thermograms of complexes corresponded to the expulsion of water of crystallization or coordination. The end products for most complexes were NiS or NiO. The activation energies calculated in the TG thermograms of the ligands and complexes were in the ranges 83.9–127.7 and 164.0–304.0 kJ mol^{-1}, respectively. The cyclic voltammogram of the complexes showed that the Ni(II) compounds were reduced and oxidized to form the Ni(I) and Ni(III) compounds by the strong reducing and oxidizing agents, respectively. The redox capability of Ni^{I}/Ni^{II} and Ni^{II}/Ni^{III} was resulted from solvents, electrolyte solutions and structures of ligands and complexes.

Abildgaard *et al.* (2006) synthesized and characterized the complexes of platinum(II), nickel(II) and palladium(II) with three *o,o´*-dihydroxydiarylazo dyes. 5, 5´-dichloro-2, 2´-dihydroxyazobenzene (dhabH$_2$) was prepared by coupling and reduction reaction. 2-(5-chloro-2-hydroxyphenylhydrazo)-3-oxo-*N*-phenylbutanamide (hpabH$_2$) and 2-(5-chloro-2-hydroxyphenylazo)-2-naphthol (hpanH$_2$) were prepared by diazotization followed with coupling reaction. Their complexes with platinum(II), nickel(II) and palladium(II) were synthesized by mixing the solutions and reflux for 1 hour. The structures of the complexes were confirmed by XRD, NMR (^{13}C Chemical Shift) and compared with the theoretical calculation by *ab initio* method. The results showed that the calculated structures and the calculated ^{13}C chemical shifts corresponded well to the X-ray structures and the measured ^{13C} chemical shifts in solution showing that the structures were the same in the solid and in solution.

Senapoti *et al.* (2006) studied the reaction between 2-(arylazo)pyrimidine (aapm) which were *N,N'*-chelating ligands with K_2PtCl_4 to give the product Pt(appm)Cl_2. The reaction of Pt(appm)Cl_2 with $C_6H_5NH_2$ were also synthesized under reflux for 4 hours to give Pt(aapm-*N*-C_6H_5)Cl. The arylamination of $C_6H_5NH_2$ took places at the *ortho* position to azo group of aapm and formed platinum(II) complex of tridentate *N,N',N''*-chelating ligand. The structure of Pt(aapm-*N*-C_6H_5)Cl is shown in Figure 8. The FT-IR spectra showed the elongation of N=N azo of complex in comparison to that of the free ligand aapm which was due to the electron donation of ligand to platinum(II) ion. The spectral data showed the low energy band in Pt(aapm-*N*-C_6H_5)Cl which was associated with HOMO→LUMO charge transfer. From ^{1}H NMR, a significant observation was that azo-aryl protons in Pt(aapm-*N*-C_6H_5)Cl were shifted to highfield relative to Pt(appm)Cl_2. The structures of complexes were also characterized by X-ray crystallography.
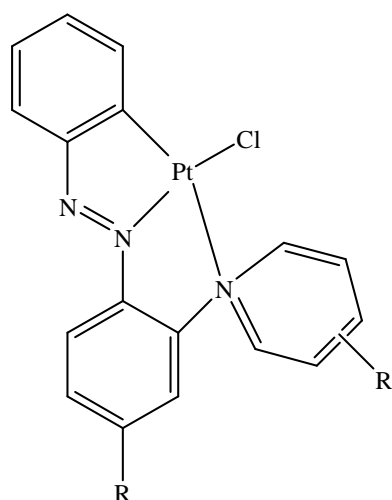
Figure 8 The structure of Pt(aapm-N-C$_6$H$_5$)Cl.

Chen *et al.* (2007) synthesized the azo dye by using a diazo component ((2-aminothiazole-4-yl) acetic acid) and a coupling component (3-(N, N-diethylamino) trifluoromethanesulfonanilide) and purified by column chromatography. The complexes of the azo dye with copper(II) and nickel(II) were also synthesized. Their structures were confirmed by elemental analysis, UV–Vis spectroscopy, FT-IR, ^{1}H NMR and MALDI-MS. The results indicated that the molar ratio of metal to ligand

was 1:2. The thin films of complexes were prepared on single crystal silicon substrates by the spin-coating method. The absorption spectra of the metal–azo complexes thin films were compared with the absorption spectra of the azo dye and a metal complex film, respectively. From the differences and the shifts of absorption spectra suggested that the complexes had formed.

Garza-Ortiz *et al.* (2007) synthesized the new Au(III) coordination compound with the ligand 2-(phenylazo)pyridine and characterized by various techniques. Dichlorido{2-(phenylazo)pyridine}gold(III) chloride dihydrate, [Au(azpy)Cl$_2$] Cl$\cdot$2H$_2$O (abbreviated: *Au-azpy*): was synthesized by keeping the mixture solution under reflux for 1 hour. The IR studies showed the changes in spectrum of *Au-azpy* comparing to the free ligand and also showed the characteristic peak assigned to Au-Cl bond at 352cm^{-1} which was accordance with a chloride ion in a *trans* position to the nitrogen of the azo group as shown in Figure 9. The electronic spectra showed that the energy of the $\pi \rightarrow \pi^*$ transition in a free azpy at 315 nm was lower than *Au-azpy* at 335 nm which was corresponding with coordination of *azpy*. Cytotoxicity activities were studied by using tumor cell lines and murine cell. The *Au-azpy* showed high cytotoxic activity in the human solid tumors, but lower toxicity in leukemia cells. This evidence indicated that *Au-azpy* was able to travel inside the cells.
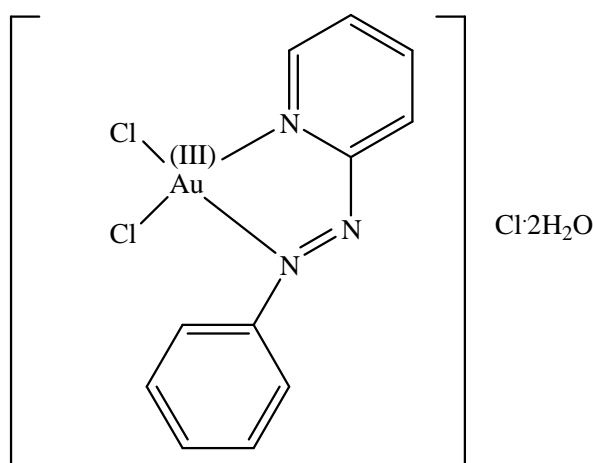
Figure 9 The structure of *Au-azpy* compound.

Mansouri and *et al.* (2007) prepared the cyclometalated Rh(III) complex, $[Rh(phpy-\kappa^2N,C^{2'})_2(phen-dione)]PF_6$, where phpy-$\kappa^2$N, $C^{2'}$ was pyridine-2-yl-2-phenyl and phen-dione was 1,10-phenanthroline-5,6-dione, respectively. The complexes were characterized by elemental analysis, IR, ^{1}H NMR and electronic absorption spectroscopies, cyclic voltammetry and X-ray crystallography. The cyclic voltammogram showed that two reversible reduction couples of $[Rh(phpy-\kappa^2N,C^{2'})_2$ (phen-dione)]PF_6 were assigned to the reduction of phen-dione ligand to phen-semiquinonate and phen-diolate, respectively. Furthermore, the mononuclear $[M(phpy-\kappa^2N, C^{2'})_2(N-N)]^+$ series were also investigated which shown that the reduction of the pyridine-2-yl-2-phenyl ligands took place at the low potential energy. These results indicated that the coordinating N–N ligands (phen or bpy) were much easier to reduce than the orthometalated pyridine-2-yl-2-phenyl ligand. Besides, the crystal structure of $[Rh(phpy-\kappa^2N,C^{2'})_2(phen-dione)]PF_6$ in acetonitrile showed that the coordination geometry around the Rh(III) was a distorted octahedron for the three bidentate ligands.

Steyl (2007) synthesized the rhodium(I) complexes, [Rh(TropNMe)(CO) (PPh$_3$)] (TropNMe = 2-(*N*-methylamino)tropone, C_8H_9ON) and [Rh(Trop)-(CO) (PPh$_3$)]˙acetone (Trop = Tropolone, $C_7H_6O_2$) and characterized by single-crystal X-ray diffraction analysis. A distorted square planar geometry of the rhodium(I) metal center was also studied and indicated that the changes in geometrical parameters depending on a methylamino moiety on the troponoid ring system did not seem to affect the coordination to the rhodium(I) center. Substitution of an oxygen atom with a methyl functionalized nitrogen atom did not significantly alter the bond distances and angles in the rhodium(I) complex. A theoretical study at B3LYP/6-31G(d) (main group) and LANL2DZ (Rh) level was presented to clarify the solid state behavior of these complexes. The calculated result confirmed the similarity of the structural between Rh(TropNMe)(CO)(PPh$_3$)] and [Rh(Trop)-(CO)(PPh$_3$)]˙acetone.

Szymczyk *et al.* (2007) synthesized and characterized dye ligands containing *ortho*-trifluoroacetamido or mesylamido groups in the diazo components. The iron complexes with azo dyes were also synthesized to compare the acidity and metallizing

properties with an *ortho*-OH group. The conversion of these dyes to their complexes
1:2 Fe complexes was conducted in DMF/H_2O using Fe(III) sulfate in the presence of
NaOAc. The molecular modeling studies using semi-empirical method with DFT
calculations showed that the electron density at N-22 was significantly diminished by
the electron-withdrawing power of the CF_3 moiety which causing the inhibiting
complex formation. The calculated structure is shown in Figure 10 (X = $COCF_3$).
From negative ion FAB mass spectrometry, a weak molecular ion [M^+] peak and a
strong pseudo molecular ion [M-Na]$^-$ peak were detected. The absorption spectra
showed that Fe-atom into dyes caused a 20-nm bathochromic shift in λ_{max} and an
increase in ε_{max}. The color strengths and light fastness studies showed that the
presence of azo and formazan dye ligand were not influent to Fe-complex formation
when an *ortho*-NHCOCF$_3$ group of trifluoroacetamido component replaced an *ortho*-
OH group.
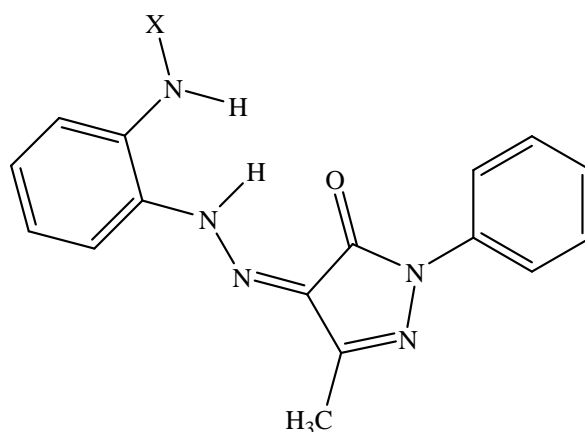
Figure 10 The calculated structure of *ortho*-trifluoroacetamido or mesylamido
groups (X = $COCF_3$ or SO_2Me).

4. Quantum chemical calculation

Kishner *et al*. (2000) used Density functional (DF) and MØller-Plesset second
order perturbation (MP2) calculations to study on *N*-acetyl-duocarmycin SA (*N*-Ac-
DSA). These levels were used to determine the degree of ground state destabilization
of the ligand along with examination of structures and electronic changes that could
cause the enhanced rate of DNA alkylation. The conformation of *N*-Ac-DSA and

protonated *N*-Ac-DSA was calculated to study the effect of proton on the structure. The results showed that the protonated species appeared to be influenced more by changes in the torsion angles than the neutral species. The electronic energies, the molecular geometries, partial charges, HOMO and LUMO differences of *N*-Ac-DSA in gas phase, DNA-unbound and DNA bound *N*-Ac-DSA were examined for evidence of disruption of electron delocalization. The results suggested that the binding-induced changes in the ligand structure can result in large changes in reactivity. In addition, bond lengths changes upon protonation were of the magnitude which was suggested to account for ligand activation due to ground state destabilization. These concluded that the changes in ground state stabilization energies may not fully account for the significant rate increasing of alkylation of *N*-Ac-DSA upon binding to DNA.

Andre *et al.* (2007) studied the formation of a complex between Al(III) and protocatechuic acid (PCAH) by electronic absorption spectroscopy in acidic aqueous and in methanol. The structural, electronic and optical properties were also studied by the DFT/TD-DFT calculations with 6-31G(d,p) basis set. For the free and complexed forms, harmonic vibrational frequency calculations were performed to ensure that the optimized structures corresponded to the minimum energy. The calculation of the stability constants of the two complexes indicated that the formation of complex was occured easier in methanol than in acidic aqueous. The frontier orbitals of $[AlPCAH(H_2O)_4]^+$ had the difference in energy compared to the free PCAAH which explained the bathochromic shifts observed upon complexation. The results from electronic spectroscopy and quantum chemical calculations were in good agreement with those obtained for other ligands involving the same complexing group.

El-Gogary and Koehler (2007) studied the interaction of psoralen and 8-methoxy psoralen (8-MOP) with DNA-bases; thymine, adenine and thymine-adenine base pair by using high level quantum chemical method, an *ab initio* quantum chemical. The calculations were performed by using DFT, HF and MP2 methods with correlation functional B3LYP. Different basis sets were used with these methods as 6-31G(d,p) and (cc-pVDZ). The results showed that psoralen molecule had a planar

geometry, on the other hand, 8-MOP was not fully planar due to out of plane of methoxy group. The optimized structures of these compounds are shown in Figure 11. The calculated natural atomic charges of compounds were studied via the dipole moment and polarizability. The results showed the high values for these values which suggested that the electrostatic contribution played a role in the interaction with nucleobases. The interaction of compounds was calculated for both co-planar and stacked complexes geometry. The results indicated that the thymine-adenine was more stable than the complexes of psoralen and 8-MOP with thymine and adenine which meaned that these compounds were not able to replace nucleic acid bases from their base pair H-bond complexes. So, the optimized structures of the complexes were the interaction of psoralen and 8-MOP with thymine-adenine base pair by electrostatic in nature. The complexes geometrical calculation indicated that stacking stabilization energies were lower than the stabilization energies for the optimized planar geometry. These could be concluded that *ab initio* methods were the minimum level for investigating the non-covalent (H-bond) interactions.
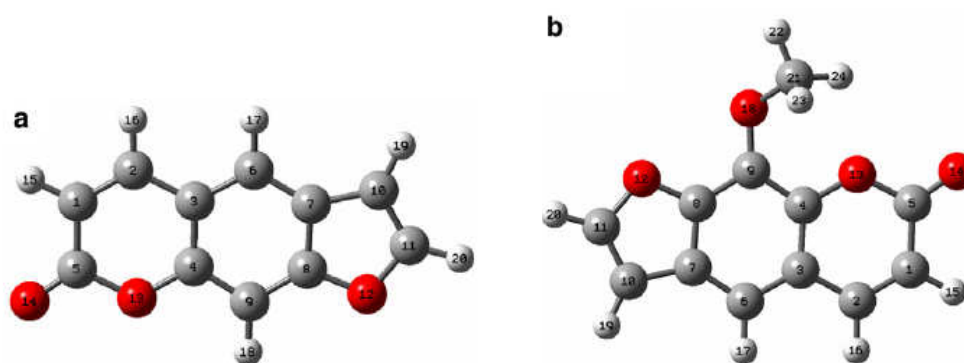
Figure 11 The optimized structures of (a) psoralen and (b) 8-MOP.

Burda and Gu (2008) studied the thermodynamic behavior for the replacement reaction of one and two acetyl-ligands from the diaqua-tetrakis(μ-acetylato) dirhodium(II,II) complex by purine DNA bases. The optimization of the structures was performed by using DFT techniques with the B3PW91 functional and 6-31G(d) basis set. For rhodium atom, the Stuttgart-Dresden pseudopotentials (SDD) were used. The final energy analyses (reaction, stabilization and bonding energies) were determined at the B3LYP/6-31++G(d,p) level of DFT. The starting point for the

substitution reactions was the neutral molecule of rhodium compound and one of acetyl groups was replaced by deprotonated guanine, then the replacement of adjacent acetyl ligand by another deprotonated base was simulated. The binding energies of the DNA bases showed that adenine bonds were slightly stronger in comparison with guanine bonds. The higher affinity of dirhodium to nitrogen atom in adenine than oxygen atom in guanine was corresponded with the Pearson's Hard-Soft-Acid-Base (HSAB) principle. The reaction energies (ΔG) for the acetyl ligand replacement were also determined. Although the thermodynamic potential for guanine in the first reaction step was lower than for adenine, the binding energies of DNA showed the higher energy in adenine than guanine. Therefore, adenine complexes had the higher reactivity than guanine complexes.

Machura *et al.* (2008) studied the reaction of copper dichloride dihydrate and bis(3,5dimethylpyrazol-1-yl)methane which afforded $[Cu\{H_2C(3,5\text{-}Me_2pz)_2\}_2 Cl]$ $Cl \cdot 3H_2O$. The electronic structure of the $[Cu\{H_2C(3,5\text{-}Me_2pz)_2\}_2Cl]^+$ cation was calculated with the density functional theory (DFT) method with the B3LYP functional. The calculations were performed by using the LANL2DZ effective core potential (ECP) set of Hay and Wadt for Cu atom and the standard 6-31+G** basis for Cl and N atoms, 6-31G* for C and 6-31G for hydrogen atoms. The results observed in the experiment data were in good agreement with the calculations. The transitions in the UV–Vis spectrum of the complex were studied by the time-dependent density functional (TDDFT) method. The results showed that the two longest wavelengths from the experiment at 1011.0 and 738.5 nm were due to the transitions of Cl/bis(3,5-dimethylpyrazol-1-yl)methane $\rightarrow$ Cu (LMCT) and $d \rightarrow d$ (Ligand Field; LF) transitions, respectively.

Teimouri *et al.* (2008) synthesized a new azo reactive dye by the reaction of *p*-thiazonium benzene sulfonyl azide with 1,1′-binaphthalene-2,2′-diol (BINOL) as coupling component in the presence of base. The molecular structures of six compounds in the ground state had been optimized by the Hartree–Fock (HF) method, Becke 3–Lee–Yang–Parr (B3LYP) functional and by combining the results of the GaussView program. The vibrational frequencies of normal modes, the visible

absorption maxima, NMR and thermodynamic properties were also calculated with these methods and HF/6-31G* and B3LYP/6-31G*, CIS, ZNIDO, and the time-dependent density functional theory (TD-DFT) calculations. The observed and calculated vibrational spectra were found to be in good agreement with each other. The calculated chemical shifts and coupling constants for ^{1}H, ^{13}C NMR was in line with the experimental findings. The calculated NMR spectra also revealed that the coupling had occurred at position 6 as shown in Figure 12. These results indicated that the computational analysis of this compound by HF and B3LYP methods was in excellent agreement with all the experimental findings.
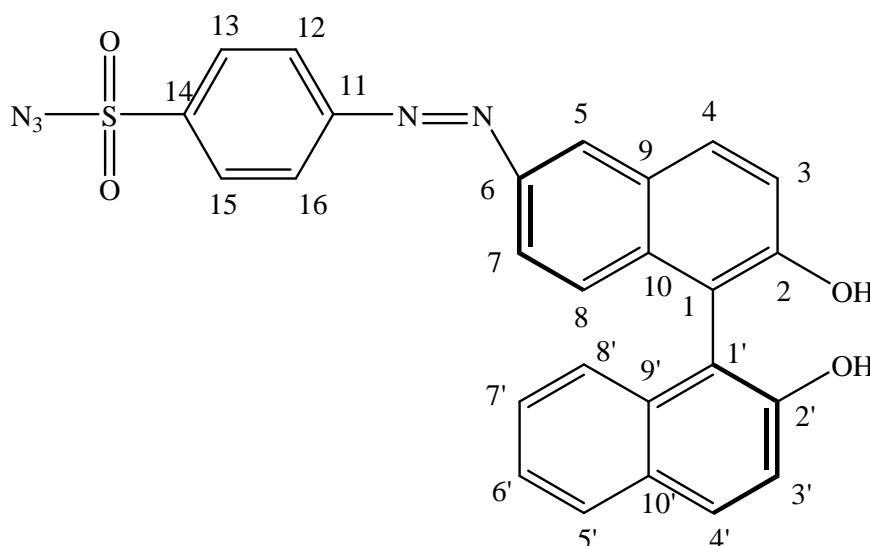
Figure 12 Chemical structure of 6-[4-(azidosulfonyl)phenyl]-1-diazenyl-1,1′-
binaphthalen-2,2′-diol.

Rakic *et al.* (2009) synthesized the new complexes of platinum(II) with 3- (**1**) or 4-acetylpyridine (**2**) and characterized by elemental analyses, IR, ^{1}H and ^{13}C NMR spectroscopy. DFT calculations were used to confirm the formation for both complexes. The possible isomers, *cis* and *trans*, of both complexes were optimized, the most stable isomers gave the lowest energy and thermodynamically the most stable form. Calculations of their geometrical parameters were performed by the DFT method, the B3LYP total energies calculated with SDD basis set. The results showed

that the total energies obtained for (**1**) and (**2**) indicated the formation of *trans* geometrical isomers. The optimized structures of both complexes are shown in Figure 13. The results also showed that data from X-ray crystallography studies and DFT calculations were in very good agreement.

(a)

(b)
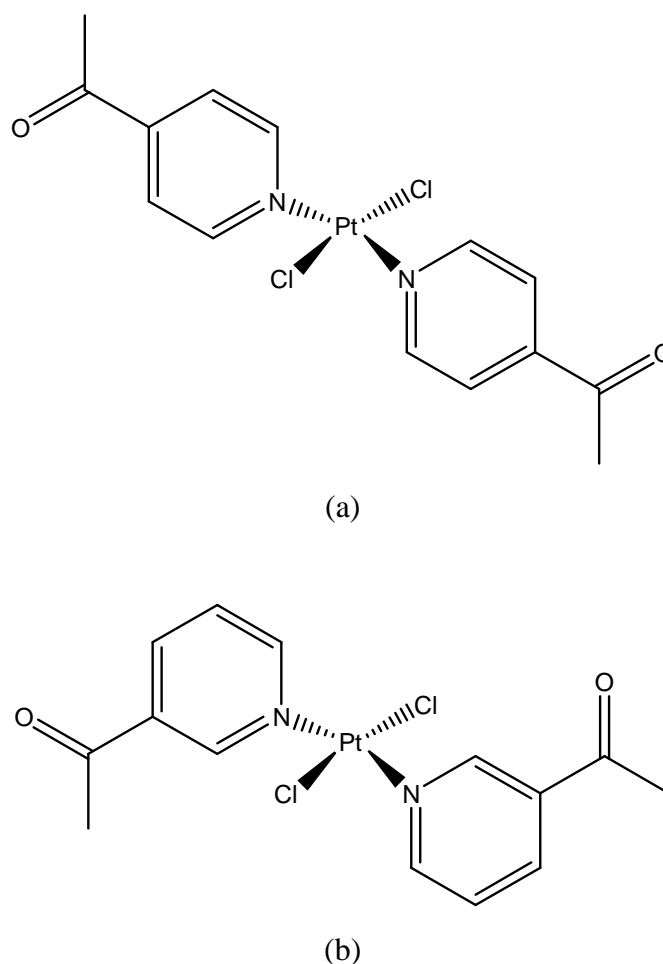
Figure 13 The optimized structures of (a) *trans*-[PtCl$_2$(3-acetylpyridine)$_2$] (**1**) and
(b)*trans*-[PtCl$_2$(4-acetylpyridine)$_2$] (**2**) complexes.

Ucun *et al.* (2009) studied the optimized molecular structures, vibrational frequencies of ten tautomeric forms of a heterocyclic disazo dye, [5-(3-methyl-4 phenylazo-1H-pyrazole-5-ylazo) barbituric acid]. The results from the experiment could be suggested that the disazo dye was predominantly in the azo-hydrazo-keto form. All computations were calculated by using Gaussian 03 program. The

vibrational frequencies and optimized structure parameters of all tautomeric forms of disazo dye were calculated by using HF and DFT methods at 6-31G(d,p) basis set level. The results showed that the calculated and experimental geometric parameters were good agreement. So, it can conclude that the hetero-cyclic disazo dye may exist in azo-hydrazo-keto form in the ground state. The optimized structure is shown in Figure 14.
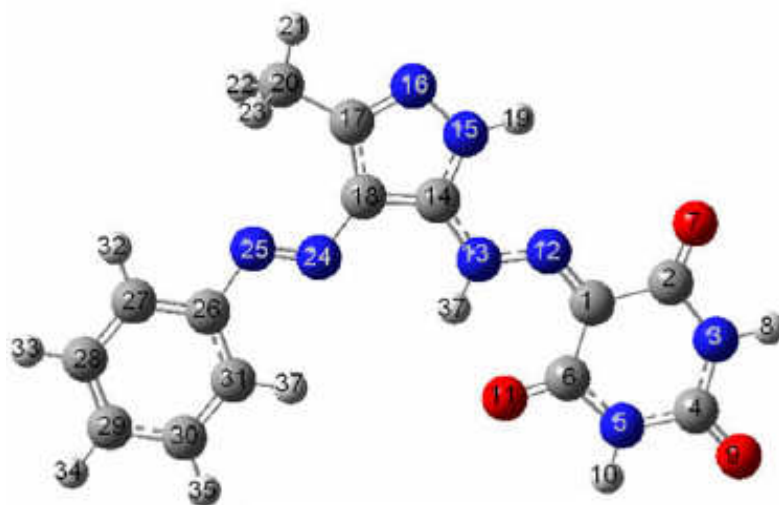
Figure 14 Calculated optimized structure of azo-hydrazo-keto form of the compound.

5. Interaction of transition metal complexes with biomolecules

Nair *et al.* (1997) synthesized and characterized the complex of $[Ru(NH_3)_4dppz]^{2+}$ (dppz = dipyridophenazine) and also studied the DNA-binding properties of this complex. The absorption spectrum of complex showed the maximum absorption at wavelength 370 nm which was characteristic of $\pi \rightarrow \pi^*$ transition of the dppz ligand and the broad peak at 554 nm which assigned as a MLCT band. The absorption spectrum of $[Ru(NH_3)_4dppz]^{2+}$ with calf thymus DNA did not show any wavelength shift in the charge transfer band, however, the addition of DNA caused to the absorbance hypochromism (H% = [(A$_{free}$-A$_{bound}$)/A$_{free}$] × 100%) of 13.6% which was indicated the intercalative binding of the complex with the helix of DNA. The binding constant (*K*) of complex for DNA was determined to be 1.24×10^5

M^{-1}. The thermal denaturation was studied for the melting temperature of DNA. Intercalation mode of binding should promote base stacking in DNA and hence should lead to an increase in the melting temperature of DNA. The result showed that thermal denaturation of $[Ru(NH_3)_4dppz]^{2+}$ (ΔT_m) was $+5.2^oC$ compared to calf thymus DNA alone. The results from both binding constant 10^{-5} M^{-1} and ΔT_m $+5.2^oC$ were on the border between simple electrostatic association with the helix and intercalation.

Wu *et al.* (1998) synthesized the new ligand 2-(4-methoxyphenyl)imidazo[4,5-f] [1,10] phenanthroline (MOP) and studied the interaction of $Ru(bpy)_2MOP^{2+}$ with calf thymus DNA (CT DNA). The structure of MOP was the planarity which might provide the intercalation of MOP into DNA base pairs. The UV-Vis spectra showed that the visible band at 460 nm was due to the metal to ligand charge transfer transition and the ultraviolet band at 285 nm belonged to $\pi \rightarrow \pi^*$ transition of the ligand. After addition of DNA, the drops in the absorptivity of the MLCT and $\pi \rightarrow \pi^*$ of complex were observed and also showed a slight red shift of these bands. So, it can be concluded that the complex can bind to DNA through the intercalation of MOP into the base pairs. The CD spectra were also used to study the interaction of $Ru(bpy)_2MOP^{2+}$ complex with CT DNA. The result showed that the maximal ellipticity arised at the shorter wavelength whereas the minimal arised at the longer which indicated the interaction of this complex with CT DNA. The luminescence studies were also shown the interaction of complex with CT DNA.

Hao and Shen (2000) used the Pd(II) complex with 2-(5-Bromo-2-pyridylazo)-5-diethylaminophenol (5-Br-PADAP) as a new absorption spectroscopic probe for nucleic acids. The absorption spectra showed that in the presence of nucleic acids, there was little variation in the absorption spectrum of (5-Br-PADAP), whereas in the presence of nucleic acids, the absorbance of Pd(II)–5-Br-PADAP complex decreased which was related to the concentration of nucleic acids. The binding constants (K) of nucleic acids to the complex were also studied. The values of K for calf thymus DNA by the two methods based on different modes were almost close to some degree. The structure planarity and non-negative charge, generally, interacted with nucleic acids in the intercalative mode. The Pd(II)–5-Br-PADAP complex had these two features

including the hypochromic shift in absorption spectra which corresponding to the intercalation. So, the binding of Pd(II)–5-Br-PADAP with nucleic acids can be assumed to occur in an intercalation way.

Messori *et al*. (2001) studied the interaction of calf thymus DNA (CT DNA) with gold(III) complexes by using various physicochemical techniques including circular dichroism, absorption spectroscopy, DNA melting and ultradialysis. Electronic spectra of complexes were recorded before and after mixing with DNA at ratio 0.1 metal per DNA in phosphate buffer pH 7.4. The spectra showed that addition of DNA produced significant effects on the charge transfer transition bands in the visible after the samples were carried out over a period of 24 hours at room temperature. For the ultradialysis experiments, the samples were dialyzed to separate CT DNA in upper solution and complexes in lower solution. The spectra of two phases showed similar spectral patterns and comparable intensities suggesting that the binding of the various complexes to CT DNA was weak and reversible which corresponding to the electrostatic binding mode of cation of metal with the polyanionic nature of CT DNA. Circular dichroism used to determine the effects that gold(III) complexes produced on the structure and conformation of CT DNA. The results showed that the disappearance of negative band was observed as well as a reduction in intensity and a characteristic shape of positive band when the ratio increased. The effects of complexes on the DNA melting indicated that all complexes did not favor appreciably the renaturation process.

Deng *et al.* (2003) synthesized the new ligand acenaphthereno[1,2-*b*]-1,4,8,9-tetraazariphenylene (actatp) and its complexes [Ru(bpy)$_2$(actatp)](ClO$_4$)$_2$·2H$_2$O (**1**) (bpy = 2,2' –bipyridine) and [Ru(phen)$_2$(actatp)](ClO$_4$)$_2$·2H$_2$O (**2**) (phen = 1,10-phenanthroline) and also studied the interaction of the complexes with DNA. From the characterization, both complexes showed a strong MLCT band at 400-500 nm attributed to the overlap of Ru(II)$\rightarrow$ bpy or phen(π*) and Ru(II)$\rightarrow$ actatp(π*). The electronic absorption titration for DNA-binding studies showed that, as the concentration of DNA was increased, the MLCT transition bands of complexes exhibited hypochromism and insignificant bathochromism which presumed that there

were some interaction between complexes and DNA. The intrinsic binding constant (K_b) of the two complexes with CT DNA were obtained from the changes in absorbance with increasing the concentration of DNA. The results showed that K_b of complex (**1**) and (**2**) were $(8.3\pm0.5)\times10^5$ M^{-1} ($s = 0.5$) and $(1.2\pm0.3)\times10^5$M^{-1} ($s = 3.1$), respectively. These results might be attributed to the rigid plane of phen in complex (**2**) which effected to the depth of intercalation in the base pairs of DNA.

Gao *et al.* (2003) synthesized the complex [(DOTA)Co(II)(TPY)](ClO$_4$)$_2$ (DOTA = 1,4,7,10-tetraaza-cyclododecane-2,9-dione, TPY = 2, 2':6',2"-terpyridine) and studied the binding properties with calf thymus DNA (CT DNA). The structure was confirmed by crystallographic analysis which shown the tridentate coordination of DOTA to Co(II). The complex of DOTA-Co(II) in the absence of TPY was also studied and showed tetra coordinate by four nitrogen atoms. The structures of complexes are shown in Figure 15. Spectrophotometric titration method was used to study the interaction of complexes with CT DNA. The changes from UV-Vis spectra in the 280-320 nm range were significant which indicated high affinity association of the chromophore with double-stranded nucleic acid. The spectra were also shown the isobestic point at 325 nm which was consistent with the presence of two forms of the complex, free and intercalated.

(a)   (b)
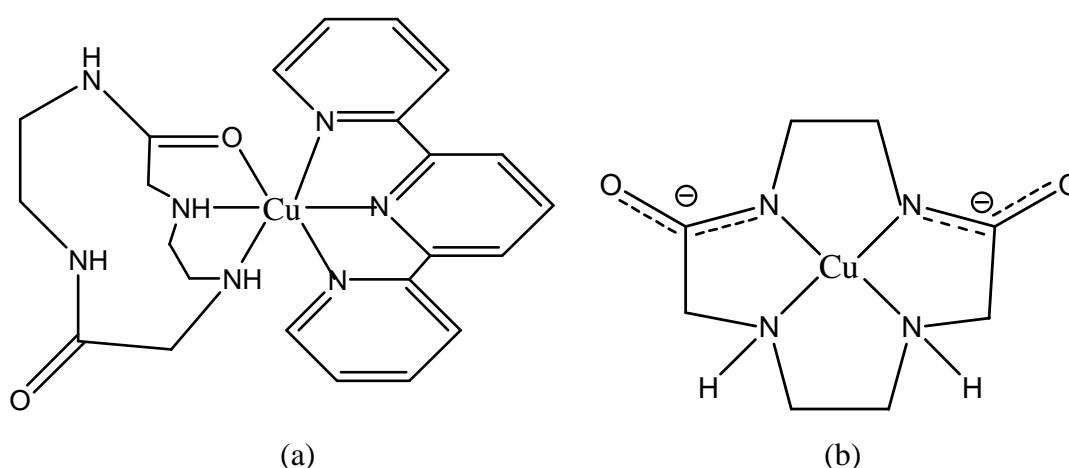
Figure 15 The molecular structures of (a) DOTA–Co(II) –TPY and (b) DOTA–
Co(II) complexes.

Efthimiadou *et al.* (2007) studied the interaction of Cu(II) with the quinolones, *N*-propyl-norfloxacin and pipermidic acid, in the presence or absence of nitrogen-donor heterocyclic ligands. These complexes were studied the interaction with calf thymus DNA (CT DNA) by using spectroscopic techniques, UV and circular dichroism spectroscopies. Generally, DNA can provide three distinctive binding sites for quinolone metal complexes, namely, groove-binding, binding to phosphate group and intercalation. The results from UV spectroscopy showed the changes in UV spectra of the complexes after mixing with CT DNA. The increase of the intensity at $\lambda_{max} = 258$ nm and the shift of the λ_{max} up to 270 nm indicated that the interaction of complexes with DNA took place by the direct formation of complexes with double-helical CT DNA. So, it can be concluded that complexes can interact with CT DNA and can bind to DNA by the intercalative mode.

Kashanain *et al.* (2007) studied the DNA interaction with [*N,N'*-bis (salicylidene)-1,2-phenylenediaminoaluminum(III) nitrate]. The Al–salophen complex showed an absorbance at the range of 310-390 nm which was due to MLCT transition. Upon the addition of DNA, the complex had a hyperchromism and a slight red shift which was due to higher formation of the complex to DNA. The fluorescence spectra of complex showed an increase in the intensity of excitation and emission along with a red shift, indicating the interaction of Al–salophen with DNA. The binding site size can identify the mode of binding, intercalating and non-intercalating mode. Complex showed large binding site sizes which indicated the non-intercalation as a probable mode of binding. The interaction of the Al–salophen with DNA induced a change in the CD spectrum of DNA and their intensities of both the negative and positive bands decreased significantly. The small changes in the CD spectra were due to the non-intercalative mode of binding of complex with CT DNA.

Basu *et al.* (2008) studied the interaction of 1-(2'-pyridylazo)-2-naphthol (Hpan) with [Ru(dmso)$_4$Cl$_2$] (dmso = dimethylsulfoxide) to give the [Ru(pan)$_2$] by refluxing mixture solutions for 24 hours. The structure showed that Hpan was coordinated to the metal center, via dissociation of the phenolic proton, as a monoanionic *N,N,O*-donor. The coordination of this compound is shown in Figure 16.

The complexes showed several absorptions, in the UV region was due to the transition within the ligand orbitals and in the visible region was due to the metal to ligand charge transfer transition. For the DNA binding studies, the absorbance at 480 nm assigned to complex was found to increase the intensity upon addition of DNA. The results indicated that the complex can bind to DNA without causing damage to the DNA double helix.
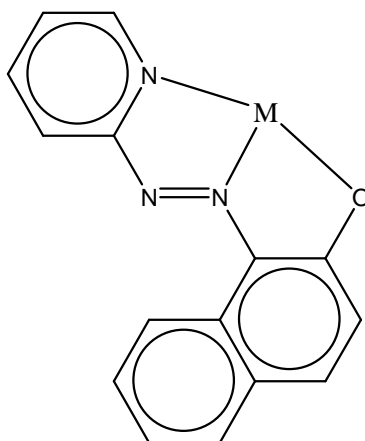
Figure 16 The coordination via a monoanionic *N,N,O*-donor of 1-(2'-pyridylazo)-2-
naphthol (Hpan) to Ru(II).

Gu *et al.* (2008) synthesized a dinuclear copper(II) complex [Cu$_2$(TATP)$_2$ (*L*-Leu)(ClO$_4$)$_2$]$_2$·2H$_2$O (TATP = I,4,8,9-tetraazatriphenylene and *L*-Leu=*L*-leucinate) and studied the interaction of this complex with CT DNA. The electronic absorption spectra of the complex showed the band in the region of 200-300 nm attributed to $\pi \rightarrow \pi^*$ transition of TATP. After the addition of DNA, the complex had a hypochromism which indicated that the complex might bind to DNA by intercalation of TATP to adjacent base pairs to DNA. The fluorescence spectra showed the reduction in fluorescence intensity with the addition of complex. The results indicated that the complex can interact with DNA. The viscosity measurement was also studied. The result showed that the presence of complex increased the viscosity of DNA which indicated the intercalation mode of binding of complex with DNA.

Sun *et al.* (2008) studied the trend in DNA-binding affinities of two ruthenium(II) complexes, $[Ru(phen)_2L^1]^{4+}$ (**1**) and $[Ru(phen)_2L^2]^{4+}$ (**2**) (phen = 1,10-phenanthroline, L^1 = 5,5′-di(1-(triethylammonio)methyl)-2,2′-dipyridyl cation, L^2 = 5,5′-di(1-(tributylammonio)methyl)-2,2′-dipyridyl cation) and the important difference in some properties. The intrinsic binding constants (K_b) of these complexes to DNA were determined by studying the change of absorbance in the metal to ligand charge transfer (MLCT) band with increasing concentration of DNA. The results showed that the binding activity of (**1**) and (**2**) were much higher than $[Ru(phen)_3]^{2+}$ and $[Ru(phen)_2(bpy)](PF_6)_2$ which indicated that the increasing of the charge of the ligands could enhance the affinity of complexes and DNA. The emission spectra showed the fluorescence intensity of these complexes increased with the increasing of DNA concentration. The CD spectral technique had been used to study the enantiomer that prefering to bind with DNA. The results showed that the Δ-enantiomer of the complex had a greater affinity than the Λ-enantiomer with the right-handed calf-thymus DNA helix which was due to the appropriate steric matching of former enantiomer. The results from the viscosity studies suggested that the binding mode of complex (**1**) might partially intercalate between DNA base pair due to the decreasing of viscosity of DNA decreased with increasing concentration of (**1**). Conversely, the binding mode of complex (**2**) most likely interacted with DNA in an electrostatic mode due to the unchanged viscosity of DNA when increasing the concentration of complex (**2**).

Wang *et al.* (2008) synthesized a new dinuclear complex, $[Ag(L)(CH_3CN)]_2$ $(C1O_4)_2 \cdot 2H_2O$ (L=2,3-di-2-pyridylquinoxaline) and studied the interaction of complex with CT DNA by absorption, fluorescence spectroscopies, and viscosity measurement. Absorption spectroscopic studies showed that the increasing amounts of DNA resulted in the hypochromism and bathochromism of the absorption bands. These results might be attributed to the intercalation binding mode which was corresponding to the $\pi*$ orbital of the intercalated ligand couple with the π orbital of the base pairs, thus reducing the $\pi \rightarrow \pi *$ transition energy and resulting in bathochromism. From the luminescent spectroscopic studies, the main emission peak positions of the Ag(I) complex had a blue-shift compared to that of the free ligand

which would be assigned to the emission of the intraligand $\pi \rightarrow \pi^*$ transition. The quenching of the luminescence of the Ag(I) complex by DNA was resulting from the interactions between the aromatic rings of ligand and the base pairs. The viscosity studies indicated that increasing the amount of Ag complex increased the viscosity of DNA. This could be suggested that the dinuclear Ag complex could intercalate into DNA base pairs.

MATERIALS AND METHODS

Materials

1. Apparatus

Absorbance measurements were carried out on a Perkin Elmer Lambda 35 UV-Vis spectrophotometer. Melting Point of p-amino TAA, o-amino TAA and their rhodium(III) complexes were measured by melting point SMP10 Stuart Scientific. Infrared spectra (4000-370 cm^{-1}) were obtained by a Perkin Elmer system 2000 Fourier transform infrared spectrometer. All absorption were reported in wavenumber (cm^{-1}). Nuclear magnetic resonance spectra were recorded at 400 MHz on an INNOVA VARION NMR spectrometer 400 MHz. An elemental analyzer was performed with a LECO CHNS-932 and VTF-900. Mass spectrum of p-amino TAA and o-amino TAA were obtained from Mass Spectrometer (Agilent 1100). The pH values were measured by using an inolab level 1-pH meter. Quantum chemical calculations were performed using Guassian 03 program on a Linux PC 2.4 GHz. and a windows XP (home edition) operating system laptop 2.19 GHz.

2. Reagents

- 2-aminothiazole ($C_7H_6N_2S$, Lab. grade, Fluka, Buchs, Switzerland)
- Sodium nitrite ($NaNO_2$, Lab. grade, Merck, Darmstadt, Germany)
- m-anisidine (C_7H_9NO, Lab. grade, Fluka, Buchs, Switzerland)
- Sodium hydroxide (NaOH, Lab. grade, Carlo Erba, Rodano, Milan, Italy)
- Hydrochloric acid (HCl, Lab. grade, Lab Scan, Bangkok, Thailand)
- Hexane (C_6H_{14}, A.R. grade, Fisher Scientific, Leicestershire, UK)
- Ethyl acetate ($C_4H_8O_2$, A.R. grade, J.T. Baker Chemicals, Deventer, Holland)
- Thin layer chromatography (TLC) : aluminium sheet Silica gel 60 F_{254} (MERCK, Darmstadt, Germany)
- Silica gel 60 0.040-0.063mm (A.R. grade, Merck, Darmstadt, Germany)
- Ethyl alcohol (C_2H_5OH, AR. grade, Mallinckrodt, St. Louis, Missouri, USA.)

- Boric acid (H_3BO_3, A.R. grade, Fisher Scientific, Leicestershire, UK)
- Citric acid ($C_6H_8O_7$, A.R. grade, APS Finechem, Seven Hills, Australia)
- Sodium phosphate ($Na_3PO_4 \cdot 12H_2O$, A.R. grade, Fluka, Buchs, Switzerland)
- Rhodium(III)trichloride hydrate ($RhCl_3.xH_2O$, A.R. grade, Fluka, Buchs, Switzerland)
- Potassium hexachloroplatinate(IV) (K_2PtCl_6, A.R. grade, Carlo Erba, Rodano, Milan, Italy)
- Perchloric acid ($HClO_4$, Lab. Grade, BDH, Poole, England)
- Methyl alcohol (CH_3OH, A.R. grade, Fisher Scientific, Leicestershire, UK)
- Pyridine (C_5H_5N, A.R. grade, Merck, Darmstadt, Germany)
- *N,N*-dimethylformamide (C_3H_7NO, A.R. grade, Merck, Darmstadt, Germany)
- Acetonitrile (CH_3CN, A.R. grade, Merck, Darmstadt, Germany)
- Tetrahydrofuran (C_4H_8O, HPLC grade, Scharlau, Port Adelaide, Australia)
- Chloroform-*d* ($CDCl_3$-*d*) TMS(1 vol%) : for NMR spectroscopy (Merck, Darmstadt, Germany)
- Potassium bromide (KBr, A.R. grade, Merck, Darmstadt, Germany)
- Dimethylsulfoxide, D-6 (C_2D_3OS, AR. grade, Merck, Darmstadt, Germany)
- Deoxyribonucleic acid sodium salt from calf thymus lyoph. (AR. grade, Fluka, Steinheim, Germany)
- Tris(hydroxymethyl)aminomethane ($C_4H_{11}NO_3$, Lab. grade, Fluka, Buchs, Switzerland)
- Double distilled water

Methods

1. **Synthesis of 2-(2′-thiazolylazo)-5-aminoanisole (*p*-amino TAA) and 4-(2′-thiazolylazo)-3-aminoanisole (*o*-amino TAA)**

One gram of 2-aminothiazole was dissolved in 16 ml of 6M hydrochloric acid and cooled in an ice-bath. Sodium nitrite (0.70 g) was dissolved in a small amount of water. After crushed ice was added to both solutions, nitrite solution was slowly poured into the 2-aminothiazole solution while stirring with a glass rod under low temperature (-5 to 0 °C). The solution of diazonium salt was slowly dropped while stirring into a well cooled solution of *m*-anisidine (1.12 ml) in 40 ml of 4 M hydrochloric acid. The mixture was stirred in the ice-bath for 1 hour and then 0.001 M sodium hydroxide solution was added into the mixture until pH 6 was reached which an orange-red precipitate began to settle immediately. The solution was filtered and the precipitate was washed with water and dried at 80°C in an oven to give the mixture product consisted of 2-(2′-thiazolylazo)-5-aminoanisole (*p*-amino TAA) and 4-(2′-thiazolylazo)-3-aminoanisole (*o*-amino TAA).

2. **Separation and purification of *p*-amino TAA and *o*-amino TAA**

To separate *p*-amino TAA from *o*-amino TAA, the crude product was tested by thin layer chromatography (TLC) over various mobile phases such as hexane, dichloromethane, ethanol and ethyl acetate. For the suitable solvent, the TLC plate coated with silicondioxide (SiO_2), was placed in the chamber which contained a mobile phase of ethyl acetate: hexane (50:50). Flash column chromatography was used as a purification technique. The stationary phase, silica gel 60 (0.040-0.063 mm), was placed 8 inch height in glass column and the mobile phase, a mixture of ethyl acetate: hexane (30:70), was added to the top and flowed down through the column by external pressure. The individual components were collected and tested by TLC with a mixture of ethyl acetate: hexane as mobile phase again to confirm the purity of each component. A mixture solvent was evaporated by the rotary evaporator. The products were purified by recrystallization with a mixture of ethanol-water (3:1) to give red

needles-shaped crystals of *p*-amino TAA with melting point of 170-173°C and green needles-shaped crystals of *o*-amino TAA with melting point of 207-211°C. The resultant products were characterized by FT-IR, ^{1}H NMR, mass spectroscopy and elemental analysis.

3. Preparation of solutions

3.1 Preparation of buffer solutions

Universal buffer solutions used in this work were prepared by mixing of mixture of 0.30 M boric acid and 0.05 M citric acid with 0.10 M sodium phosphate at various ratios as stated in Table 3.

3.2 Preparation of 1.0×10^{-3} M *p*-amino TAA and *o*-amino TAA solution

For the preparation of 1.0×10^{-3} M solution, 0.0177 g of each TAA was dissolved and made up to 50 ml by absolute ethanol in a volumetric flask.

3.3 Preparation of 1.0×10^{-3} M rhodium(III) solution

For the preparation of 1.0×10^{-3} M rhodium(III) solution, 0.0105 g of $RhCl_3 \cdot xH_2O$ was dissolved and made up to 50 ml by 0.10 M HCl in a volumetric flask.

3.4 Preparation of 1.0×10^{-3} M platinum(IV) solution

For the preparation of 1.0×10^{-3} M platinum(IV) solution, 0.0244 g of K_2PtCl_6 was dissolved and made up to 50 ml by 0.10 M HCl in a volumetric flask.

Table 3 The preparation of universal buffer solutions at pH range from 2 to 6

pH	Mixture of 0.20 M H_3BO_3 and 0.05 M $C_6H_8O_7$ (1:1) (ml)	0.10 M Na_3PO_4 (ml)
2	188	12
3	176	24
4	155	45
5	134	66
6	118	82

4. Determination of the acid dissociation constants (pK_a) of *p*-amino TAA and *o*-amino TAA

Separately added 0.5 ml of 1.0×10^{-3} M of both *p*-amino TAA and *o*-amino TAA into each of 10 ml volumetric flasks and then made up volume by universal buffer solution at pH 2 to 6 (shown in table 3). The absorbances of the solutions were measured by UV-Vis spectrophotometer at 400-700 nm. The pK_a of *p*-amino TAA and *o*-amino TAA were determined by two different methods; the half height method and the limiting absorbance method (Masoud, 2003). The calculations are shown in Appendix B and Appendix C.

5. Complex formation of *p*-amino TAA and *o*-amino TAA with rhodium(III) and platinum(IV)

Both *p*-amino TAA and *o*-amino TAA are thiazolylazo dye, which could form color complexes with transition metals. The reactions of *p*-amino TAA and *o*-amino TAA with rhodium(III) and platinum(IV) at various pH and in various concentrations of perchloric acid were investigated in order to determine the appropriate pH for studying on the formation of complexes of rhodium(III) and platinum(IV) with TAA. The following procedure for formation of complexes was used in this work. Pipetted

0.50 ml of 1.0×10^{-3} M of each TAA into 10 ml volumetric flasks and then 0.50 ml of 1.0×10^{-3} M rhodium(III) or platinum(IV) solution in buffer solution (pH range 2 to 6) and 1.0 M to 6.0 M $HClO_4$ was pipetted into the previous volumetric flasks. The complex solutions were then diluted to the mark with buffer solutions and perchloric acid. The formation of complexes of rhodium(III) and platinum(IV) with TAA were studied by spectrophotometric method. The results are shown in Figure 36 to Figure 45 for rhodium(III) complexes and Figure 46 to Figure 55 for platinum(IV) complexes, respectively.

6. **Stability of complexes between *p*-amino TAA and *o*-amino TAA with rhodium(III)**

The stability of complexes between *p*-amino TAA and rhodium(III) and between *o*-amino TAA and rhodium(III) were determined by measuring the absorbance every five minutes over a period of 2 hours at wavelength 478 nm for rhodium(III)-(*p*-amino TAA) complex and 553 nm for rhodium(III)-(*o*-amino TAA) complex in universal buffer at pH 5 and pH 3, respectively. The results are shown in Figure 56 and Figure 57.

7. **Stability of complexes between *p*-amino TAA and *o*-amino TAA with platinum(IV)**

The stability of complexes between *p*-amino TAA and platinum(IV) and between *o*-amino TAA and platinum(IV) were determined by measuring the absorbance every five minutes over a period of 2 hours at wavelength 554 nm for platinum(IV)-(*p*-amino TAA) complex and 543 nm for platinum(IV)-(*o*-amino TAA) complex in universal buffer at pH 3 for both complexes. The results are shown in Figure 58 and Figure 59.

8. **Stoichiometric determination of complexes between *p*-amino TAA and rhodium(III)) and between *o*-amino TAA and rhodium(III)**

From the studying on the complex formation in the previous section, the suitable pH for studying on the stoichiometry of complexes of rhodium(III) were pH 5 for *p*-amino TAA and pH 3 for *o*-amino TAA, respectively.

8.1 Stoichiometric determination of complexes between *p*-amino TAA and *o*-amino TAA with rhodium(III) by mole ratio method

Pipetted 0.50 ml of 1.0×10^{-3} M rhodium(III) into each of eleven 10 ml volumetric flask. After that, 0.00, 0.10, 0.20, 0.30, 0.40, 0.50, 0.60, 0.70, 0.80, 0.90 and 1.00 ml of 1.0×10^{-3} M solution of both of *p*-amino TAA and *o*-amino TAA were separately pipetted into each volumetric flask, respectively. Then, the mixture solutions were diluted to the mark with universal buffer solution at pH 5 for *p*-amino TAA complexes and at pH 3 for *o*-amino TAA complexes. The buffer solutions used in this study were stated in Table 3. The absorbances of the solutions were measured by UV-Vis spectrophotometer at 478 nm and 553 nm for *p*-amino TAA complexes and *o*-amino TAA complexes, respectively. The results are shown in Figure 60 and Figure 61.

8.2 Stoichiometric determination of complex between *p*-amino TAA and *o*-amino TAAwith rhodium(III) by continuous variation method

Pipetted 0.00, 0.10, 0.20, 0.30, 0.40, 0.50, 0.60, 0.70, 0.80, 0.90 and 1.00 ml of 1.0×10^{-3} M rhodium(III) into each of eleven 10 ml volumetric flask. After that, 1.00, 0.90, 0.80, 0.70, 0.60, 0.50, 0.40, 0.30, 0.20 and 0.10 ml of 1.0×10^{-3} M solution of both of *p*-amino TAA and *o*-amino TAA were separately pipetted into each volumetric flask, respectively. Then, the mixture solutions were diluted to the mark with universal buffer solution at pH 5 for *p*-amino TAA complexes and at pH 3 for *o*-amino TAA complexes. The buffer solutions used in this study were stated in Table 3. The absorbances of the solutions were measured by UV-Vis spectrophotometer at 478 nm and 553 nm for

p-amino TAA complexes and *o*-amino TAA complexes, respectively. The results are shown in Figure 62 and Figure 63.

9. Stoichiometric determination of complexes between *p*-amino TAA and *o*-amino TAA with platinum(IV)

From the studying on the complex formation in the previous section, the suitable pH for studying on the stoichiometry of complexes of platinum(IV) was pH 3 for both *p*-amino TAA and *o*-amino TAA.

9.1 Stoichiometric determination of complex between *p*-amino TAA and *o*-amino TAA with platinum(IV) by mole ratio method

Pipetted 0.50 ml of 1.0×10^{-3} M rhodium(III) into each of eleven 10 ml volumetric flask. After that, 0.00, 0.10, 0.20, 0.30, 0.40, 0.50, 0.60, 0.70, 0.80, 0.90 and 1.00 ml of 1.0×10^{-3} M solution of both of *p*-amino TAA and *o*-amino TAA were separately pipetted into each volumetric flask, respectively. Then, the mixture solutions were diluted to the mark with universal buffer solution at pH 3 for both complexes. The buffer solutions used in this study were stated in Table 3. The absorbances of the solutions were measured by UV-Vis spectrophotometer at 554 nm and 543 nm for *p*-amino TAA complexes and *o*-amino TAA complexes, respectively. The results are shown in Figure 64 and Figure 65.

9.2 Stoichiometric determination of complex between *p*-amino TAA and *o*-amino TAA with platinum(IV) by continuous variation method

Pipetted 0.00, 0.10, 0.20, 0.30, 0.40, 0.50, 0.60, 0.70, 0.80, 0.90 and 1.00 ml of 1.0×10^{-3} M platinum(IV) into each of eleven 10 ml volumetric flask. After that, 1.00, 0.90, 0.80, 0.70, 0.60, 0.50, 0.40, 0.30, 0.20 and 0.10 ml of 1.0×10^{-3} M solution of both of *p*-amino TAA and *o*-amino TAA were separately pipetted into each volumetric flask, respectively. Then, the solutions were diluted to the mark with

universal buffer solution at pH 3 for both complexes. The buffer solutions used in this study were stated in Table 3. The absorbances of the solutions were measured by UV-Vis spectrophotometer at 554 nm and 543 nm for *p*-amino TAA complex and *o*-amino TAA complex, respectively. The results are shown in Figure 66 and Figure 67.

10. Determination for stability constant of *p*-amino TAA and *o*-amino TAA with rhodium(III) and platinum(IV)

10.1 Equilibrium constant by continuous variation method

The stability constant of the complexes can be determined by using data from the continuous variation method (Job's plot) by assuming that only single complex is present (Likussar, 1971). The complexes of *p*-amino TAA and *o*-amino TAA with rhodium(III) in universal buffer solution of pH 5 and pH 3 were studied by UV-Vis spectrophotometer at wavelength 478 and 553 nm, respectively. The complexes of *p*-amino TAA and *o*-amino TAA with platinum(IV) in universal buffer solution of pH 3 for both complexes were studied by UV-Vis spectrophotometer at wavelength 554 and 543 nm, respectively. The calculation of stability constants of complexes are shown in Appendix E.

10.2 Equilibrium constant by Benesi-Hildebrand's Equation

The solutions of rhodium(III) and platinum(IV) complexes were prepared by mixing variable amounts of *p*-amino TAA or *o*-amino TAA solutions into a constant volume of rhodium(III) or platinum(IV) solution The concentrations of TAA ranged between 1.0×10^{-5} M and 1.0×10^{-4} M while the concentrations of metal remained constant at 5.0×10^{-5} M. The series of complex solutions were prepared in universal buffer at pH 5 for *p*-amino TAA and at pH 3 for *o*-amino TAA in rhodium(III) complexes and at pH 3 for both complexes of platinum(IV). The absorbances were measured by using UV-Vis spectrophotometer at the wavelength 478 and 553 nm for *p*-amino TAA and *o*-amino TAA with rhodium(III) and at the wavelength 554 nm and

543 nm for *p*-amino TAA and *o*-amino TAA with platinum(IV). The calculation of stability constants of complexes are shown in Appendix D.

11. Structural determination of complexes between *p*-amino TAA and rhodium(III) and between *o*-amino TAA and rhodium(III)

These complexes were synthesized according to the following procedure. Each TAA 0.0655 g (0.28 mmol) was dissolved in absolute tetrahydrofuran (THF) 8 ml and then 0.0293 g (0.140 mmol) of $RhCl_3 \cdot xH_2O$ dissolved in 2 ml of 0.10 M HCl was added to TAA solution in 50 ml round bottom flask. Next, 0.0058 g (0.1 mmol) of NaCl was added in the mixture solution. The system was kept under reflux for eight hours. The precipitate was collected after evaporation. Finally, the precipitate of complex was dried at room temperature under low pressure and studied by FT-IR and ^{1}H NMR.

12. Calculation of the complex formation energy of complexes between *p*-amino TAA and rhodium(III)

All quantum chemical calculations of various rhodium(III) complex structures were performed with the Gaussian 03 suite of programs on a Linux PC 2.4 GHz and windows XP (home edition) operating system laptop 2.19 GHz. The study of molecular structure of complex between rhodium(III) and *p*-amino TAA was predicted. Therefore, the formation energy of the complex was theoretically calculated to predict the possible structure by using the Density Functional Theory (DFT) at B3LYP level of theory using 6-31G* basis set for each atom on thiazolylazo compounds and the effective core potential (ECP) of SDD was employed on transition metal of rhodium. The theoretical background and examples of method for quantum chemical calculation are shown in Appendix G.

The formation energy of the complex when bound with nucleobases and the optimized structures were also calculated by the same method.

13. Preparation of calf thymus DNA solution

Fifty mg of deoxyribonucleic acid sodium salt from calf thymus (CT-DNA) was dissolved in 50 mM tris-HCl (tris-hydroxymethlyaminomethane hydrochloride) buffer and 5 mM NaCl pH 7.4 which prepared in boiled deionized water (Tercero, 2003). CT-DNA solution was stored at low temperature (4°C). The concentration of the DNA solution was determined by spectroscopic method at wavelength 260 nm using $\varepsilon = 6600$ M^{-1}cm^{-1}.

14. Nucleic acid purity assessment by using A260/A280 ratios

Calf thymus DNA should be test to confirm that it free of any proteins by measuring the absorbance at wavelengths 280 and 260 nm. Absorbance at 260 nm (A260) is frequently used to measure DNA or RNA concentration and absorbance at 280 nm (A280) is used to measure protein concentration. A ratio of A260/A280 > 1.8 suggests little protein contamination in a DNA/RNA sample (Glasel, 1995). This method is fully explained in Appendix F.

To determine the absorbance ratio, the sample was measured by spectrophotometer at wavelengths 260 and 280 nm. Finally, the ratio of absorbance at A260 and A280 was calculated. The result is shown in Figure 108.

15. DNA-binding investigation of rhodium(III)-(*p*-amino TAA) and rhodium(III)-(*o*-amino TAA) with calf thymus DNA

To determine the interaction between the complexes and calf thymus DNA (CT DNA), the solutions were prepared by mixing of rhodium(III)-(*p*-amino TAA) or rhodium(III)-(*o*-amino TAA) 1.0×10^{-4} M and CT DNA 2.0×10^{-4} M in 50 mM tris-HCl buffer. The solutions were kept under room temperature for 1 hour before the absorption measurement. The absorption spectra were recorded for both a constant complexes concentration in the presence of CT DNA at various concentration ratios (r = mole DNA: mole complex) and a constant CT DNA concentration in the presence

of complexes at various concentration ratios (r = mole complex: mole DNA). The various concentrations of complexes were also investigated to compare the absorption spectra of complexes in the presence or absence of CT DNA. The results are shown in Figure 109 to Figure114.

16. Stability of rhodium(III)-(*p*-amino TAA) and rhodium(III)-(*o*-amino TAA) with calf thymus DNA

The stability of CT DNA with rhodium(III)-(*p*-amino TAA) and rhodium(III)-(*o*-amino TAA) complexes in tris-HCl buffer pH 7.4 were determined by measuring the absorbance every five minutes over a period of 2 hours. The absorbances were measured at wavelength 260 nm which is used to measure DNA concentration, at wavelength 483 nm which gave the maximum absorption of *p*-amino TAA complex and at wavelength 513 nm which gave the maximum absorption of *o*-amino TAA complex. The results are shown in Figure 115 to Figure 118.

17. Calculation for the formation energy between rhodium(III)-(*p*-amino TAA) complex and nucleobases

The optimized structure of rhodium(III)-(*p*-amino TAA) complex which has the lowest formation energy was used as the structure for calculations. Two types of nucleobases, adenine and guanine, were optimized in their geometries by using Guassian03 program with density functional theory (DFT), B3LYP correlation functional and 6-31G* basis set. The rhodium(III)-(*p*-amino TAA) complex and each nucleobase was combined and rearranged the structure and SDD basis set was added to the function to calculate the energy of rhodium atom to optimize the formation energies of the compounds. The selected donor atoms of an adenine and a guanine base are shown in Figure 120 and Figure 121, respectively. The five coordinated intermediate of rhodium(III)-(*p*-amino TAA) complex is shown in Figure 119. The optimized structures of all adducts are shown in Figure 122 and Figure 123. The stabilization energy of all adducts are shown in Table 33.

RESULTS AND DISCUSSIONS

1. Synthesis of 2-(2′-thiazolylazo)-5-aminoanisole (*p*-amino TAA) and 4-(2′-thiazolylazo)-3-aminoanisole (*o*-amino TAA)

Figure 17 shows the synthesis pathway of 2-(2´-thiazolylazo)-5-aminoanisole (*p*-amino TAA) and 4-(2´-thiazolylazo)-3-aminoanisole (*o*-amino TAA) which were synthesized by diazotization of 2-aminothiazole in hydrochloric acid at –5 to 0 °C, then coupling with *m*-anisidine in hydrochloric acid at the same temperature. Finally, the crude of a mixture product was precipitated with 1.0×10^{-3} M sodium hydroxide solution. The components of a mixture product were investigated by thin layer chromatography (TLC) with ethyl acetate: hexane (50:50) as mobile phase. The retention factors (R_f) of two components are 0.52 and 0.32, respectively. The mixture product was then separated by flash column chromatography which the stationary phase was silica gel 60 and the mobile phase was ethyl acetate: hexane (30:70). Each component of the mixture product was purified by recrystallization from ethanol-water (3:1) solution, which gave *p*-amino TAA as red needles-shaped crystals with the melting point of 170-173°C and *o*-amino TAA as green needles-shaped crystals with melting point of 207-211ᵒC. The high melting point of *o*-amino TAA in comparison to that of *p*-amino TAA may be attributed to the hydrogen bonding in *o*-amino TAA as shown in Figure 18. The %yield of *p*-amino TAA and *o*-amino TAA from the crude of mixture product are 21.43 and 29.40 % respect to the starting materials.

The crystalline of *p*-amino TAA and *o*-amino TAA were characterized by FT-IR, ^{1}H NMR, mass spectrometry and elemental analysis. The results are shown in Figure 19 and Figure 20 for FT-IR, Figure 21 and Figure 22 for ^{1}H NMR Figure 23 to Figure 26 for mass spectrometry and Table 4 for elemental analysis, respectively. The solution of *p*-amino TAA and *o*-amino gave various colors in universal buffer pH 2 to 6. The results are shown in Table 7 for *p*-amino TAA and Table 8 for *o*-amino TAA.
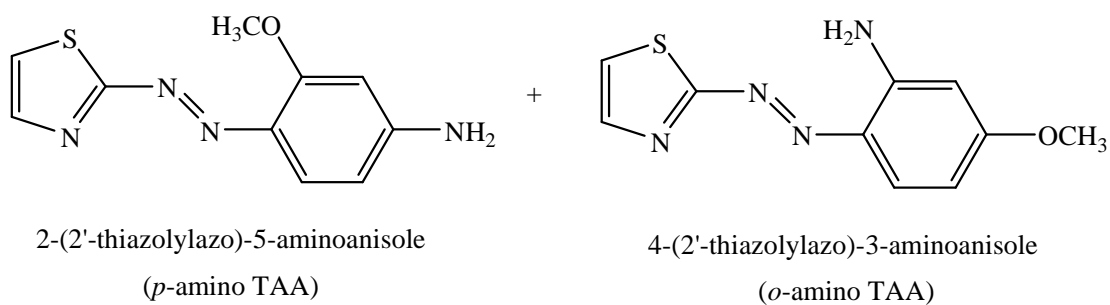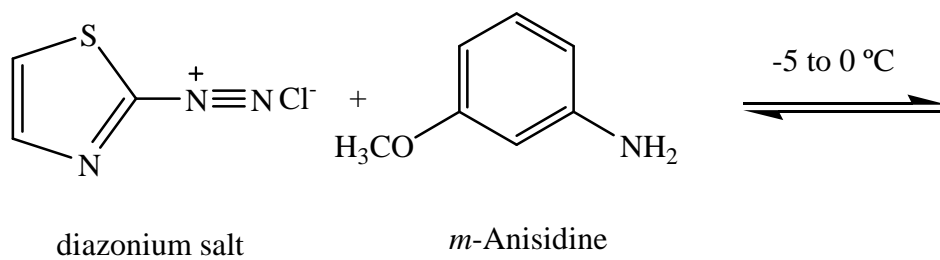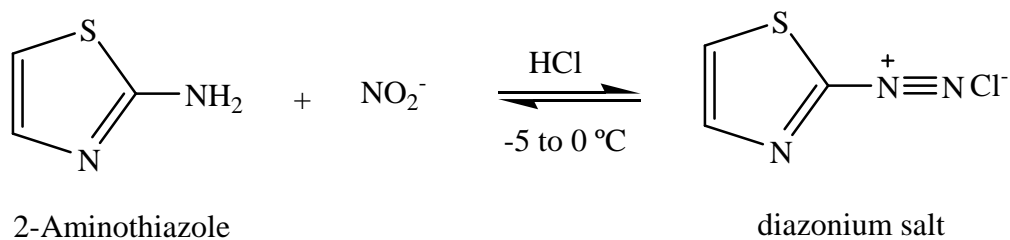
Figure 17 Synthesis pathway of 2-(2´-thiazolylazo)-5-aminoanisole (*p*-amino TAA) and 4-(2´-thiazolylazo)-3-aminoanisole (*o*-amino TAA).
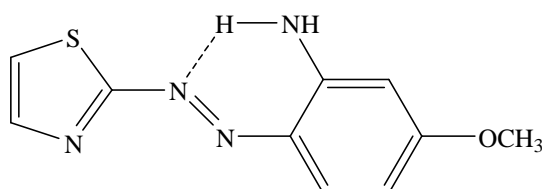
Figure 18 The intramolecular hydrogen bonding in *o*-amino TAA.

Mechanism of the reaction (Wade, 1999)

1. The unstable nitrous acid is generated in situ by mixing sodium nitrite with cold and dilute hydrochloric acid.

$$Na^+ + \ddot{\overset{..}{O}}-\ddot{N}=\ddot{O}H + H^+Cl^- \rightleftharpoons HO-\ddot{N}=\ddot{O} + Na^+Cl^-$$

sodium nitrite   nitrous acid
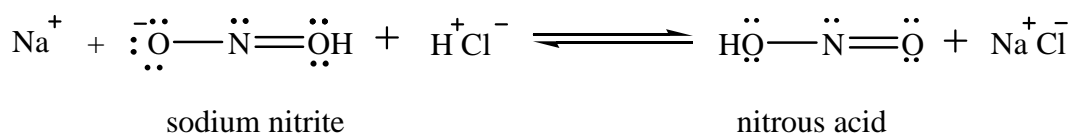
2. In an acidic solution, nitrous acid is protonated and lost water to give the reactive intermediate, nitrosonium ion.

$$H\ddot{O}-\ddot{N}=\ddot{O} + H^+ \rightleftharpoons H_2\overset{+}{\ddot{O}}-\ddot{N}=\ddot{O} \xrightarrow{-H_2O} \left[\ddot{N}=\ddot{O} \longleftrightarrow \ddot{N}\equiv\overset{+}{\ddot{O}} \right]$$

nitrous acid   protonated nitrous acid   nitrosonium ion
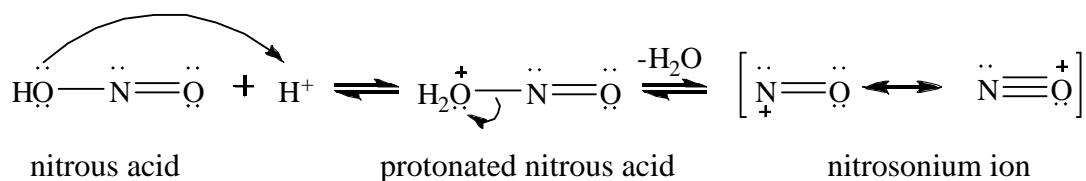
3. A nucleophilic attack on nitrosonium ion from primary amine (2-aminothiazole) forms an unstable N-nitrosoammonium ion as an intermediate.

2-aminothiazole   nitrosonium ion N-nitrosoammonium ion
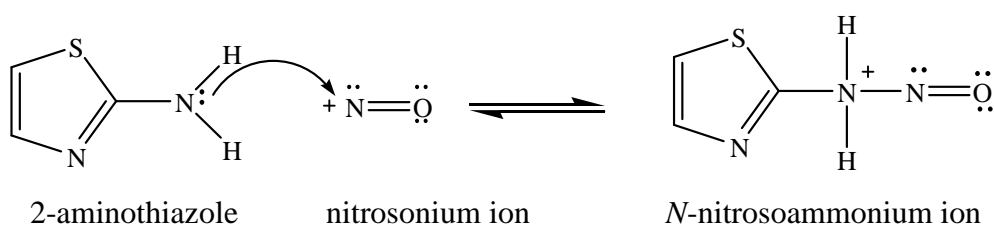
4. This N-nitrosoammonium ion then loses a proton to form an N-nitrosamine.

$-H_3O^+$
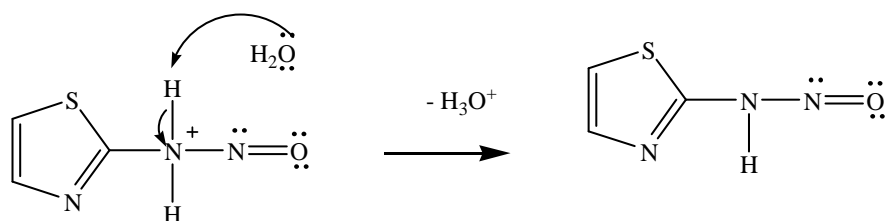
N-nitrosoammonium ion   N-nitrosamine

5. *N*-nitrosamine then tautomerizes to a diazohydroxide.

N-nitrosamine   diazohydroxide
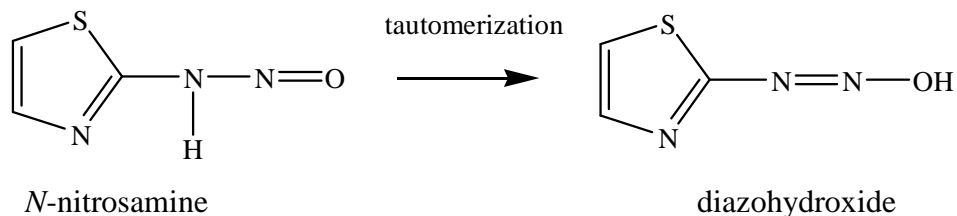
6. In the presence of acid, the diazohydroxide loses water to form the diazonium ion.

diazohydroxide
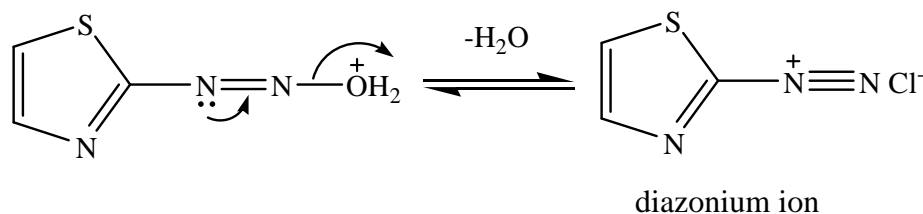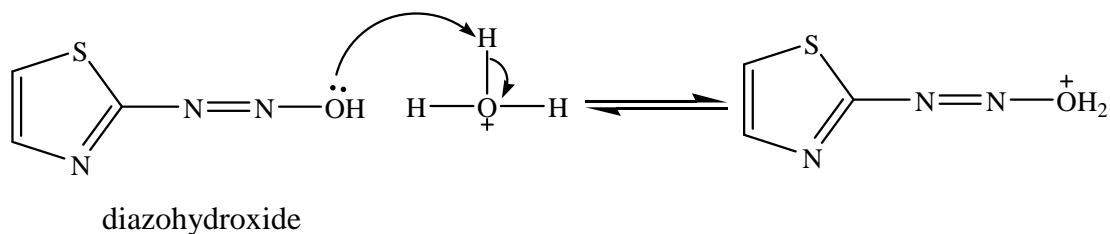
diazonium ion

7. Finally, diazonium ion reacts with aromatic compounds to give a thiazolylazo dye.
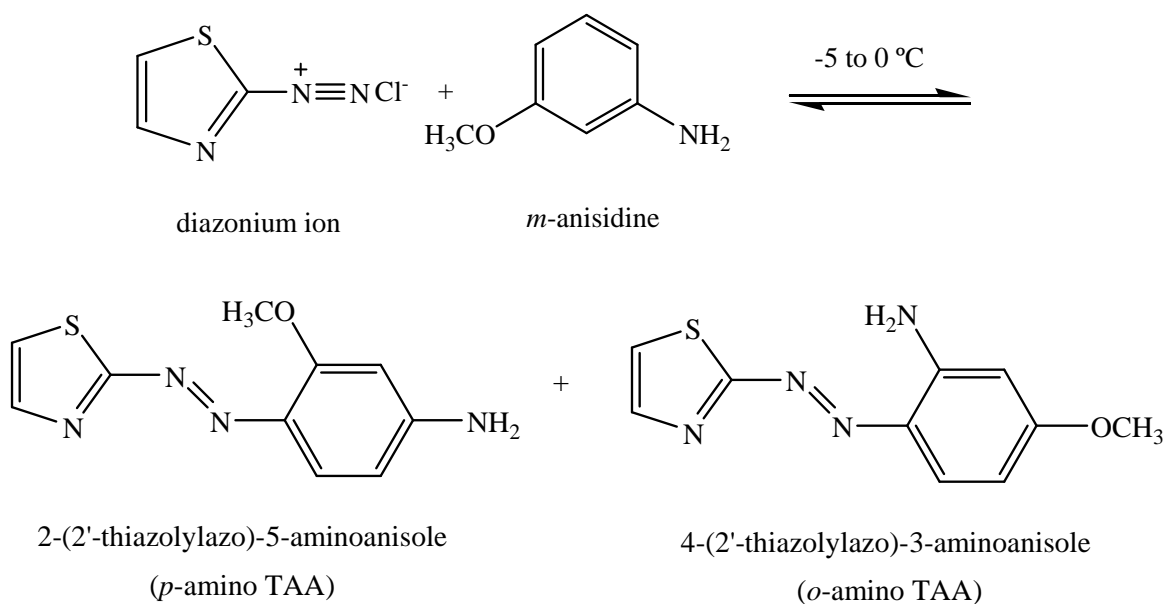
diazonium ion   *m*-anisidine

2-(2'-thiazolylazo)-5-aminoanisole   4-(2'-thiazolylazo)-3-aminoanisole

(*p*-amino TAA)   (*o*-amino TAA)

2. Characterization of 2-(2′-thiazolylazo)-5-aminoanisole and 4-(2′-thiazolylazo)-3-aminoanisole

2.1   Infrared spectrum

The KBr disks of *p*-amino TAA and *o*-amino TAA which ground and dried at 120°C were prepared by mixing of these compounds with KBr. FT-IR spectra were run in KBr disks in the 4000-370 cm^{-1} region.
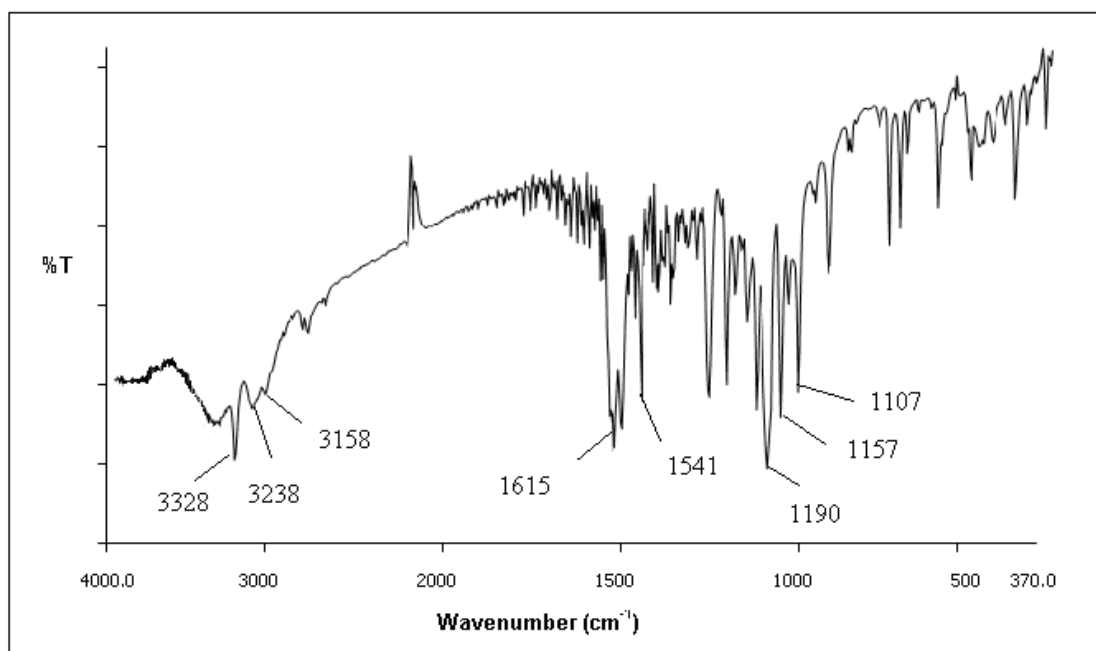
Figure 19 The IR spectrum of 2-(2′-thiazolylazo)-5-aminoanisole (*p*-amino TAA).

The infrared spectrum (KBr: cm^{-1}) is as followed: 3328, 3238 (w, N-H stretch), 3158 (w, C-H stretch aromatic), 1615 (s, C=N stretch), 1541 (m, N=N stretch), 1190 (s, C-N stretch), 1157 (m, C-S stretch) and 1107 (m, C-O-C stretch) (Pavia, 1996).
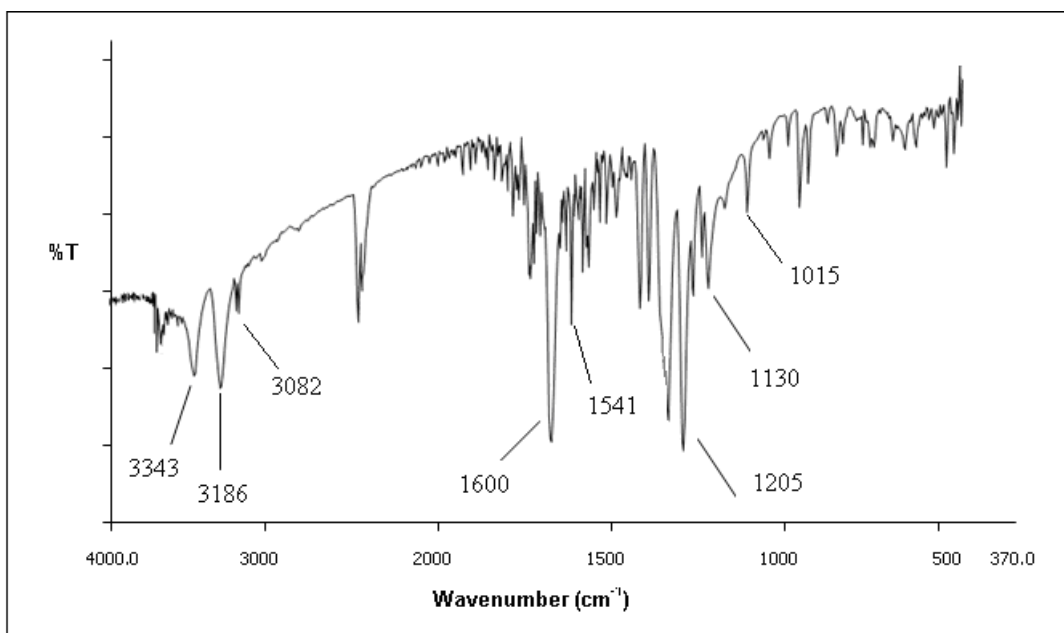
Figure 20 The IR spectrum of 4-(2′-thiazolylazo)-3-aminoanisole (*o*-amino TAA).

The infrared spectrum (KBr: cm^{-1}) is as followed: 3343, 3186 (w, N-H stretch), 3082 (w, C-H stretch aromatic), 1600 (s, C=N stretch), 1541 (m, N=N stretch), 1205 (s, C-N stretch), 1130 (m, C-S stretch) and 1015 (m, C-O-C stretch) (Pavia, 1996).

2.2   Elemental analysis

Compounds of *p*-amino TAA and *o*-amino TAA were ground and dried at
120°C. Two mg of *p*-amino TAA and *o*-amino TAA were analyzed to find the
percentage of each element excepting oxygen atom. The percentage of oxygen atom can
obtain from one hundred percent of total elements minus by the percentage of carbon,
sulfur, hydrogen and nitrogen atoms.

Table 4 The elemental analysis of *p*-amino TAA and *o*-amino TAA

Element	Theoretical value	*p*-amino TAA		*o*-amino TAA	
		Experimental value	% Error	Experimental value	% Error
C	51.28	51.34	0.06 %	49.34	-1.94%
H	4.29	4.20	-0.09 %	4.31	0.02%
O	6.83	7.31	0.48 %	8.72	2.09%
N	23.91	23.98	0.07 %	23.90	-0.01%
S	13.69	13.17	-0.52 %	13.73	0.04%

2.3 ^{1}H NMR spectrum

For ^{1}H NMR, 0.020 g of *p*-amino TAA and *o*-amino TAA were dissolved in dimethylsulfoxide, D-6 (C$_2$D$_3$OS). The ^{1}H NMR spectra were recorded at 400 MHz on an INNOVA VARION NMR spectrometer 400 MHz.
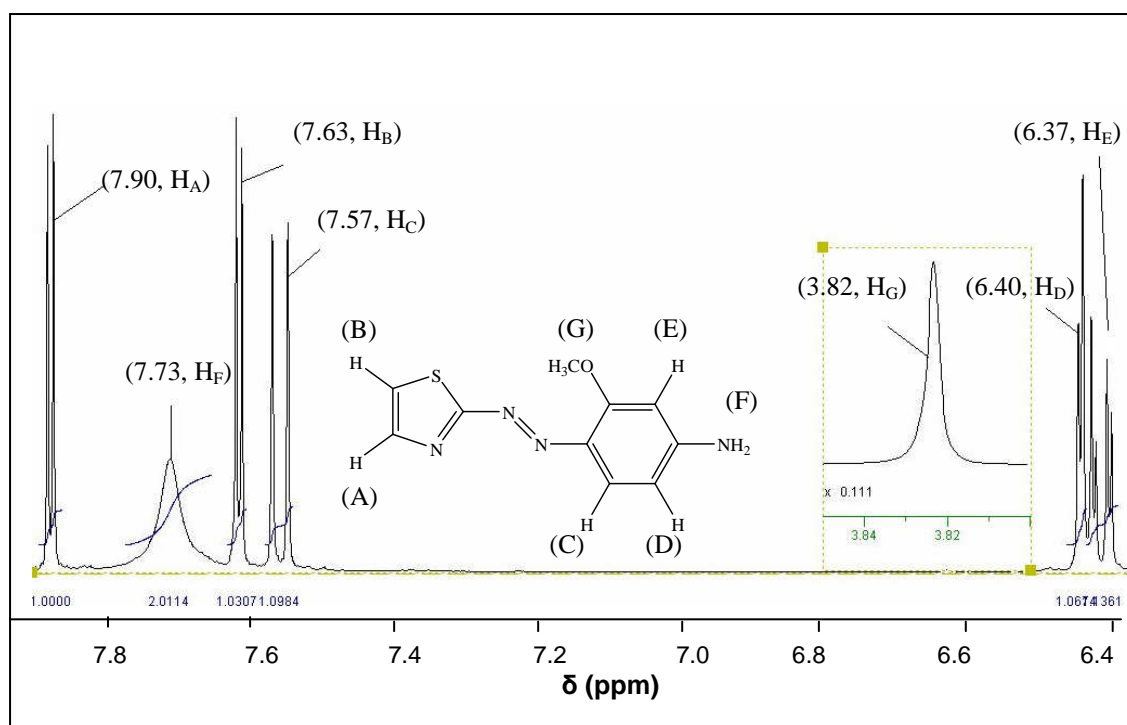
Figure 21 The ^{1}H NMR spectrum of 2-(2′-thiazolylazo)-5-aminoanisole
(*p*-amino TAA) in DMSO-*d*$_6$.

The ^{1}H NMR spectrum (DMSO-*d*$_6$, 400 MHz) of 2-(2′-thiazolylazo)-5-aminoanisole (*p*-amino TAA) shows chemical shifts at δ 7.90 (1H, *d*, H$_A$, J$_{AB}$ = 3.44 Hz), 7.73 (2H, *bs*, H$_F$), 7.63 (1H, *d*, H$_B$, J$_{BA}$ = 3.44 Hz), 7.57 (1H, *d*, H$_C$, J$_{CD}$ = 9.04 Hz), 6.40 (1H, *dd*, H$_D$, J$_{DE}$ = 2.60 Hz, J$_{DC}$ = 9.04 Hz), 6.37 (1H, *d*, H$_E$, J$_{ED}$ = 2.60 Hz) and 3.82 (3H, *s*, H$_G$).

The peak of the two protons on the amino group of *p*-amino TAA is not sharp and without any coupling to hydrogens on an adjacent carbon atom. This may be caused by chemical exchange of proton with deuterium atoms of solvent (DMSO-d_6) and acidity of the hydrogen atom on the amino group (Pavia, 1996).
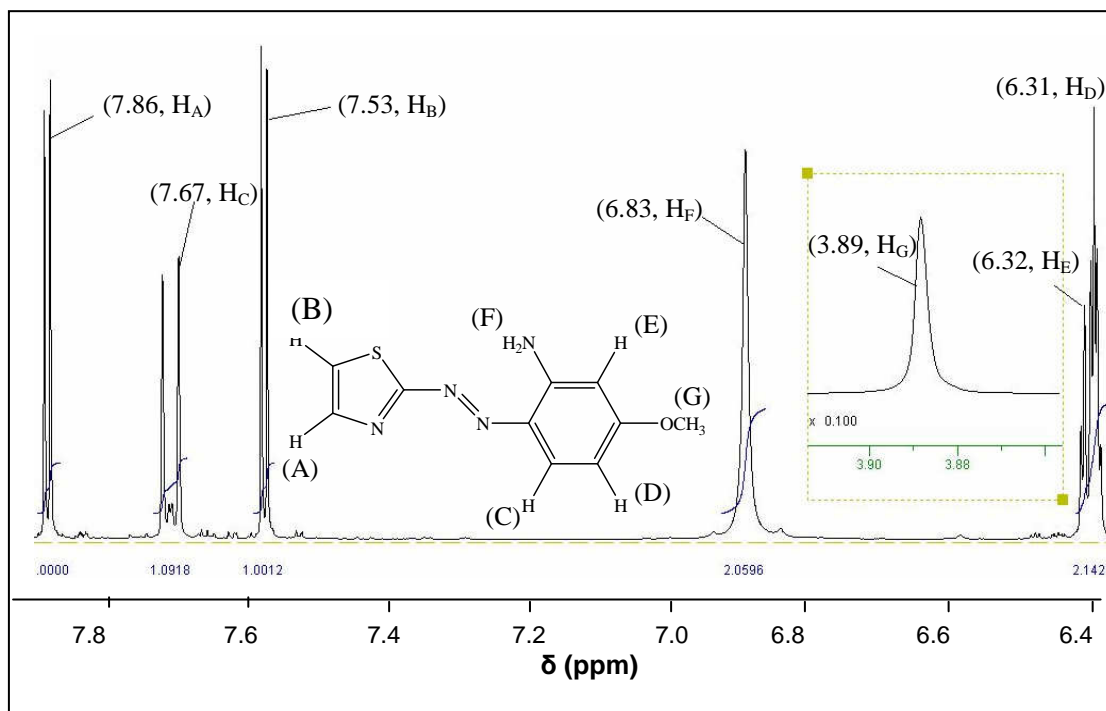
Figure 22 The ^{1}H NMR spectrum of 4-(2′-thiazolylazo)-3-aminoanisole
(*o*-amino TAA) in DMSO-d_6.

The ^{1}H NMR spectrum (DMSO-d_6, 400 MHz) of 4-(2′-thiazolylazo)-3-aminoanisole (*o*-amino TAA) shows chemical shifts at δ 7.86 (1H, *d*, H_A, J_{AB} = 3.44), 7.67 (1H, *d*, H_C, J_{CD} = 9.47 Hz), 7.53 (1H, *d*, H_B, J_{BA} = 3.44), 6.83 (2H, *s*, H_F), 6.32 (1H, *d*, H_E, J_{ED} = 2.16), 6.31 (1H, *dd*, H_D, J_{DE} = 2.16, J_{CD} = 3.88) and 3.89 (3H, *s*, H_G).

The peak of the two protons on the amino group of *o*-amino TAA is sharper than *p*-amino TAA and without any coupling to hydrogens on an adjacent carbon atom. This may be caused by chemical exchange of proton with deuterium atoms of solvent (DMSO-d_6) the same as *p*-amino TAA. The peaks also show low chemical

shift in comparison to that of *p*-amino TAA which might be attributed to the hydrogen bonding in *o*-amino TAA as mentioned in the results of their melting points. This is resulting from protons on the amino group are shielded by electrons from nitrogen atom of azo group resulting in the peak shift to highfield.

     2.4   ESI-Mass spectrum
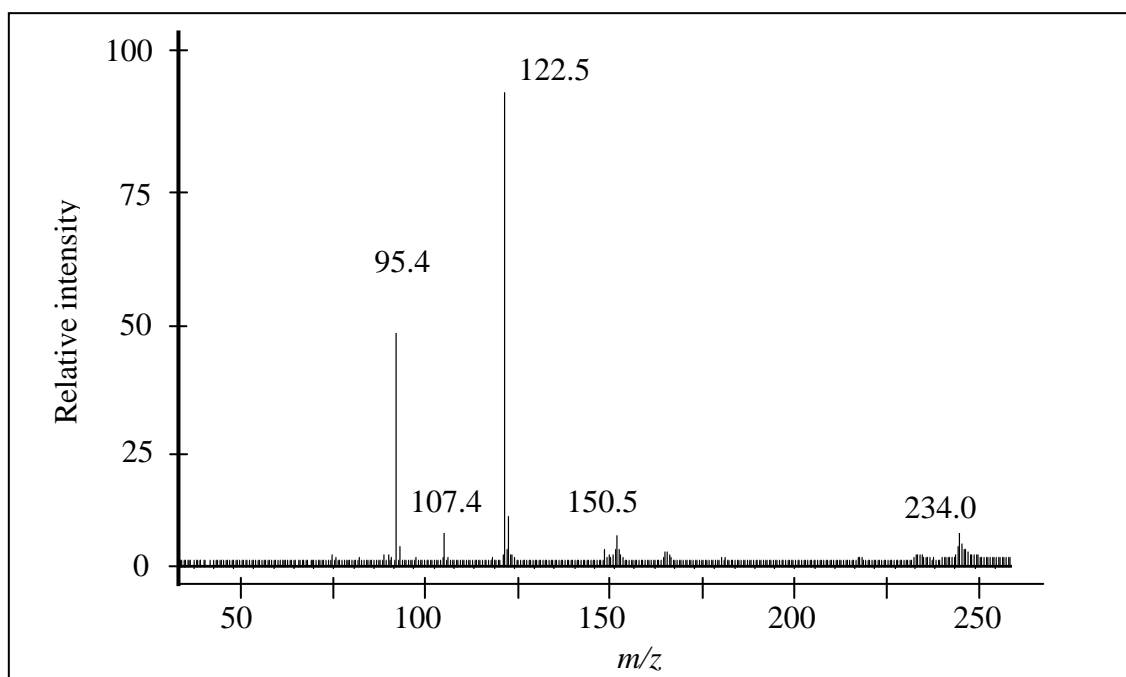
Figure 23 The ESI-Mass spectrum of 2-(2′-thiazolylazo)-5-aminoanisole

           (*p*-amino TAA)**.**

     The *m/z* (relative intensity) of *p*-amino TAA is as followed: 234.0 (10.48), 150.5 (7.36), 122.5 (100.00), 107.4 (11.40) and 95.4 (57.30). The possible pathway of the fragmentation of 2-(2′-thiazolylazo)-5-aminoanisole (*p*-amino TAA) is shown in Figure 24.
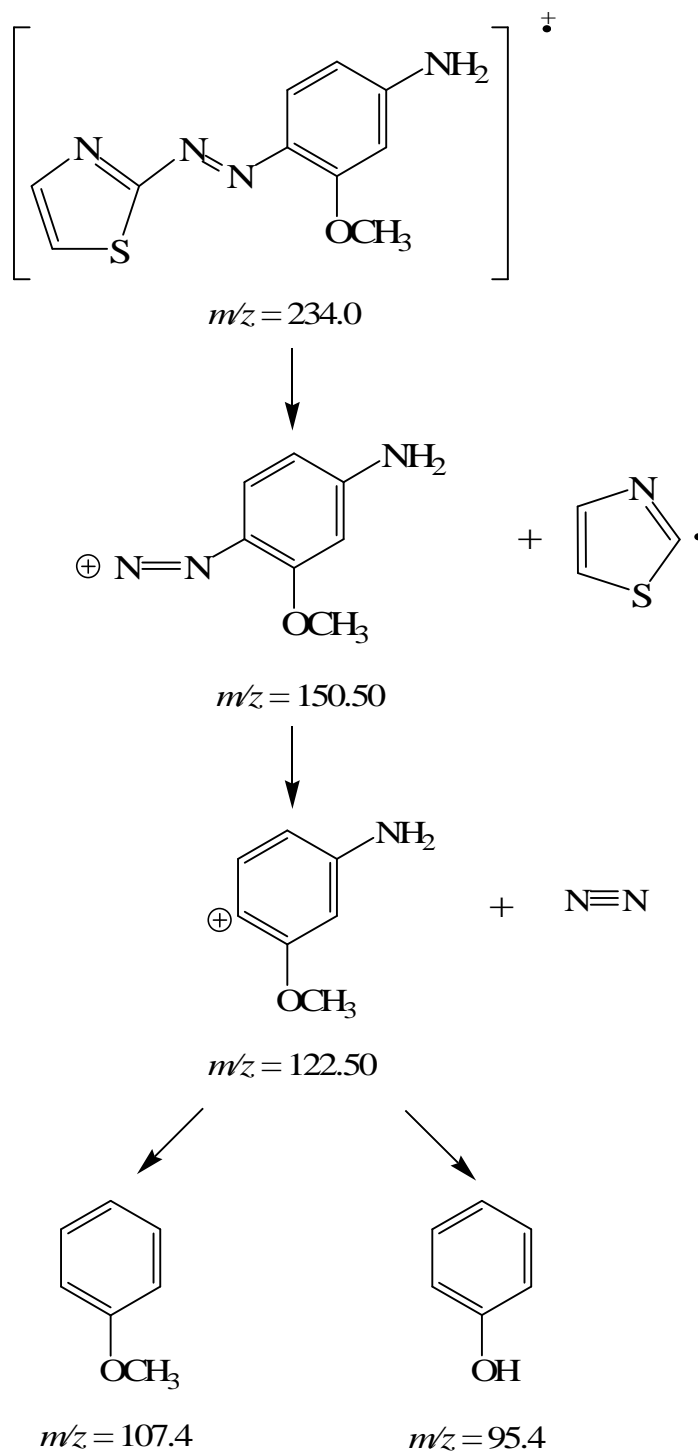
Figure 24 Pathway of the fragmentation of 2-(2′-thiazolylazo)-5-aminoanisole (*p*-amino TAA).
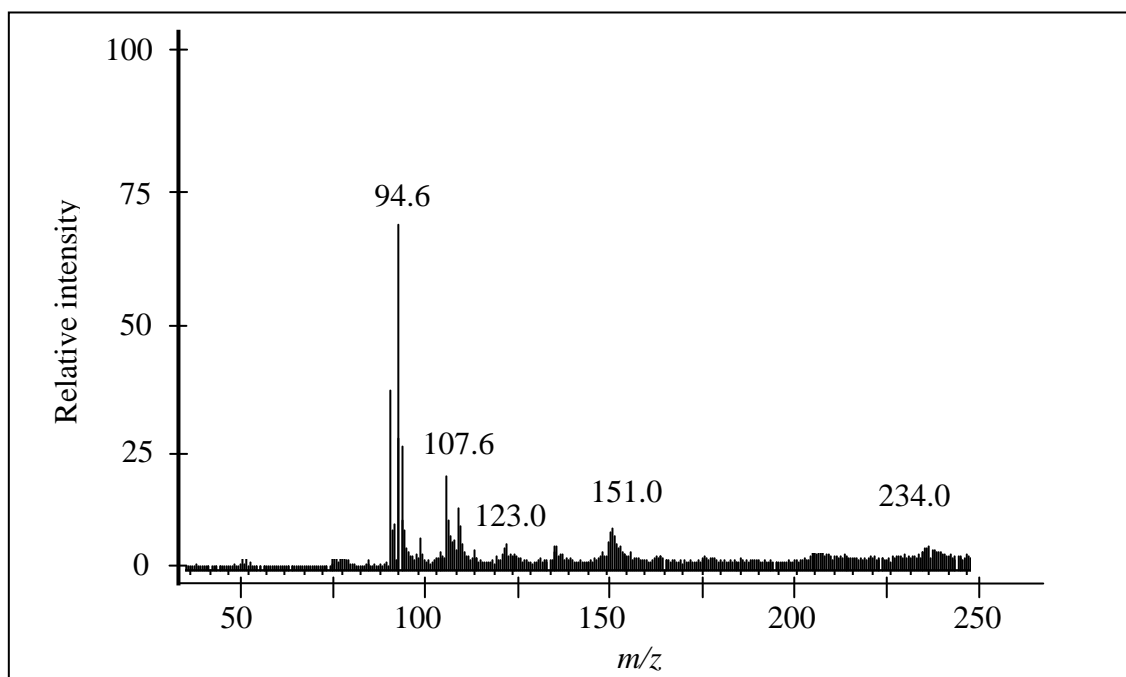
Figure 25 The ESI-Mass spectrum of 4-(2′-thiazolylazo)-3-aminoanisole
(*o*-amino TAA).

The *m/z* (relative intensity) of *o*-amino TAA is as followed: 234.0 (17.21),
151.0 (22.56), 123.0 (16.80), 107.6 (35.30) and 94.6 (100.0). The possible pathway of the
fragmentation of of 4-(2′-thiazolylazo)-3-aminoanisole (*o*-amino TAA) is shown in
Figure 26.
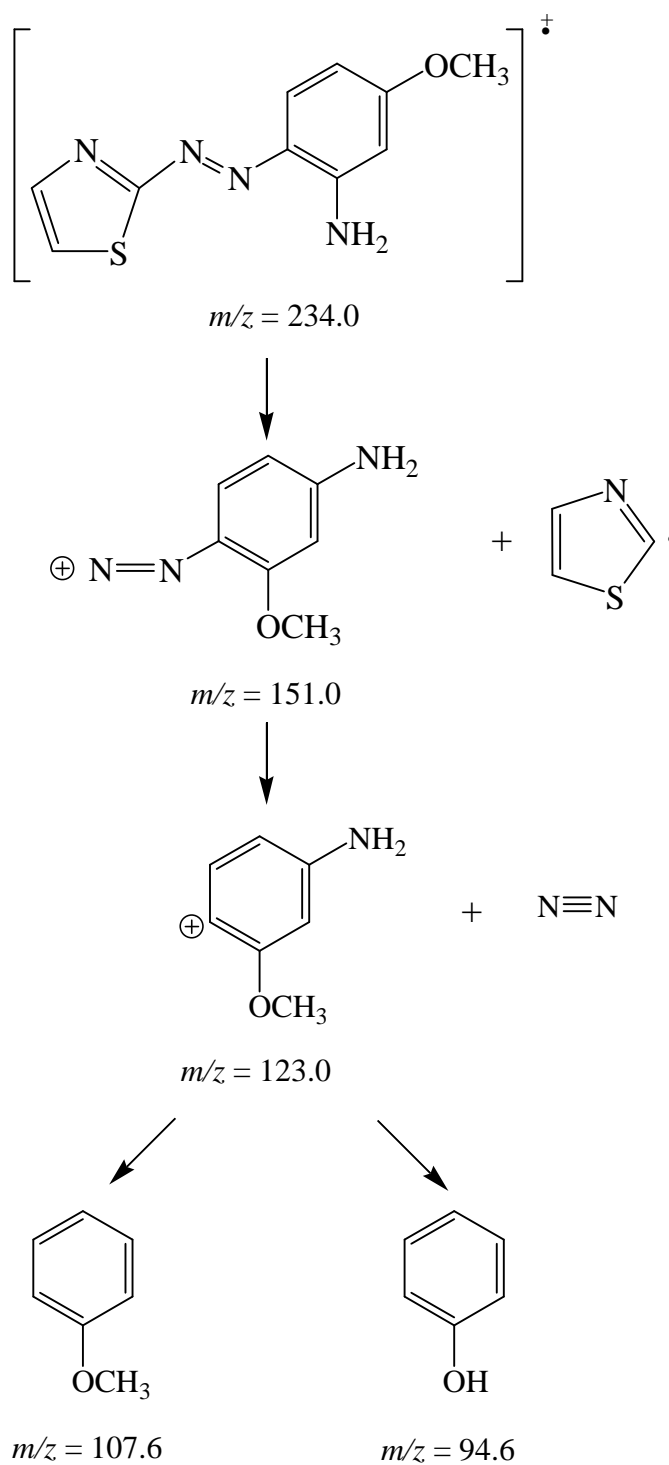
Figure 26 Pathway of the fragmentation of 4-(2′-thiazolylazo)-3-aminoanisole
(*o*-amino TAA).

FT-IR, ^{1}H NMR, mass spectroscopy and elemental analysis were used to identify the structures of *p*-amino TAA and *o*-amino TAA. IR peaks of functional groups of both *p*-amino TAA and *o*-amino TAA such as N=N, N-H, C-S, C=N and C-O-C were identified as shown in Figure 19 and Figure 20. ^{1}H NMR spectrum showed chemical shifts and integration of protons in both compounds including intramolecular hydrogen bonding of proton from amino group on *o*-amino TAA, the results corresponded to the structures of *p*-amino TAA and *o*-amino TAA, respectively. Mass spectrum gave the molecular ion base peak at *m/z* 234.0 of both compounds and their successive fragmentation pathway as shown from Figure 23 to Figure 26. In addition, the percentage of theoretical and experimental values from C, H, N, S and O analysis in *p*-amino TAA and *o*-amino TAA were insignificantly different as seen in Table 4.

From the results of these methods, it can be concluded that the synthesized products were *p*-amino TAA and *o*-amino TAA.

3. **Determination of the acid dissociation constants (pK_a) of *p*-amino TAA and *o*-amino TAA**

The absorption spectra of *p*-amino TAA and *o*-amino TAA in universal buffer solutions at pH 2.0 to 5.0 were measured in the wavelength range of 300-700 nm and the results are shown in Figure 27 and Figure 28
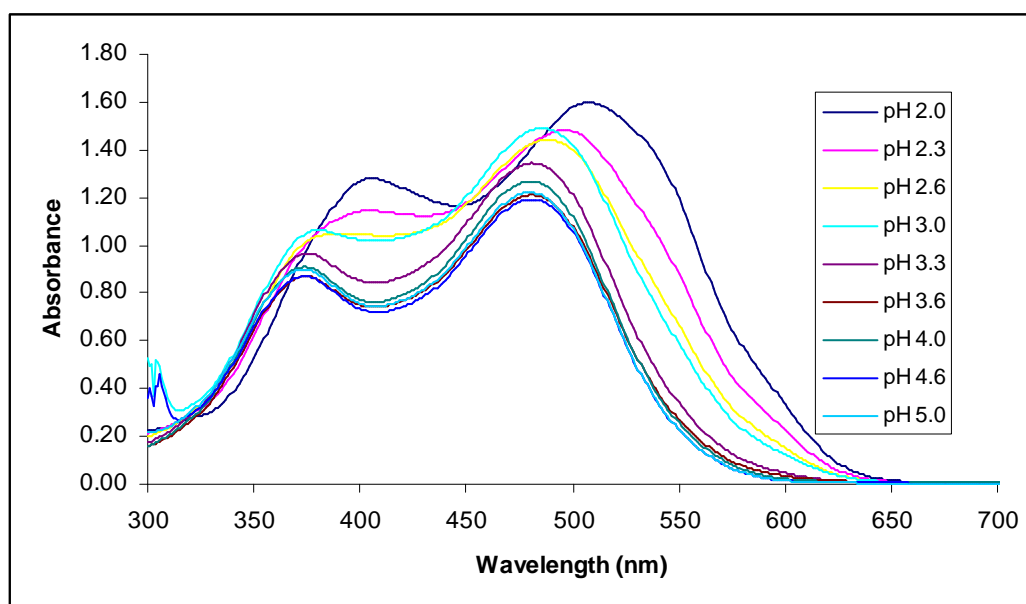
Figure 27 The absorption spectra of 1.0×10^{-3} M *p*-amino TAA at pH 2.0 to 5.0.
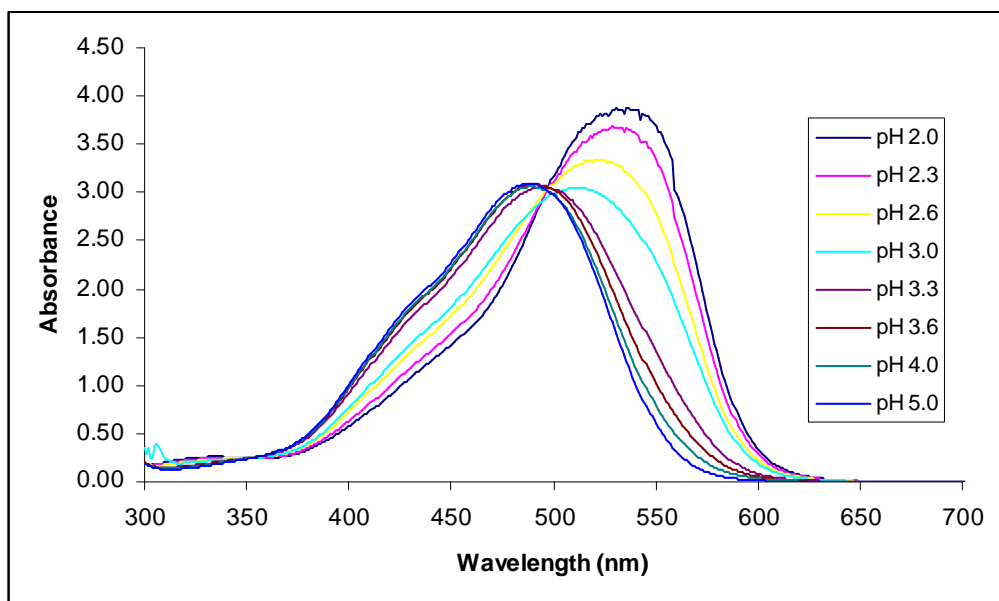
Figure 28 The absorption spectra of 1.0×10^{-3} M *o*-amino TAA at pH 2.0 to 5.0.

The spectra of *p*-amino TAA and *o*-amino TAA show the shift of maximum absorption to lower wavelength when pH increase which might be attributed to the dissociation of proton from each compound.

The dissociation constant values of *p*-amino TAA and *o*-amino TAA have been determined by two methods, half-height method and limiting absorbance methods (Masoud, 2003). The pK_a values are readily obtained from the absorbance-pH curves by application of these methods as shown in Appendix B and Appendix C. The quantum chemical calculations were also used to propose the dissociation mechanism of these compounds.

3.1   Half Height Method

This method was studied in the range of wavelength 510-530 nm for both *p*-amino TAA and *o*-amino TAA which show the maximum difference of absorption between low pH and high pH. The results from this method indicate that the

calculated pK_a of *p*-amino TAA and *o*-amino TAA are approximately 3.0 and 3.3, respectively. The log $\dfrac{As}{As_{max} - As}$ -pH curves are shown in Figure 29 and Figure 30.
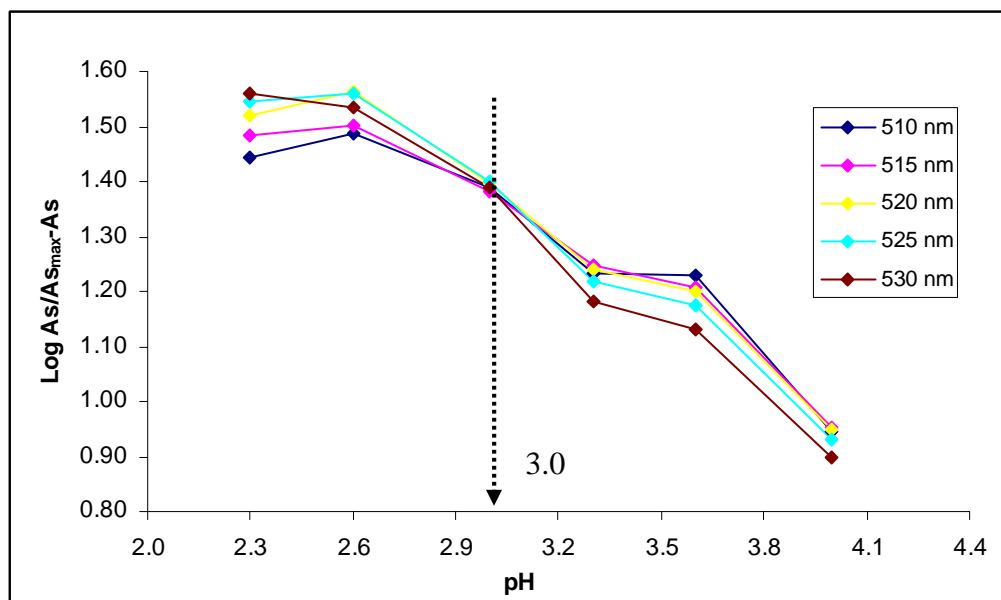
Figure 29 The absorbance-pH curve of *p*-amino TAA (half-height method).
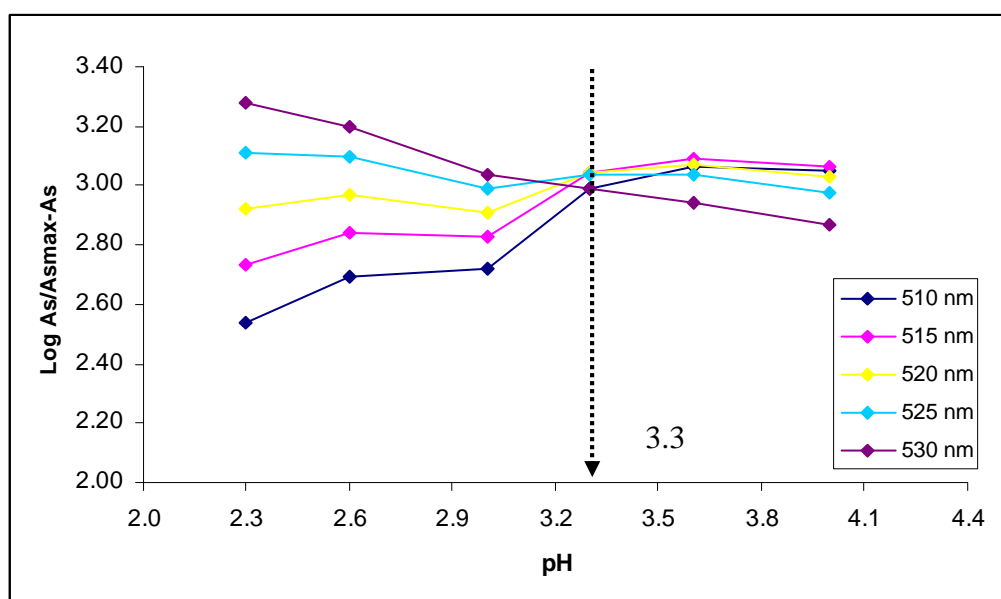
Figure 30 The absorbance-pH curve of *o*-amino TAA (half-height method).

3.2   Limiting Absorbance Method

This method was studied in the range of wavelength 505-530 nm for both *p*-amino TAA and *o*-amino TAA which show the maximum difference of absorption between low pH and high pH. The results from this method indicate that the calculated pK_a of *p*-amino TAA and *o*-amino TAA are approximately 3.0 and 3.3, respectively. The log $\dfrac{As - As_{min}}{As_{max} - As}$ - pH curves are shown in Figure 31 and Figure 32.
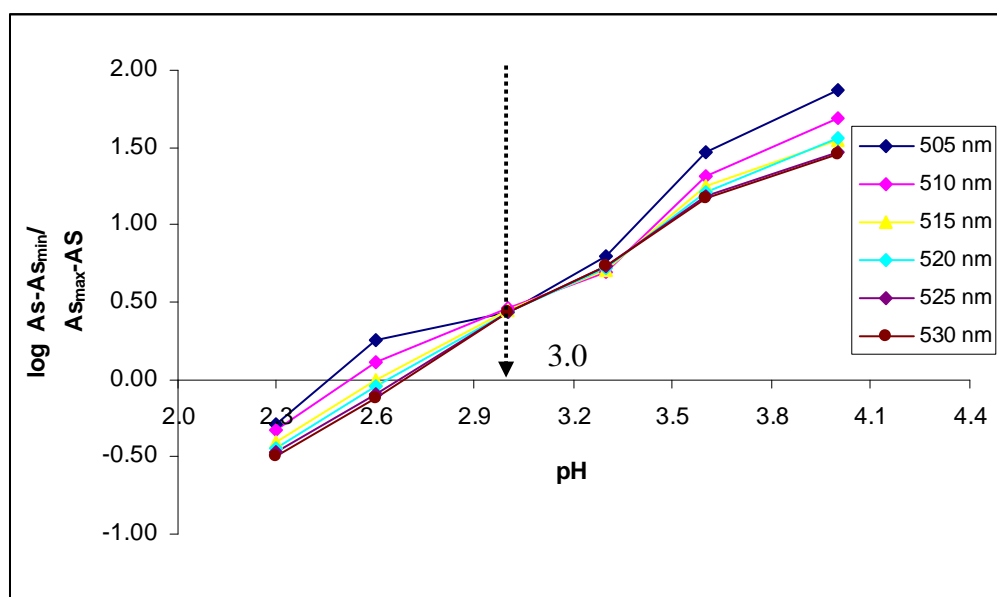
Figure 31 The log $\dfrac{As - As_{min}}{As_{max} - As}$ - pH curve of *p*-amino TAA (limiting absorbance method).
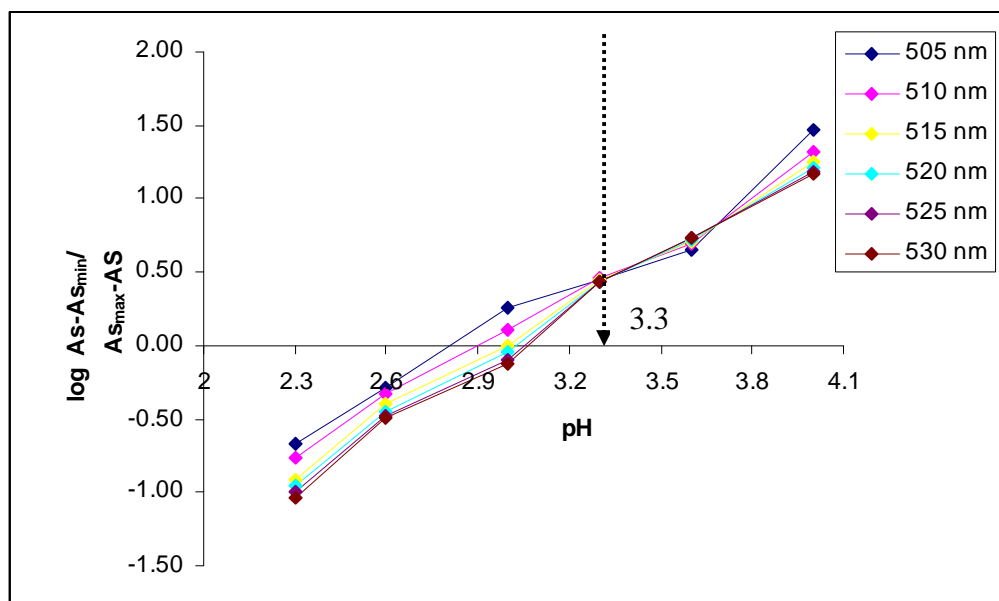
Figure 32 The log $\dfrac{As - As_{min}}{As_{max} - As}$ - pH curve of *o*-amino TAA (limiting absorbance method).

3.3 The quantum chemical calculations

The molecular structures for determining the protonated position of both *p*-amino TAA and *o*-amino TAA were optimized by the Density Functional Theory (DFT) method, Becke 3–Lee–Yang–Parr (B3LYP) functional with the Guassian 03 program. The change in colors with the pH modification from pink to orange in *p*-amino TAA and from orange-red to orange in *o*-amino TAA suggested that the change in their structures by the dissociation of proton in each molecule can occur. The noticeable change in maximum wavelength of each compound can observe once in this pH region which indicated that there is only one proton that can dissociate from *p*-amino TAA and *o*-amino TAA. Moreover, the spectra in each case show an isobestic point which indicates that two species are in equilibrium, protonated by one proton and deprotonated in the neutral forms. In acid solution (pH 2.0 to pH 5.0), there are five positions on *p*-amino TAA and *o*-amino TAA that can be protonated. So, the protonated structures of these compounds in the possibly various positions are

proposed as shown from Figure 34 and Figure 35. The protonated position that gives the lowest energy may be assigned to the structure in protonated form before the dissociation of proton occurs to form the neutral structures for each ligand. The energies of protonated *p*-amino TAA and *o*-amino TAA are shown in Table 5 and Table 6.

(a)

(b)
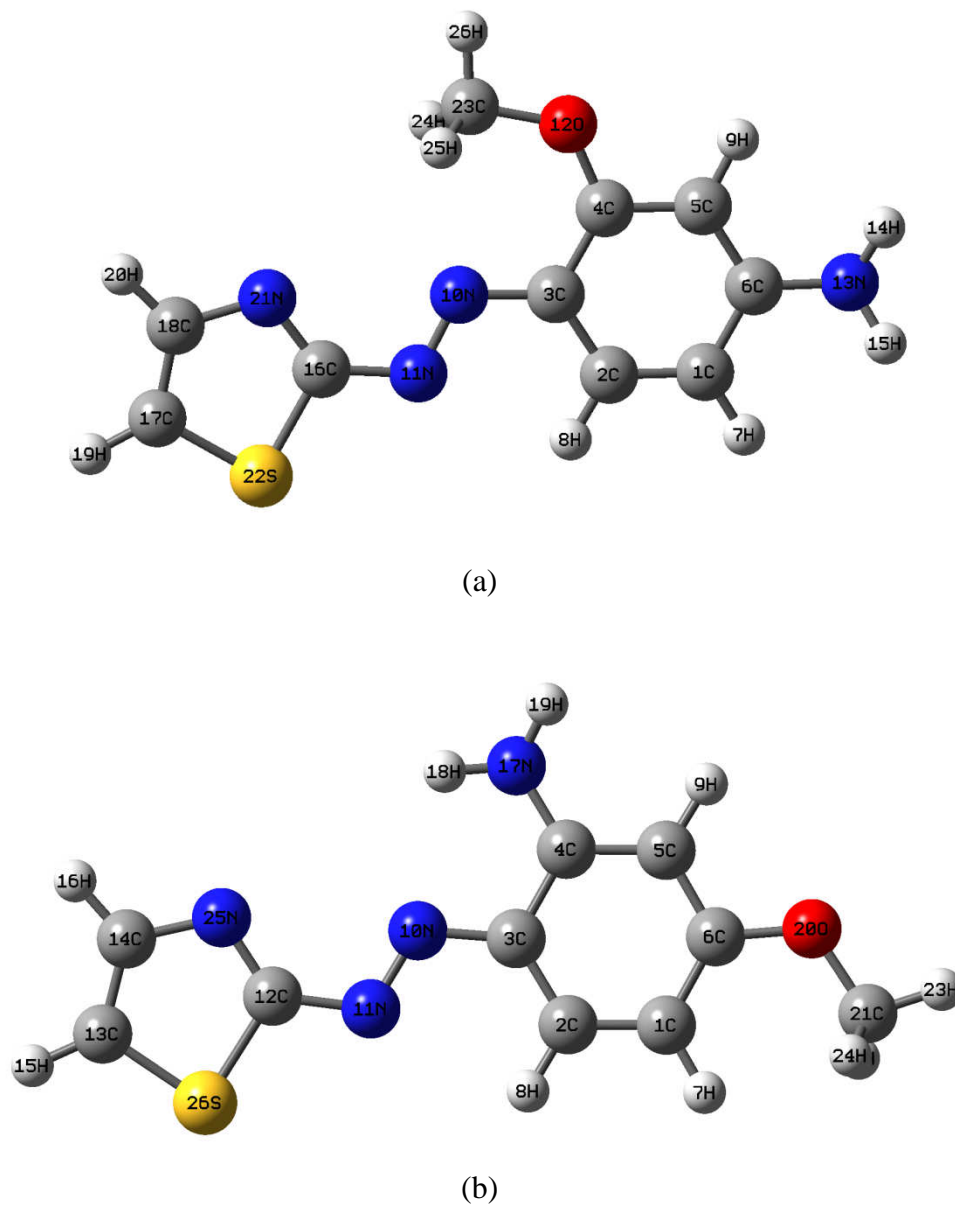
Figure 33 The optimized structure of (a) *p*-amino TAA and (b) *o*-amino TAA
(GaussView 3.09).
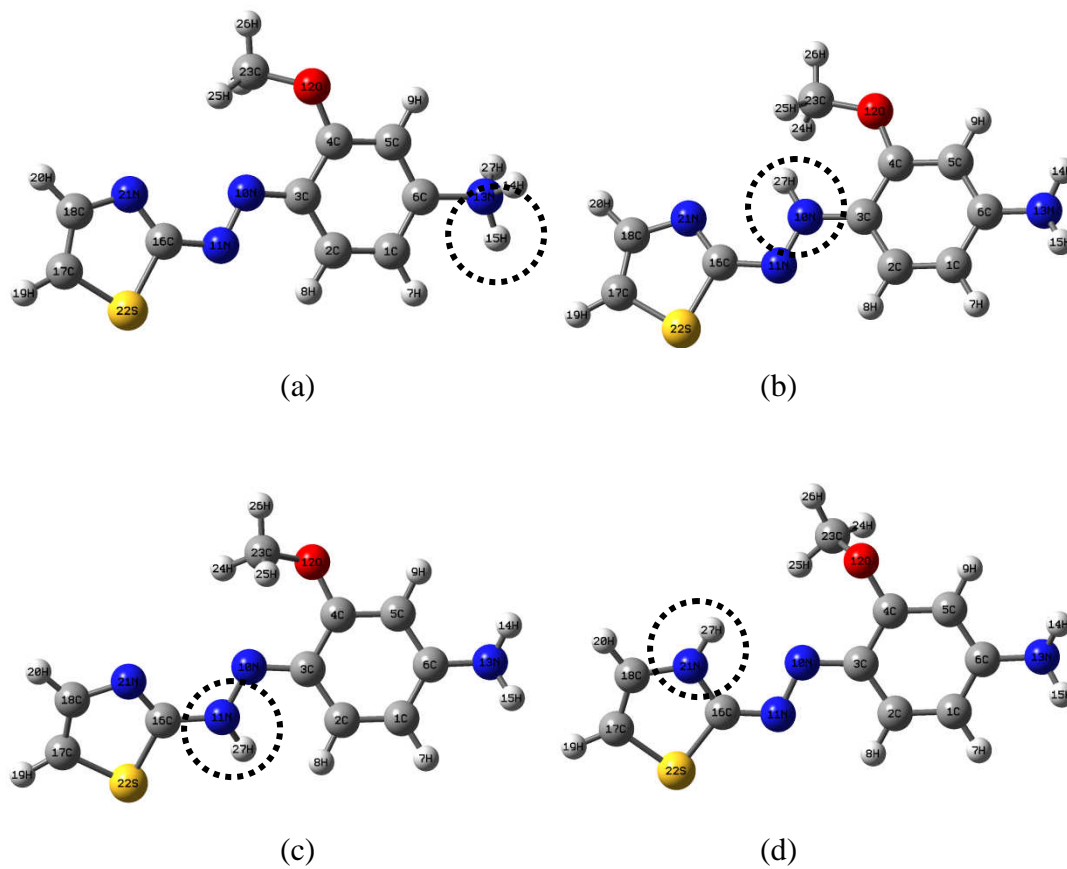
Figure 34 The proposed structures in protonated forms of *p*-amino TAA for
the possibly various positions
(a) nitrogen atom of amino group
(b) nitrogen atom of azo group that adjacent to the aromatic ring
(c) nitrogen atom of azo group that adjacent to the thiazole ring
(d) nitrogen atom of thiazole ring.
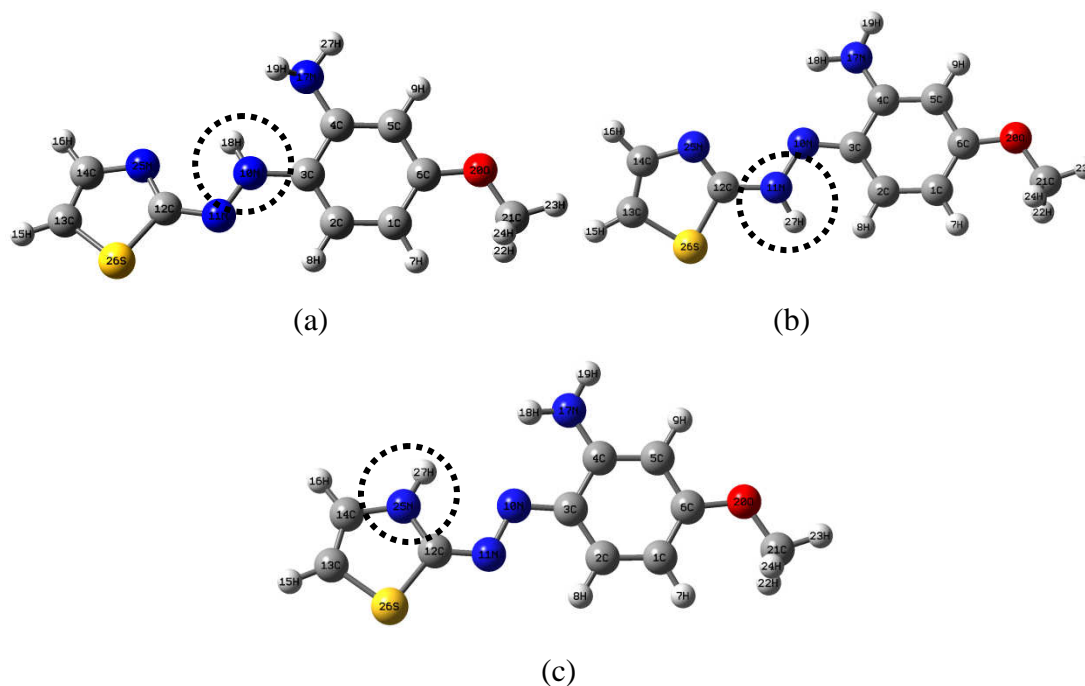
Figure 35 The proposed structures in protonated forms of *o*-amino TAA for the
possibly various positions
- (a) nitrogen atom of azo group that adjacent to the aromatic ring
- (b) nitrogen atom of azo group that adjacent to the thiazole ring
- (c) nitrogen atom of thiazole ring.

Table 5 Energies of the proposed structures in protonated forms of *p*-amino TAA for
the possibly various positions

protonated position	energy (a.u.)
p-amino TAA (amino)	-1079.944099
p-amino TAA (n-thiazole)	-1080.020949
p-amino TAA (s-thiazole)*	-1079.974032
p-amino TAA (azo-thiazole)	-1080.018306
p-amino TAA (azo-aromatic)	-1080.042442

Table 6 Energies of the proposed structures in protonated forms of *o*-amino TAA for
the possibly various positions

protonated position	energy (a.u.)
o-amino TAA (amino)**	-1080.040727
o-amino TAA (n-thiazole)	-1080.02937
o-amino TAA (s-thiazole)*	-1079.983961
o-amino TAA (azo-thiazole)	-1080.028272
o-amino TAA (azo-aromatic)	-1080.040727

*   distorted structure

**   changed structure

The results show that the protonation on nitrogen atom of azo group which is
adjacent to the aromatic ring for both *p*-amino TAA and *o*-amino TAA give the
lowest energies. It can conclude that these forms might be the structures of
p-amino TAA and *o*-amino TAA before the dissociation of proton occurs to form the
neutral structures for each ligand. For the protonation on sulfur atom of thiazole ring,
the structures of *p*-amino TAA and *o*-amino TAA are converted to be other structures.
So, this position is not expected to be the protonated position. Similarly, the
protonation on nitrogen atom of amino group of *o*-amino TAA is changed in its
position. The proton transfers from nitrogen atom of amino group to nitrogen atom of
azo group which is adjacent to aromatic ring, so their energies are equal. These results
can confirm by their energies which have high values in comparison to other
protonated structures.

4. Complex formation of *p*-amino TAA and *o*-amino TAA with rhodium(III)

The absorption of *p*-amino TAA and *o*-amino TAA in visible region were studied in universal buffer solutions at various pH. The azo compound displays mainly a broad band in the visible region (479-535 nm). The formation of complex between *p*-amino TAA and rhodium(III) and between *o*-amino TAA and rhodium(III) at various pH were studied by UV-Vis spectroscopy. The spectra showed that at pH 5 was the optimum pH for the formation of rhodium(III)-(*p*-amino TAA) complex because of the highest difference between the absorption bands of the rhodium(III)-(*p*-amino TAA) complex and *p*-amino TAA. For *o*-amino TAA, pH 3 was the most suitable pH for the formation of rhodium(III)-(*o*-amino TAA) complex due to the shift in wavelength of rhodium(III)-(*o*-amino TAA) from *o*-amino TAA. The absorption spectra of the complexes at various pH are shown in Figure 36 to Figure 45. Moreover, color and λ_{max} of *p*-amino TAA, *o*-amino TAA and their complexes at various pH are shown in Table 7 and Table 8.
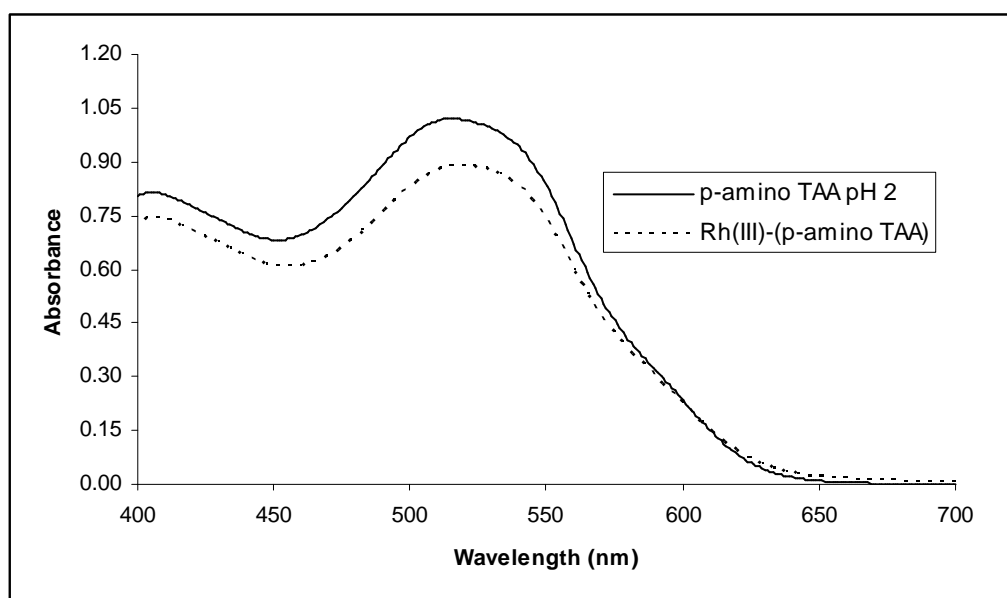
Figure 36 Absorption spectra of *p*-amino TAA and rhodium(III)-(*p*-amino TAA) complex at pH 2.
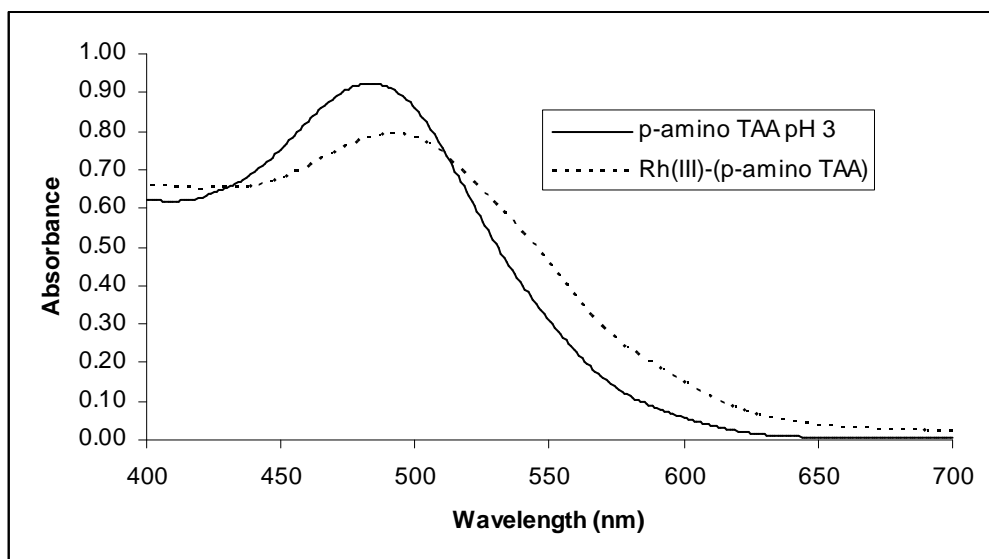
Figure 37 Absorption spectra of *p*-amino TAA and rhodium(III)-(*p*-amino TAA) complex at pH 3.
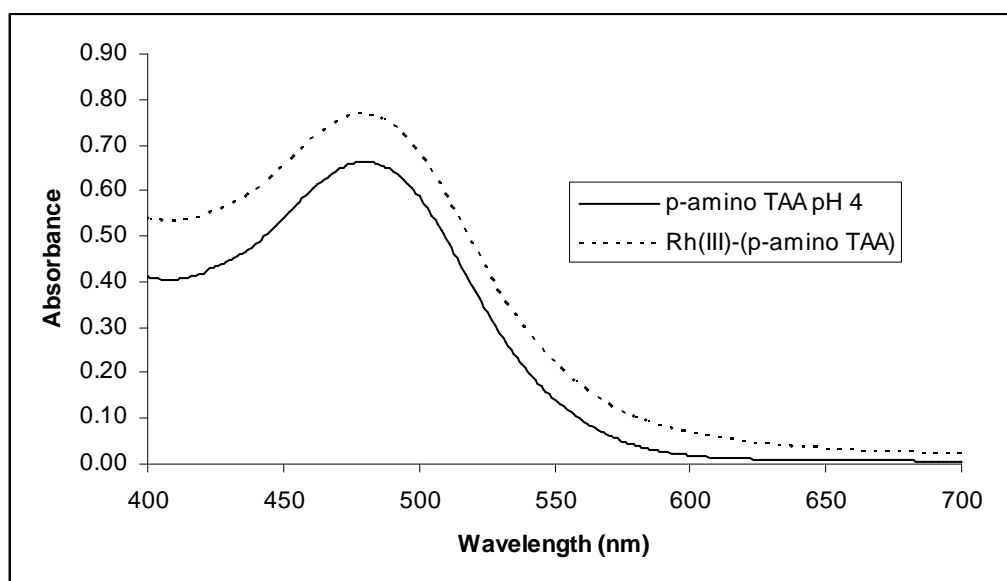
Figure 38 Absorption spectra of *p*-amino TAA and rhodium(III)-(*p*-amino TAA) complex at pH 4.
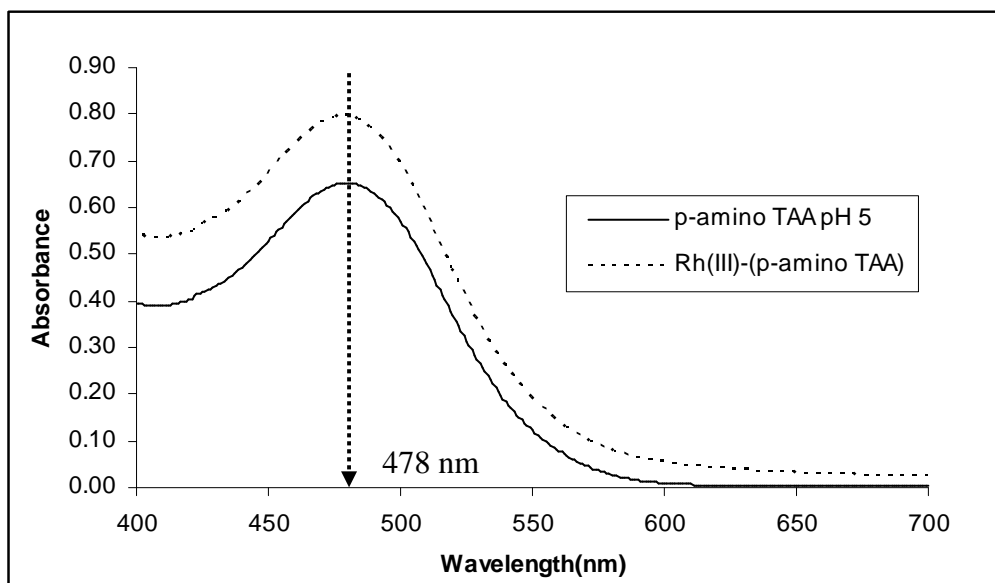
Figure 39 Absorption spectra of *p*-amino TAA and rhodium(III)-(*p*-amino TAA) complex at pH 5.
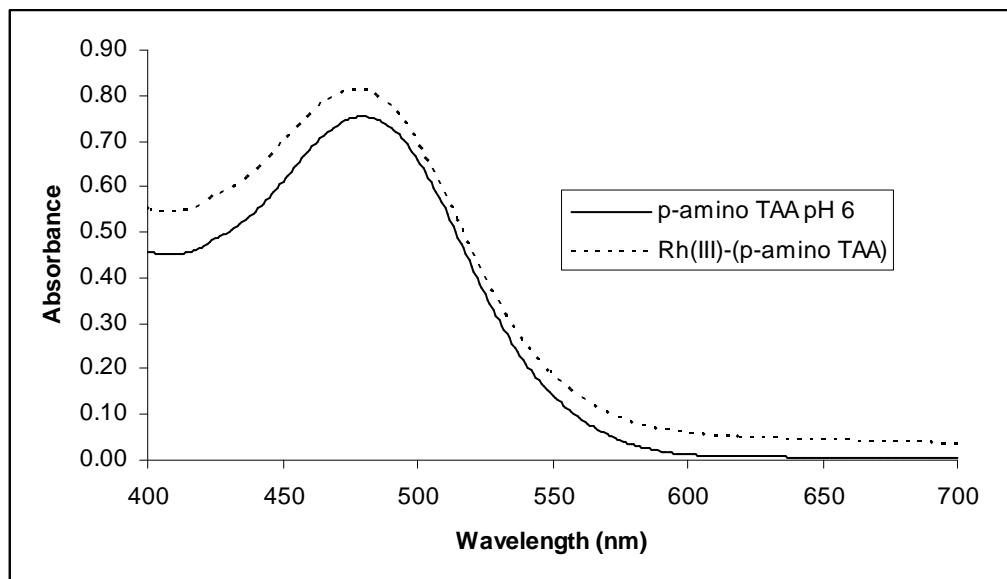
Figure 40 Absorption spectra of *p*-amino TAA and rhodium(III)-(*p*-amino TAA) complex at pH 6.
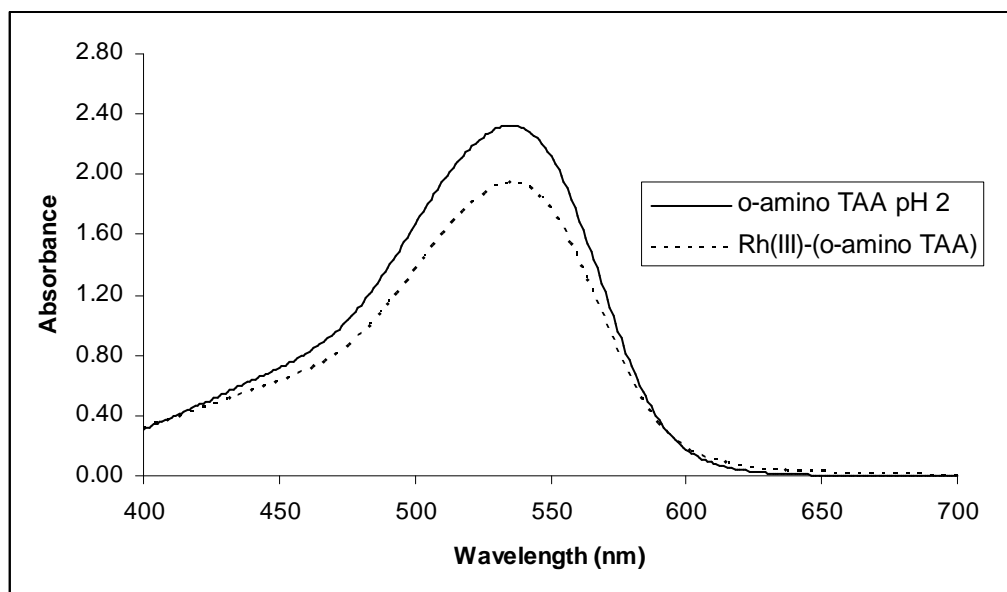
Figure 41 Absorption spectra of *o*-amino TAA and rhodium(III)-(*o*-amino TAA) complex at pH 2.
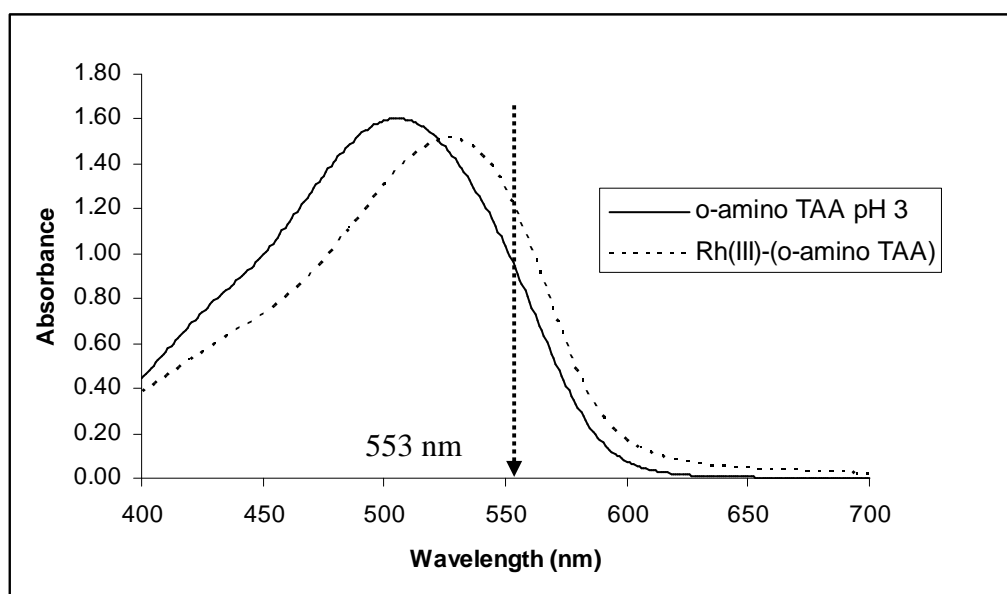
Figure 42 Absorption spectra of *o*-amino TAA and rhodium(III)-(*o*-amino TAA) complex at pH 3.
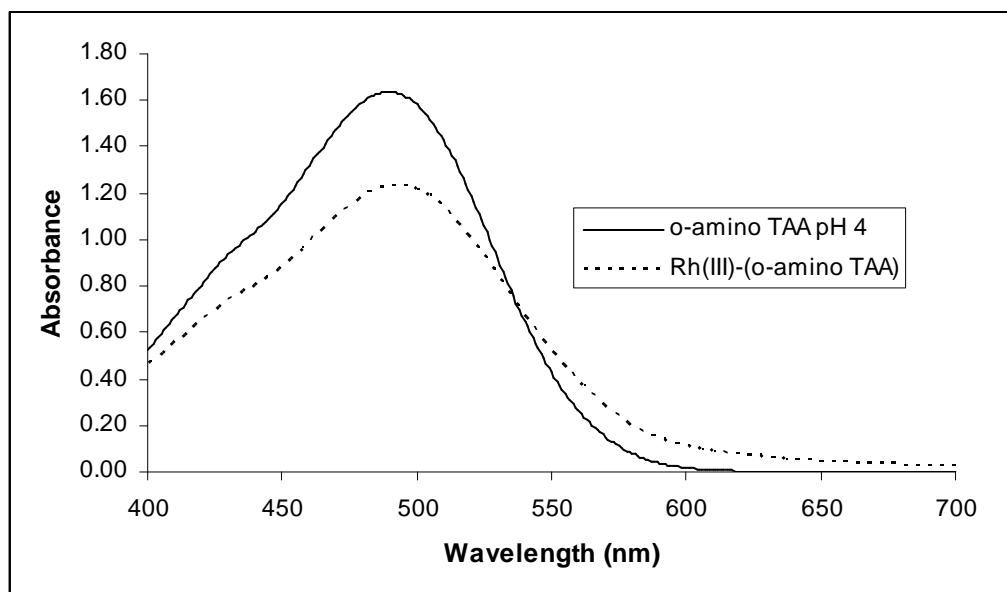
Figure 43 Absorption spectra of *o*-amino TAA and rhodium(III)-(*o*-amino TAA) complex at pH 4.
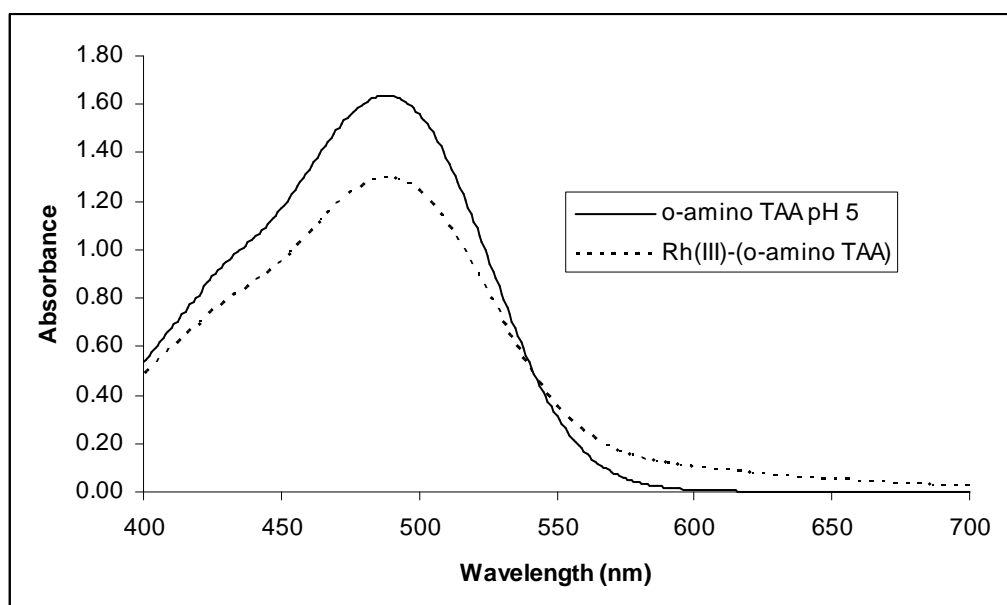
Figure 44 Absorption spectra of *o*-amino TAA and rhodium(III)-(*o*-amino TAA) complex at pH 5.
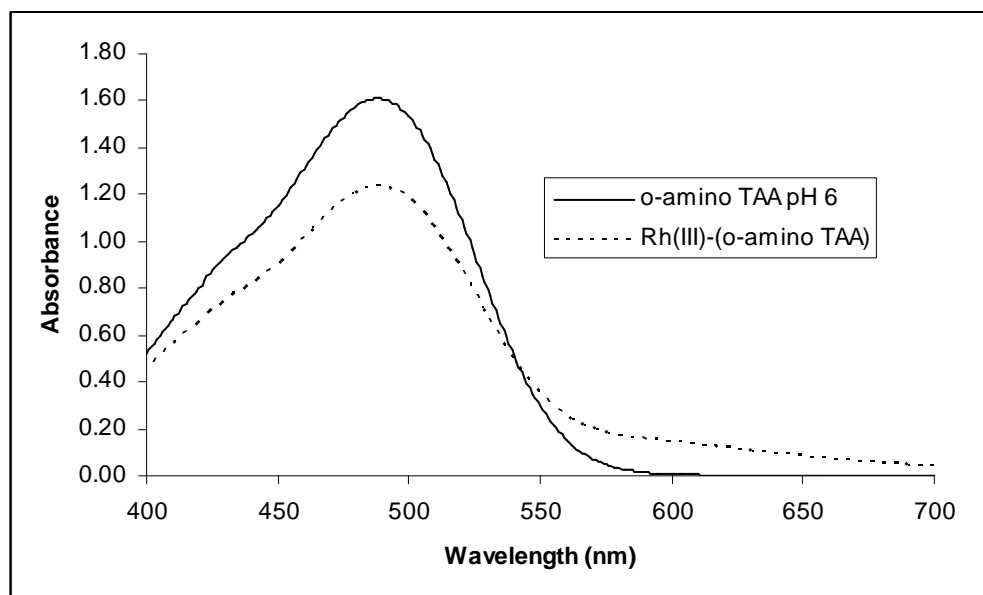
Figure 45 Absorption spectra of *o*-amino TAA and rhodium(III)-(*o*-amino TAA) complex at pH 6.

Table 7 The color and λ_{max} of *p*-amino TAA and rhodium(III) complex at various pH

pH	*p*-amino TAA		Rhodium(III)-(*p*-amino TAA) complex	
	color	λ_{max}	color	λ_{max}
2	Pink	523	Pink	519
3	Orange	483	Orange	493
4	Orange	480	Orange	479
5	Orange	479	Orange	478
6	Orange	479	Orange	477

Table 8 The color and λ_{max} of o-amino TAA and rhodium(III) complex at various pH

pH	o-amino TAA		Rhodium(III)-(o-amino TAA) complex	
	color	λ_{max}	color	λ_{max}
2	Deep-pink	535	Deep-pink	535
3	Orange-red	505	Deep-pink	527
4	Orange	489	Orange	492
5	Orange	488	Orange	489
6	Orange	488	Orange	489

5. Complex formation of *p*-amino TAA and *o*-amino TAA with platinum(IV)

The same as rhodium(III) complexes, the formation of complex between p-amino TAA and o-amino TAA with platinum(IV) at various pH were studied by UV-Vis spectroscopy. The spectra show that pH 3 was the suitable pH for the formation of platinum(IV)-(p-amino TAA) and platinum(IV)-(o-amino TAA) complexes because of the shift in wavelength of their complexes from p-amino TAA and o-amino TAA. The absorption spectra at various pH for the complexes formation are shown in Figure 46 to Figure 55. Moreover, color and λ_{max} of p-amino TAA, o-amino TAA and their complexes at various pH are shown in Table 9 and Table 10.
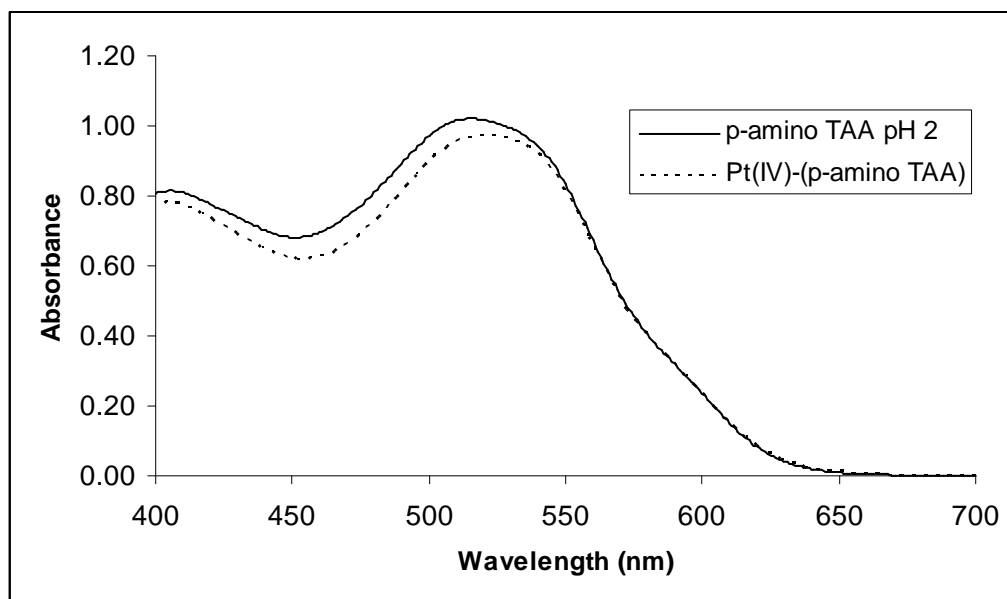
Figure 46 Absorption spectra of *p*-amino TAA and platinum(IV)-(*p*-amino TAA) complex at pH 2.
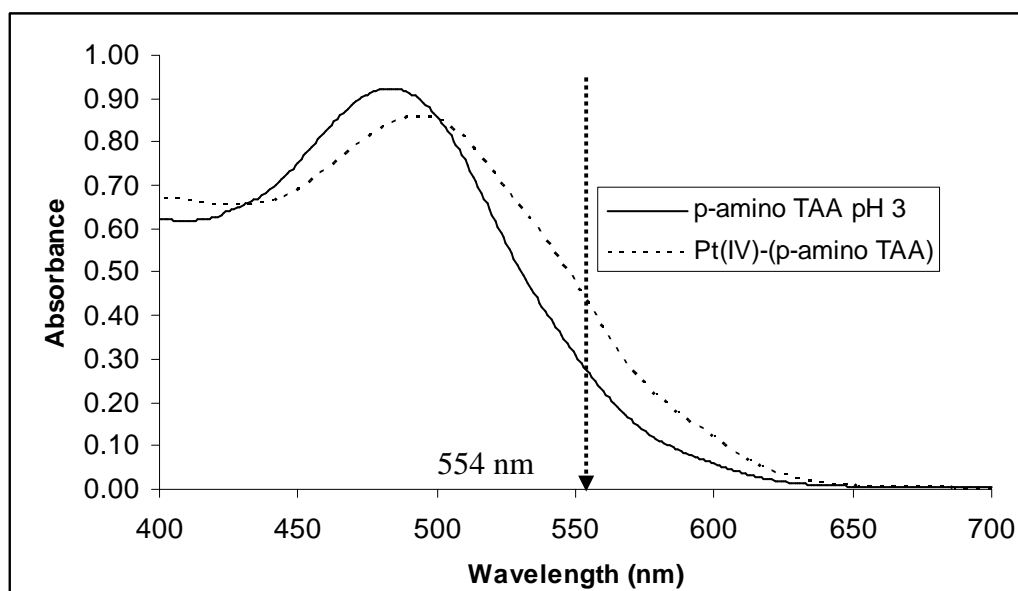
Figure 47 Absorption spectra of *p*-amino TAA and platinum(IV)-(*p*-amino TAA) complex at pH 3.
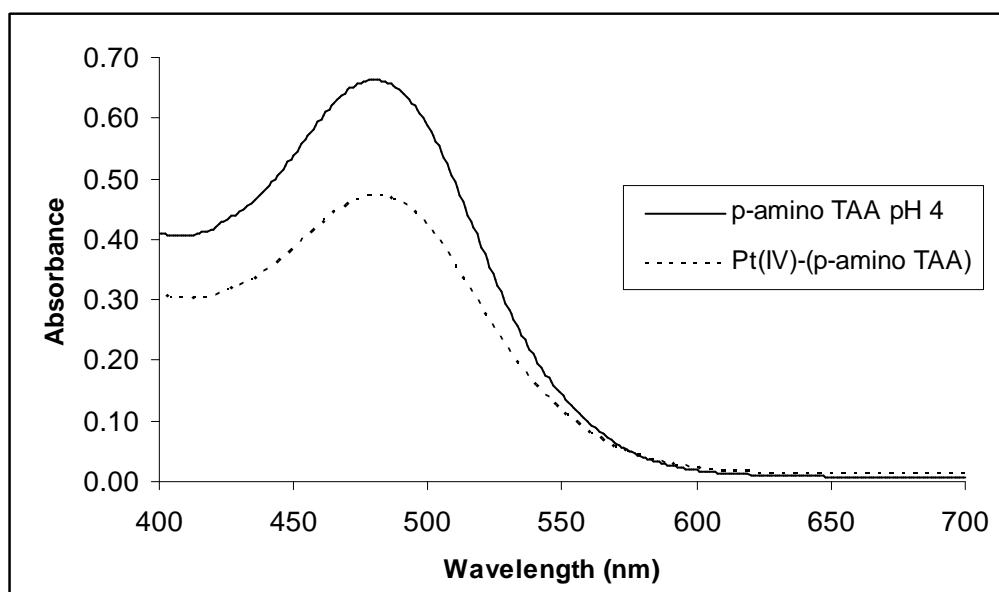
Figure 48 Absorption spectra of *p*-amino TAA and platinum(IV)-(*p*-amino TAA) complex at pH 4.
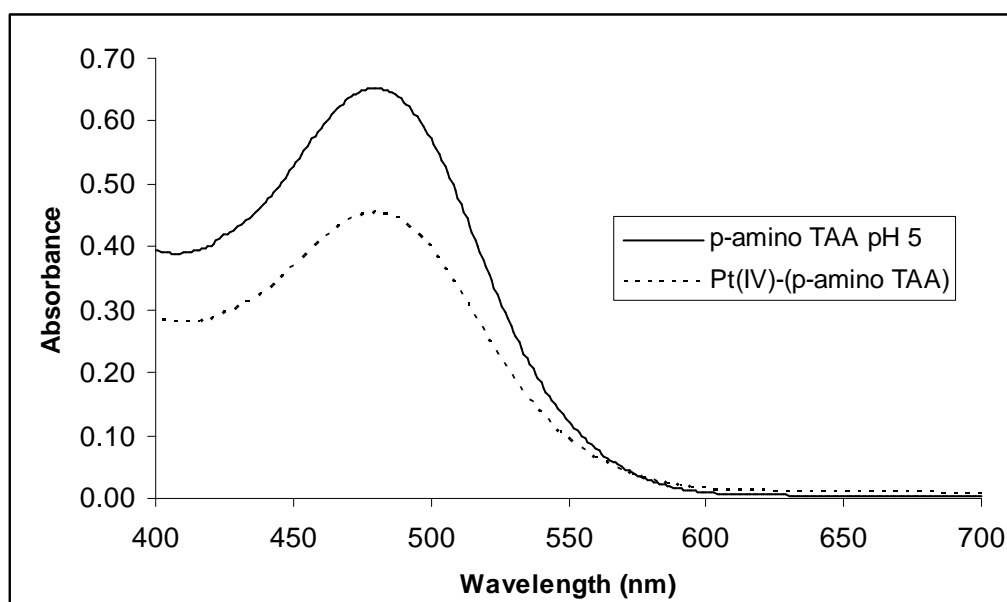
Figure 49 Absorption spectra of *p*-amino TAA and platinum(IV)-(*p*-amino TAA) complex at pH 5.
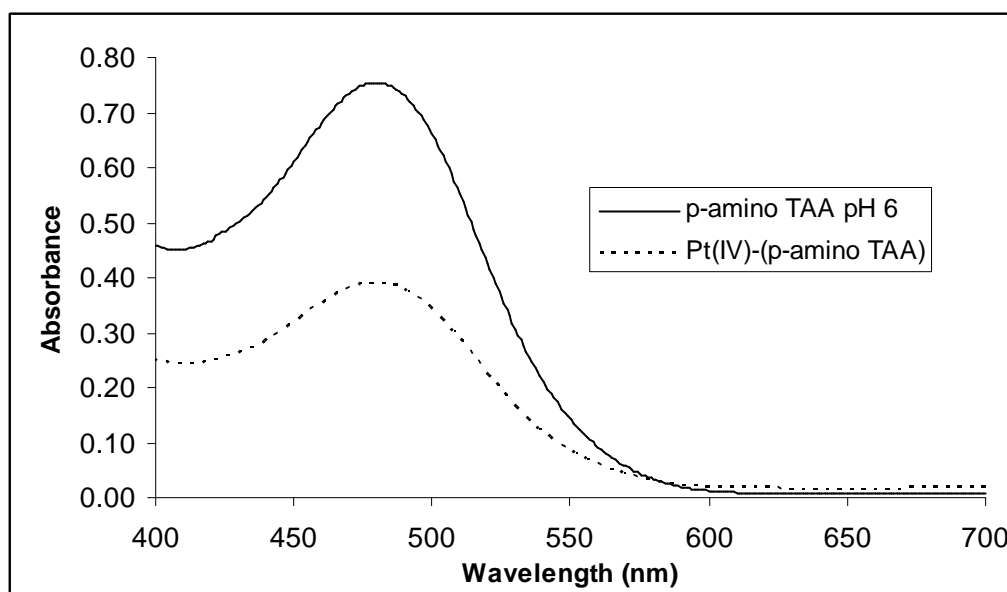
Figure 50 Absorption spectra of *p*-amino TAA and platinum(IV)-(*p*-amino TAA) complex at pH 6.
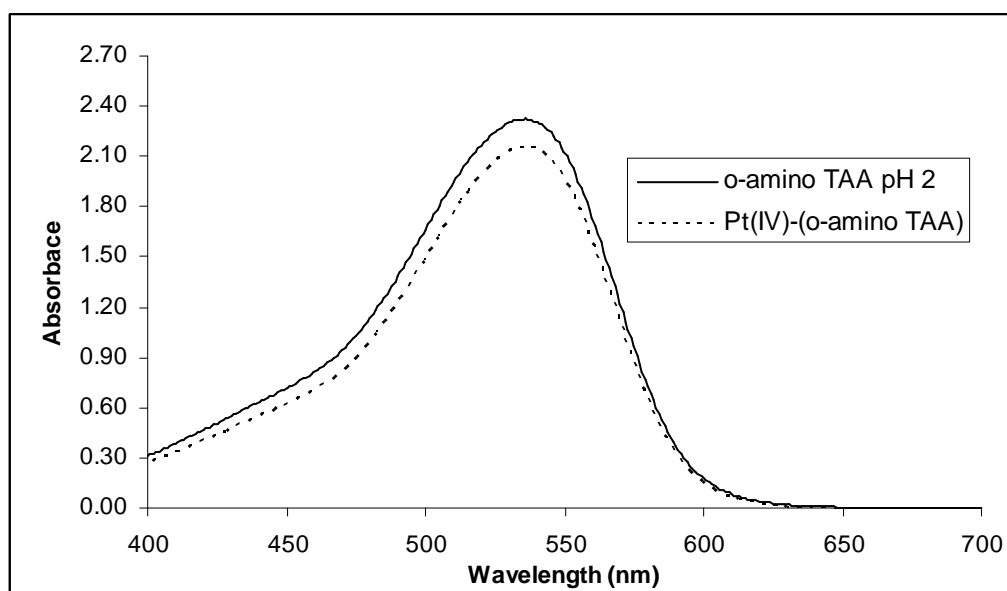
Figure 51 Absorption spectra of *o*-amino TAA and platinum(IV)-(*o*-amino TAA) complex at pH 2.
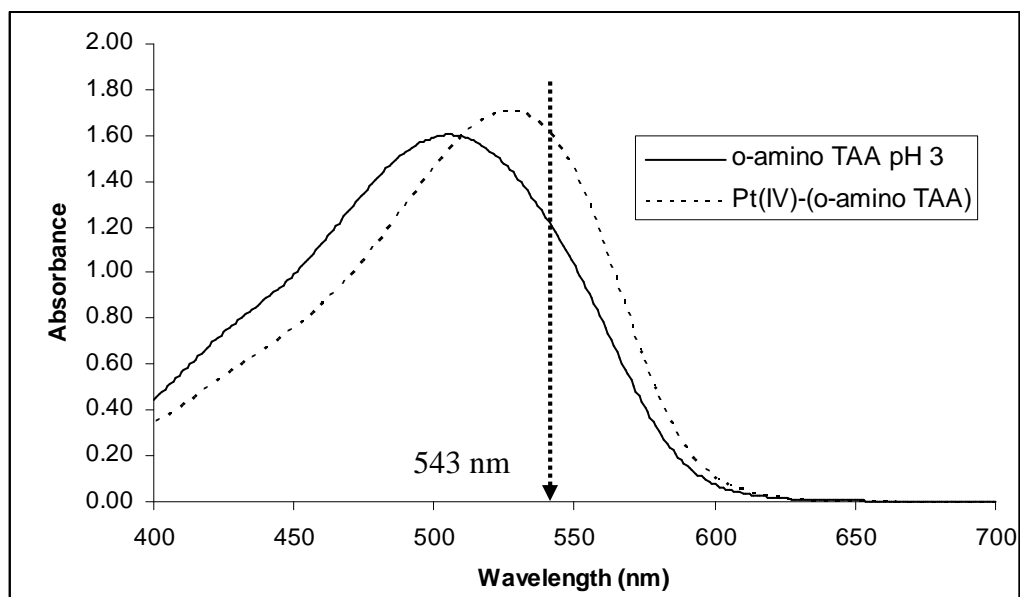
Figure 52 Absorption spectra of *o*-amino TAA and platinum(IV)-(*o*-amino TAA)
complex at pH 3.
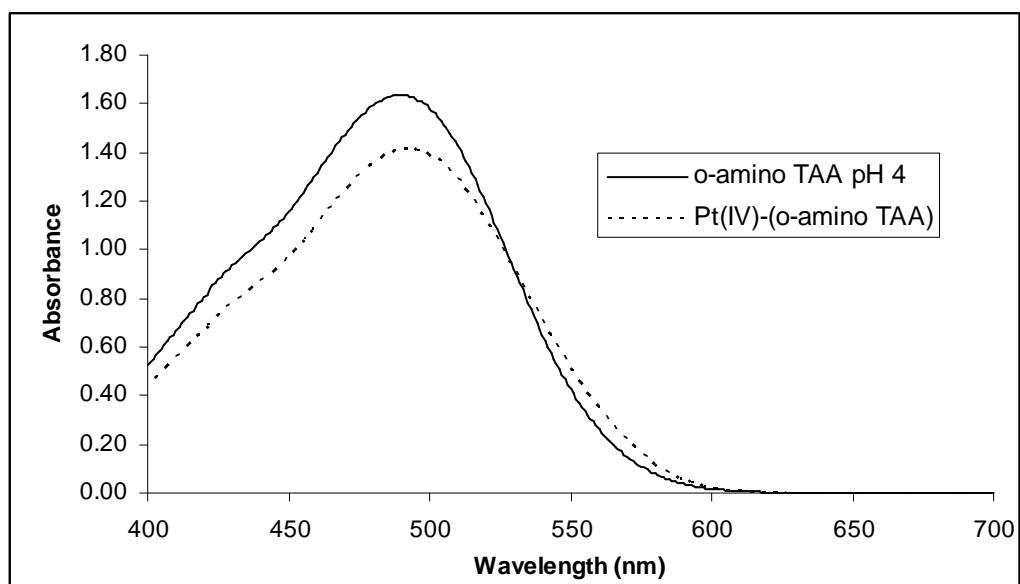
Figure 53 Absorption spectra of *o*-amino TAA and platinum(IV)-(*o*-amino TAA)
complex at pH 4.
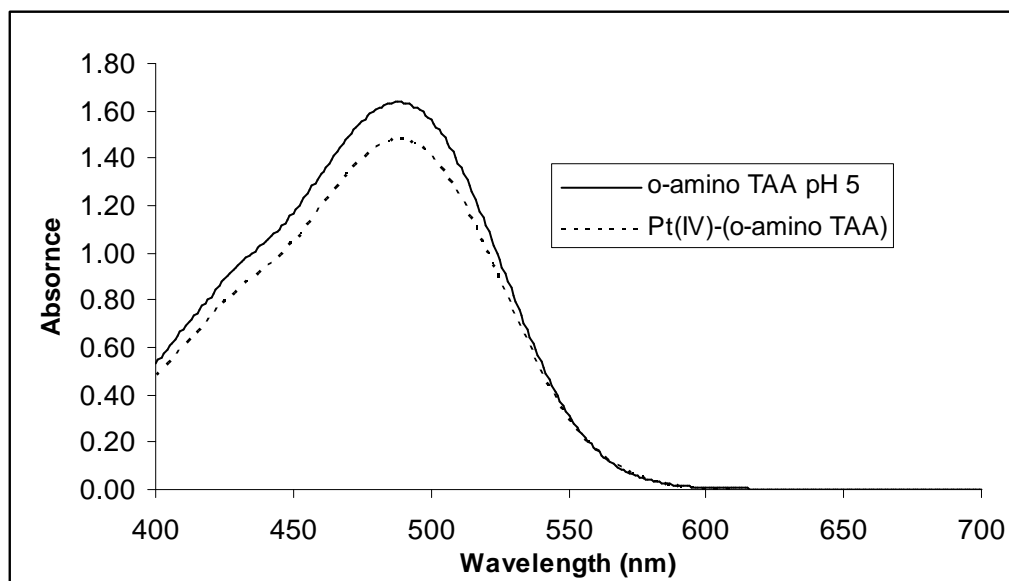
Figure 54 Absorption spectra of *o*-amino TAA and platinum(IV)-(*o*-amino TAA) complex at pH 5.
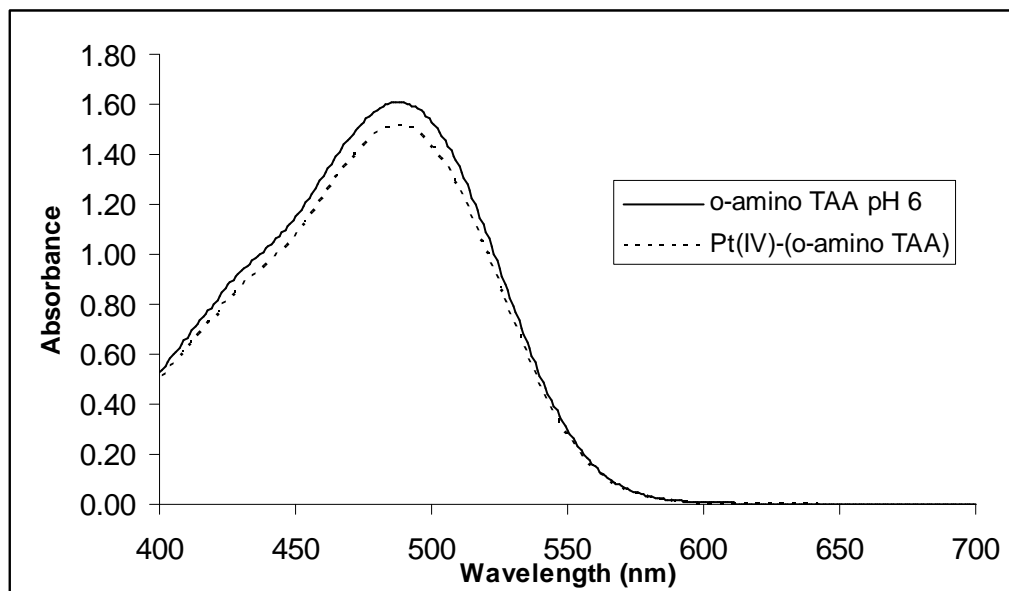
Figure 55 Absorption spectra of *o*-amino TAA and platinum(IV)-(*o*-amino TAA) complex at pH 6.

Table 9 The color and λ_{max} of *p*-amino TAA and platinum(IV) complex at various pH

pH	*p*-amino TAA		Platinum(IV)-(*p*-amino TAA) complex	
	color	λ_{max}	color	λ_{max}
2	Pink	523	Orange-Pink	520
3	Orange	483	Orange	494
4	Orange	480	Orange	480
5	Orange	479	Orange	479
6	Orange	479	Orange	480

Table 10 The color and λ_{max} of *o*-amino TAA and platinum(IV) complex at various pH

pH	*o*-amino TAA		Platinum(IV)-(*o*-amino TAA) complex	
	color	λ_{max}	color	λ_{max}
2	Deep-pink	535	Deep-pink	536
3	Orange-red	505	Deep-pink	528
4	Orange	489	Orange	493
5	Orange	488	Orange	488
6	Orange	488	Orange	488

6. **Stability of rhodium(III)-(*p*-amino TAA) and rhodium(III)-(*o*-amino TAA) complexes**

The stability of complexes between *p*-amino TAA and rhodium(III) at pH 5 and between *o*-amino TAA and rhodium(III) at pH 3 were studied. The results in Figure 56 and Figure 57 show that *p*-amino and *o*-amino simultaneously formed complex with rhodium(III) and the absorbance remained constant for at least 2 hours.
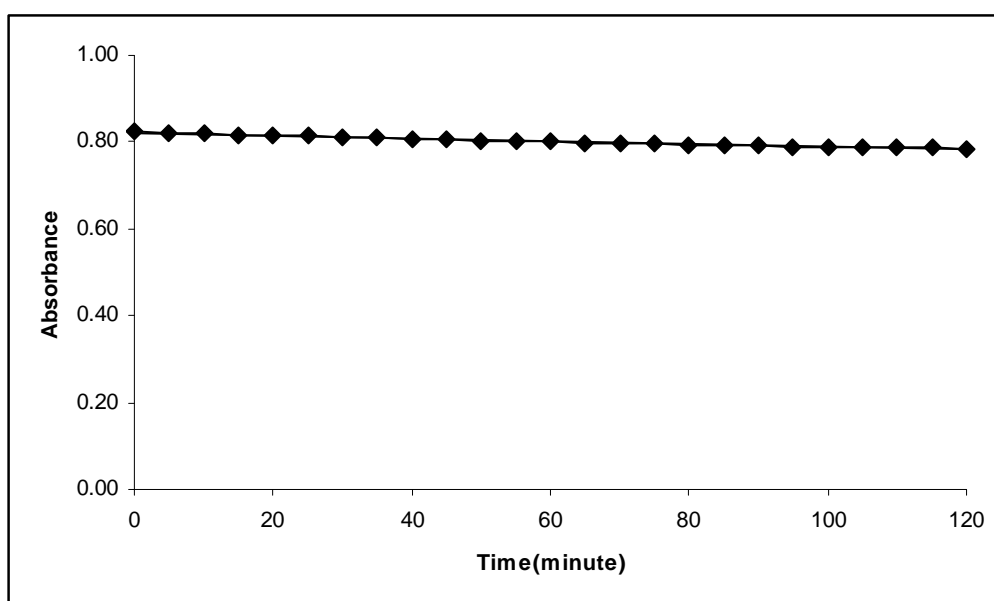
Figure 56 Relationship between absorbance of rhodium(III)-(*p*-amino TAA) complex and time.
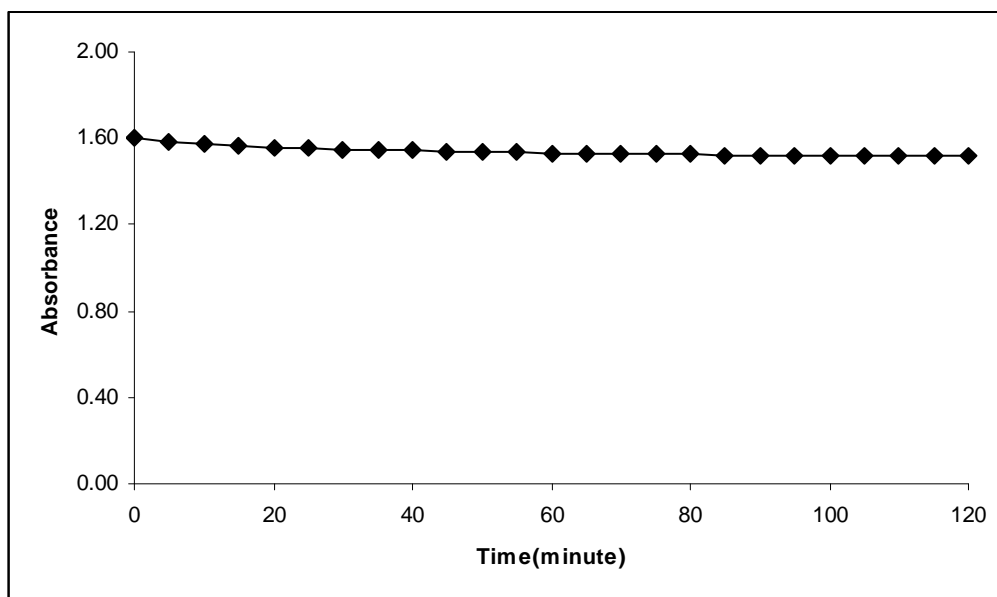
Figure 57 Relationship between absorbance of rhodium(III)-(*o*-amino TAA) complex and time.

7. Stability of platinum(IV)-(*p*-amino TAA) and platinum(IV)-(*o*-amino TAA) complexes

The stability of complexes of *p*-amino TAA and *o*-amino TAA with platinum(IV) at pH 3 were studied. Figure 58 and Figure 59 show that *p*-amino and *o*-amino simultaneously formed complex with platinum(IV) and the absorbance remained constant for at least 2 hours.
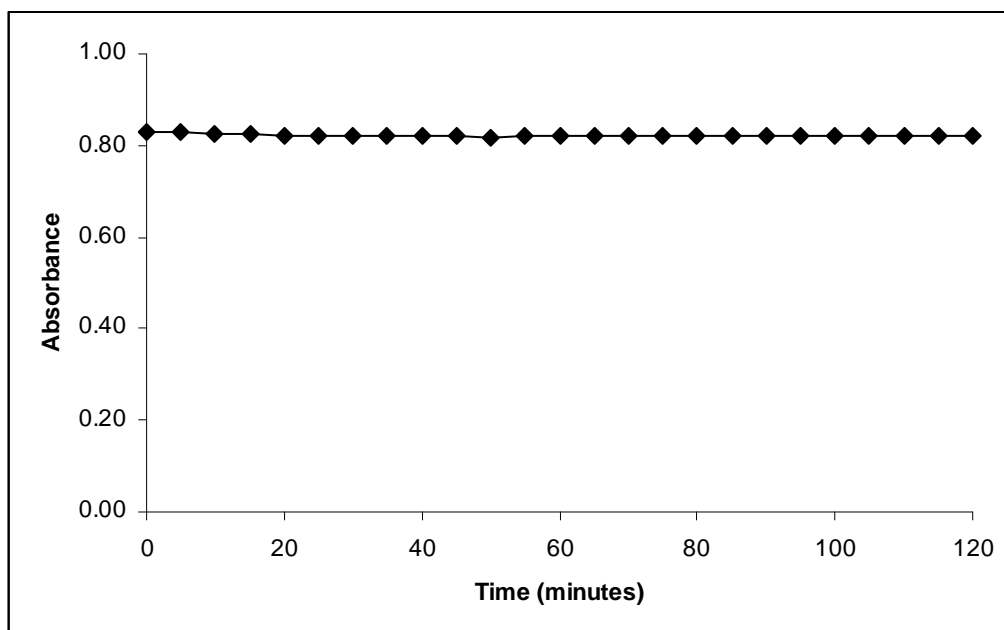
Figure 58 Relationship between absorbance of platinum(IV)-(*p*-amino TAA) complex and
time.
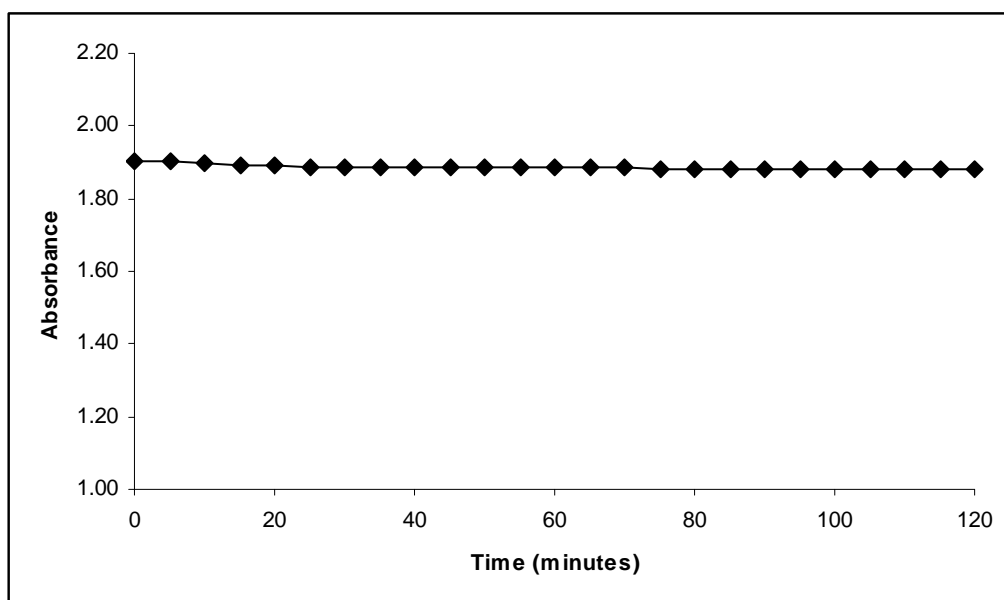
Figure 59 Relationship between absorbance of platinum(IV)-(*o*-amino TAA) complex and
time.

8. Stoichiometric determination of rhodium(III)-(*p*-amino TAA) and rhodium(III)-(*o*-amino TAA) complexes

From the previous sections, the suitable pH for complexes formation of *p*-amino TAA and *o*-amino TAA with rhodium(III) were 5 and 3, respectively. Stoichiometric determination of these complexes were performed by mole ratio method and continuous variation method (Job's method) in universal buffer at pH 5 for *p*-amino TAA complex and at pH 3 for *o*-amino TAA complex.

8.1 Mole ratio method

The stoichiometry of *p*-amino TAA and *o*-amino TAA with rhodium(III) complexes were determined by mole ratio method at pH 5 for the *p*-amino TAA complex and pH 3 for the *o*-amino TAA complex. The plot between absorbance and the fraction of mole of rhodium(III) per mole of *p*-amino TAA is shown in Figure 60 and the plot between absorbance and the fraction of mole of rhodium(III) per mole of *o*-amino TAA is shown in Figure 61. The results show that the stoichiometric ratio between rhodium(III) and *p*-amino TAA and between rhodium(III) and *o*-amino TAA are 1:2.
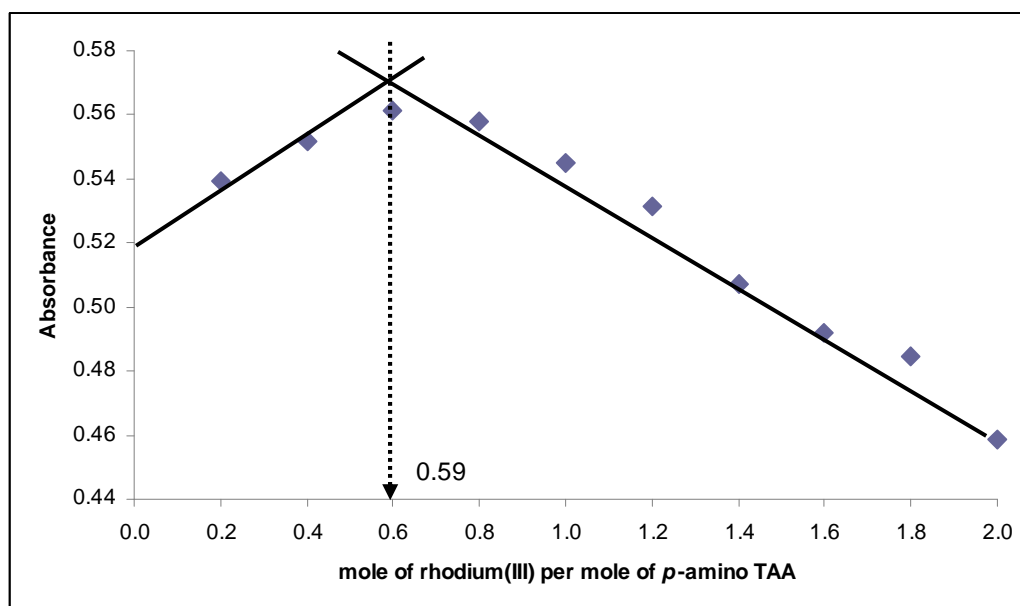
Figure 60 Mole ratio plot of complex between rhodium(III) and *p*-amino TAA in
universal buffer at pH 5.
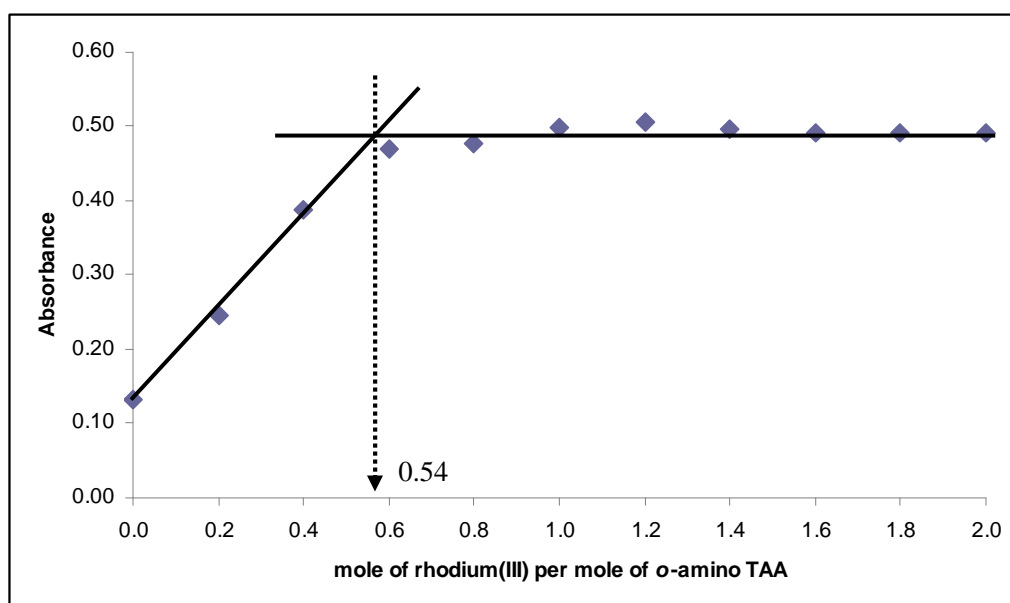
Figure 61 Mole ratio plot of complex between rhodium(III) and *o*-amino TAA in
universal buffer at pH 3.

8.2   Continuous variation method

The stoichiometry of *p*-amino TAA and *o*-amino TAA with rhodium(III) complexes were determined by continuous variation method at pH 5 for the *p*-amino TAA complex and pH 3 for the *o*-amino TAA complex. The plot between absorbance and mole fraction of *p*-amino TAA is shown in Figure 62 and the plot between absorbance and mole fraction of *o*-amino TAA is shown in Figure 63. The results show that the stoichiometric ratio between rhodium(III) and *p*-amino TAA and between rhodium(III) and *o*-amino TAA are also 1:2.
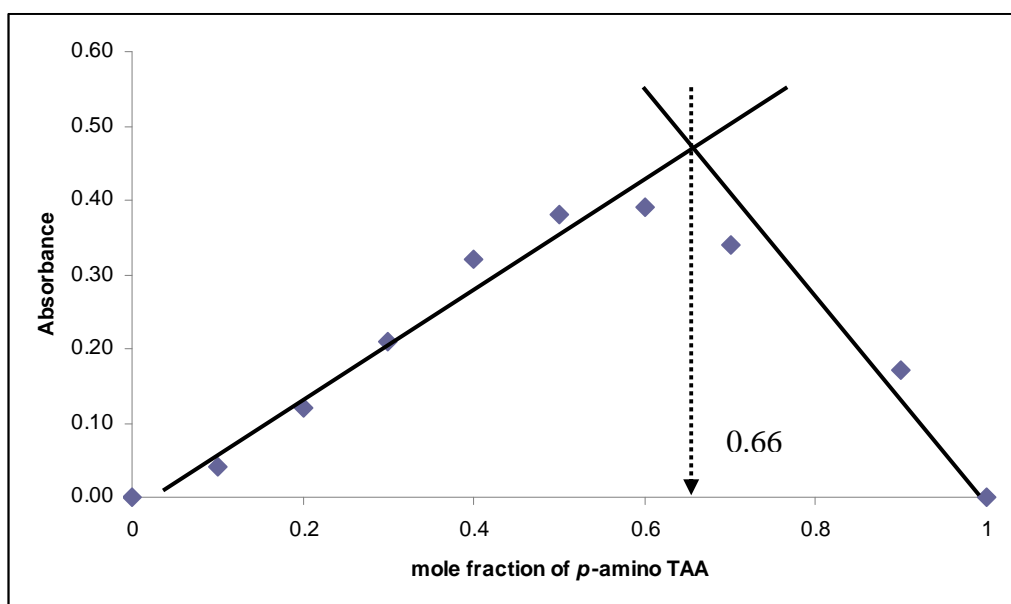
Figure 62 Job's plot of complex between rhodium(III) and *p*-amino TAA in
          universal buffer at pH 5.
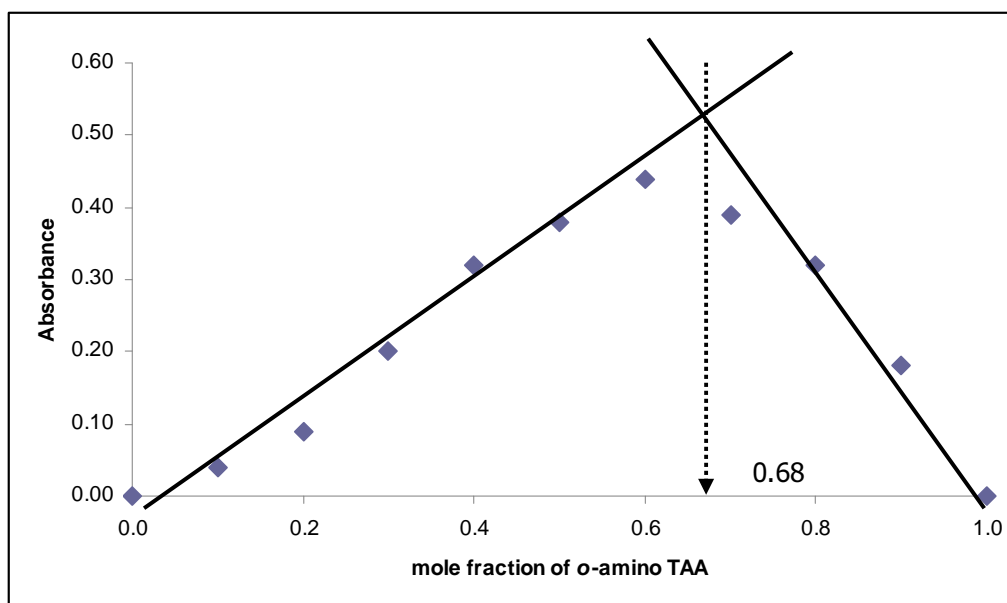
Figure 63 Job's plot of complex between rhodium(III) and *o*-amino TAA in
universal buffer at pH 3.

The results from mole ratio method agree well with the results from
continuous variation method, which indicated that the stoichiometry of rhodium(III)-
(*p*-amino TAA) and rhodium(III)-(*o*-amino TAA) complexes are 1:2 (metal: ligand).

9. Stoichiometric determination of platinum(IV)-(*p*-amino TAA) and platinum(IV)-(*o*-amino TAA) complexes

From the previous sections, the suitable pH for complexes formation of
p-amino TAA and *o*-amino TAA with platinum(IV) were 3. Stoichiometric
determination of these complexes were performed by mole ratio method and
continuous variation method (Job's method) in universal buffer at pH 3.

9.1 Mole ratio method

The stoichiometry of *p*-amino TAA and *o*-amino TAA with platinum(IV)
complexes were determined by mole ratio method at pH 3. The plot between

absorbance and the fraction of mole of platinum(IV) per mole of *p*-amino TAA is shown in Figure 64 and the plot between absorbance and the fraction of mole of platinum(IV) per mole of *o*-amino TAA is shown in Figure 65. Figure 64 shows that the fraction of mole of platinum(IV) per mole of *p*-amino TAA is 0.73 which correspond to the stoichiometric ratio in the range 1:1 to 1:2 between platinum(IV) and *p*-amino TAA while Figure 65 shows that the stoichiometric ratio between platinum(IV) and *o*-amino TAA is 1:2.
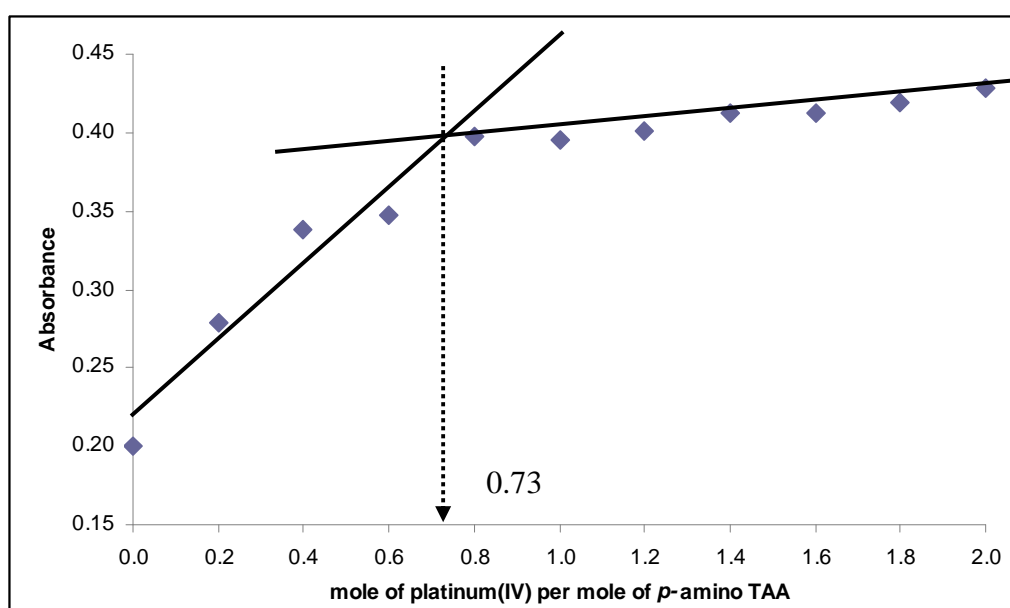
Figure 64 Mole ratio plot of complex between platinum(IV) and *p*-amino TAA in universal buffer at pH 3.
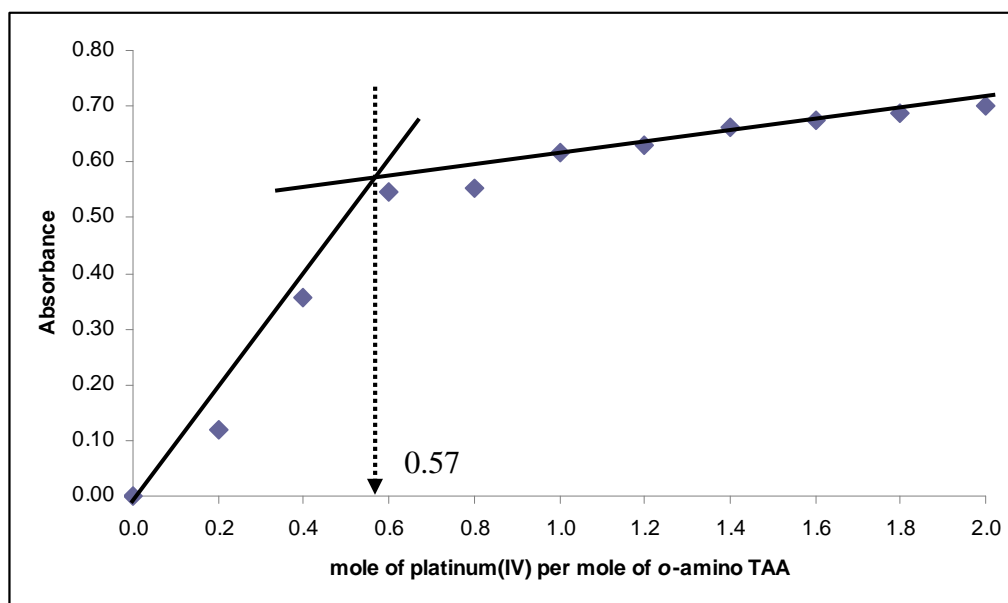
Figure 65 Mole ratio plot of complex between platinum(IV) and *o*-amino TAA in universal buffer at pH 3.

9.2 Continuous variation method

The stoichiometry of complexes of *p*-amino TAA and *o*-amino TAA with platinum(IV) were determined by continuous variation method at pH 3. The plot between absorbance and mole fraction of *p*-amino TAA is shown in Figure 66 and the plot between absorbance and mole fraction of *o*-amino TAA is shown in Figure 67. The results show that the stoichiometric ratio between platinum(IV) and *p*-amino TAA is 1:1 and the stoichiometric ratio between platinum(IV) and *o*-amino TAA is 1:2.
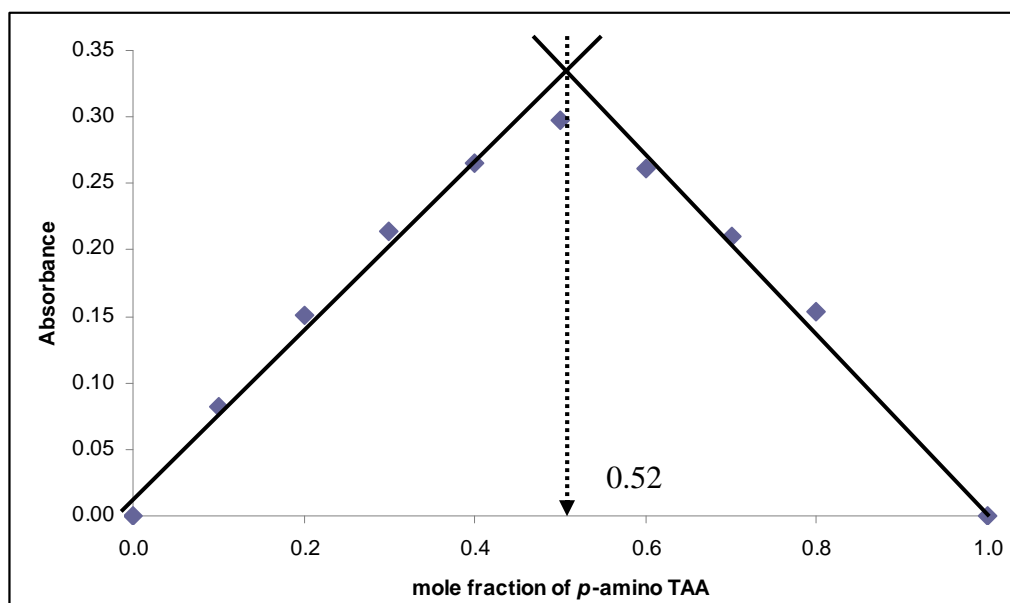
Figure 66 Job's plot of complex between platinum(IV) and *p*-amino TAA in
universal buffer at pH 3.
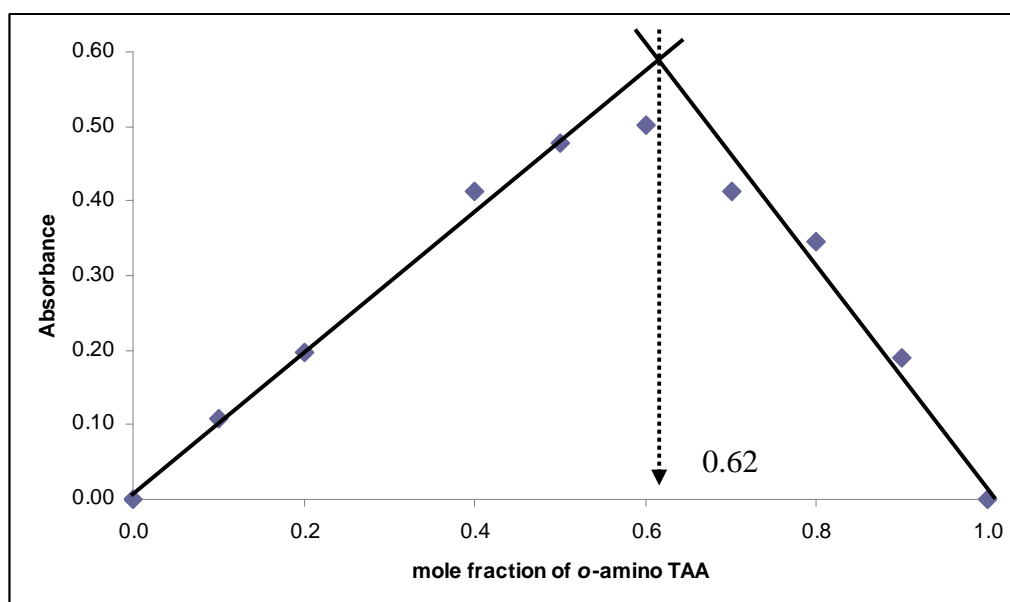
Figure 67 Job's plot of complex between platinum(IV) and *o*-amino TAA in
universal buffer at pH 3.

The results from mole ratio method agree well with the results from continuous variation method in platinum(IV)-(*o*-amino TAA) which indicated that the stoichiometry of platinum(IV)-(*o*-amino TAA) complex is 1:2 (metal: ligand). On the other hand, platinum(IV)-(*p*-amino TAA), the result from mole ratio method shows the stoichiometry of metal: ligand is between 1:1 and 1:2, however, the result from continuous variation method shows the stoichiometry of metal: ligand is 1:1 which indicated that the stoichiometry of platinum(IV)-(*o*-amino TAA) complexe tend to be 1:1.

10. Determination for stability constant of rhodium(III)-(*p*-amino TAA) and rhodium(III)-(*o*-amino TAA) complexes

The stability constant of complexes between *p*-amino TAA and rhodium(III) at pH 5 and between *o*-amino TAA and rhodium(III) at pH 3 were studied by continuous variation method (Job's method) and Benesi-Hildebrand's equation. The results are shown in Table 11.

Table 11 The stability constants of rhodium(III)-(*p*-amino TAA) and rhodium(III)-(*o*-amino TAA) by continuous variation method (Job's method) and Benesi-Hildebrand's equation

Complexes	Stability constant	
	Job's method	Benesi-Hildebrand
Rh(III)-(*p*-amino TAA)	3.59×10^{10}	1.82×10^{9}
Rh(III)-(*o*-amino TAA)	2.69×10^{10}	1.26×10^{9}

The stability constants of rhodium(III)-(*p*-amino TAA) and rhodium(III)-(*o*-amino TAA) complexes from both methods have different values due to the different process in calculation which described in Appendix D for Benesi-

Hildebrand's Equation and Appendix E for continuous variation method. From these methods, it is found that the stability constant of rhodium(III)-(p-amino TAA) is higher than rhodium(III)-(o-amino TAA). These results might be attributed to the intramolecular hydrogen bonding in free o-amino TAA which enhance the stability of this compound, so its complex is less stable than that of p-amino TAA complex.

11. Determination for stability constant of platinum(IV)-(p-amino TAA) and platinum(IV)-(o-amino TAA) complexes

The stability constant of complexes between p-amino TAA and platinum(IV) and between o-amino TAA and platinum(IV) at pH 3 were studied by continuous variation method (Job's method) and Benesi-Hildebrand's equation. The results are shown in Table 12.

Table 12 The stability constants of platinum(IV)-(p-amino TAA) and platinum(IV)-(o-amino TAA) by continuous variation method (Job's method) and Benesi-Hildebrand's equation

complexes	Stability constant	
	Job's method	Benesi-Hildebrand
Pt(IV)-(p-amino TAA)	8.00×10^5	1.62×10^5
Pt(IV)-(o-amino TAA)	9.02×10^9	5.35×10^8

As in rhodium(III) complexes, the stability constants of complexes of platinum(IV)-(p-amino TAA) and platinum(IV)-(o-amino TAA) from both methods have different values but still in the same order. From the two methods, it is found that the stability constants of platinum(IV)-(o-amino TAA) are higher than platinum(IV)-(p-amino TAA). These might be resulting from the oxidation state +4 of platinum which have characterized as octahedral with low spin t^6_{2g} configuration.

These structures are stabilized by the influence of the highest crystal field stabilization energy (CFSE), $^{12}/_5\Delta_O$, which is the maximum possible for any d^x configuration (Greenwood, 1997). The stoichiometric of platinum(IV) with o-amino TAA which might be acted as tridentate ligand is 1: 2 corresponding to the octahedral structure of platinum(IV)-(o-amino TAA) complex. On the other hand, the stoichiometric of platinum(IV) with p-amino TAA is 1:1 which might be attributed to the square planar or tetrahedral structure of platinum(IV)-(p-amino TAA) complex. These results can be concluded that the octahedral geometric structure of platinum(IV)-(o-amino TAA) leading to the higher stability constant of this complex than platinum(IV)-(p-amino TAA).

For o-amino TAA complexes, rhodium(III)-(o-amino TAA) has higher stability constant than platinum(IV)-(p-amino TAA). This result can consider from hard and soft acids and bases characteristic as shown in Table 13 and Table 14. The ligand, o-amino TAA, is a polydentate ligand which can form complex with metal ions via nitrogen atom of amino group classified as borderline base. Rhodium(III) is a borderline acid, while platinum(IV) is a soft acid which results in the more stable of rhodium(III)-(o-amino TAA) than platinum(IV)-(p-amino TAA) complex.

Table 13 Hard and soft bases

Hard bases	Borderline bases	Soft bases
F^-, Cl^-	Br^-	H^-
H_2O, OH^-, O^{2-}		I^-
ROH, RO^-, CH_3COO^-		H_2S, HS^-, S^{2-}
NO_3^-, ClO_4^-	NO^{2-}, N_3^-	RSH, RS^-, R_2S
CO_3^{2-}, SO_4^{2-}, PO_4^{3-}	SO_3^{2-}	SCN^-, CN^-, RNC, CO
NH_3, RNH_2, N_2H_4	$C_6H_5NH_2$, C_5H_5N, N_2	$S_2O_3^{2-}$
		R_3P, $(RO)_3P$, C_2H_4, C_6H_6

Source: Miessler (1999)

Table 14 Hard and soft acids

Hard acids	Borderline acids	Soft acids
H^+, Li^+, Na^+, K^+		
Be^{2+}, Mg^{2+}, Ca^{2+}, Sr^{2+}		
BF_3, BCl_3, $B(OR)_3$	$B(CH_3)_3$	BH_3, Tl^+, $Tl(CH_3)_3$
Al^{3+}, $Al(CH_3)_3$, $AlCl_3$		
Cr^{3+}, Mn^{2+}, Fe^{3+}, Co^{3+}	Fe^{2+}, Co^{2+}, Ni^{2+}, Cu^{2+},	Cu^+, Ag^+, Au^+, Cd^{2+},
	Zn^{2+}, Rh^{3+}, Ir^{3+}, Ru^{3+}, Os^{2+}	Hg_2^{2+}, Hg^{2+}, CH_3Hg^+,
		Pd^{2+}, Pt^{2+}, Pt^{4+}

Source: Miessler (1999)

12. Characterization of rhodium(III)-(*p*-amino TAA) and rhodium(III)-(*o*-amino TAA) complexes

Complexes of Rh(III)-(*p*-amino TAA) and Rh(III)-(*o*- amino TAA) were synthesized by mixing of ligands and RhCl$_3$·xH$_2$O in tetrahydrofuran (THF) solution under reflux for 8 hours. The products were precipitated to give Rh(III)-(*p*-amino TAA) as dark brown precipitate and Rh(III)-(*o*-amino TAA) as black precipitate with melting point more than 300°C for both complexes. The % yield of Rh(III)-(*p*-amino TAA) and Rh(III)-(*o*-amino TAA) are 60.13 and 64.77%, respectively. The products were characterized by using FT-IR and ^{1}H NMR.

12.1   Infrared spectrum

The KBr disks of rhodium(III)-(*p*-amino TAA) and rhodium(III)-(*o*-amino TAA) which ground and dried at 120°C were prepared by mixing of these compounds with KBr. FT-IR spectra were operated as KBr disks in the 4000-370 cm^{-1} region.

IR spectroscopy is a technique that can be used to identify the donor atoms in the molecule of *p*-amino TAA and *o*-amino TAA in a complex, observed by the red shift of the spectrum due to the decreasing of the bond order of the donor atoms. The IR spectra and their assigned peaks of *p*-amino TAA, *o*-amino TAA and their rhodium(III) complexes are shown in Figure 68 and Table 15 for *p*-amino TAA, and in Figure 69 and Table 16 for *o*-amino TAA. The peaks assigned for *p*-amino and rhodium(III)-(*p*-amino TAA) showed C-O-C stretching was shifted from 1107 cm^{-1} to 1015 cm^{-1}, N=N stretching was shifted from 1541 cm^{-1} to 1537 cm^{-1}, C=N stretching was shifted from 1615 cm^{-1} to 1605 cm^{-1} and C-S stretching was shifted from 1157 cm^{-1} to 1126 cm^{-1} and the peaks assigned for *o*-amino TAA amino and rhodium(III)-(*o*-amino TAA) showed N-H stretching was shifted from 3343 cm^{-1} and 3186 cm^{-1} to 3195 cm^{-1}, N=N stretching was shifted from 1541 cm^{-1} to 1505 cm^{-1}, C=N stretching was shifted from 1600 cm^{-1} to 1598 cm^{-1} and C-S stretching was shifted from 1130 cm^{-1} to 1129 cm^{-1}. Therefore, *p*-amino TAA and *o*-amino TAA might acted as tridentate ligands by using nitrogen atom

of –NH$_2$ for *p*-amino TAA and oxygen atom of –OCH$_3$ for *o*-amino TAA, nitrogen atom of N=N and nitrogen or sulfur atom in thiazole ring as donor atoms. From the differences in the shift (red shift) of wavenumber of C=N ($\Delta\upsilon^{-1}$ = 10 cm^{-1}) and C-S ($\Delta\upsilon^{-1}$ = 31 cm^{-1}) bonds in the *p*-amino TAA complex, the sulfur atom in the thiazole ring should act as the donor atom in the rhodium(III)-(*p*-amino TAA) complex. Since the differences in the shift of wavenumber of C=N and C-S bonds in the *o*-amino TAA complex were equal ($\Delta\upsilon^{-1}$ = 1 cm^{-1}) so IR spectrum could not be used to identify that nitrogen or sulfur atom in the thiazole ring should be the donor atom in the rhodium(III)-(*o*-amino TAA) complex.
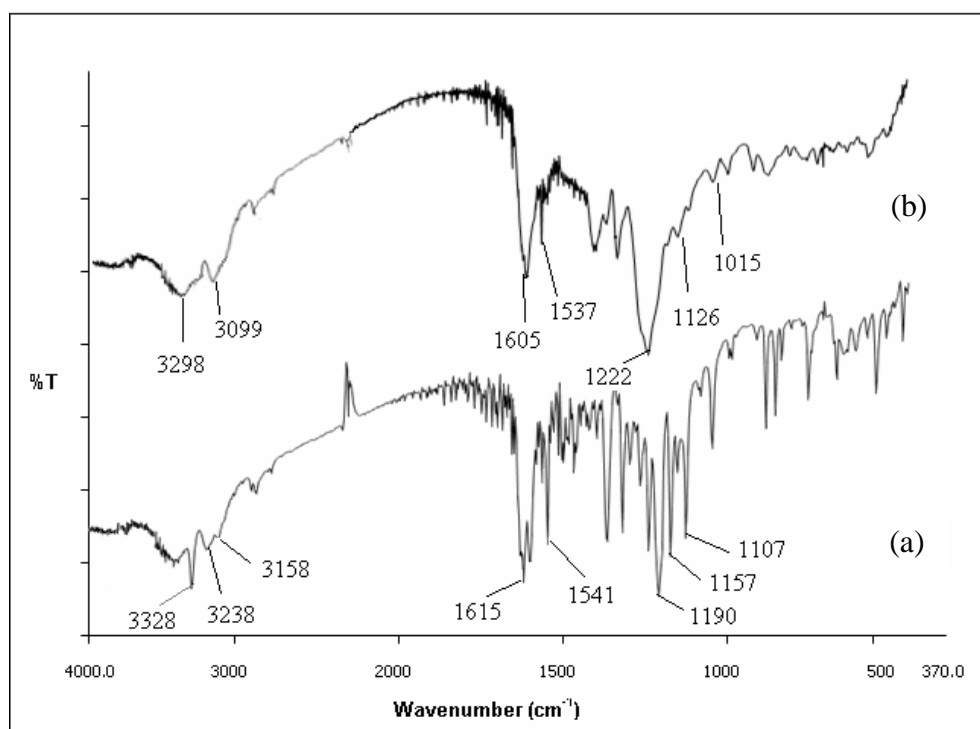
Figure 68 Infrared spectra of (a) *p*-amino TAA and (b) rhodium(III)-(*p*-amino TAA) complex.

Table 15 Data from the IR spectra of *p*-amino TAA and rhodium(III)-
(*p*-amino TAA) complex

Wavenumber (cm^{-1}) of *p*-amino TAA	Functional group	Wavenumber (cm^{-1}) of rhodium(III)-(*p*-amino TAA) complex
3328 and 3228	N-H stretch	3198
3158	C-H Stretch aromatic	3099
1615	C=N stretch	1605
1541	N=N stretch	1537
1190	C-N stretch	1222
1157	C-S stretch	1126
1107	C-O-C stretch	1015
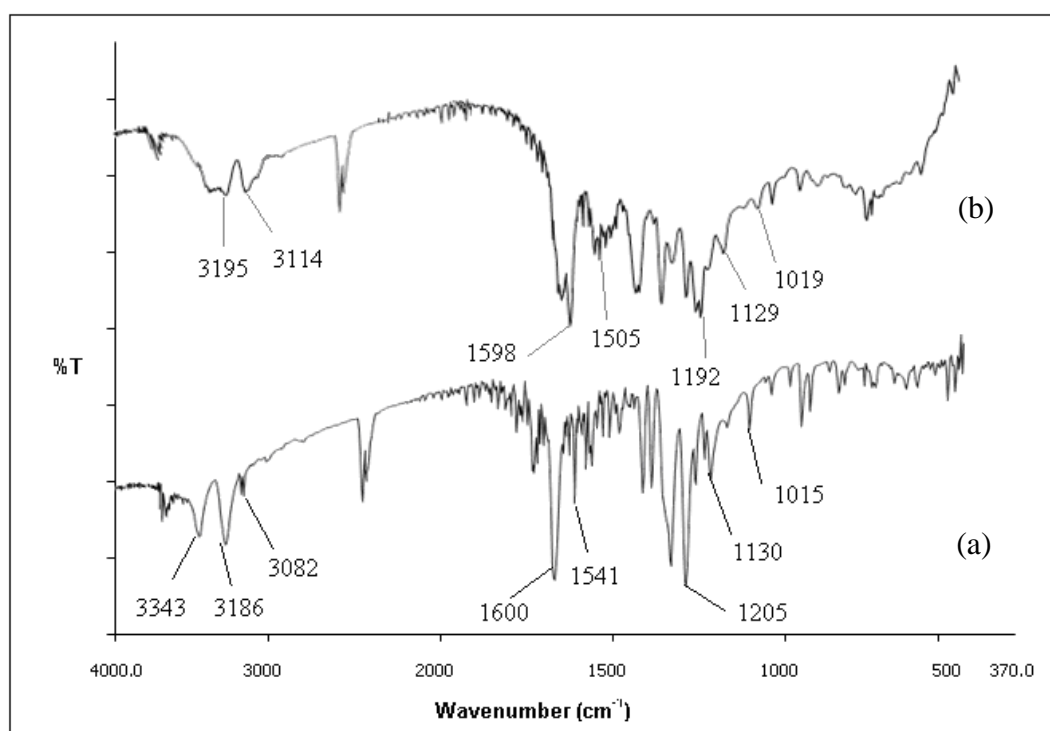
Figure 69 Infrared spectra of (a) *o*-amino TAA and (b) rhodium(III)-(*o*-amino TAA)
complex.

Table 16 Data from the IR spectra of *o*-amino TAA and rhodium(III)-
(*o*-amino TAA) complex

Wavenumber (cm^{-1}) of *o*-amino TAA	Functional group	Wavenumber (cm^{-1}) of rhodium(III)-(*o*-amino TAA) complex
3343 and 3186	N-H stretch	3195
3082	C-H Stretch aromatic	3114
1600	C=N stretch	1598
1541	N=N stretch	1505
1205	C-N stretch	1192
1130	C-S stretch	1129
1015	C-O-C stretch	1019

12.2 ^{1}H NMR spectrum

For ^{1}H NMR, 0.020 g of rhodium(III)-(*p*-amino TAA) and rhodium(III)-
(*o*-amino TAA) were dissolved in dimethylsulfoxide, D-6 (C$_2$D$_3$OS). The ^{1}H NMR
spectra were recorded at 400 MHz on an INNOVA VARION NMR spectrometer 400
MHz.
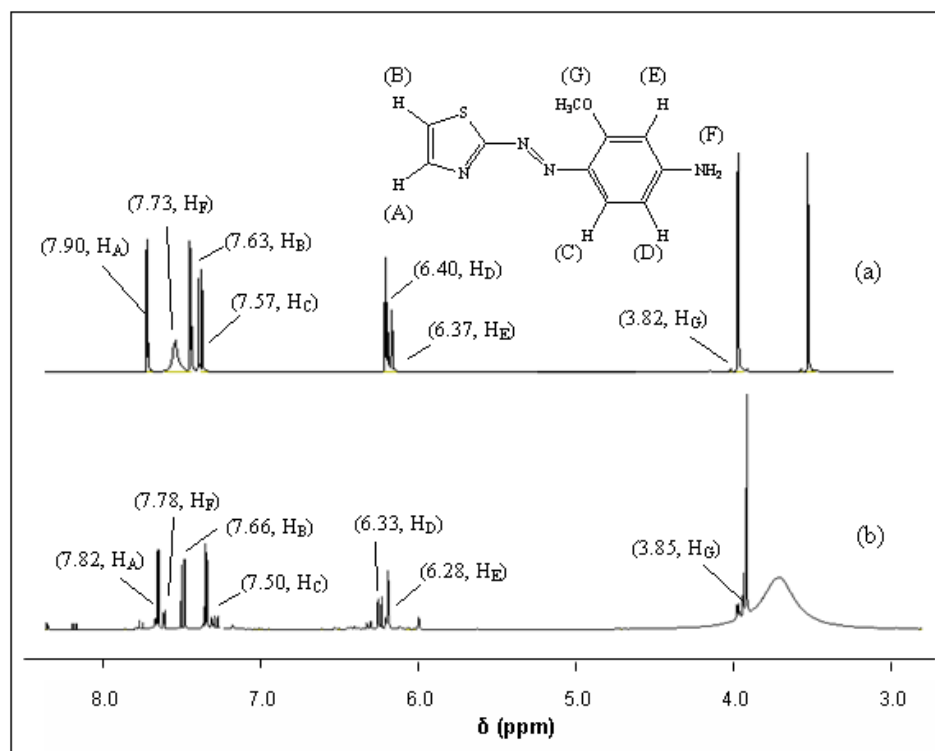
Figure 70 ^{1}H NMR spectra (DMSO-d_6) of

(a) *p*-amino TAA and (b) rhodium(III)-(*p*-amino TAA) complex.

Table 17 Data from the ^{1}H NMR spectra of *p*-amino TAA and rhodium(III)-
(*p*-amino TAA) complex

p-amino TAA		rhodium(III)-(p-amino TAA) complex	
Chemical shift (ppm)	Proton	Chemical shift (ppm)	Proton
7.90	H_A	7.82	H_A
7.63	H_B	7.66	H_B
7.57	H_C	7.50	H_C
6.40	H_D	6.33	H_D
6.37	H_E	6.28	H_E
7.73	H_F	7.78	H_F
3.82	H_G	3.85	H_G
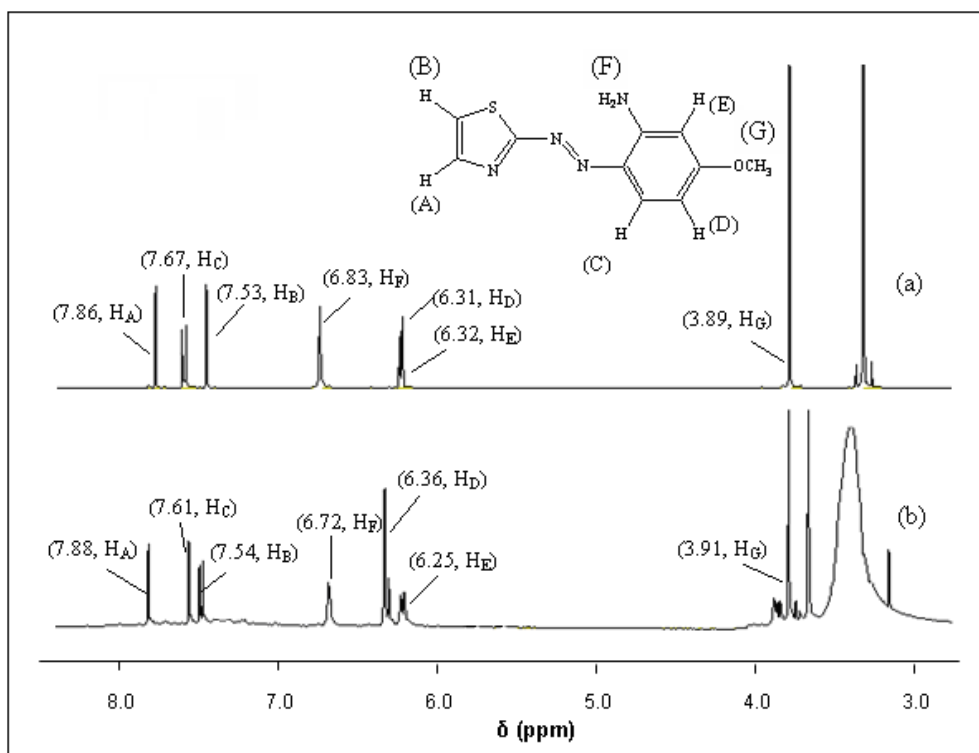
Figure 71 ^{1}H NMR spectra (DMSO-d_6) of

(a) *o*-amino TAA and (b) rhodium(III)-(*o*-amino TAA) complex.

Table 18 Data from the ^{1}H NMR spectra of *o*-amino TAA and rhodium(III)-
(*o*-amino TAA) complex

o-amino TAA		rhodium(III)-(*o*-amino TAA) complex	
Chemical shift (ppm)	Proton	Chemical shift (ppm)	Proton
7.86	H_A	7.88	H_A
7.53	H_B	7.54	H_B
7.67	H_C	7.61	H_C
6.31	H_D	6.36	H_D
6.32	H_E	6.25	H_E
6.83	H_F	6.72	H_F
3.89	H_G	3.91	H_G

^{1}H NMR spectrum can be used to indicate the donor atom of ligand for bonding with metal ions. Generally, the chemical shift of the proton close to the donor atom is changed to the higher chemical shift (downfield) due to the decreasing of electron density (deshielded) of that proton. The ^{1}H NMR spectra of *p*-amino TAA, rhodium(III)-(*p*-amino TAA) complex and their assigned chemical shifts are shown in Figure 70 and Table 17. The ^{1}H NMR spectra of *o*-amino TAA and rhodium(III)-(*o*-amino TAA) are shown in Figure 71 and Table 18. The peak assigned for *p*-amino TAA and its complex show that H_A atom at 7.90 ppm was shifted to 7.82 ppm, H_B atom was shifted from 7.63 ppm to 7.66 ppm, H_C was shifted from 7.57 to 7.50, H_D was shifted from 6.40 to 6.33, H_E was shifted from 6.37 to 6.28, H_F was shifted from 7.73 to 7.78 and H_G was shifted from 3.82 to 3.85. It was found that chemical shift of protons from –OCH_3 group (H_G) was shifted to downfield because of electrons donation from oxygen atom to rhodium(III). However, for the thiazole ring which π-backbonding can possibly occur, nitrogen atom might act as donor atom due to the higher change of chemical shift of H_A compared to H_B. The π-backbonding will increase the electron density in the thiazole ring which changed the chemical shift to higher filed (lower chemical shift). In addition, there were changes in chemical shift of protons in benzene ring (H_C, H_D and H_E) which indicated some interactions between benzene ring and rhodium(III).

In the case of *o*-amino TAA, the peak assigned for *o*-amino TAA and its complex show that H_A atom at 7.86 ppm was shifted to 7.88 ppm, H_B atom was shifted from 7.53 ppm to 7.54 ppm, H_C was shifted from 7.76 to 7.61, H_D was shifted from 6.31 to 6.36, H_E was shifted from 6.32 to 6.25, H_F was shifted from 6.83 to 7.72 and H_G was shifted from 3.89 to 3.91. It was found that the difference of chemical shift of H_A is higher than the difference of chemical shift of H_B. This result indicated that nitrogen atom of thiazole ring might act as donor atom to rhodium(III). In addition, there were some protons that changed to the lower chemical shift. These might be attributed to π-backbonding similar to the case of *p*-amino TAA complex as previously mentioned.

From IR and ^{1}H NMR spectra, it can be concluded that donor atoms of *p*-amino TAA to rhodium(III) might be the nitrogen atom of thiazole ring, the nitrogen atom of the azo group and the oxygen atom of the methoxy group in *m*-anisidine ring while donor atoms of *o*-amino TAA to rhodium(III) might be the nitrogen atom of thiazole ring, the nitrogen atom of the azo group and the nitrogen atom of the amino group in *m*-anisidine ring.

13. Structural determination of complexes between *p*-amino TAA and rhodium(III) by quantum chemical calculations

According to the high stability constant of complex between rhodium(III) and *p*-amino TAA, the quantum chemical calculations and application for binding with DNA of this complex have been studied. The ligand, *p*-amino TAA, is polydentate ligand which can form complexes with metal ions by using nitrogen or sulfur atom of thiazole ring and oxygen atom of –OCH$_3$ group as donor atoms. They may act as either bidentate or tridentate ligands to form chelating complexes. In the case of bidentate ligand, Cl⁻ from starting material, RhCl$_3$·xH$_2$O, and H$_2$O are two potential ligands in the complex formation. The formation of complex between rhodium(III) and *p*-amino TAA should be as followed:

$$Rh^{3+} + 2p\text{-amino TAA} \rightleftharpoons [Rh(p\text{-amino TAA})_2]^{3+}$$

Therefore, the stabilization energies of possible complex structures as shown in Figure 72 to Figure 75 were calculated by Gaussian03 program.

(i)   (ii)
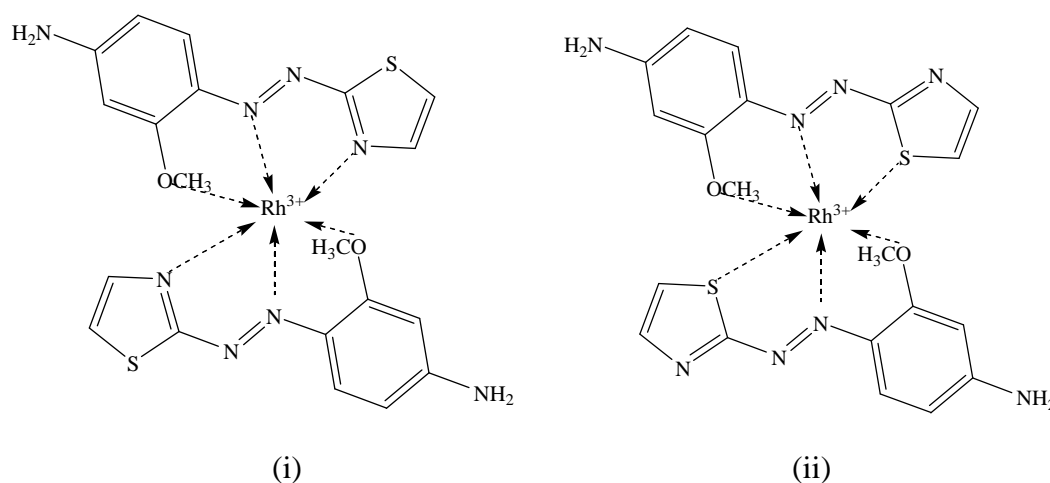
Figure 72 Postulated structures of complexes between rhodium(III) and *p*-amino TAA as tridentate ligand

(i) nitrogen atoms of thiazole rings as donor atoms-[Rh(*p*-TAA-n)$_2$]$^{3+}$

(ii) sulfur atoms of thiazole rings as donor atoms-[Rh(*p*-TAA-s)$_2$]$^{3+}$.
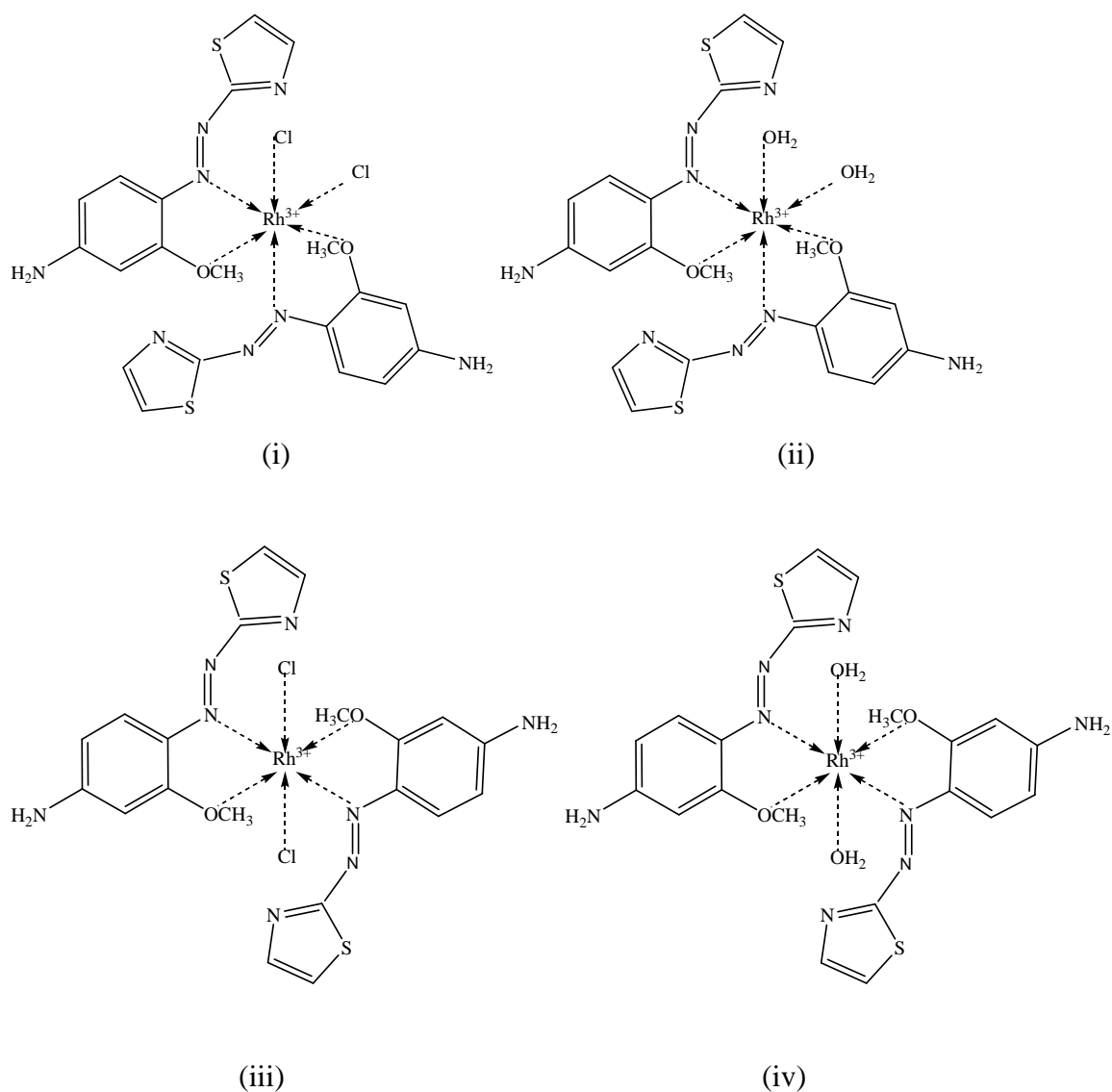
Figure 73 Postulated structures of complexes between rhodium(III) and *p*-amino TAA

as bidentate ligand using oxygen atoms of methoxy groups as donor atoms

(i)   *cis* structure with chloride atoms as donor atoms-

cis-[Rh(*p*-TAA)$_2$(Cl)$_2$]$^+$

(ii) *cis* structure with oxygen atoms of water as donor atoms-

cis-[Rh(*p*-TAA)$_2$(H$_2$O)$_2$]$^{3+}$

(iii) *trans* structure with chloride atoms as donor atoms-

trans-[Rh(*p*-TAA)$_2$(Cl)$_2$]$^+$

(iv) *trans* structure with oxygen atoms of water as donor atoms-

trans-[Rh(*p*-TAA)$_2$(H$_2$O)$_2$]$^{3+}$.

128
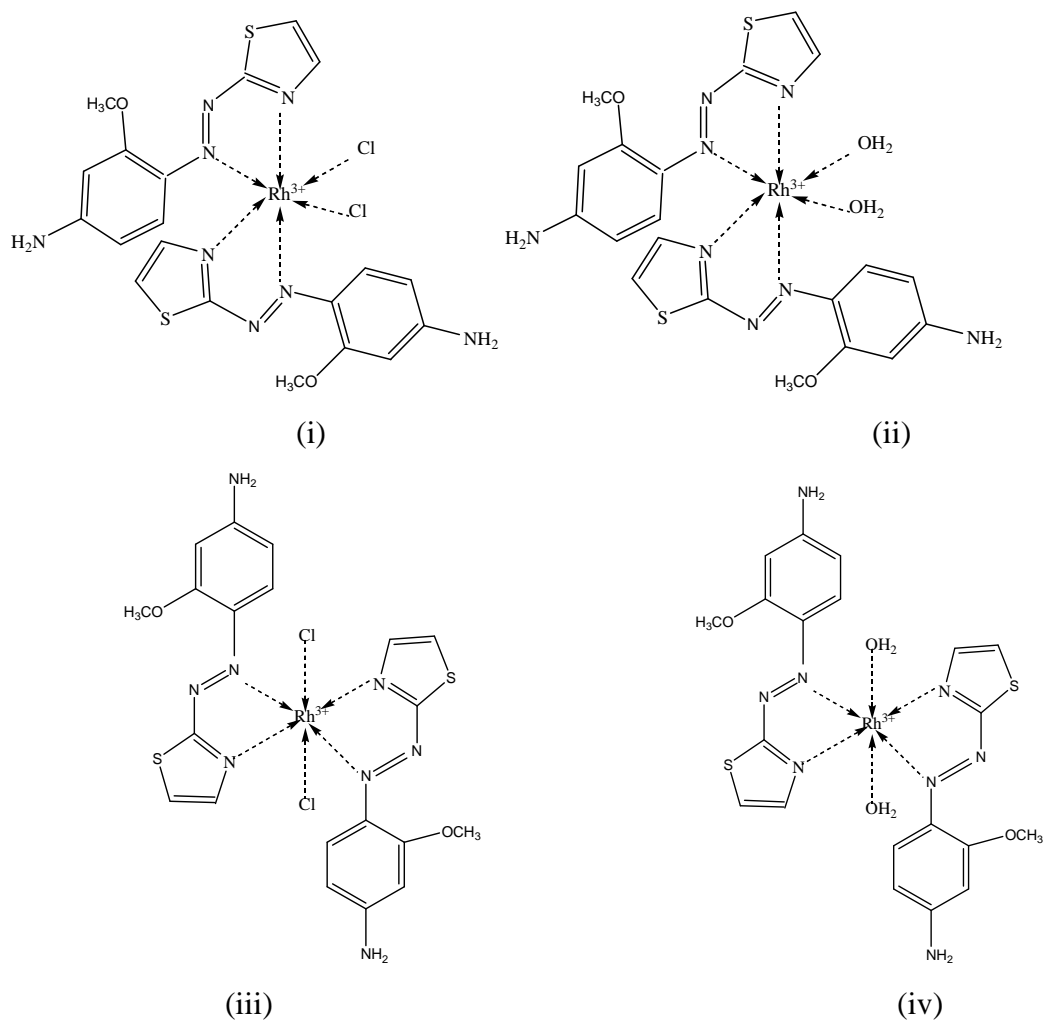
Figure 74 Postulated structures of complexes between rhodium(III) and
p-amino TAA as bidentate ligand by using nitrogen atoms of thiazole
rings as donor atoms
- (i)   *cis* structure with chloride atoms as donor atoms-
        cis-[Rh(*p*-TAA-n)$_2$(Cl)$_2$]$^+$
- (ii) *cis* structure with oxygen atoms of water as donor atoms-
        cis-[Rh(*p*-TAA-n)$_2$(H$_2$O)$_2$]$^{3+}$
- (iii) *trans* structure with chloride atoms as donor atoms-
        trans-[Rh(*p*-TAA-n)$_2$(Cl)$_2$]$^+$
- (iv) *trans* structure with oxygen atoms of water as donor atoms-
        trans-[Rh(*p*-TAA-n)$_2$(H$_2$O)$_2$]$^{3+}$.
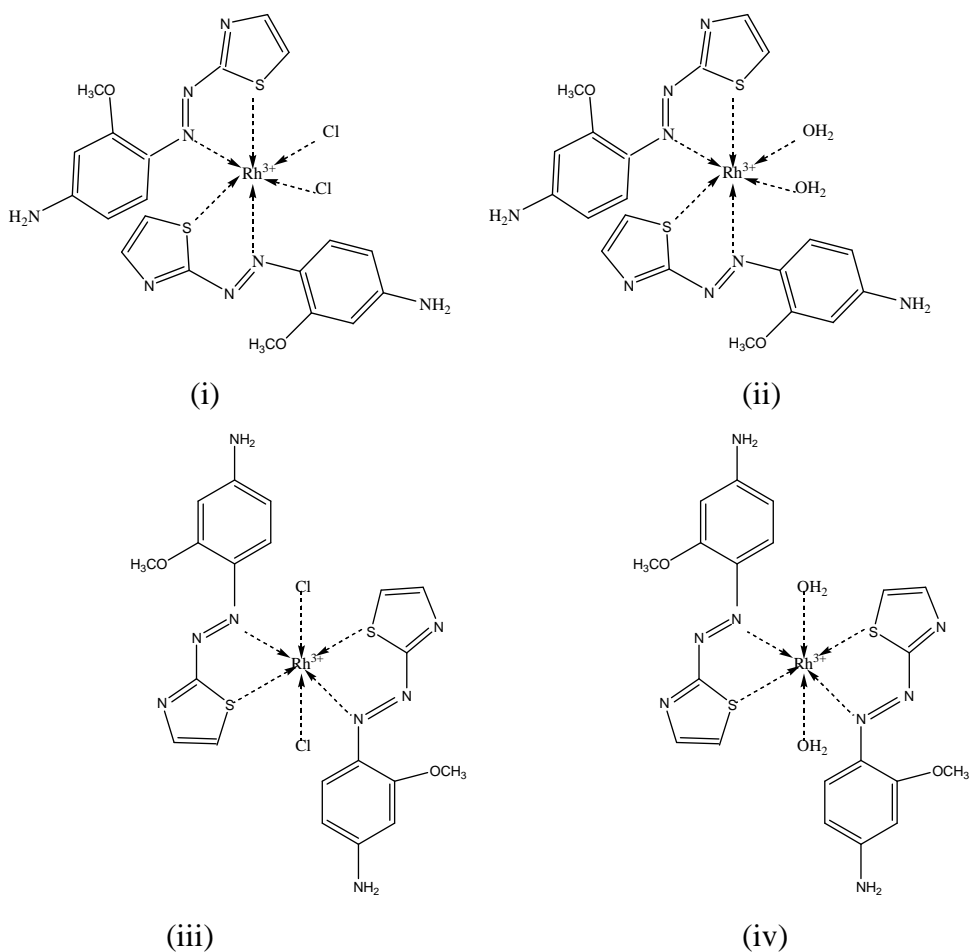
Figure 75 Postulated structures of complexes between rhodium(III) and

p-amino TAA as bidentate ligand using sulfur atoms of thiazole rings as

donor atoms

(i) *cis* structure with chloride atoms as donor atoms-

cis-[Rh(*p*-TAA-s)$_2$(Cl)$_2$]$^+$

(ii) *cis* structure with oxygen atoms of water as donor atoms-

cis-[Rh(*p*-TAA-s)$_2$(H$_2$O)$_2$]$^{3+}$

(iii) *trans* structure with chloride atoms as donor atoms-

trans-[Rh(*p*-TAA-s)$_2$(Cl)$_2$]$^+$

(iv) *trans* structure with oxygen atoms of water as donor atoms-

trans-[Rh(*p*-TAA-s)$_2$(H$_2$O)$_2$]$^{3+}$.

The optimized structures of rhodium(III)-(*p*-amino TAA) complexes obtained

from quantum chemical calculations are displayed in Figure 76 to Figure 89.
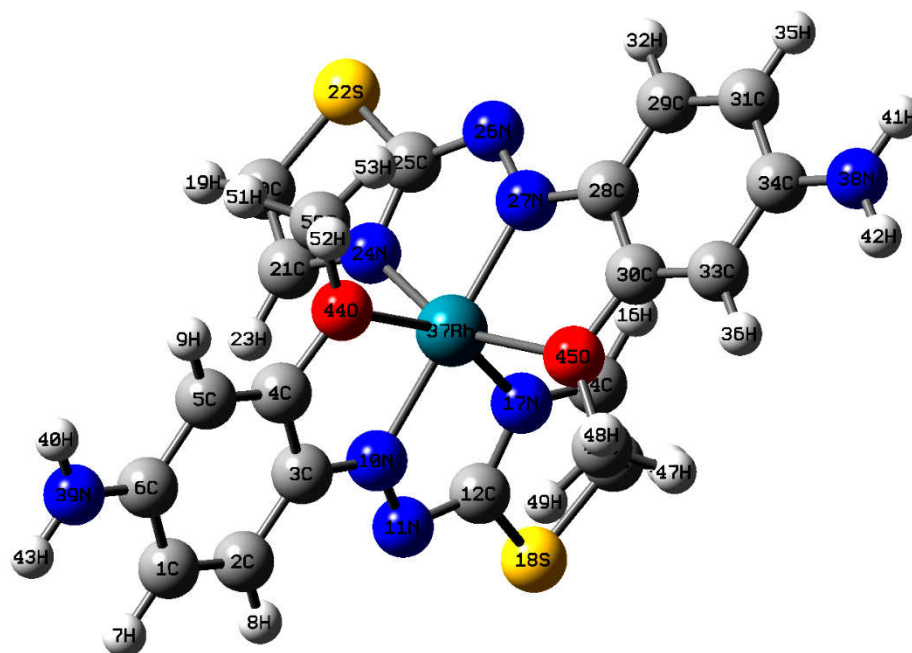
Figure 76 The optimized structure of [Rh(*p*-TAA-n)₂]³⁺ (GaussView 3.09).
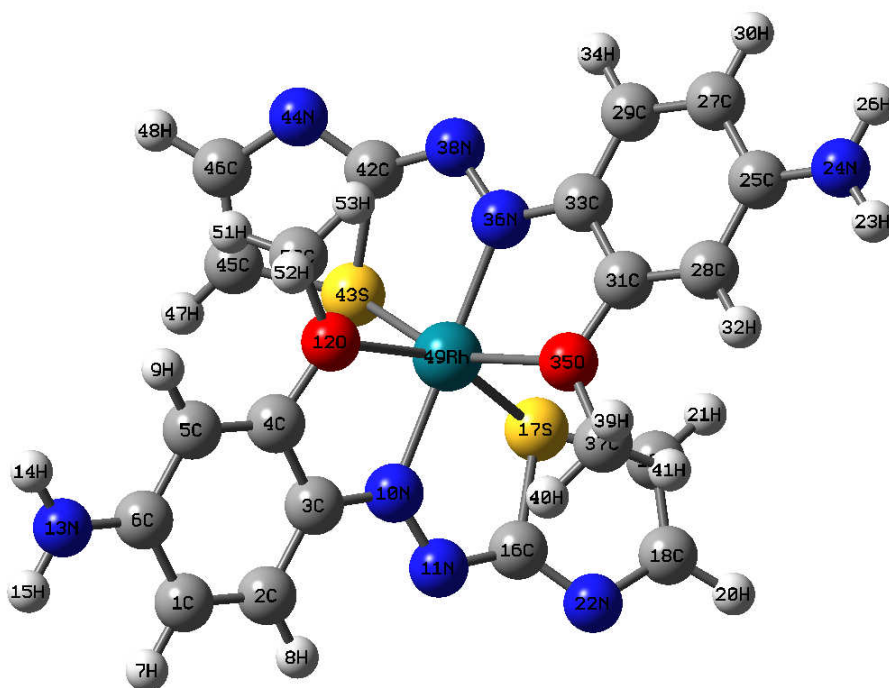
Figure 77 The optimized structure of [Rh(*p*-TAA-s)₂]³⁺ (GaussView 3.09).
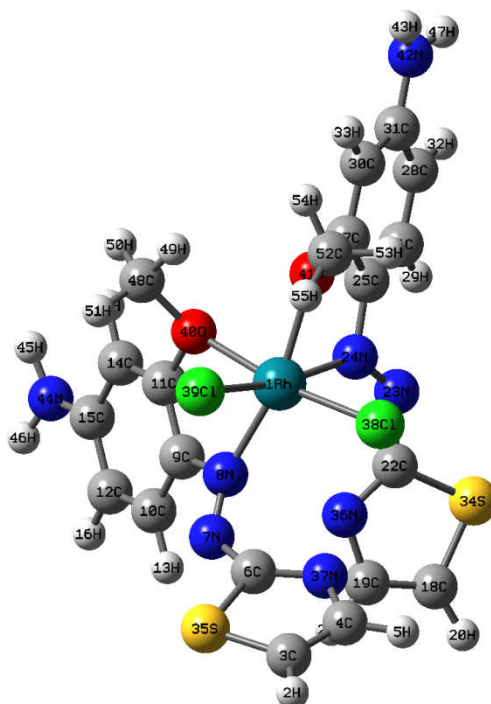
Figure 78 The optimized structure of *cis*-[Rh(*p*-TAA)$_2$(Cl)$_2$]$^+$ (GaussView 3.09).
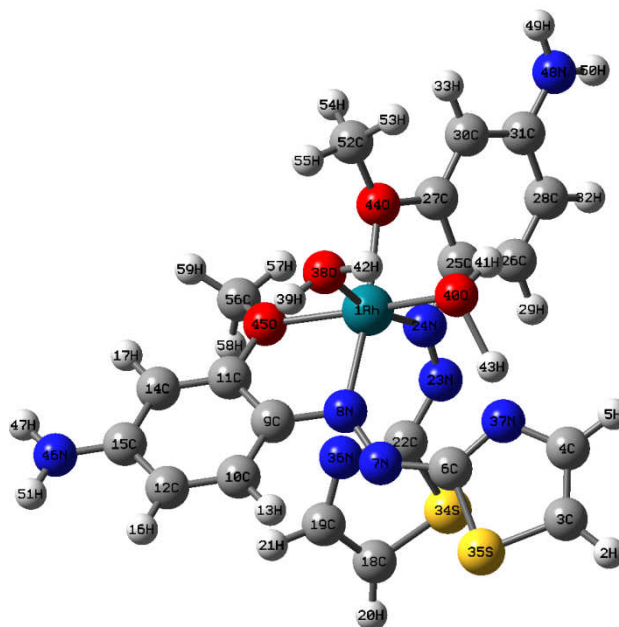
Figure 79 The optimized structure of *cis*-[Rh(*p*-TAA)$_2$(H$_2$O)$_2$]$^{3+}$ (GaussView 3.09).
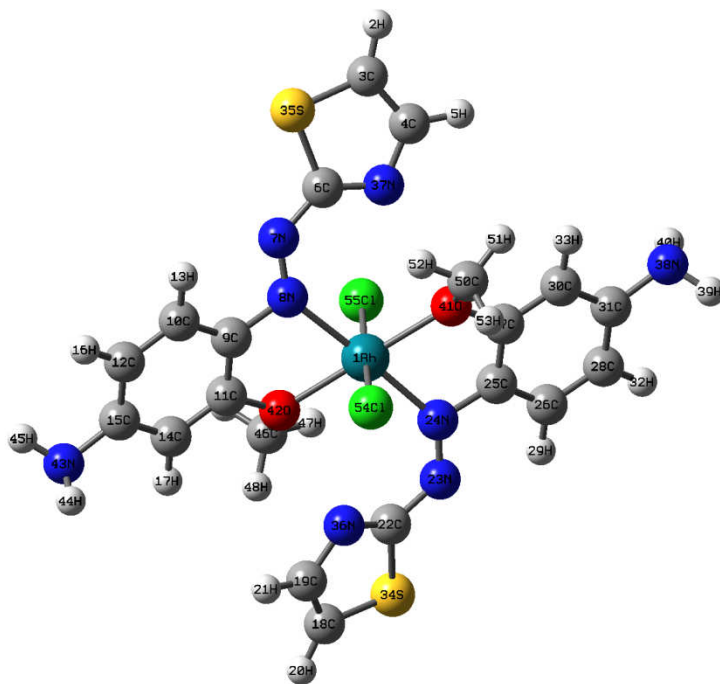
Figure 80 The optimized structure of *trans*-[Rh(*p*-TAA)$_2$(Cl)$_2$]$^+$ (GaussView 3.09).
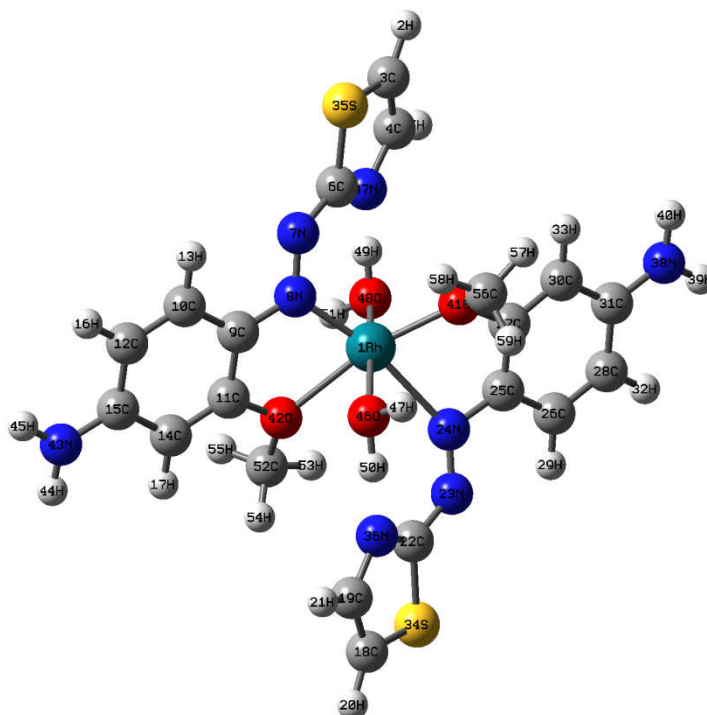
Figure 81 The optimized structure of *trans*-[Rh(*p*-TAA)$_2$(H$_2$O)$_2$]$^{3+}$

(GaussView 3.09).
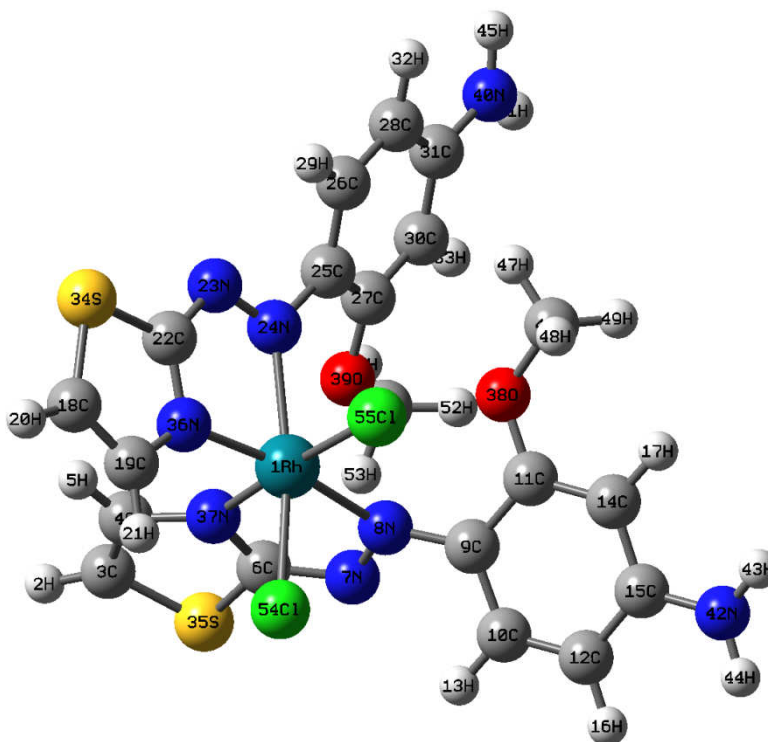
Figure 82 The optimized structure of *cis*-[Rh(*p*-TAA-n)$_2$(Cl)$_2$]$^+$ (GaussView 3.09).
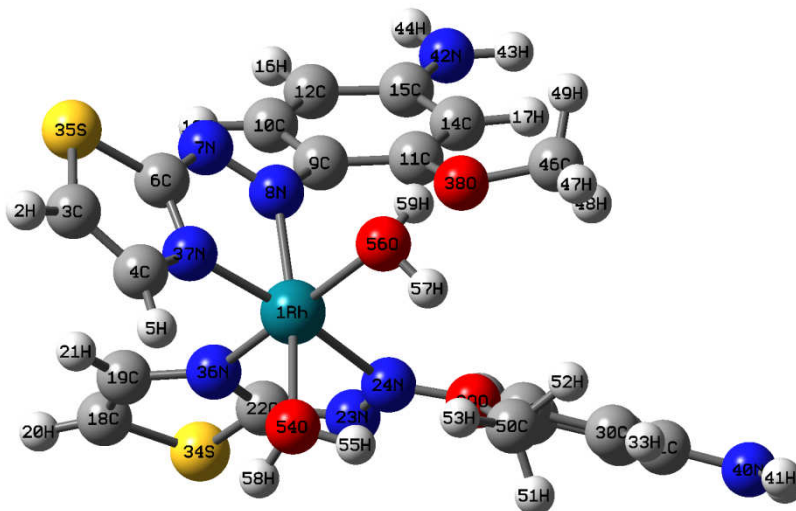
Figure 83 The optimized structure of *cis*-[Rh(*p*-TAA-n)$_2$(H$_2$O)$_2$]$^{3+}$
(GaussView 3.09).
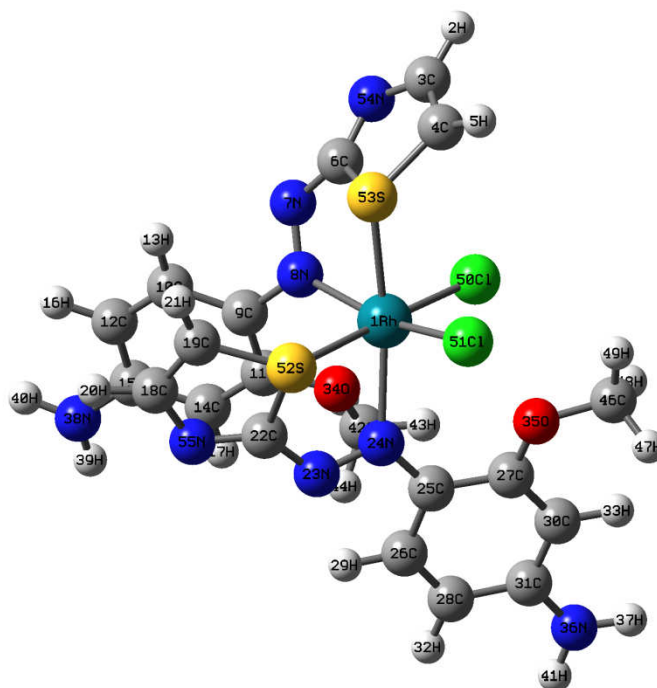
Figure 84 The optimized structure of *cis*-[Rh(*p*-TAA-s)$_2$(Cl)$_2$]$^+$ (GaussView 3.09).
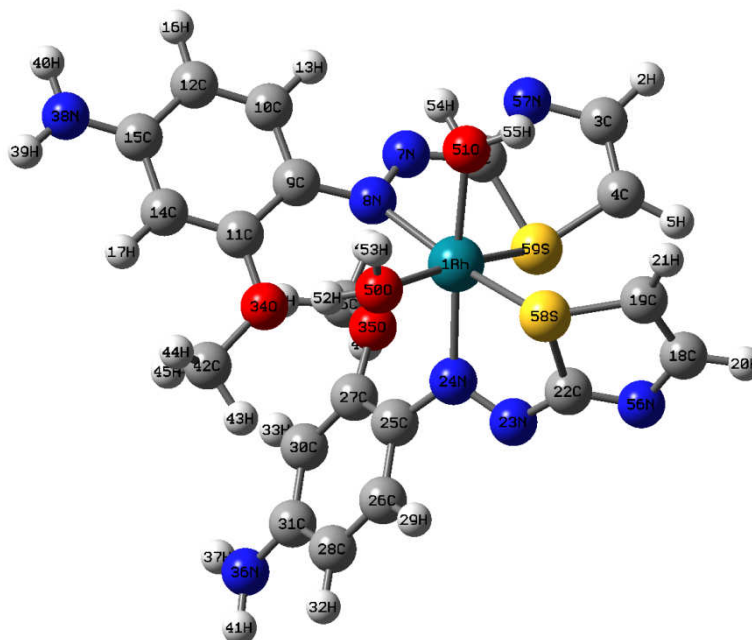
Figure 85 The optimized structure of *cis*-[Rh(*p*-TAA-s)$_2$(H$_2$O)$_2$]$^{3+}$
(GaussView 3.09).
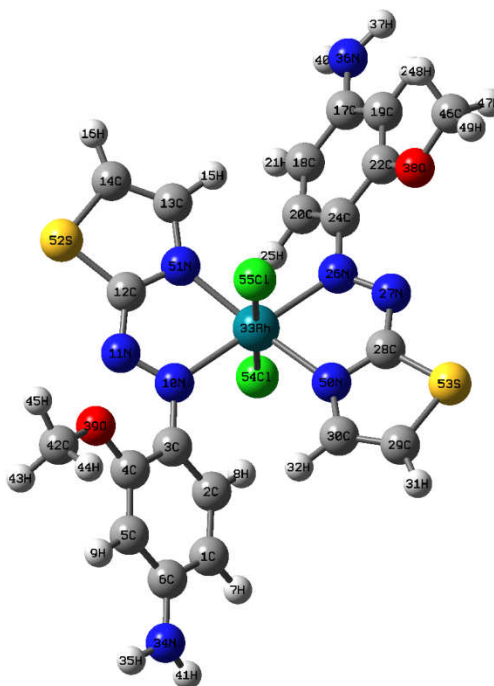
Figure 86 The optimized structure of *trans*-[Rh(*p*-TAA-n)$_2$(Cl)$_2$]$^+$ (GaussView 3.09).
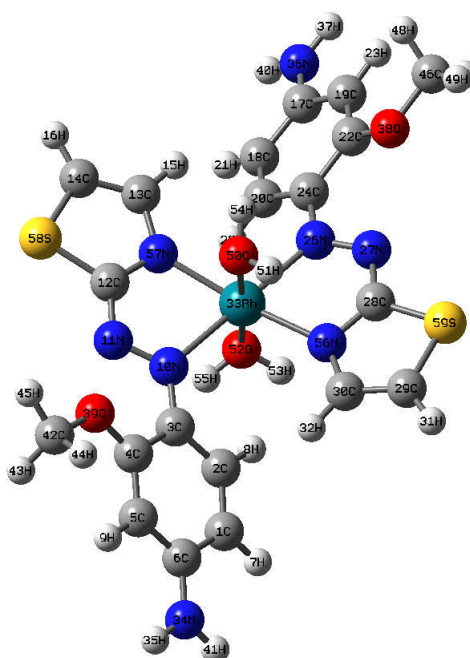
Figure 87 The optimized structure of *trans*-[Rh(*p*-TAA-n)$_2$(H$_2$O)$_2$]$^{3+}$ (GaussView 3.09).
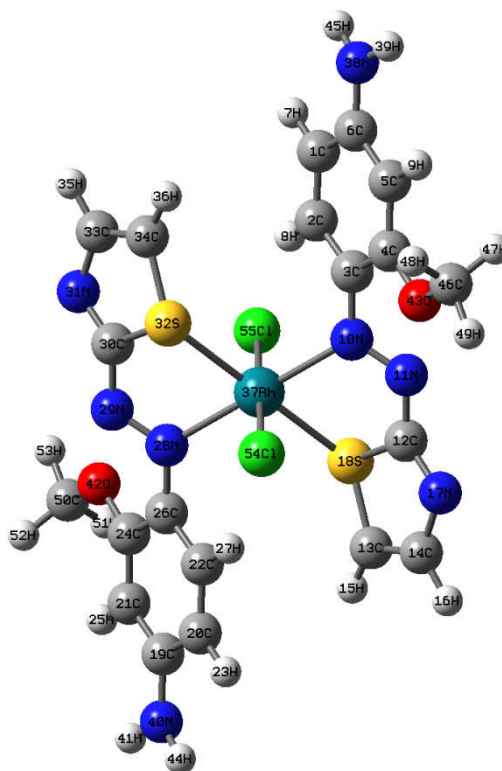
Figure 88 The optimized structure of *trans*-[Rh(*p*-TAA-s)$_2$(Cl)$_2$]$^+$ (GaussView 3.09).
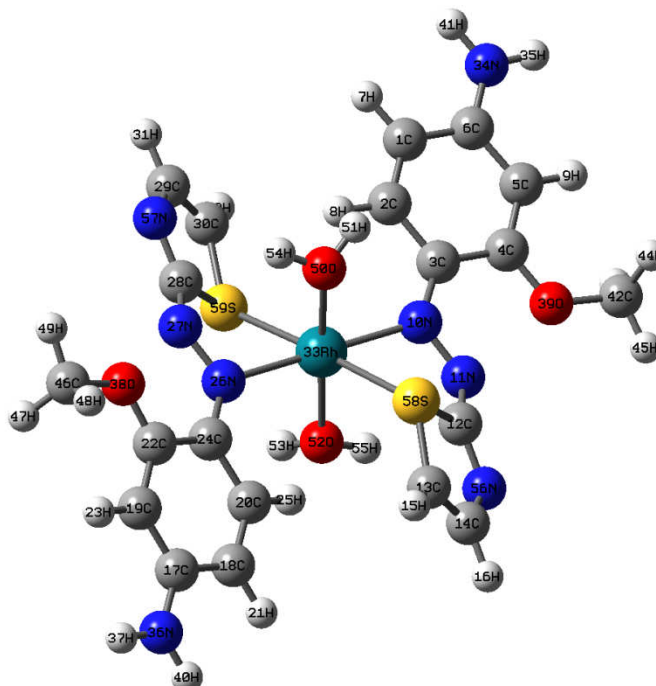
Figure 89 The optimized structure of *trans*-[Rh(*p*-TAA-s)$_2$(H$_2$O)$_2$]$^{3+}$

(GaussView 3.09).

The geometric parameters of all optimized structures were selected to describe the orientation of atoms in each complex. The stability of these compounds were compared to identify the most possible structure of rhodium(III) complex. Firstly, *cis* and *trans* isomers with the same donor atoms, i.e. bond angles of *cis*-[Rh(*p*-TAA-n)$_2$(Cl)$_2$]$^+$ and *trans*-[Rh(*p*-TAA-n)$_2$(Cl)$_2$]$^+$, were compared as shown from Figure 90 to Figure 96 and from Table 19 to Table 25. Secondly, the same isomers of complexes with different donor atoms, i.e. bond lengths of *cis*-[Rh(*p*-TAA)$_2$(Cl)$_2$]$^+$, *cis*-[Rh(*p*-TAA-n)$_2$(Cl)$_2$]$^+$ and *cis*-[Rh(*p*-TAA-s)$_2$(Cl)$_2$]$^+$ were compared as shown from Figure 97 to Figure 101 and in Table 26 to Table 30. Finally, the distinctive coordination between bidentate and tridentate characteristic of the ligand were compared in their torsion angles as shown in Figure 102 to Figure 105. Energies of atoms, molecules and possible structures of rhodium(III)-(*p*-amino TAA) complexes and formation energies of all possible structures of rhodium(III))-(*p*-amino TAA) complexes are shown in Table 31.
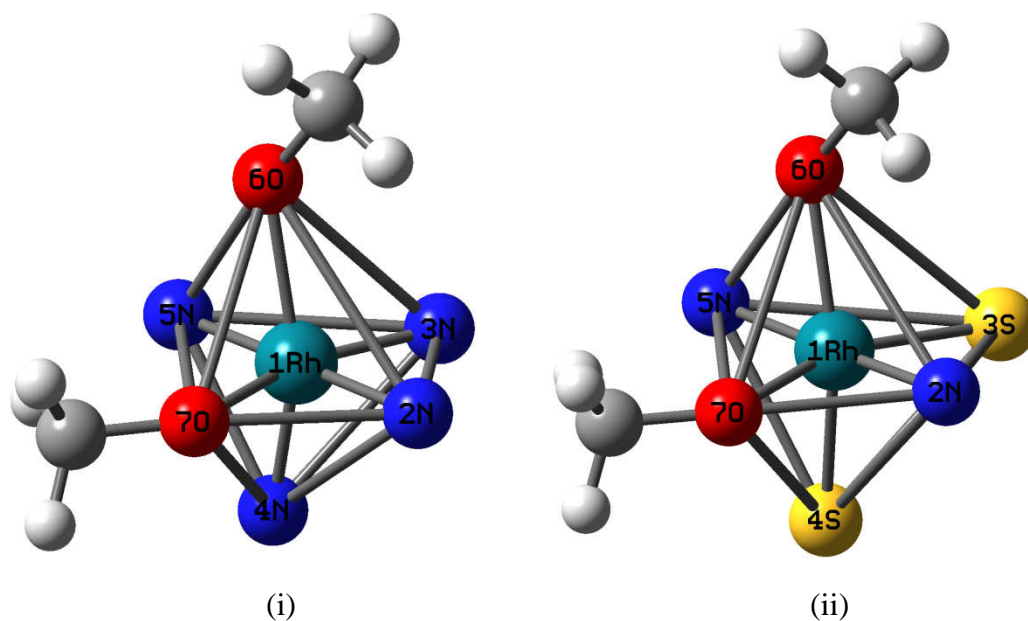
Figure 90 The geometry of coordinated bond between rhodium ion and donor atoms in (i) [Rh(p-TAA-n)$_2$]$^{3+}$ and (ii) [Rh(p-TAA-s)$_2$]$^{3+}$.

Table 19 Selected bond angles in (i) [Rh(p-TAA-n)$_2$]$^{3+}$ and (ii) [Rh(p-TAA-s)$_2$]$^{3+}$

[Rh(p-TAA-n)$_2$]$^{3+}$		[Rh(p-TAA-s)$_2$]$^{3+}$	
Bond angles	Degree	Bond angles	Degree
7O-1Rh-2N	77.4711	7O-1Rh-2N	76.2387
7O-1Rh-3N	156.1040	7O-1Rh-3S	157.1363
7O-1Rh-4N	92.9818	7O-1Rh-4S	95.2610
7O-1Rh-5N	104.0360	7O-1Rh-5N	100.6307
7O-1Rh-6O	92.3530	7O-1Rh-6O	95.5253

(i)   (ii)
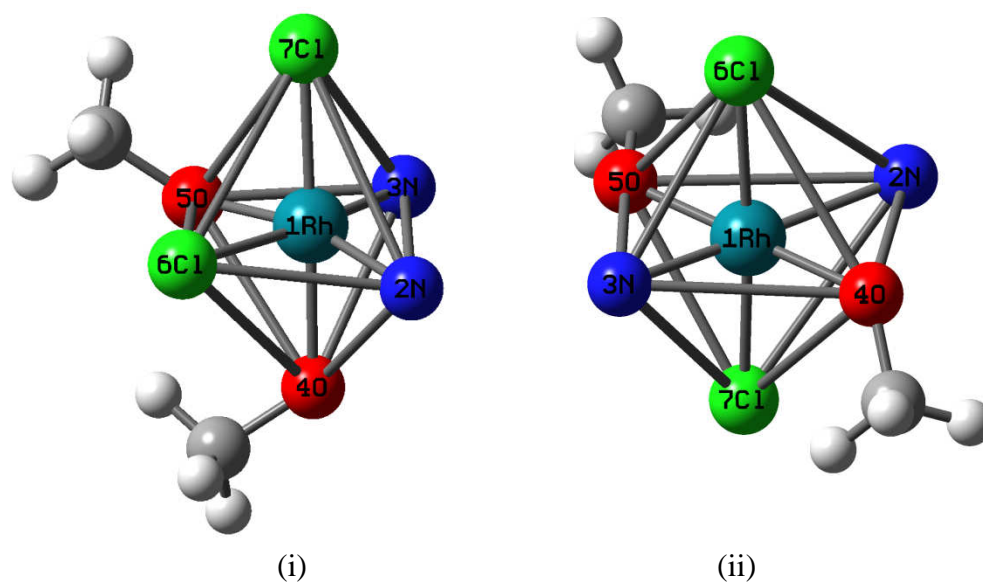
Figure 91 The geometry of coordinated bond between rhodium ion and donor atoms
in (i) *cis*-[Rh(*p*-TAA)$_2$(Cl)$_2$]$^+$ and (ii) *trans*-[Rh(*p*-TAA)$_2$(Cl)$_2$]$^+$.

Table 20 Selected bond angles in (i) *cis*-[Rh(*p*-TAA)$_2$(Cl)$_2$]$^+$ and (ii) *trans*-[Rh(*p*-TAA)$_2$(Cl)$_2$]$^+$

cis-[Rh(*p*-TAA)$_2$(Cl)$_2$]$^+$		*trans*-[Rh(*p*-TAA)$_2$(Cl)$_2$]$^+$	
Bond angles	Degree	Bond angles	Degree
2N-1Rh-3N	104.6604	2N-1Rh-3N	170.9533
2N-1Rh-4O	79.7417	2N-1Rh-4O	101.5164
2N-1Rh-5O	165.9013	2N-1Rh-5O	78.4836
2N-1Rh-6Cl	85.3788	2N-1Rh-6Cl	88.8082
2N-1Rh-7Cl	107.2909	2N-1Rh-7Cl	89.4519

(i)   (ii)
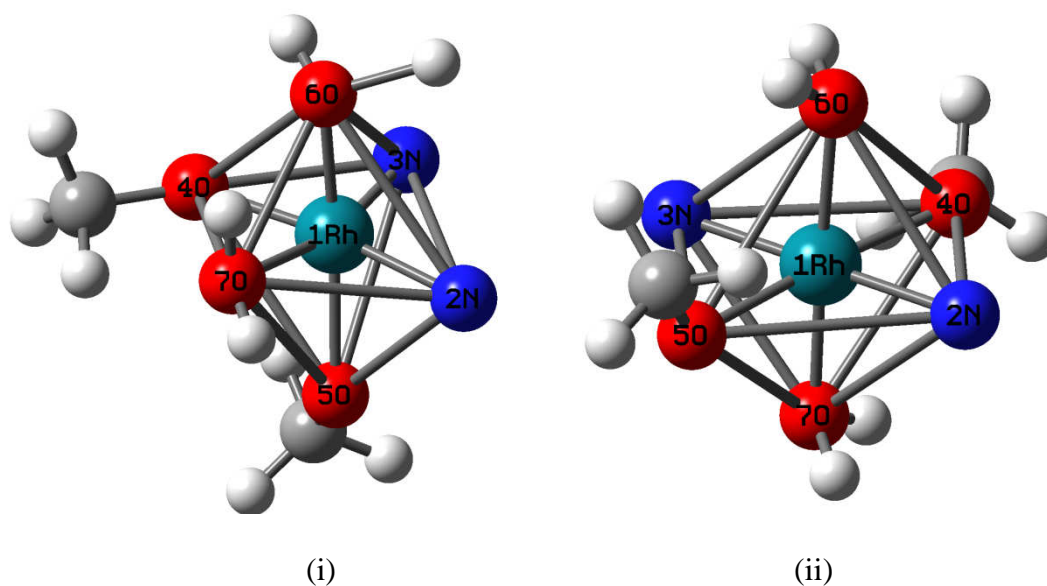
Figure 92 The geometry of coordinated bond between rhodium ion and donor atoms in (i) *cis*-[Rh(*p*-TAA)$_2$(H$_2$O)$_2$]$^{3+}$ and (ii) *trans*-[Rh(*p*-TAA)$_2$(H$_2$O)$_2$]$^{3+}$.

Table 21 Selected bond angles in (i) *cis*-[Rh(*p*-TAA)$_2$(H$_2$O)$_2$]$^{3+}$ and (ii) *trans*-[Rh(*p*-TAA)$_2$(H$_2$O)$_2$]$^{3+}$

cis-[Rh(*p*-TAA)$_2$(H$_2$O)$_2$]$^{3+}$		*trans*-[Rh(*p*-TAA)$_2$(H$_2$O)$_2$]$^{3+}$	
Bond angles	Degree	Bond angles	Degree
2N-1Rh-3N	104.5651	2N-1Rh-3N	179.4221
2N-1Rh-4O	173.4285	2N-1Rh-4O	103.5057
2N-1Rh-5O	79.9203	2N-1Rh-5O	78.5699
2N-1Rh-6O	97.5543	2N-1Rh-6O	91.7508
2N-1Rh-7O	86.6736	2N-1Rh-7O	89.4005
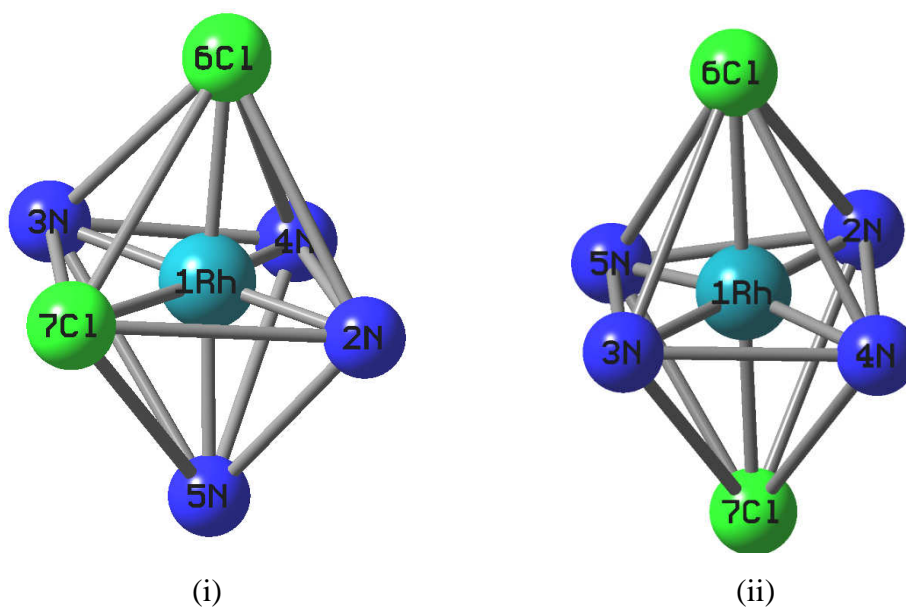
Figure 93 The geometry of coordinated bond between rhodium ion and donor atoms
in (i) *cis*-[Rh(*p*-TAA-n)$_2$(Cl)$_2$]$^+$ and (ii) *trans*-[Rh(*p*-TAA-n)$_2$(Cl)$_2$]$^+$.

Table 22 Selected bond angles in (i) *cis*-[Rh(*p*-TAA-n)$_2$(Cl)$_2$]$^+$ and (ii) *trans*-[Rh(*p*-TAA-n)$_2$(Cl)$_2$]$^+$

cis-[Rh(*p*-TAA-n)$_2$(Cl)$_2$]$^+$		*trans*-[Rh(*p*-TAA-n)$_2$(Cl)$_2$]$^+$	
Bond angles	Degree	Bond angles	Degree
2N-1Rh-3N	178.7708	2N-1Rh-3N	179.3817
2N-1Rh-4N	103.6750	2N-1Rh-4N	103.4947
2N-1Rh-5N	76.7366	2N-1Rh-5N	76.5631
2N-1Rh-6Cl	93.2386	2N-1Rh-6Cl	89.6906
2N-1Rh-7Cl	86.8692	2N-1Rh-7Cl	90.3099

(i)   (ii)
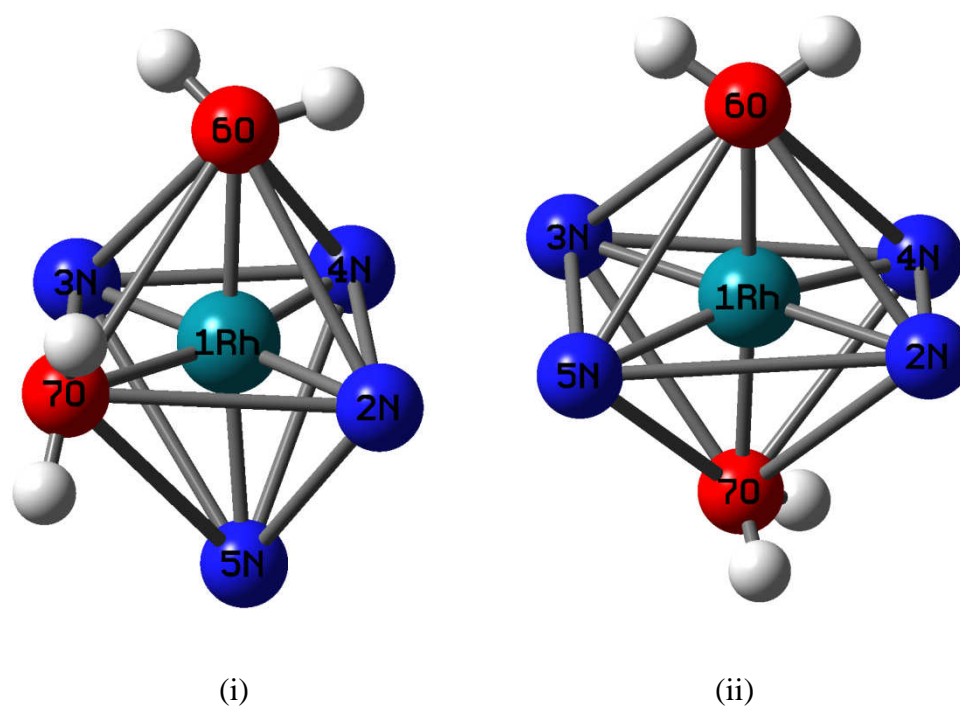
Figure 94 The geometry of coordinated bond between rhodium ion and donor atoms

in (i) *cis*-[Rh(*p*-TAA-n)$_2$(H$_2$O)$_2$]$^{3+}$and (ii) *trans*-[Rh(*p*-TAA-n)$_2$(H$_2$O)$_2$]$^{3+}$.

Table 23 Selected bond angles in (i) *cis*-[Rh(*p*-TAA-n)$_2$(H$_2$O)$_2$]$^{3+}$ and (ii) *trans*-

[Rh(*p*-TAA-n)$_2$(H$_2$O)$_2$]$^{3+}$

cis-[Rh(*p*-TAA-n)$_2$(H$_2$O)$_2$]$^{3+}$		*trans*-[Rh(*p*-TAA-n)$_2$(H$_2$O)$_2$]$^{3+}$	
Bond angles	Degree	Bond angles	Degree
5N-1Rh-2N	78.1683	7O-1Rh-2N	88.2849
5N-1Rh-3N	100.5288	7O -1Rh-3N	97.4993
5N-1Rh-4N	97.5483	7O -1Rh-4N	93.9813
5N-1Rh-6O	88.1312	7O -1Rh-5N	91.4839
5N-1Rh-7O	168.5477	7O-1Rh-6O	176.9363
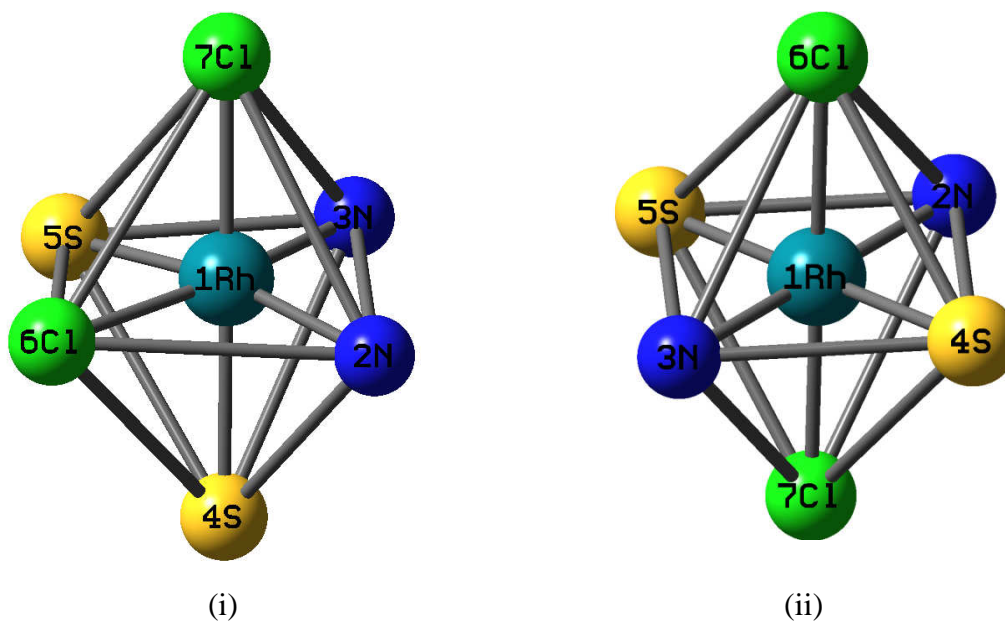
Figure 95 The geometry of coordinated bond between rhodium ion and donor atoms in (i) *cis*-[Rh(*p*-TAA-s)$_2$(Cl)$_2$]$^+$ and (ii) *trans*-[Rh(*p*-TAA-s)$_2$(Cl)$_2$]$^+$.

Table 24 Selected bond angles in (i) *cis*-[Rh(*p*-TAA-s)$_2$(Cl)$_2$]$^+$ and (ii) *trans*-[Rh(*p*-TAA-s)$_2$(Cl)$_2$]$^+$

cis-[Rh(*p*-TAA-s)$_2$(Cl)$_2$]$^+$		*trans*-[Rh(*p*-TAA-s)$_2$(Cl)$_2$]$^+$	
Bond angles	Degree	Bond angles	Degree
3N-1Rh-2N	101.1027	7Cl-1Rh-2N	86.6128
3N-1Rh-4S	96.0499	7Cl-1Rh-3N	93.4085
3N-1Rh-5S	80.1557	7Cl-1Rh-4S	94.6689
3N-1Rh-6Cl	165.9672	7Cl-1Rh-5S	85.3269
3N-1Rh-7Cl	85.8008	7Cl-1Rh-6Cl	179.9661

(i)   (ii)
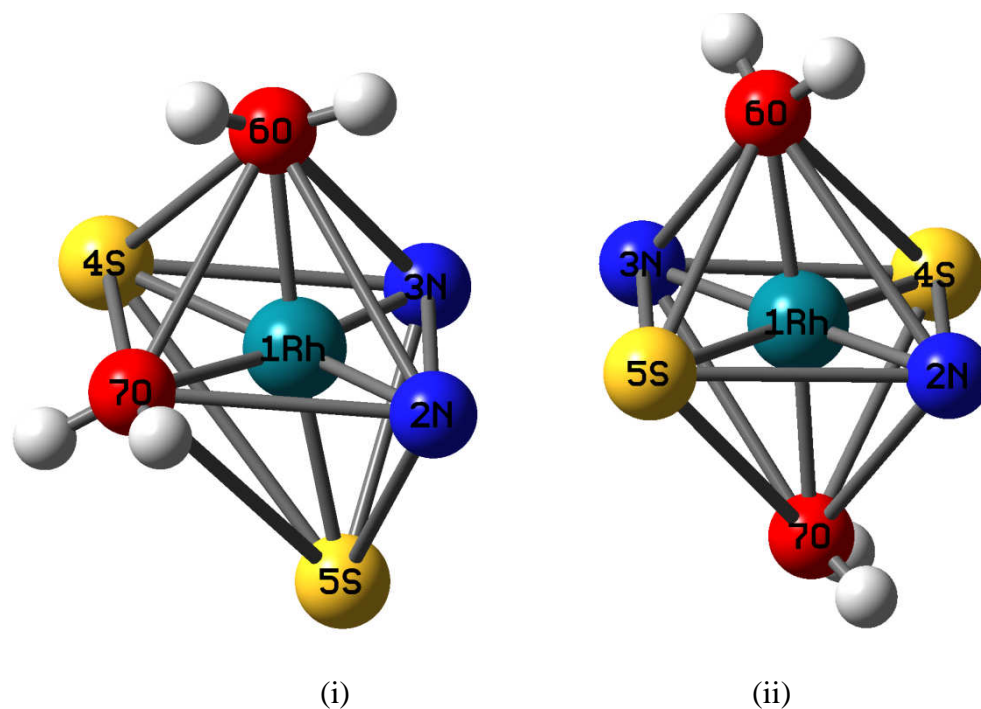
Figure 96 The geometry of coordinated bond between rhodium ion and donor atoms
in (i) *cis*-[Rh(*p*-TAA-s)$_2$(H$_2$O)$_2$]$^{3+}$ and (ii) *trans*-[Rh(*p*-TAA-s)$_2$(H$_2$O)$_2$]$^{3+}$.

Table 25 Selected bond angles in (i) *cis*-[Rh(*p*-TAA-s)$_2$(H$_2$O)$_2$]$^{3+}$ and (ii) *trans*-
[Rh(*p*-TAA-s)$_2$(H$_2$O)$_2$]$^{3+}$

cis-[Rh(*p*-TAA-s)$_2$(H$_2$O)$_2$]$^{3+}$		*trans*-[Rh(*p*-TAA-s)$_2$(H$_2$O)$_2$]$^{3+}$	
Bond angles	Degree	Bond angles	Degree
2N-1Rh-3N	107.4777	7O -1Rh -2N	94.5343
2N-1Rh -4S	169.1682	7O -1Rh-3N	86.7677
2N-1Rh -5S	83.0441	7O -1Rh -4S	83.4412
2N-1Rh -6O	96.8697	7O -1Rh -5S	95.3607
2N-1Rh -7O	80.7724	7O -1Rh -6O	174.8533
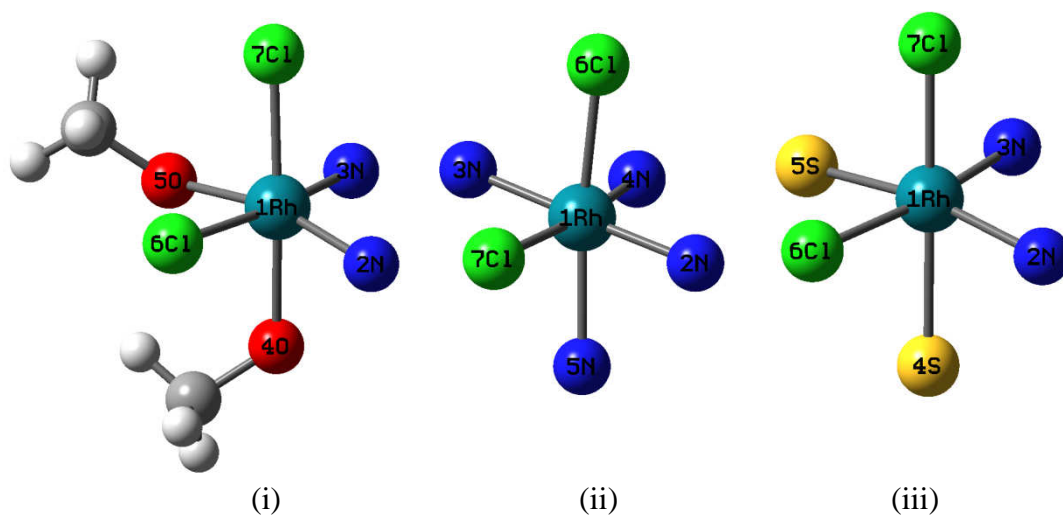
Figure 97 The coordination of different donor atoms to rhodium ion in

(i) *cis*-[Rh(*p*-TAA)$_2$(Cl)$_2$]$^+$, (ii) *cis*-[Rh(*p*-TAA-n)$_2$(Cl)$_2$]$^+$ and

(iii) *cis*-[Rh(*p*-TAA-s)$_2$(Cl)$_2$]$^+$.

Table 26 Selected bond lengths in (i) *cis*-[Rh(*p*-TAA)$_2$(Cl)$_2$]$^+$, (ii) *cis*-[Rh(*p*-TAA-n)$_2$(Cl)$_2$]$^+$ and (iii) *cis*-[Rh(*p*-TAA-s)$_2$(Cl)$_2$]$^+$

cis-[Rh(*p*-TAA)$_2$(Cl)$_2$]$^+$		*cis*-[Rh(*p*-TAA-n)$_2$(Cl)$_2$]$^+$		*cis*-[Rh(*p*-TAA-s)$_2$(Cl)$_2$]$^+$	
Bond	Distance (Å)	Bond	Distance (Å)	Bond	Distance (Å)
1Rh-2N	2.0468	1Rh-2N	2.0399	1Rh-2N	2.2293
1Rh-3N	2.1316	1Rh-3N	2.0384	1Rh-3N	2.2516
1Rh-4O	2.1903	1Rh-4N	2.1411	1Rh-4S	2.4981
1Rh-5O	2.1714	1Rh-5N	2.1810	1Rh-5S	2.3691
1Rh-6Cl	2.3543	1Rh-6Cl	2.3480	1Rh-6Cl	2.3650
1Rh-7Cl	2.3123	1Rh-7Cl	2.3603	1Rh-7Cl	2.3439

(i)   (ii)   (iii)
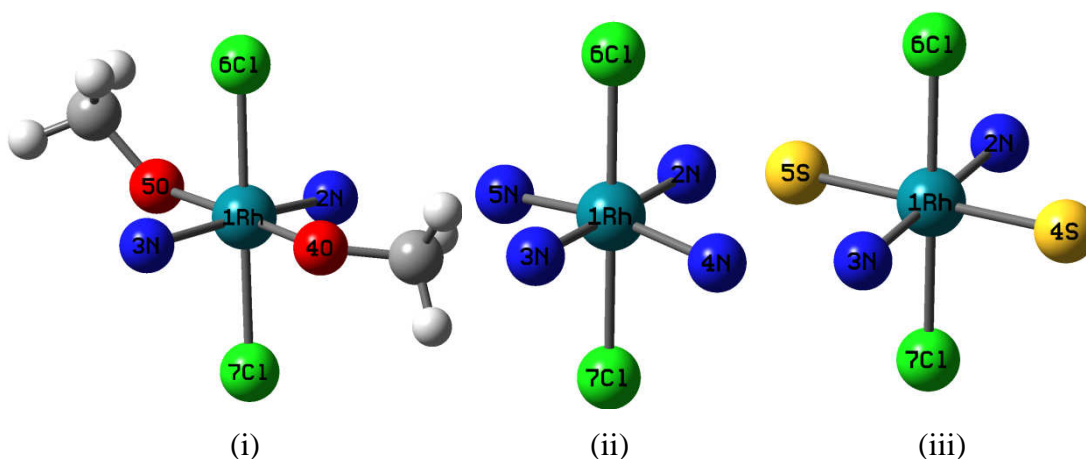
Figure 98 The coordination of different donor atoms to rhodium ion in

(i) *trans*-[Rh(p-TAA)$_2$(Cl)$_2$]$^+$, (ii) *trans*-[Rh(p-TAA-n)$_2$(Cl)$_2$]$^+$ and

(iii) *trans*-[Rh(p-TAA-s)$_2$(Cl)$_2$]$^+$.

Table 27 Selected bond lengths in (i) *trans*-[Rh(p-TAA)$_2$(Cl)$_2$]$^+$, (ii) *trans*-[Rh(p-TAA-n)$_2$(Cl)$_2$]$^+$ and (iii) *trans*-[Rh(p-TAA-s)$_2$(Cl)$_2$]$^+$

trans-[Rh(p-TAA)$_2$(Cl)$_2$]$^+$		*trans*-[Rh(p-TAA-n)$_2$(Cl)$_2$]$^+$		*trans*-[Rh(p-TAA-s)$_2$(Cl)$_2$]$^+$	
Bond	Distance (Å)	Bond	Distance (Å)	Bond	Distance (Å)
1Rh-2N	2.1449	1Rh-2N	2.1173	1Rh-2N	2.1684
1Rh-3N	2.1417	1Rh-3N	2.1173	1Rh-3N	2.1683
1Rh-4O	2.1271	1Rh-4N	2.0812	1Rh-4S	2.4290
1Rh-5O	2.1260	1Rh-5N	2.0813	1Rh-5S	2.4295
1Rh-6Cl	2.3869	1Rh-6Cl	2.3893	1Rh-6Cl	2.3891
1Rh-7Cl	2.3681	1Rh-7Cl	2.3852	1Rh-7Cl	2.3892

(i)   (ii)   (iii)
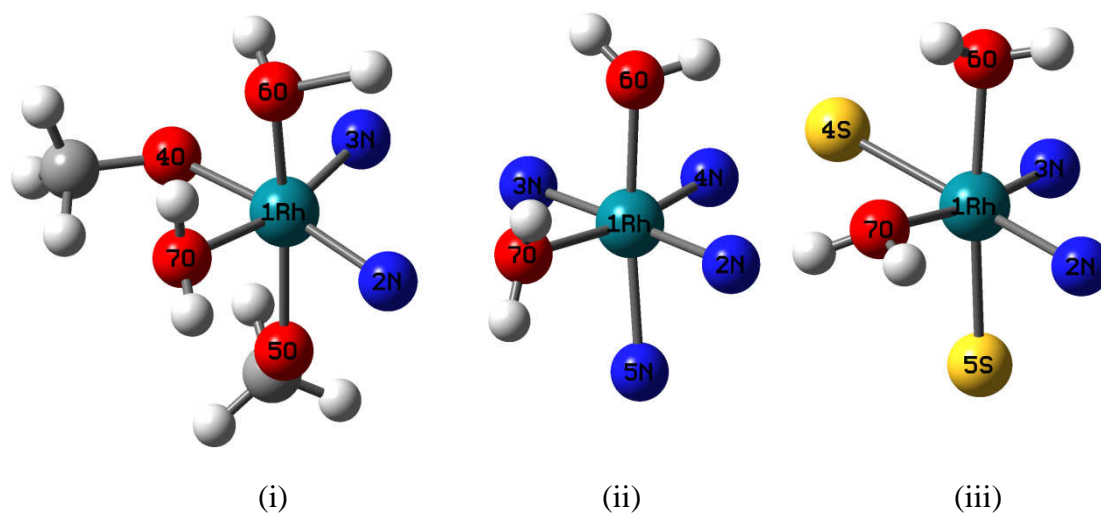
Figure 99 The coordination of different donor atoms to rhodium ion in

(i) *cis*-[Rh(*p*-TAA)$_2$(H$_2$O)$_2$]$^{3+}$, (ii) *cis*-[Rh(*p*-TAA-n)$_2$(H$_2$O)$_2$]$^{3+}$ and

(iii) *cis*-[Rh(*p*-TAA-s)$_2$(H$_2$O)$_2$]$^{3+}$.

Table 28 Selected bond lengths in (i) *cis*-[Rh(*p*-TAA)$_2$(H$_2$O)$_2$]$^{3+}$, (ii) *cis*-[Rh(*p*-TAA-n)$_2$(H$_2$O)$_2$]$^{3+}$ and (iii) *cis*-[Rh(*p*-TAA-s)$_2$(H$_2$O)$_2$]$^{3+}$

cis-[Rh(*p*-TAA)$_2$(H$_2$O)$_2$]$^{3+}$		*cis*-[Rh(*p*-TAA-n)$_2$(H$_2$O)$_2$]$^{3+}$		*cis*-[Rh(*p*-TAA-s)$_2$(H$_2$O)$_2$]$^{3+}$	
Bond	Distance (Å)	Bond	Distance (Å)	Bond	Distance (Å)
1Rh-2N	2.0818	1Rh-2N	2.0682	1Rh-2N	2.1966
1Rh-3N	2.0724	1Rh-3N	2.0520	1Rh-3N	2.1221
1Rh-4O	2.1297	1Rh-4N	2.0749	1Rh-4S	2.4737
1Rh-5O	2.1282	1Rh-5N	2.1251	1Rh-5S	2.3930
1Rh-6O	1.9914	1Rh-6O	2.1395	1Rh-6O	2.1563
1Rh-7O	2.1763	1Rh-7O	2.1894	1Rh-7O	2.1979

(i) (ii) (iii)
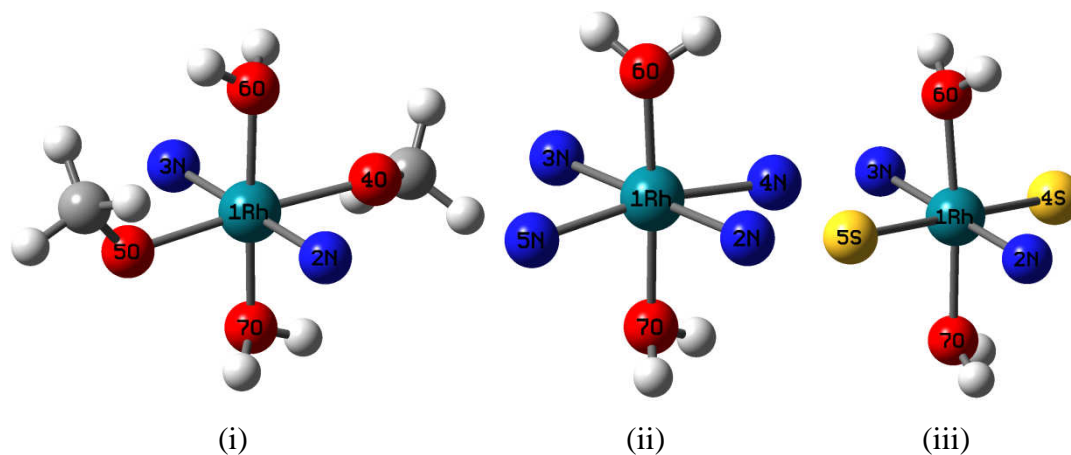
Figure 100 The coordination of different donor atoms to rhodium ion in
(i) *trans*-[Rh(*p*-TAA)$_2$(H$_2$O)$_2$]$^{3+}$, (ii) *trans*-[Rh(*p*-TAA-n)$_2$(H$_2$O)$_2$]$^{3+}$ and
(iii) *trans*-[Rh(*p*-TAA-s)$_2$(H$_2$O)$_2$]$^{3+}$.

Table 29 Selected bond lengths in (i) *trans*-[Rh(*p*-TAA)$_2$(H$_2$O)$_2$]$^{3+}$, (ii) *trans*-[Rh(*p*-TAA-n)$_2$(H$_2$O)$_2$]$^{3+}$ and (iii) *trans*-[Rh(*p*-TAA-s)$_2$(H$_2$O)$_2$]$^{3+}$

trans-[Rh(*p*-TAA)$_2$(H$_2$O)$_2$]$^{3+}$		*trans*-[Rh(*p*-TAA-n)$_2$(H$_2$O)$_2$]$^{3+}$		*trans*-[Rh(*p*-TAA-s)$_2$(H$_2$O)$_2$]$^{3+}$	
Bond	Distance (Å)	Bond	Distance (Å)	Bond	Distance (Å)
1Rh-2N	2.1312	1Rh-2N	2.1818	1Rh-2N	2.1536
1Rh-3N	2.1197	1Rh-3N	2.1821	1Rh-3N	2.1696
1Rh-4O	2.1025	1Rh-4N	2.0936	1Rh-4S	2.5547
1Rh-5O	2.0885	1Rh-5N	2.0899	1Rh-5S	2.5782
1Rh-6O	2.1255	1Rh-6O	2.0950	1Rh-6O	2.1511
1Rh-7O	1.9958	1Rh-7O	2.0959	1Rh-7O	2.1586
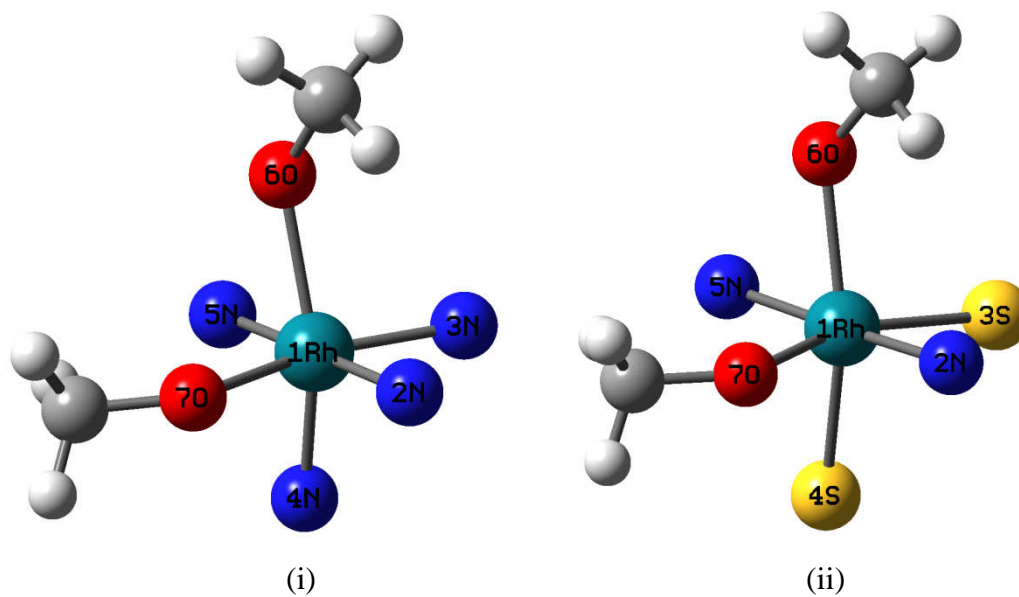
Figure 101 The coordination of different donor atoms to rhodium ion in
(i) [Rh(*p*-TAA-n)$_2$]$^{3+}$ and (ii) [Rh(*p*-TAA-s)$_2$]$^{3+}$.

Table 30 Selected bond lengths in (i) [Rh(*p*-TAA-n)$_2$]$^{3+}$ and (ii) [Rh(*p*-TAA-s)$_2$]$^{3+}$

[Rh(*p*-TAA-n)$_2$]$^{3+}$		[Rh(*p*-TAA-s)$_2$]$^{3+}$	
Bond	Distance (Å)	Bond	Distance (Å)
1Rh-2N	2.0285	1Rh-2N	2.1536
1Rh-3N	2.0107	1Rh-3N	2.1696
1Rh-4N	2.0107	1Rh-4S	2.5547
1Rh-5N	2.0285	1Rh-5S	2.5782
1Rh-6O	2.2170	1Rh-6O	2.1511
1Rh-7O	2.2170	1Rh-7O	2.1586s
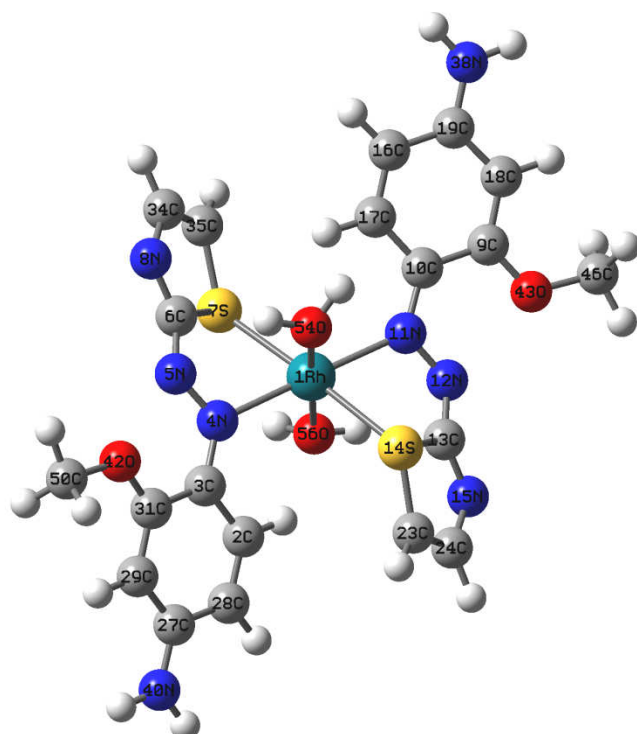
Torsion angles	Degree
2C-3C-4N-5N	168.3746
3C-4N-5N-6C	-158.8345
4N-5N-6C-7S	13.7684
4N-5N-6C-8N	-165.1109
9C-10C-11N-12N	-7.4730
10C-11N-12N-13C	154.9183
11N-12N-13C-14C	-15.2788
11N-12N-13C-15N	162.6855

Figure 102 The optimized structure of *trans*-[Rh(*p*-TAA-s)$_2$(H$_2$O)$_2$]$^{3+}$ with torsion angles of *p*-amino TAA.
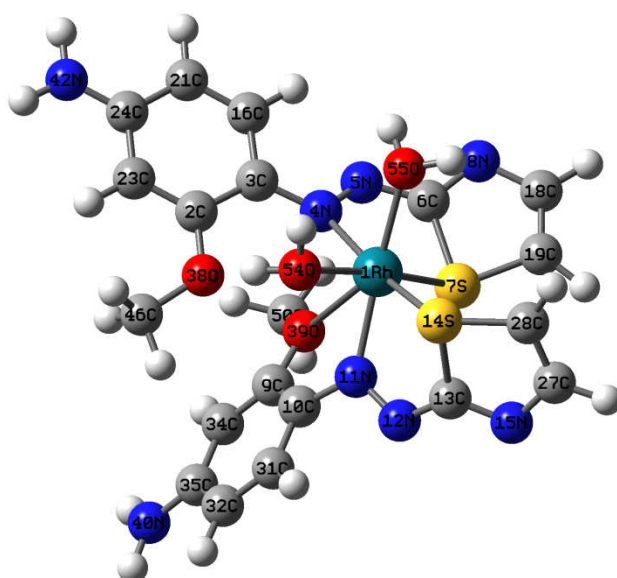
Torsion angles	Degree
2C-3C-4N-5N	-132.7762
3C-4N-5N-6C	-168.1413
4N-5N-6C-7S	26.4683
4N-5N-6C-8N	-145.9121
9C-10C-11N-12N	161.6809
10C-11N-12N-13C	170.6035
11N-12N-13C-14C	25.1091
11N-12N-13C-15N	-148.4532

Figure 103 The optimized structure of *cis*-[Rh(*p*-TAA-s)$_2$(H$_2$O)$_2$]$^{3+}$ with torsion angles of *p*-amino TAA.

Torsion angles	Degree
2C-3C-4N-5N	-179.3643
3C-4N-5N-6C	179.7965
4N-5N-6C-7S	-178.9416
4N-5N-6C-8N	0.6230
9C-10C-11N-12N	-179.3659
10C-11N-12N-13C	179.7958
11N-12N-13C-14C	-178.9497
11N-12N-13C-15N	0.6180
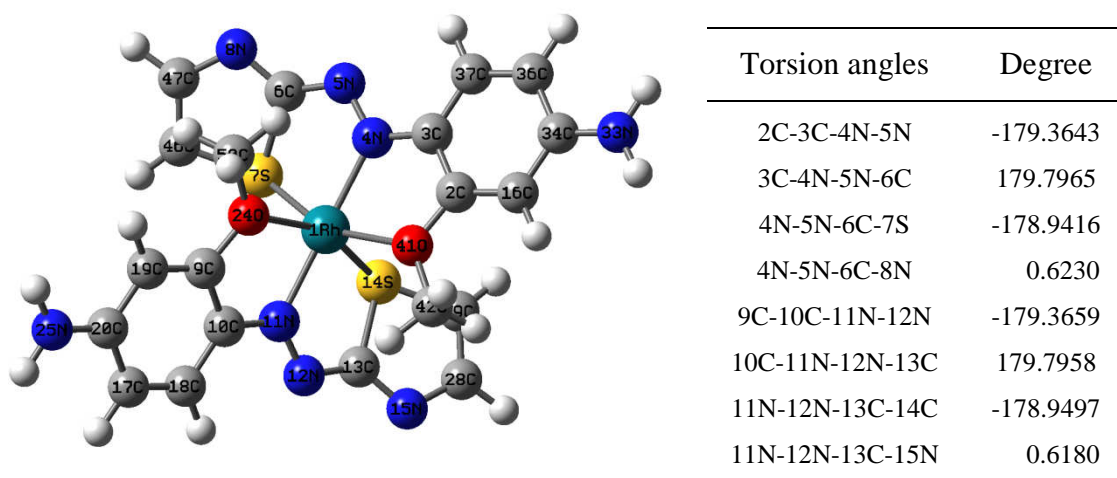
Figure 104 The optimized structure of [Rh(*p*-TAA-s)₂]³⁺ with torsion angles of *p*-amino TAA.

Torsion angles	Degree
2C-3C-4N-5N	168.7785
3C-4N-5N-6C	-178.7992
4N-5N-6C-7S	-22.6655
4N-5N-6C-8N	149.3114
9C-10C-11N-12N	170.2996
10C-11N-12N-13C	-177.7826
11N-12N-13C-14C	-23.9230
11N-12N-13C-15N	148.3061
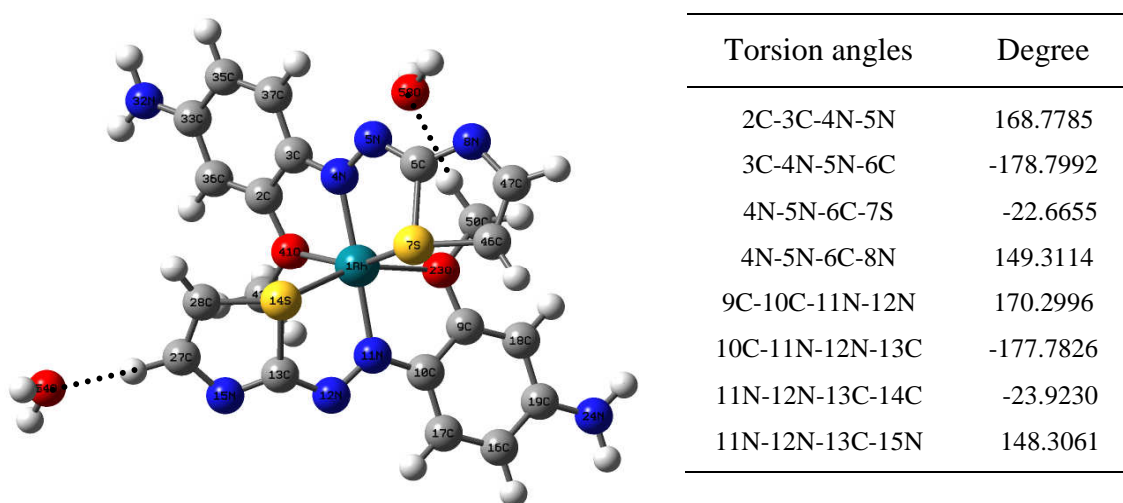
Figure 105 The optimized structure of [Rh(*p*-TAA-s)₂]³⁺ in the presence of two water molecules with torsion angles of *p*-amino TAA.

The selected bond angles of the optimized structures as shown in Table 19 to Table 25 were used to compare the distortion from octahedral geometric structure of rhodium(III) complex between *cis* and *trans* isomers with the same donor atoms. The results show that bond angles between donor atoms and rhodium(III) ion in *trans* isomers are close to 90° and 180° which indicated the smaller distortion from octahedral geometry of *trans* than *cis* isomers. For example in Figure 95 and Table 24, the angles 7Cl-1Rh-6Cl and 7Cl-1Rh-3N in *trans*-[Rh(*p*-TAA-n)$_2$(Cl)$_2$]$^+$ (i) are 179.97 and 93.41 degrees while the angles 3N-1Rh-6Cl and 3N-1Rh-5S in *cis*-[Rh(*p*-TAA-n)$_2$(Cl)$_2$]$^+$ (ii) are 165.97 and 80.16 degrees. This might be attributed to the less steric hindrance of *p*-amino TAA in *trans* than in *cis* isomers of which two molecules of *p*-amino TAA are approached resulting in the distorted angles between donor atoms and rhodium(III) ion for the formation of optimized octahedral structure. These results are also corresponding with the stabilization energies of these structures as shown in Table 31. The optimized structure which has the smaller distortion from octahedral geometry of *trans*-[Rh(*p*-TAA-n)$_2$(Cl)$_2$]$^+$ with the energy of -1350.72 kcal/mol indicates the more stable structure than the optimized structure of *cis*-[Rh(*p*-TAA-n)$_2$(Cl)$_2$]$^+$ with the stabilization energy of -1348.33 kcal/mol. The bond angles of other optimized structures were compared and the similar results were observed.

The selected bond lengths of the optimized structures as collected in Table 26 to Table 30 were used to compare the distances from rhodium(III) ion to each donor atom in the same isomers with different donor atoms. The shorter distances between donor atoms and rhodium(III) ion signify to the more stable of the structure. The results show that bond lengths between rhodium(III) ion and donor atoms decrease in the order of Rh-S > Rh-O > Rh-N, respectively. For example in Figure 98 and Table 27, the distances of 1Rh-4O in *trans*-[Rh(*p*-TAA)$_2$(Cl)$_2$]$^+$ (i) is 2.13 Å, 1Rh-4N in *trans*-[Rh(*p*-TAA-n)$_2$(Cl)$_2$]$^+$ (ii) is 2.08 Å and 1Rh-4S in *trans*-[Rh(*p*-TAA- s)$_2$(Cl)$_2$]$^+$ (iii) is 2.43 Å, respectively. This implied that rhodium(III) ion preferred to form complex with nitrogen atoms and this structure should be the most stable form for rhodium(III) complex. These results might be described by hard and soft acids and bases characteristic of each atom as shown in Table 13 and Table 14. Rhodium(III) is a borderline acid as well as nitrogen atom of thiazole ring. Conversely, oxygen atom

is classified as hard base and sulfur atom is classified as soft base, so these atoms are less preferable to form complex with rhodium(III) ion than nitrogen atom resulting in the longer distances of oxygen and sulfur atoms to rhodium(III) ion.

The stabilization energies of these complexes as shown in Table 31 show that the energies of *trans*-[Rh(*p*-TAA)$_2$(Cl)$_2$]$^+$, *trans*-[Rh(*p*-TAA-n)$_2$(Cl)$_2$]$^+$ and *trans*-[Rh(*p*-TAA- s)$_2$(Cl)$_2$]$^+$ are -1304.69, -1350.72 and -1297.08 kcal/mol, respectively. These indicate that the stability of *trans*-[Rh(*p*-TAA-n)$_2$(Cl)$_2$]$^+$ > *trans*-[Rh(*p*-TAA)$_2$(Cl)$_2$]$^+$ > *trans*-[Rh(*p*-TAA- s)$_2$(Cl)$_2$]$^+$ which corresponding to their bond strength as mentioned which decrease in the order of Rh-N > Rh-O > Rh-S, respectively. Besides, the bond distances between rhodium(III) ion and chloride ions and between rhodium(III) ion and oxygen atoms of water are insignificant differences for all of the optimized structures. The selected bond lengths of others were compared and gave the similar results.
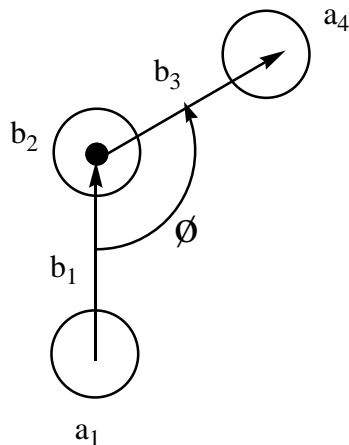
Figure 106 Dihedral angle defined by three bond vectors of four atoms.

Torsion angles of the complexes are useful information to explain the planarity of the ligand *p*-amino TAA and the orientation of octahedral structure in each complex. Figure 106 shows the torsion angle of four atoms; a_1, a_2, a_3 and a_4 which a_2 and a_3 are located in the center and the second bond vector (b_2) is coming out of the page. The dihedral angle (ø) is the angle made by the vectors b_1 and b_3. The

planarity of the ligand p-amino TAA in the complexes $trans$-[Rh(p-TAA-s)$_2$(H$_2$O)$_2$]$^{3+}$ (Figure 102), cis-[Rh(p-TAA-s)$_2$(H$_2$O)$_2$]$^{3+}$ (Figure 103), [Rh(p-TAA-s)$_2$]$^{3+}$ (Figure 104) and [Rh(p-TAA-s)$_2$](H$_2$O)$_2$$^{3+}$ (Figure 105) were considered. These optimized structures were selected because all compounds have sulfur atoms of thiazole ring and nitrogen atoms of azo group as donor atoms. The results show that two p-amino TAA molecules of [Rh(p-TAA-s)$_2$]$^{3+}$ have planar geometry as seen in Figure 104 which torsion angles are nearly 180° i.e. torsion angle 10N-11N-12C-13N is 179.79 degree. This may be due to their tridentate character and less steric repulsion between each p-amino TAA molecule. In contrast, all p-amino TAA molecules in $trans$-[Rh(p-TAA-s)$_2$(H$_2$O)$_2$]$^{3+}$ and cis-[Rh(p-TAA-s)$_2$(H$_2$O)$_2$]$^{3+}$ have distorted planar geometry as shown in Figure 102 and Figure 103 which torsion angles in p-amino TAA are in the range of 150° to 170° i.e. torsion angle 11N-12N-13C-15C of $trans$-[Rh(p-TAA-s)$_2$(H$_2$O)$_2$]$^{3+}$ is 162.69 degrees and torsion angle 9C-10C-11N-12N of cis-[Rh(p-TAA-s)$_2$(H$_2$O)$_2$]$^{3+}$ is 161.68 degrees, respectively. This may be because of their bidentate character of p-amino TAA and steric repulsion between p-amino TAA and H$_2$O in these two compounds.

From the stabilization energies as shown in Table 31, the energies of $trans$-[Rh(p-TAA-s)$_2$(H$_2$O)$_2$]$^{3+}$ and cis-[Rh(p-TAA-s)$_2$(H$_2$O)$_2$]$^{3+}$ are -966.32 and -899.55 kcal/mol which less than [Rh(p-TAA-s)$_2$]$^{3+}$ with the stabilization energy -875.21 kcal/mol. This can be described by using their bond angles. The bond angles between donor atoms and rhodium(III) ion (Table 25) indicate that structures of cis-[Rh(p-TAA-s)$_2$(H$_2$O)$_2$]$^{3+}$ and $trans$-[Rh(p-TAA-s)$_2$(H$_2$O)$_2$]$^{3+}$ are close to octahedral geometry than [Rh(p-TAA-s)$_2$]$^{3+}$ which the bond angles between donor atoms and rhodium(III) ion (Table 19) show a distorted octahedral geometry. This is due to p-amino TAA in [Rh(p-TAA-s)$_2$]$^{3+}$ acted as tridentate ligand, so it has more steric hindrance and more rigidity. On the other hand, bidentate character of p-amino TAA in cis-[Rh(p-TAA-s)$_2$(H$_2$O)$_2$]$^{3+}$ and $trans$-[Rh(p-TAA-s)$_2$(H$_2$O)$_2$]$^{3+}$ made this structure more flexible. So, it can be concluded that rhodium(III) complex with the higher planarity of p-amino TAA is not necessary to be the most stable structure for rhodium(III) complex. This is because it is not only planarity of p-amino TAA but also other effects as mentioned above that affect the stability of the complex.

The effect of water molecules that solvate [Rh(p-TAA-s)$_2$]$^{3+}$ complex was also studied. The results show that the torsion angles 4N-5N-6C-8N and 11N-12N-13C-15C of [Rh(p-TAA-s)$_2$]$^{3+}$with two water molecules (Figure 105) are 149.31 and 148.31degree which indicated the distorted planarity of p-amino TAA. This is owing to hydrogen bonding between hydrogen atoms of p-amino TAA and oxygen atom of water molecules as shown in Figure 105. The hydrogen bonding also causes the less stability of this compound which can be seen in Table 31. The stabilization energy of [Rh(p-TAA-s)$_2$]$^{3+}$with two water molecules is -824.33 kcal/mol while that of [Rh(p-TAA-s)$_2$]$^{3+}$ is -875.21 kcal/mol.

Table 31 Energies of atoms, molecules and possible structures of Rh(III)-(p-amino TAA) complexes and formation energies of possible structures of Rh(III))-(p-amino TAA) complexes obtained by the calculation on Gaussian03 at B3LYP level of theory using 6-31G* and SDD basis sets

Atoms, molecules and complexes	Figure	Energy (a.u.)	Stabilization Energy (a.u.)	Stabilization Energy (kcal/mol)
Atoms and molecules				
Rh(III)	-	-108.26190	-	-
Cl$^-$	-	-460.25223	-	-
H$_2$O	-	-76.40895	-	-
p-amino TAA	33	-1079.43408	-	-

Table 31 (Continued)

Atoms, molecules and complexes	Figure	Energy (a.u.)	Stabilization Energy (a.u.)	Stabilization Energy (kcal/mol)
complexes				
• tridentate ligand				
$[Rh(p\text{-}TAA\text{-}n)_2]^{3+}$	77	-2268.63477	-1.50471	-944.22
$[Rh(p\text{-}TAA\text{-}s)_2]^{3+}$	78	-2268.52479	-1.39473	-875.21
$[Rh(p\text{-}TAA\text{-}s)_2](H_2O)_2{}^{3+}$	106	-2421.26164	-1.31368	-824.33
• bidentate ligand (methoxy group)				
$cis\text{-}[Rh(p\text{-}TAA)_2(Cl)_2]^+$	79	-3189.72042	-2.0859	-1308.90
$cis\text{-}[Rh(p\text{-}TAA)_2(H_2O)_2]^{3+}$	80	-2421.45747	-1.50951	-947.22
$trans\text{-}[Rh(p\text{-}TAA)_2(Cl)_2]^+$	81	-3189.73172	-2.09719	-1315.99
$trans\text{-}[Rh(p\text{-}TAA)_2(H_2O)_2]^{3+}$	82	-2421.45744	-1.50948	-947.20
• bidentate ligand (n-thiazole rings)				
$cis\text{-}[Rh(p\text{-}TAA\text{-}n)_2(Cl)_2]^+$	83	-3189.78326	-2.14874	-1348.33
$cis\text{-}[Rh(p\text{-}TAA\text{-}n)_2(H_2O)_2]^{3+}$	84	-2421.49022	-1.54226	-967.77
$trans\text{-}[Rh(p\text{-}TAA\text{-}n)_2(Cl)_2]^+$	87	-3189.78706	-2.15254	-1350.72
$trans\text{-}[Rh(p\text{-}TAA\text{-}n)_2(H_2O)_2]^{3+}$	88	-2421.47556	-1.52760	-958.57
• bidentate ligand (s-thiazole rings)				
$cis\text{-}[Rh(p\text{-}TAA\text{-}s)_2(Cl)_2]^+$	85	-3189.68019	-2.04567	-1283.66
$cis\text{-}[Rh(p\text{-}TAA\text{-}s)_2(H_2O)_2]^{3+}$	86	-2421.48792	-1.53996	-966.32
$trans\text{-}[Rh(p\text{-}TAA\text{-}s)_2(Cl)_2]^+$	89	-3189.70158	-2.06706	-1297.08
$trans\text{-}[Rh(p\text{-}TAA\text{-}s)_2(H_2O)_2]^{3+}$	90	-2421.38151	-1.43355	-899.55

The data in Table 31 show that the optimized structures with chloride ions acted as donor atoms, all *trans* isomers have larger stabilization energies than *cis* isomers (more negative) which is referred to the more stability of these geometric structures. On the other hand, the optimized structures with oxygen atoms of water molecules acted as donor atoms, all *cis* isomers have larger stabilization energies than *trans* isomers. This can be described by hydrogen bonding that occurs in these structures as shown in Figure 107. Hydrogen atom of water molecule can interact with nitrogen atom of thiazole ring led to intramolecular hydrogen bonding and resulted in the higher stability of *cis* isomers than *trans* isomers.
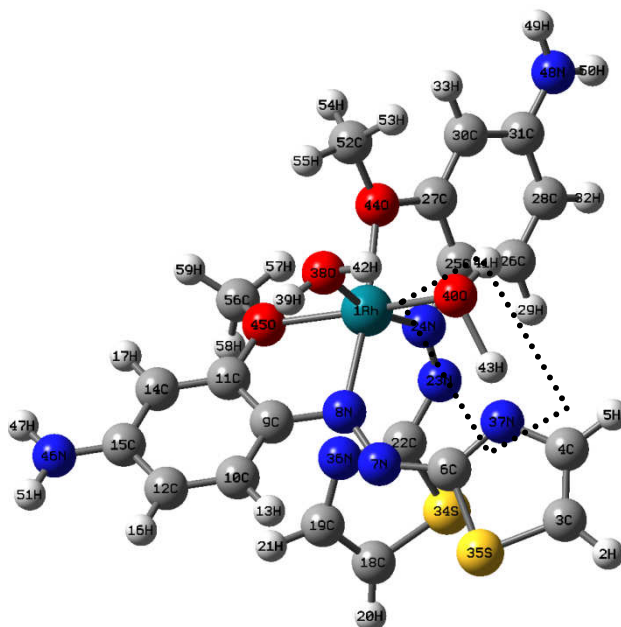
Figure 107 The optimized structure of *cis*-[Rh(p-TAA)$_2$(H$_2$O)$_2$]$^{3+}$ with
intramolecular hydrogen bonding.

Due to the size, electronic configuration of rhodium(III) and geometric parameters from quantum chemical calculations, it prefers an octahedral structure and stable with six coordinated bonds. It was found that *trans*-[Rh(p-TAA-n)$_2$(Cl)$_2$]$^+$ as shown in Figure 86 should be the possible structure because of its largest stabilization energy. The stabilization energy of this complex -1350.72 kcal/mol was the lowest because its structure was less rigid than the others. The twist of benzene ring in

p-amino TAA suggested from calculations also agree well with the results from ^{1}H NMR that indicated some interaction between benzene ring in *p*-amino TAA with rhodium(III) ion as previously mentioned. The results from the quantum chemical calculations was supported the results from ^{1}H NMR which indicated that nitrogen atom in thiazole ring was the donor atom.

14. Binding of calf thymus DNA with rhodium(III)-(*p*-amino TAA*)* and rhodium(III)-(*o*-amino TAA)

14.1   Nucleic acid purity assessment by using A260/A280 ratios

The spectroscopic study of the CT DNA solution was determined at wavelength 260 nm with molar absorptivity (ε) 6600 $M^{-1}cm^{-1}$ (Sun *et al*, 2008). The procedure of this method is shown in Appendix F. The result shows that the concentration of CT DNA is 4.09×10^{-4} M. The absorbances of CT DNA at 260 and 280 nm are 2.6987 and 1.4550, respectively. So, the A260/A280 ratios at wavelength 200 nm to 350 nm are shown in Figure 108 which approximately 1.85 indicated a slightly contamination of CT DNA sample by protein.
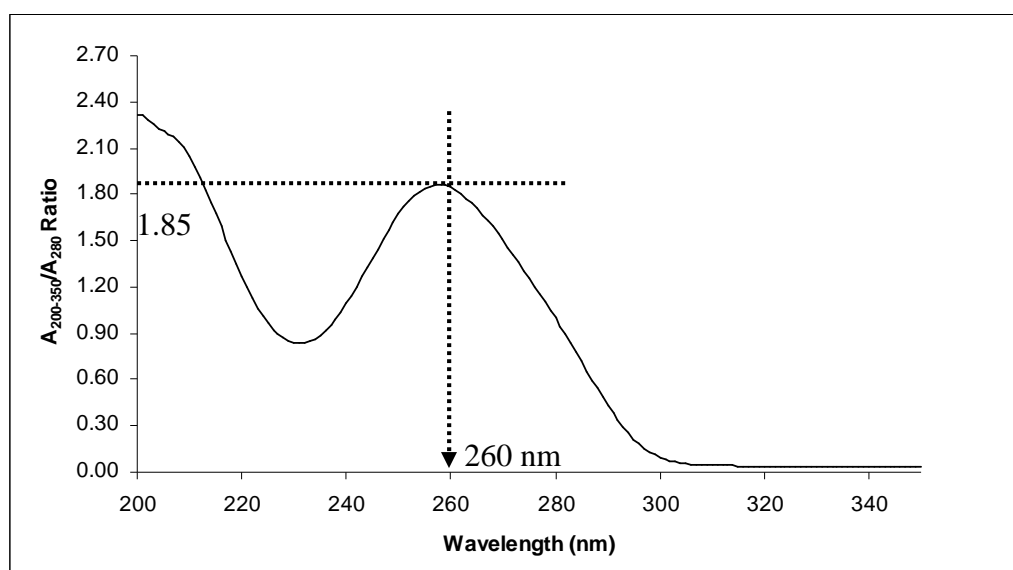
Figure 108 A260/A280 ratios of CT DNA containing DNA and/or protein.

14.2   The binding of rhodium(III)-(*p*-amino TAA) and rhodium(III)-(*o*-amino TAA) with calf thymus DNA
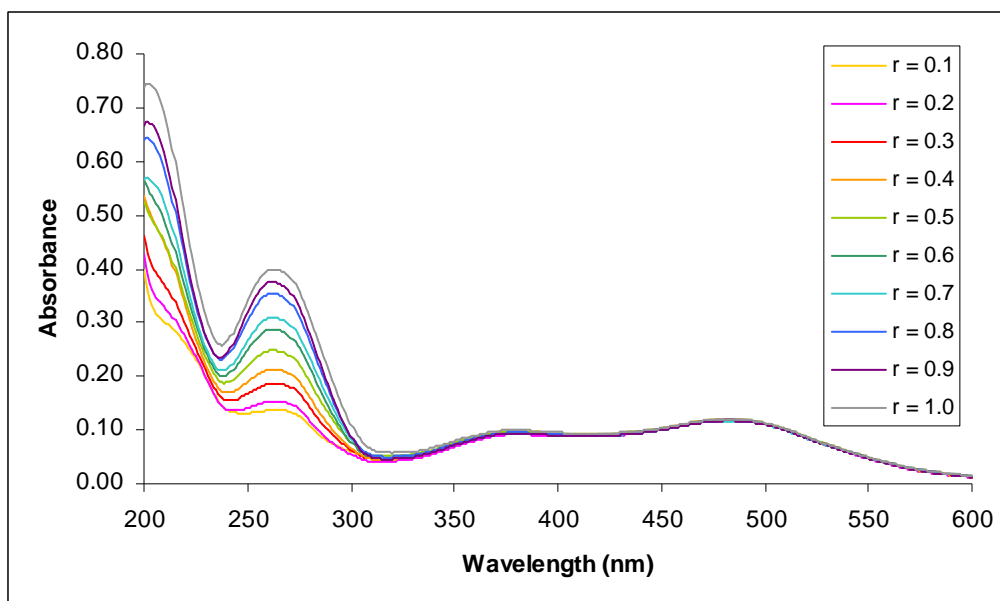
Figure 109 The absorption spectra of Rh(III)-(*p*-amino TAA) 1.0×10^{-4} M in the presence of CT DNA at various concentration ratios (r = mole DNA: mole complex).
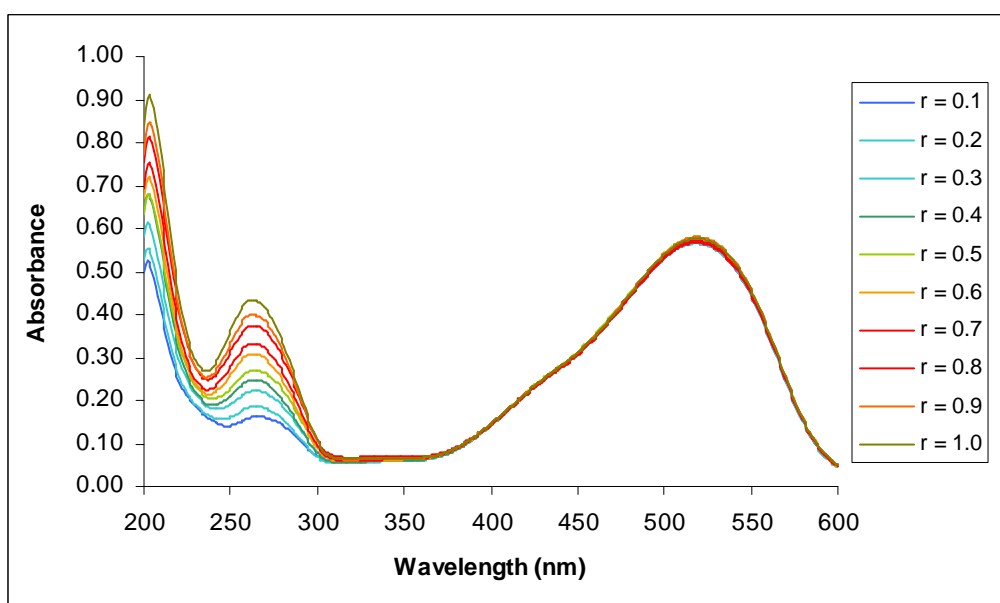
Figure 110 The absorption spectra of Rh(III)-(*o*-amino TAA) 1.0×10^{-4} M in the presence of CT DNA at various concentration ratios (r = mole DNA: mole complex).

The DNA-binding of rhodium(III)-(*p*-amino TAA) and rhodium(III)-(*o*-amino TAA) complexes were studied. The constant concentration of the complexes 1.0×10^{-4} M was studied in the presence of DNA at various concentration ratios. The absorption spectra of the DNA-complexes are shown in Figure 109 and Figure 110. The spectra of rhodium(III)-(*p*-amino TAA) with DNA show that the absorbance at 260 nm which is the characteristic peak for DNA are slightly changed to lower wavelength (blue shift) from 266 nm with the absorbance 0.113 to the wavelength 263 nm with the absorbance 0.400 while increasing the DNA concentration. Similar to rhodium(III)-(*p*-amino TAA), the DNA-binding of rhodium(III)-(*o*-amino TAA) show that the absorbance are also slightly change to lower wavelength from 262 nm with the absorbance 0.133 to the wavelength 255 nm with the absorbance 0.433 while increasing the DNA concentration. However, there is no change in the absorbance at the maximum wavelength of rhodium(III)-(*p*-amino TAA) at 483 nm and of rhodium(III)-(*o*-amino TAA) at 518 nm.
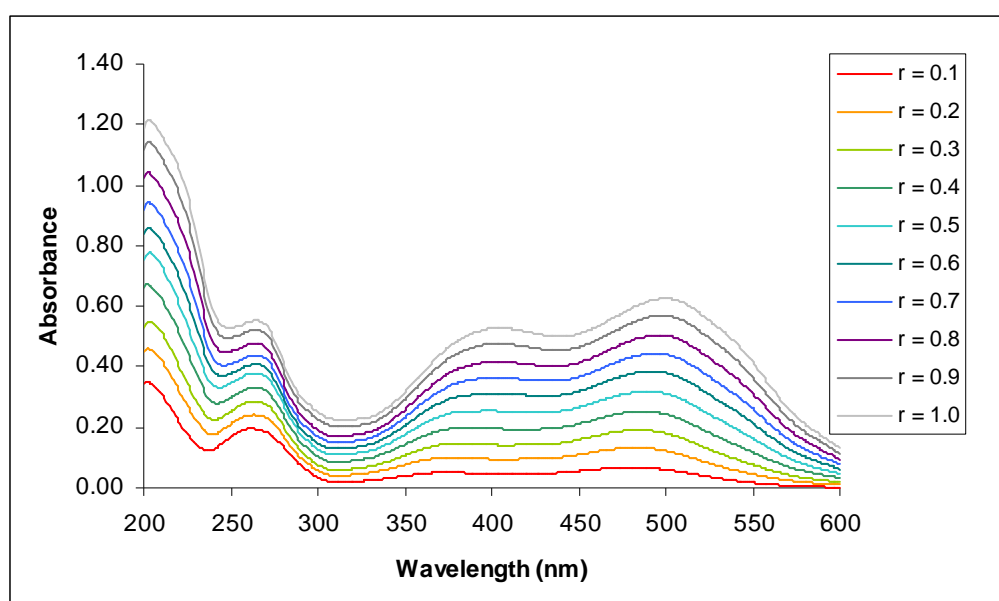
Figure 111 The absorption spectra of CT DNA 2.0×10^{-4} M in the presence of Rh(III)-(*p*-amino TAA) at various concentration ratios (r = mole complex: mole DNA).
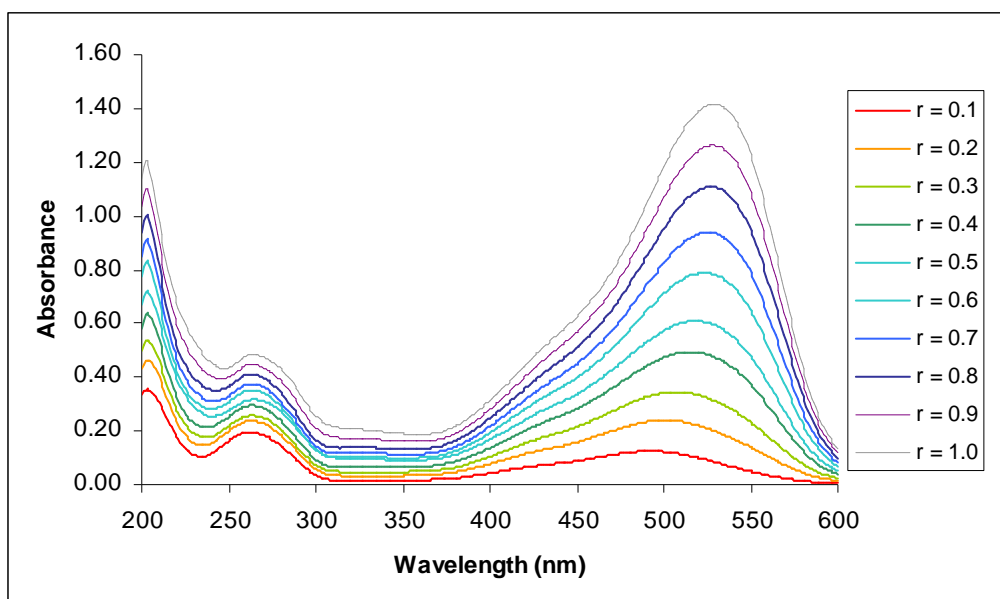
Figure 112 The absorption spectra of CT DNA 2.0 $\times 10^{-4}$ M in the presence of
Rh(III)-(*o*-amino TAA) at various concentration ratios (r = mole
complex: mole DNA).

The DNA-binding of rhodium(III)-(*p*-amino TAA) and rhodium(III)-
(*o*-amino TAA) complexes by using the constant concentration of CT DNA 2.0 $\times 10^{-4}$
M was also studied at various concentration ratios. The absorption spectra of these
DNA-complexes are shown in Figure 111 and Figure 112. The spectra of rhodium(III)
-(*p*-amino TAA) with DNA show that the absorbance at 260 nm which is the
characteristic peak for DNA are slightly changed to higher wavelength (red shift)
from 260 nm with the absorbance 0.176 to the wavelength 265 nm with the
absorbance 0.552 while increasing the rhodium(III)-(*p*-amino TAA) concentration. In
addition, the absorption spectra in visible range which showed the band of
rhodium(III)-(*p*-amino TAA) are also changed. The maximum absorption of the
complexes is significantly changed to higher wavelength (red shift) from 480 nm with
the absorbance 0.036 to the wavelength 499 nm with the absorbance 0.626. Similar to
rhodium(III)-(*p*-amino TAA), the DNA-binding of rhodium(III)-(*o*-amino TAA) show
that the absorption of DNA are slightly changed to lower wavelength from 258 nm
with the absorbance 0.133 to the wavelength 264 nm with the absorbance 0.484 while

increasing the rhodium(III)-(*o*-amino TAA) concentration. Similarly, the maximum absorption of the rhodium(III)-(*o*-amino TAA) is also significantly changed to higher wavelength (red shift) from 488 nm with the absorbance 0.001 to the wavelength 529 nm with the absorbance 1.416.
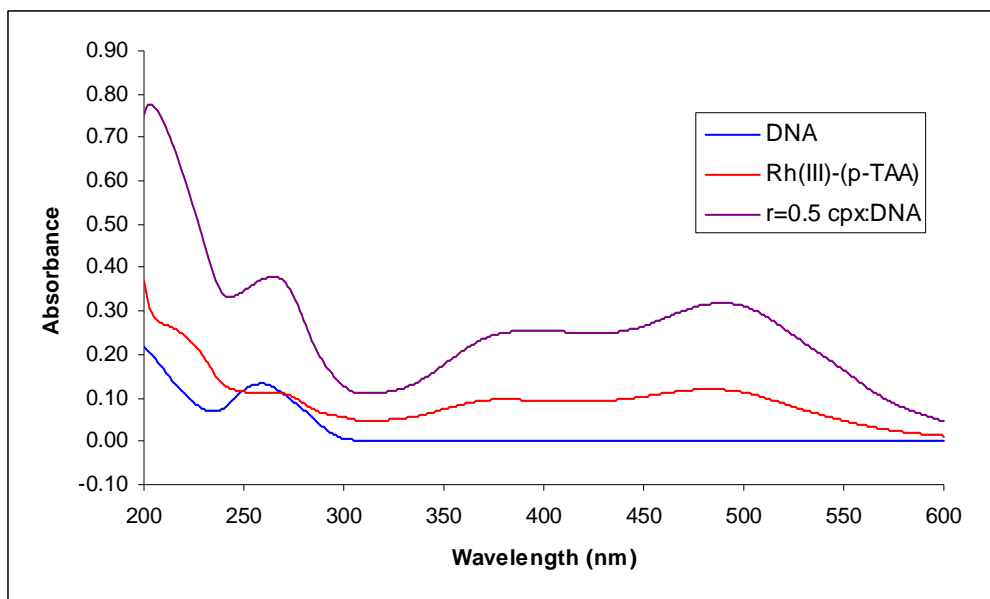
Figure 113 The absorption spectra of Rh(III)-(*p*-amino TAA) 1.0×10^{-4} M, CT DNA 2.0×10^{-4} M and Rh(III)-(*p*-amino TAA) in the presence of CT DNA at concentration ratio 0.5.
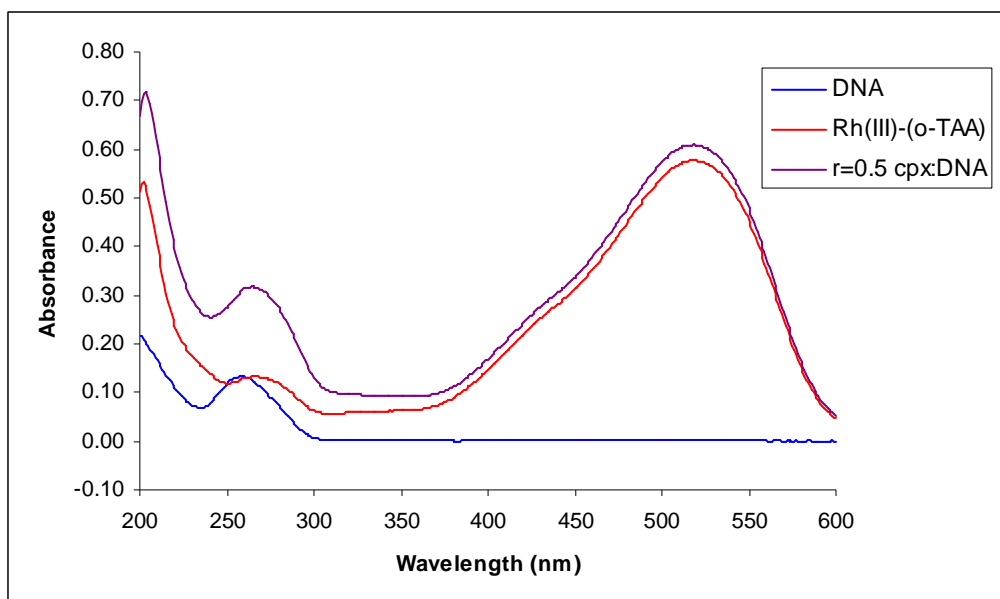
Figure 114 The absorption spectra of Rh(III)-(o-amino TAA) 1.0×10^{-4} M, CT DNA
2.0×10^{-4} M and Rh(III)-(o-amino TAA) in the presence of CT DNA at
concentration ratio 0.5.

The figures show the absorption spectra of rhodium(III)-(p-amino TAA)
complex, pure DNA and rhodium(III)-(p-amino TAA) in the presence of DNA in
Figure 113 and the absorption of rhodium(III)-(o-amino TAA) complex, pure DNA
and rhodium(III)-(o-amino TAA) in the presence of DNA in Figure 114. From the
spectra, it is evidence that there is the change in absorption characteristic of both
complexes and DNA. So, it can be concluded that there might be an interaction
between the complexes and DNA. To determine the binding character between calf
thymus DNA and the complex, the more appropriate condition and other techniques
should be used for the further study.

14.3   Stability of rhodium(III)-(p-amino TAA) and rhodium(III)-
(o-amino TAA) complexes with calf thymus DNA

The stability of rhodium(III)-(p-amino TAA) and rhodium(III)-
(o-amino TAA) complexes with CT DNA in tris-HCl buffer pH 7.4 were investigated.

Figure 115 show the stability of rhodium(III)-(*p*-amino TAA) with DNA at wavelength 260 nm which is used to measure DNA concentration and at wavelength 483 nm which gave the maximum absorption of *p*-amino TAA complex. Similarly, the Figure 116 show the stability of rhodium(III)-(*o*-amino TAA) with DNA at wavelength 260 nm and at wavelength 513 nm which gave the maximum absorption of *o*-amino TAA complex. The results show that rhodium(III)-(*p*-amino TAA) and rhodium(III)-(*o*-amino TAA) complexes simultaneously formed with calf thymus DNA and the absorbance of each complex and DNA remained constant (not change in the range 0.01 of the absorbance) for at least 2 hours.
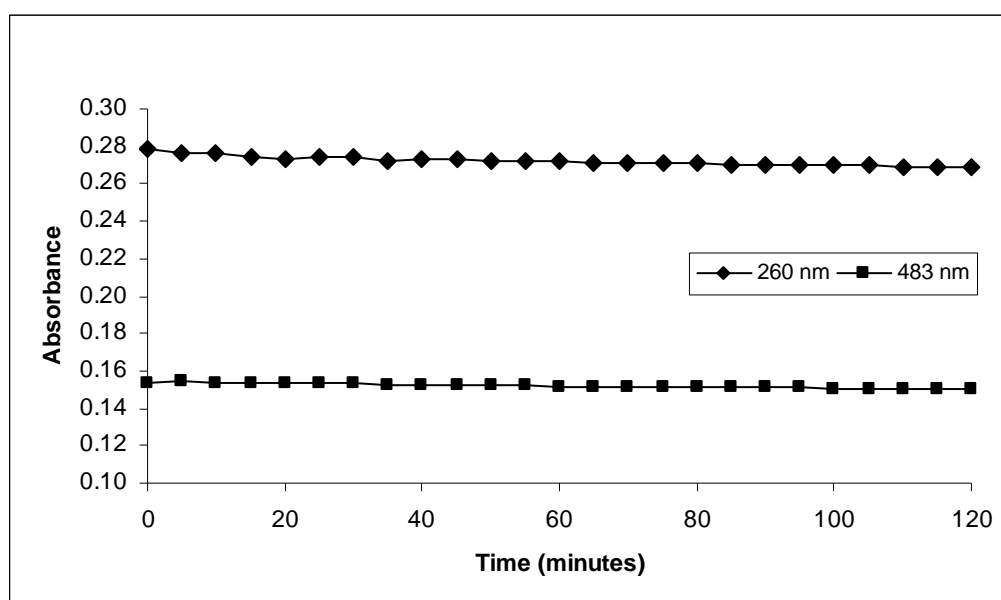
Figure 115 Relationship between absorbance of rhodium(III)-(*p*-amino TAA) complex in the presence of CT DNA and time at $\lambda = 260$ nm and $\lambda = 483$ nm.
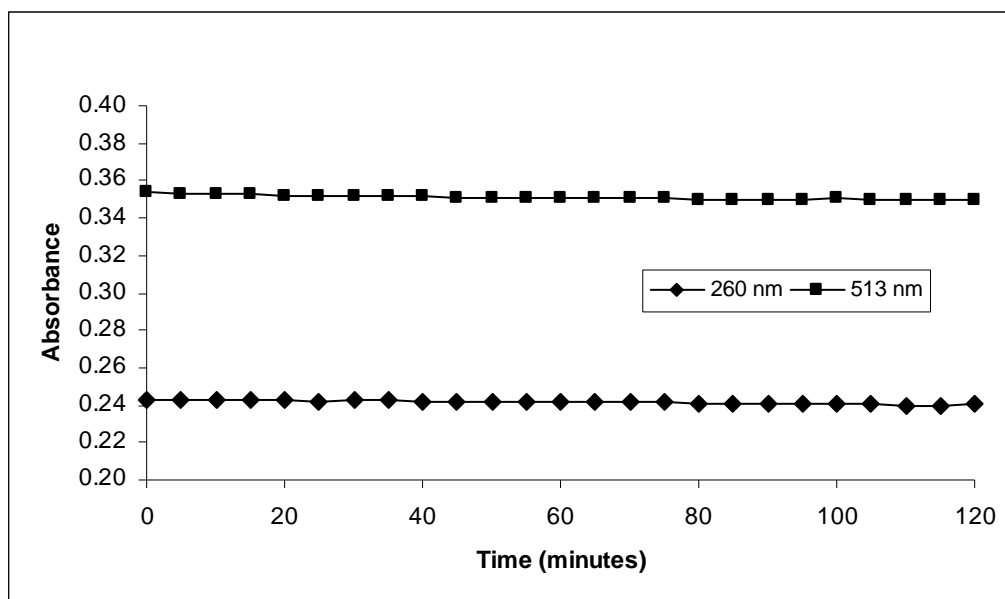
Figure 116 Relationship between absorbance of rhodium(III)-(*o*-amino TAA) complex in the presence of CT DNA and time at $\lambda = 260$ nm and $\lambda = 513$ nm.

Furthermore, the formation of rhodium(III)-(*p*-amino TAA) and rhodium(III)-(*o*-amino TAA) complexes with CT DNA after mixing for 24, 48 and 78 hours were also studied. The absorption spectra of complexes with CT DNA in tris-HCl buffer pH 7.4 are shown in Figure 117 and Figure 118.
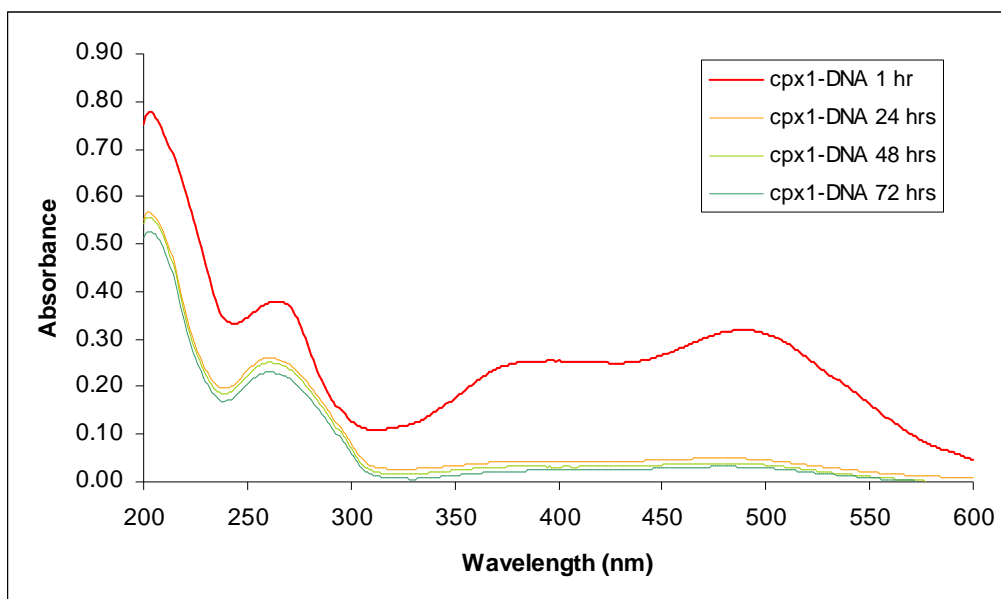
Figure 117 Absorption spectra of rhodium(III)-(*p*-amino TAA) in the presence of CT
DNA after mixing for 1, 24, 48 and 72 hours.
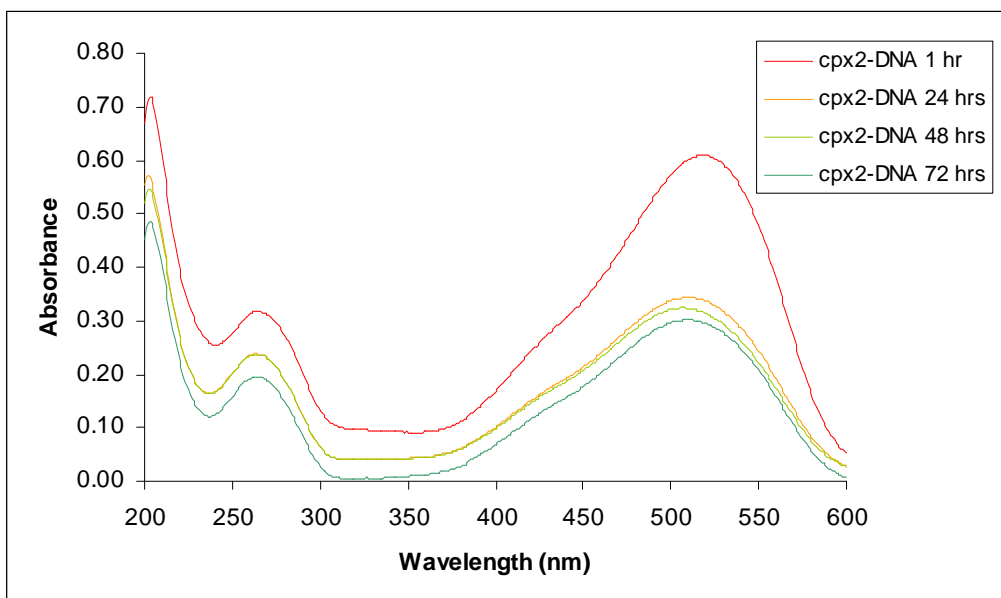
Figure 118 Absorption spectra of rhodium(III)-(*o*-amino TAA) in the presence of CT
DNA after mixing for 1, 24, 48 and 72 hours.

The absorption spectra show that the absorbance at 260 nm of DNA and the absorbance at 483 and 518 nm of rhodium(III)-(p-amino TAA) and rhodium(III)-(o-amino TAA are decrease upon the increasing of mixing time. The spectra dramatically decrease after mixing of solutions for 24 hours, after that there are slight decreases in the absorbance of both bands. The results indicate that the interaction between complexes and CT DNA is not stable under room temperature upon the increasing of time to 1 day. This might be attributed to the decomposition of complex solution by light resulting in the drops of their intensities. According with the nature of DNA, generally, CT DNA should be kept under low temperature (4°C) for preventing their denaturation. So, DNA might denatured at room temperature resulting in the decrease of absorbance at 260 nm assigned for DNA.

Furthermore, the spectra also show slight bathochromic shifts (red shifts) for both bands of complexes-DNA after mixing for 1 hour up to 24 hours, after that the maximum wavelengths remain constant. These results can confirm the loss of their stabilities upon the increasing of time.

14.4 Calculation for the stabilization energy between rhodium(III)-(p-amino TAA) complex and nucleobases

The interaction between rhodium(III)-(p-amino TAA) complex and nucleobase was studied by quantum chemical calculation via the Gaussian03 program with density functional theory (DFT) and B3LYP correlation function. The optimized structure of rhodium(III)-(p-amino TAA) complex which has the lowest formation energy, $trans$-[Rh(p-TAA-n)$_2$(Cl)$_2$]$^{+}$ as shown in Figure 86, was used as the starting of complex formation with adenine and guanine bases. In order to form bond with DNA base, one of the donor atom of the complex has to dissociate from rhodium(III) ion to give five coordinated intermediate complex. Therefore, the structure of five coordinated structure of the starting complex was optimized. One chloride ion was removed from $trans$-[Rh(p-TAA-n)$_2$(Cl)$_2$]$^{+}$ (Figure 119) due to the longest distance between this donor atom and rhodium(III) ion in complex. Then, adenine and guanine were inserted to the available site of each complex. The donor atoms of adenine and

guanine were chosen from the free nitrogen of A–T and C–G base pairs as shown in Figure 120 and Figure 121, respectively. The optimized structures of complexes bound with DNA bases are shown in Figure 122 and Figure 123. The stabilization energy of all compounds is shown in Table 32.
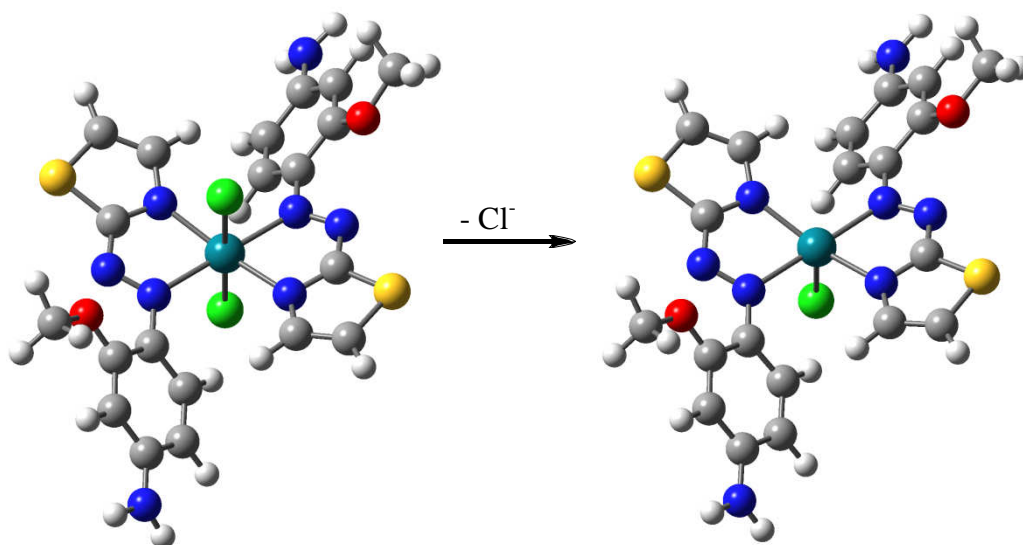
Figure 119 The five coordinated complex of *trans*-[Rh(*p*-TAA-n)$_2$(Cl)$_2$]$^+$ by removing Cl ion.
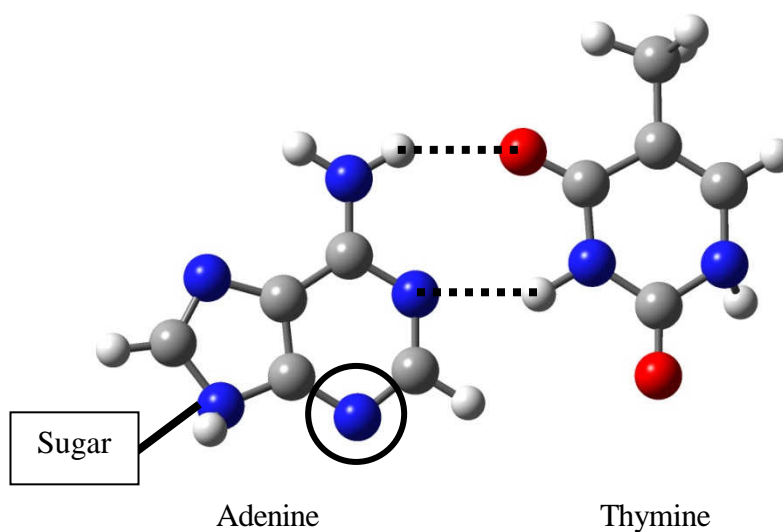
Figure 120 The available donor atom of adenine base (the nitrogen atom in a circle).
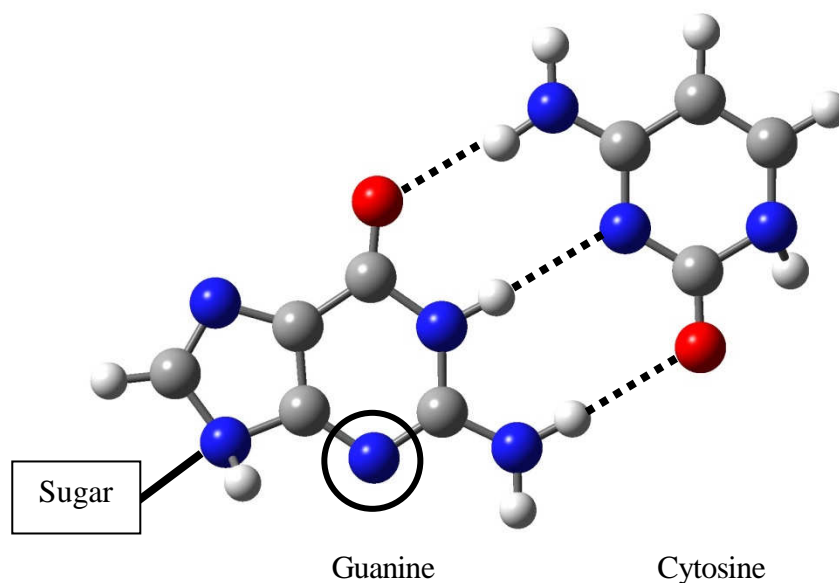
Figure 121 The available donor atom of guanine base (the nitrogen atom in a circle).

The chosen donor atoms of adenine and guanine bases were nitrogen as shown in Figure 120 and Figure 121, respectively. For adenine, the other two nitrogen atoms in six membered ring form double hydrogen bonds with thymine base (Wade, 1999). The other nitrogen atom in five membered ring is screened by deoxyribose sugar and phosphate group. For guanine, an oxygen and two nitrogen atom in six membered ring form triple hydrogen bonds with cytosine base (Wade, 1999). The other nitrogen atom is also screened by deoxyribose sugar and phosphate group.
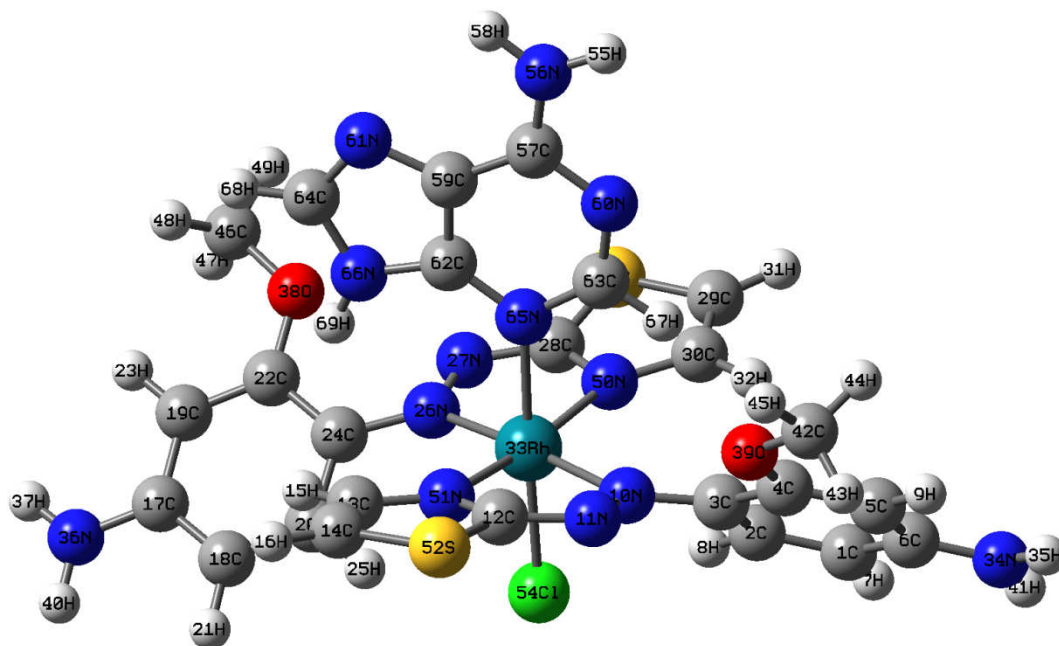
Figure 122 The optimized structure of *trans*-[Rh(*p*-TAA-n)$_2$(Cl)]$^{2+}$ bonding with adenine
base.
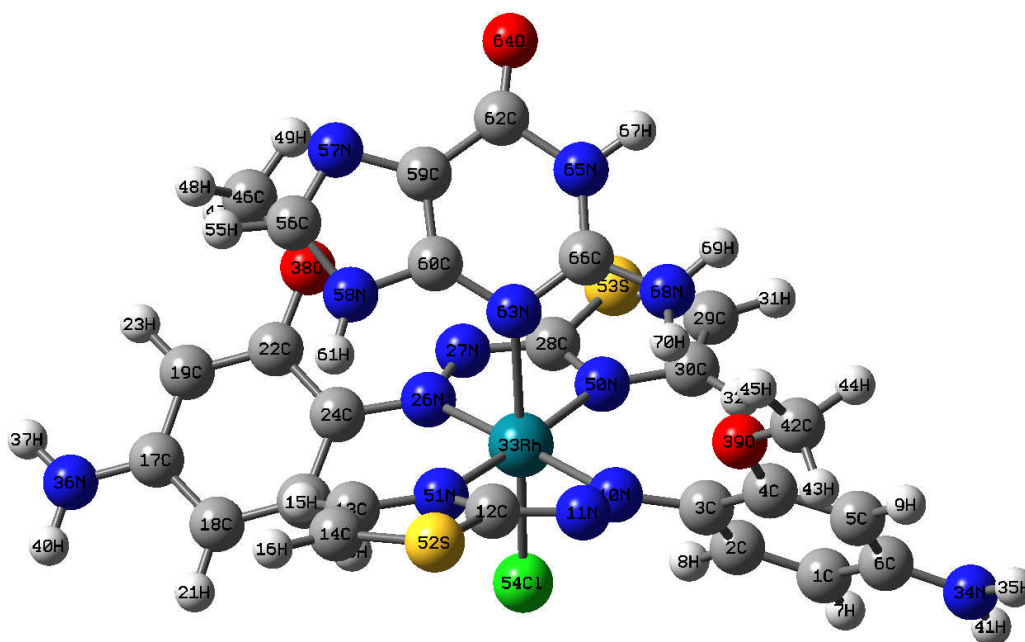
Figure 123 The optimized structure of *trans*-[Rh(*p*-TAA-n)$_2$(Cl)]$^{2+}$ bonding with guanine
base.

Table 32 Energies of atoms, molecules, adenine base, guanine base, and compound of
trans-[Rh(*p*-TAA-n)$_2$Cl]$^{2+}$ with adenine and guanine base obtained by the
calculation on Gaussian03 at B3LYP level of theory using 6-31G* and SDD
basis sets.

Atoms, molecules and complexes	Energy (a.u.)	Stabilization Energy (a.u.)	Stabilization Energy (kcal/mol)
Atoms and molecules			
Rh(III)	-108.26190	-	-
Cl$^-$	-460.25223	-	-
p-amino TAA	-1079.43408	-	-
Compounds			
Adenine base	-467.29017	-	-
Guanine base	-542.50466	-	-
trans-[Rh(*p*-TAA-n)$_2$(Cl)$_2$]$^+$	-3189.78706	-2.15254	-1350.72
trans-[Rh(*p*-TAA-n)$_2$Cl]$^{2+}$	-2729.23238	-1.85009	-1160.93
trans-[Rh(*p*-TAA-n)$_2$Cl]$^{2+}$–A*	-3196.60950	-1.93704	-1215.49
trans-[Rh(*p*-TAA-n)$_2$Cl]$^{2+}$–G**	-3271.81276	-1.92581	-1208.45

According to the structure of the five coordinated complex, *trans*-[Rh(*p*-TAA-n)$_2$Cl]$^{2+}$ has the higher energy and available space for the nucleobase. This is due to the bidentate character and the orientation of *p*-amino TAA as described in the previous section. The energies of nucleobase binding studies as collected in Table 32 show that all binding compounds have larger stabilization energies than its parent six coordinated complex. The results also show that *trans*-[Rh(*p*-TAA-n)$_2$Cl]$^{2+}$–Adenine with the stabilization energy of -1215.49 kcal/mol is more stable than *trans*-[Rh(*p*-TAA-n)$_2$Cl]$^{2+}$–Guanine with the stabilization energy of -1208.45 kcal/mol.

This is probably due to the structures of the nucleobases. Adenine base has three nitrogen atoms in the pyrimidine ring (six membered ring) and two nitrogen atoms in the imidazole ring (five membered ring). Similarly, guanine base has two nitrogen atoms in the imidazole ring and three nitrogen atoms in the pyrimidine ring with one extra oxygen atom. As the nitrogen donor atom is in the six membered ring as shown in Figure 120 and Figure 121, consequently, the electron density in the pyrimidine ring of the guanine is lower than the adenine due to the electron withdrawing character of the oxygen atom. Therefore, nitrogen atom of adenine base can act as donor atom better than nitrogen atom of guanine. So the chemical bond between adenine and the complex is stronger than the bond between a guanine and the complex. Another reason may be because the structure of adenine in complex is perpendicular to the plane as shown in Figure 124 which unlikely to occur in guanine. The geometric structure of *trans*-[Rh(*p*-TAA-n)$_2$Cl]$^{2+}$–Guanine shows that guanine base bends and gets close to *p*-amino TAA ligand of complex. This might cause the repulsion between *p*-amino TAA and guanine resulting in the higher stabilization energy and more steric in their compound. So, if the interaction occurs via the dissociation of chloride ion and replacing by nitrogen atom of each base, *trans*-[Rh(*p*-TAA-n)$_2$Cl]$^{2+}$–Adenine will be the most stable structure for this formation.

(i)   (ii)
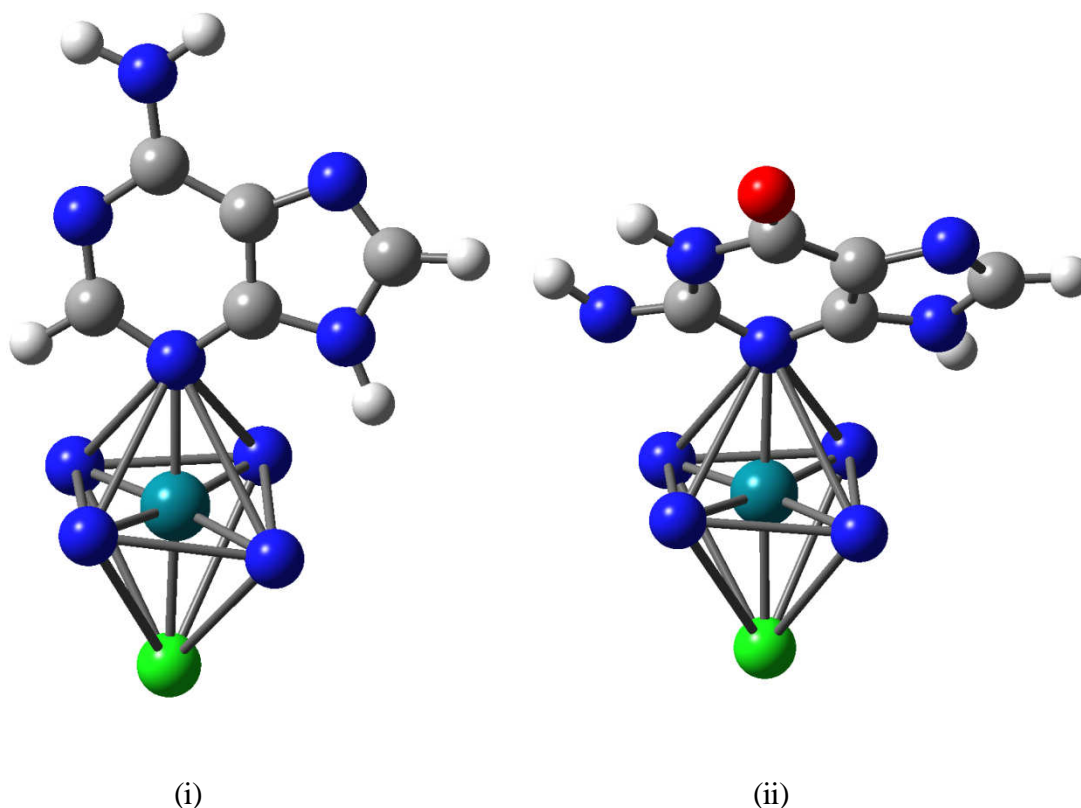
Figure 124 The geometric structures of *trans*-[Rh(*p*-TAA-n)$_2$(Cl)]$^{2+}$ bonding with (i)
adenine and (ii) guanine bases.

From Table 32, the stabilization energies of *trans*-[Rh(*p*-TAA n)$_2$Cl]$^{2+}$–
Adenine and *trans*-[Rh(*p*-TAA-n)$_2$Cl]$^{2+}$–Guanine are -1215.49 and -1208.45 kcal/mol
which larger than its parent six coordinated complex, *trans*-[Rh(*p*-TAA-n)$_2$(Cl)$_2$]$^+$
with the stabilization energy of -1350.72 kcal/mol. The results from total energies of
six coordinated complex with free base, five coordinated complex with free base and
chloride ion and the complex-nucleobases binding with chloride ion are shown in
Figure 125 and gave the information as well. This is indicated that the interaction
between rhodium(III)-(*p*-amino TAA) complex and DNA cannot occur via the
dissociation of chloride ion and replacing by nitrogen atom of each base. This might
be attributed to the stronger interaction between positive charge of rhodium(III) ion
and negative charge of chloride ion in comparison to ligands which are neutral
molecules such as these nucleobases. This might be also due to the larger sizes of
nucleobases for replacing the position of chloride ion. So, it was implied that this

interaction could occur via other mechanisms or mode of binding. On one side of the possible interaction is that chloride ion was replaced by other neutral ligands as well as nucleobases which had similar sizes to chloride ion such as water molecule then the neutral ligand was replaced by molecule of adenine or guanine. The other side of the possible interaction is that the complex could be bound to CT DNA by the intercalative mode which involved the insertion of a planar of aromatic ring system between the DNA base pairs (Efthimiadou, 2007).
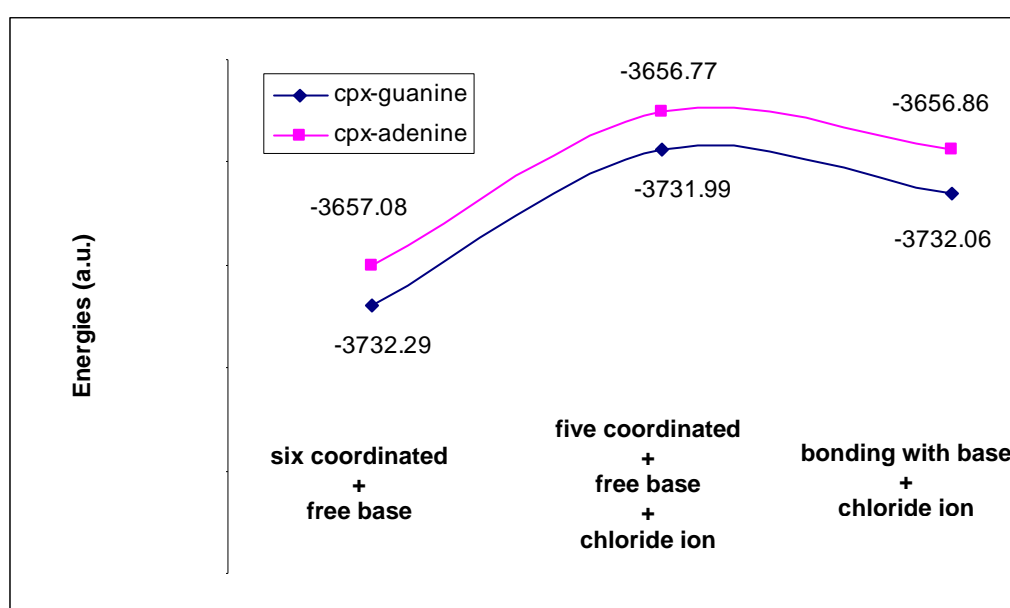
Figure 125 The total energies of six coordinated complex with free base, five coordinated complex with free base and chloride ion and the complex-nucleobases binding with chloride ion.

According to the experimental study which described in the previous section, the changes in UV-Vis spectra was probably resulted from the interaction between rhodium(III)-(*p*-amino TAA) complex and CT DNA but this interaction did not occur via the dissociation of chloride ion and replacing by nitrogen atom of each nuclelobase. This interaction could be spontaneous reaction via other mechanisms or mode of binding as mentioned above. To determine the accurately binding character between CT DNA and the complex, the more appropriate condition and other

techniques should be used for the experiment and high level of method and correlation function should be used for the quantum chemical calculations in further studies.

CONCLUSION

The structural isomer of thiazolylazo dyes, 2-(2´-thiazolylazo)-5-aminoanisole (*p*-amino TAA) and 4-(2´-thiazolylazo)-3-aminoanisole (*o*-amino TAA) were synthesized by diazotization of 2-aminothiazole and coupling with *m*-anisidine. From our knowledge, *o*-amino TAA has never been synthesized before. The components of a mixture product were separated by flash column chromatography and purified by recrystallization which gave *p*-amino TAA as red needles-shaped crystals and *o*-amino TAA as green needles-shaped crystals. The higher melting point of *o*-amino TAA in comparison to that of *p*-amino TAA might be attributed to the intramolecular hydrogen bonding in *o*-amino TAA structure. Each compound was characterized by FT-IR, ^{1}H NMR, mass spectroscopy and elemental analysis. The results of these methods indicated that the synthesized products were *p*-amino TAA and *o*-amino TAA. The acid dissociation constants (pK_a) of these compounds were determined by UV-Vis spectroscopy with two methods, half-height and limiting absorbance methods. The pK_a values of *p*-amino TAA and *o*-amino TAA from both methods were 3.0 and 3.3, respectively.

The complexes formation between rhodium(III) and platinum(IV) with these ligands were studied. The optimize condition for the formation of rhodium(III)-(*o*-amino TAA), platinum(IV)-(*p*-amino TAA) and platinum(IV)-(*o*-amino TAA) complexes were at pH 3, the formation of rhodium(III)-(*p*-amino TAA) was at pH 5. The stoichiometric studies verified by continuous variation and mole ratio methods showed that the ratio of rhodium(III) with both ligands and platinum(IV) with *o*-amino TAA were 1:2 with the stability constants in the range of 10^9 to 10^{10} while the ratio between platinum(IV) and *p*-amino TAA was 1:1 with the stability constant in the order of 10^5. The complexes of rhodium(III) were prepared by keeping the solution of these ligands and RhCl$_3$·xH$_2$O under reflux which gave dark-brown product of rhodium(III)-(*p*-amino TAA) and black product of rhodium(III)-(*o*-amino TAA). The structures of the complexes were determined by FT-IR and ^{1}H NMR spectroscopy.

According to Job's method, the optimized structure of rhodium(III)-(p-amino TAA) which had the highest stability constant, 3.59×10^{10}, was determined by theoretical calculation optimized by using the 6-31G* and SDD basis sets at B3LYP level of theory. Fourteen octahedral structures of complex between rhodium(III) and p-amino TAA were proposed. The ligand, p-amino TAA, acted as tridentate ligand by using nitrogen or sulfur atom of thiazole ring, nitrogen atom of azo group and oxygen atom of –OCH$_3$ group as donor atoms. The ligand acted as bidentate ligand by using nitrogen atom of azo group and different donor atoms, namely, nitrogen atom of thiazole ring, sulfur atom of thiazole ring, and oxygen atom of –OCH$_3$ group. Due to the octahedral structure of rhodium(III)-(p-amino TAA) complex, Cl$^-$ from starting material, RhCl$_3$·xH$_2$O, and H$_2$O were two potential ligands in the complex formation of p-amino TAA as bidentate ligand. Furthermore, geometric isomers, *cis* and *trans*, were also proposed. The geometric parameters; bond lengths, bond angles and torsion angles of the all optimized structures were selected to describe the stability and the orientation of atoms in each complex. It was found that *trans*-[Rh(p-TAA-n)$_2$(Cl)$_2$]$^+$ was the most stable complex with the stabilization energy -1350.72 kcal/mol.

Binding of CT DNA with rhodium(III)-(p-amino TAA) and rhodium(III)-(o-amino TAA) were studied by UV-Vis spectroscopy. The results showed the changes in UV-Vis spectra which possibly resulted from the interaction between *trans*-[Rh(p-TAA-n)$_2$(Cl)$_2$]$^+$ complex and CT DNA. The results from quantum chemical calculations showed that if the interaction occurred via the dissociation of chloride ion and replacing by nitrogen atom of each base, *trans*-[Rh(p-TAA-n)$_2$Cl]$^{2+}$–Adenine would be the most stable structure for this complex formation. On the other hand, the results from quantum chemical calculations also showed that the interaction did not occur via this mechanism which was due to the stabilization energies of *trans*-[Rh(p-TAA-n)$_2$Cl]$^{2+}$–Adenine and *trans*-[Rh(p-TAA-n)$_2$Cl]$^{2+}$ –Guanine which larger than its parent six coordinated complex, *trans*-[Rh(p-TAA-n)$_2$(Cl)$_2$]$^+$. So, this interaction could be spontaneous reaction via other mechanisms or mode of binding. To determine the accurately binding character between CT DNA and the complex, the more appropriate condition and other techniques should be used

for the experiment and high level of method and correlation function should be used for the quantum chemical calculations in further studies.

LITERATURE CITED

Abildgaard, J., P. E. Hensen, J. Josephsen, K. V. Hansen, H. O. SØrensen and S. Larsen. 2006. Synthesis and characterization of nickel-, palladium- and platinum(II) complexes of three *o,o´*-dihydroxydiarylazo dyes: Determination of the coordination geometry of this comprehensive series of tridentate diaryl dye complexes by combining results from NMR and X-ray experiments with theoretical *ab* initio calculations. **Inorg. Chim. Acta.** 359: 4493–4502.

Ahlstrom, L., C. S. Eskilsson and E. Bjorklund. 2005. Determination of banned azo dyes in consumer goods. **Trends Anal. Chem.** 24: 49-56.

Alder, M. J., W. I. Crose, K. R. Flower and R. G. Pritchard. 1999. Azo-containing phosphine complexes of palladium(II) and platinum(II) and their effectiveness in the Heck reaction: crystal and molecular structure of $[PdCl_2\{PPh_2\{1-(4-MeC_6H_4N_2)-2-OC(O)Me-C_{10}H_5\}]\cdot2EtOH$. **J. Organomet. Chem.** 590: 123–128.

Allardyce, C.S. and P.J. Dyson. 2001. Ruthenium in Medicine: Current Clinical Uses and Future Prospects. **Platinum Met. Rev.** 45(2): 62-69.

Andre, E., J. P. Cornard and C. Lapouge. 2007. Characterization of the Al(III) binding site of protocatechuic acid by electronic spectroscopy and quantum chemical calculations. **Chem. Phys. Lett.** 434: 155–159.

Bartak, P., D. Pechova, P. Tarkowski, P. Bednar, M. Kotoucek, Z. Stransky and R. Vespalec. 2000. Determination of the first dissociation constant of 6-benzylaminopurine A comparison of methods. **Anal. Chim. Acta.** 421: 221–229.

Basu, S., S. Halder, I. Pal, S. Samanta, P. Karmakar, M. G.B. Drew and S. Bhattacharya. 2008. 1-(2'-Pyridylazo)-2-naphtholate complexes of

ruthenium: Synthesis, characterization, and DNA binding properties. **Polyhedron.** 27: 2943–2951.

Benesi, H.A. and J.H. Hildebrand. 1949. A spectrophotometric investigation of the interaction of iodine with aromatic hydrocarbons. **J. Am. Chem. Soc.** 70: 2703-2707.

Brabec, V. and O. Nováková. 2006. DNA binding mode of ruthenium complexes and relationship to tumor cell toxicity. **Drug Resist. Update.** 9(3): 111-122.

Burda, J. V., J. Gu. 2008. A computational study on DNA bases interactions with dinuclear tetraacetato-diaqua-dirhodium(II,II) complex. **J. Inorg. Biochem**. 102: 53–62.

Castro, G.T. and S. E. Blanco. 2004. Structural and spectroscopic study of 5, 7-dihydroxy-flavone and its comlpex with aluminum. **Spectrochim. Acta, Part A.** 60: 2235–2241.

Chen, W., Y. Wu, D. Gu and F. Gan. 2007. Synthesis, optical and thermal characterization of novel thiazolyl heterocyclic azo dye. **Mater. Lett.** 61: 4181–4184.

Connors, K.A. 1987. **Binding Constants.** John Wiley and Sons, Inc., New York.

Deng, H. H. Xu, Y. Yang, H. Li, H. Zou, L. H. Qu and L. N. Ji. 2003. Synthesis, characterization, DNA-binding and cleavage studies of $[Ru(bpy)_2(actatp)]^{2+}$ and $[Ru(phen)_2(actatp)]^{2+}$ (actatp = acenaphthereno[1,2-*b*]-1,4,8,9-tetraazariphenylence). **J. Inorg. Biochem.** 97: 207–214.

Efthimiadou, E. K., N. Katsaros, A. Karaliota, and G. Psomas. 2007. Mononuclear copper(II) complexes with quinolones and nitrogen-donor heterocyclic

ligands: Synthesis, characterization, biological activity and interaction with DNA**. Inorg. Chim. Acta.** 360: 4093–4102.

El-Gogary, T.M. and G. Koehler. 2007. Interaction of psoralens with DNA-bases (I). An ab initio quantum chemical, density functional theory and second-order MØller–Plesset perturbational study. **J. Mol. Struct.** 808: 97–109.

El-Shazly, R. M., G. A. A. Al-Hazmi and S. E. Ghazy. 2005. Spectroscopic, thermal and electrochemical studies on some nickel(II) thiosemicarbazone complexes. **Spectrochim. Acta, Part A.** 61: 243–252.

Ertan, N. and P. Gürkan. 1997. Synthesis and Properties of some Azo Pyridone Dyes and their Cu(ll) Complexes. **Dyes Pigm.** 33(2): 137-147.

Fan, X. and C. Zhu. 1998. Syntheses of Three New Benzoic Acid-Type Thiazolylazo Reagents and Their Application to Spectrophotometric Determination of Microamounts of Nickel. **Microchem. J.** 59: 284–293.

Gao, J., J. H. Reibenspies and A. E. Martell. 2003. S ynthesis and DNA binding properties of a cationic 2,29:69,20-terpyridine cobalt(II) complex containing an oligopeptide. **J. Inorg. Biochem.** 94: 272–278.

Garza-Ortiz A., H. Dulk, J. Brouwer, H. Kooijman, A. L. Spek and J. Reedijk. 2007. The synthesis, chemical and biological properties of dichlorido(azpy)gold(III) chloride (*azpy* = 2-(phenylazo)pyridine) and the gold-induced conversion of the *azpy* ligand to the chloride of the novel tricyclic pyrido[2,1-*c*][1,2,4]benzotriazin-11-ium cation. **J. Inorg. Biochem**. 101: 1922–1930.

Georgiadou, K.L. and E.G. Tsatsaroni. 2001..Synthesis, characterisation and application of disperse dyes derived from N-2-hydroxyethyl-1-naphthylamine. **Dyes and Pigments.** 50: 93–97.

_____ and _____ . 2002. Hetarylazo disperse dyes derived from substituted *N,N*-bis-β-hydroxy- and *N,N*-bis-β-acetoxy-ethylaniline. **Dyes Pigm.** 53: 73–78.

Glasel, J.A. 1995. Validity of Nucleic Acid Purities Monitored by A260/A280 Absorbance Ratios. **Biotechniques.** 18(1): 62-63.

Greenwood, N.N. and A. Earnshaw. 1997. **Chemistry of the elements.** 2nd ed. Butterworth-Heinemann, Oxford.

Gu, Q., Q. B. Lin, Y. J. Liu, X. Y. Le and X. L. Feng. 2008. Synthesis, Characterization, and DNA Binding Properties of Dinuclear Copper(II) Complex [[Cu$_2$(TATP)$_2$(*L*-Leu)(ClO$_4$)$_2$]$_2$·2H$_2$O. **Chem. Res. Chin. Univ.** 24(4): 401-406.

Hao, Y. M. and H. X. Shen. 2000. Spectrophotometric determination of nucleic acids using palladium(II) complex with 2-(5-bromo-2-pyridylazo)-5-diethylaminophenol. **Anal. Chim. Acta.** 413: 87–94.

Ibrahim, S. A., N. M. Rageh, A. A. Mohamad and Y. H. Ebead. 1999. Medium Effect on the Acid Dissociation Constants of Some Heterocyclic Compounds. **J. Chem. Eng. Data.** 44: 451-455.

Kaim, W., N. Doslik, S. Frantz, T. Sixt, M. Wanner, F. Baumann, G. Denninger, H. J. Kümmererb, C. Duboc-Toia, J. Fiedler and S. Zalis. 2003. Azo compounds as electron acceptor or radical ligands in transition metal species: spectroelectrochemistry and high-field EPR studies of ruthenium, rhodium and copper complexes of 2,2′-azobis(5-chloropyrimidine). **J. Mol. Struct.** 656: 183–194.

Karet, F. and N. Ertan. 2002. Hetarylazo disperse dyes derived from 3-methyl-1-(3′,5′-dipiperidino-s-triazinyl)-5-pyrazolone as coupling Component. **Dyes Pigm.** 55: 99–108.

Karet, F. and N. Ertan. 2005. Synthesis of some novel hetarylazo disperse dyes derived from 4-hydroxy-2H-1-benzopyran-2-one (4-hydroxycoumarin) as coupling component and investigation of their absorption spectra. **Dyes Pigm.** 64: 243-249.

Kashanian, K.*,* M.B. Gholivand, F. Ahmadia, A. Taravati and A. H. Colagar. 2007. DNA interaction with Al–*N*,*N*'-bis(salicylidene)2,2'-phenylendiamine complex. **Spectrochim. Acta, Part A.** 67: 72–478.

Kirschner, K. N., M. Lee, R.C. Stanley and J. P. Bowen. 2000. Density Functional and Ab Initio Studies on N-Acetyl Duocarmycin SA: Insight Into Its DNA Interaction Properties. **Bioorg. Med. Chem.** 8: 329-335

Lemos, V.A., E.S. Santos, M.S. Santos, and R.T. Yamaki. 2007. Thiazolylazo dyes and their application in analytical methods. **Microchim. Acta.** 158: 189-204.

Lihong, W., T. Fulong. 1996. Synthesis and Characterization of 2-(2-Thiazolylazo)-5-[(*N*,*N*-dicarboxymethyl) amino]Benzoic Acid and Its Application to Spectrophotometry Determination of Microamounts of Palladium in Catalysts. **Microchem. J.** 53: 349–355.

Liu, X. G., Y. Q. Feng, Y. Zhao, H. L. Chen and X. G. Li. 2007. Synthesis, characterization and spectroscopic investigation of azo-porphyrins. **Dyes Pigm.** 75: 413-419.

Machura, B.,A. S. witlicka, R. Kruszynski, J. Kusz and R. Penczek. 2008. Synthesis, spectroscopic characterization, X-ray structure and DFT calculations of five-coordinated chlorocopper(II) complex with bis(3,5-dimethylpyrazol-1-yl)methane. **Polyhedron.** 27: 2513–2518.

Mansouri, G., A. R. Rezvan, H. Hadadzadeh, H. R. Khavasi and H. Saravani. 2007.

Cyclometalated rhodium(III) complex with phen-dione ligand. **J. Organomet. Chem.** 692: 3810–3815.

Maradiya, H. R. and V. S. Patel. 2001. Synthesis and Dyeing Performance of Some Novel Heterocyclic Azo Disperse Dyes. **J. Braz. Chem. Soc.** 12(6): 710-714.

Masoud, M. S., M. A. Mostafa, R. H. Ahmed and N. H. Abd El Moneim. 2003. Structures and Chemical Equilibria of Some N-Heterocycles Containing Amide Linkages. **Molecules.** 8: 430-438.

Matsui, M., M. Kushida, K. Funabiki, K. Shibata, H. Muramatsu, K. Hirota, M. Hosoda and K. Tai. 1998. Second-order Optical Nonlinearity of Thiazolylazo Chromophores Containing Hydroxyl Groups. **Dyes Pigm.** 37(4): 283-289.

Messori, L., P. Orioli, C. Tempi and G. Marcon. 2001. Interactions of Selected Gold(III) Complexes with Calf Thymus DNA. **Biochem. Biophys. Res. Commun.** 281: 352–360.

Miessler, G.L. and D.A. Tarr. 2004. **Inorganic Chemistry.** 3rd ed. Pearson Education International, New Jersey.

Mitchell, R.C., C. J. Salter and K. Y. Tam. 1999. Multiwavelength spectrophotometric determination of acid dissociation constants Part III. Resolution of multi-protic ionization systems. **J. Pharm. Biomed. Anal.** 20: 289–295.

Nair, R. B., E. S. Teng, S. L. Kirkland and C. J. Murphy. 1998. Synthesis and DNA-Binding Properties of $[Ru(NH_3)_4dppz]^{2+}$. **Inorg. Chem.** 37: 139-141.

Nonoyama, M. and K. Nakajima. 1999. Cyclometallation 2-(2-pyridyl)benzeo[b]furan and 1-(2-pyridyl and 2- pyrimidyl)indole with

palladium(II) and rhodium(III). Structures of unexpectedly formed nitro palladium(II) complexes. **Polyhedron.** 18: 533-543.

Perez-Urquiza, M. and J.L. Beltran. 2001. Determination of the dissociation constants of sulfonated azo dyes by capillary zone electrophoresis and spectrophotometry methods. **J. Chromatogr., A.** 917: 331–336.

Perigic-Janjic, N. U., A. A. Muk and V. D. Canic. 1973. Reaction of Lanthanum with Reagent Arsenazo-*p*-NO$_2$. **Anal. Chem.** 45(4): 798-801.

Rauth, G. K., S. Pal, D. Das, C. Sinha, A. M.Z. Slawin and J. D. Woollins. 2001. Synthesis, spectral characterization and electrochemical studies of mixed-ligand complexes of platinum(II) with 2-(arylazo)pyridines and catechols. Single-crystal X-ray structure of dichloro{2-(phenylazo) pyridine}platinum(II). **Polyhedron.** 20: 363–372.

Razus, A. C., L. Birzan, M. Cristea, V. Tecuceanu, L. Blanariu and C. Enache. 2009. Novel mono- and bis-azo dyes containing the azulen-1-yl moiety: Synthesis, characterization, electronic spectra and basicity. **Dyes Pigm.** 80: 337–342.

Ren, L., G. Y. Li, X. Hu, X. L. Xia, J. R. Shenb and D. M. Jiab. Synthesis and characterization of fluoronitroaryl azo diaminobenzene chromophores. **Tetrahedron Lett.** 46: 1511–1513.

Senapoti, S., S. Jasimuddin, G. Mostafa, T.-H. Lu and C. Sinha. 2006. Coupling of arylamine with coordinated arylazopyrimidine in platinum(II) complexes. Single crystal X-ray structure,spectra and electrochemistry. **Polyhedron.** 25: 1571–1578.

Steyl, G. 2007. Synthesis, structure and theoretical study of two rhodium(I) complexes [Rh(TropNMe)(CO)(PPh$_3$)] and [Rh(Trop)(CO)(PPh$_3$)]·Acetone. **Polyhedron.** 26: 5324–5330.

Sun, J., S. Wub, Y. An, J. Liu, F. Gao, L. N. Ji and Z. W. Mao. 2008. Synthesis, crystal structure and DNA-binding properties of ruthenium(II) polypyridyl complexes with dicationic 2,2′-dipyridyl derivatives as ligands. **Polyhedron.** 27: 2845–2850.

Szymczyk, M., A. El-Shafei and H. S. Freeman. 2007. Design, synthesis, and characterization of new iron-complexed azo dyes. **Dyes Pigm.** 72: 8-15.

Teimouri, A., A. N. Chermahini and M. Emami. 2008. Synthesis, characterization, and DFT studies of a novel azo dye derived from racemic or optically active binaphthol. **Tetrahedron.** 64: 11776–11782.

Ucun, F., A. Saglam, I. Kara and F. Karcı. 2008. Investigation of ground state tautomeric form of a heterocyclic disazo dye derived from barbituric acid by ab initio Hartree–Fock and density functional theory calculations. **J. Mol. Struct. : THEOCHEM.** 868: 94–100.

Wade, L.G. 1999. **Organic Chemistry.** 4th ed. Prentice Hall International, New Jersey.

Wang, M., K. Funabiki and M. Matsui. 2003. Synthesis and properties of bis(hetaryl)azo dyes. **Dyes Pigm.** 57: 77–86.

Wang, X. L., J. N. Fang, Y. F. Bi, H. Y. Lin and G. C. Liu. 2008. Synthesis, DNA-binding, and Photocleavage of 2,3-Di-2-pyridylquinoxaline-silver(I) Complex. **Chem. Res. Chin. Univ.** 24(1): 15-19.

Wojciechowska, M., G. Wojciechowski and W. Wasiak. 2003. Spectroscopic and semiempirical studies of the phototropic species of 8-amino-5,8'-azo-bis-naphthalene-2-sulphonic acid. **J. Mol. Struct.** 658: 125–133.

Wu, J. Z., G. Yang, S. Chen, L. N. Ji, J. Y. Zhou and Y. Xu. 1998. Intercalation into calf thymus DNA of 2-(4-arylphenyl)imidazo [4,5-f]-[1,10] phenanthroline (aryl =-OMe,-NMe2 or-NO2) in its bipyridyl ruthenium(II) complex. **Inorg. Chim. Acta.** 283: 17-23.

Yazdanbakhsh, M.R., A. Ghanadzadeh and E. Moradi. 2007. Synthesis of some new azo dyes derived from 4-hydroxy coumarin and spectrometric determination of their acidic dissociation constants**. J. Mol. Liq.** 136: 165–168.

APPENDICES

APPENDIX A

Calculation of the percentage of elements of *p*-amino TAA and *o*-amino TAA

Molecular formula of both p-amino TAA and o-amino TAA which are structural isomer are $C_{10}H_{10}ON_4S$. From molecular weight of p-amino TAA and o-amino TAA (234.28 g/mol), the percentage of elements of p-amino TAA and o-amino TAA can be determined as followed:

Percentage of carbon

$$= \frac{\text{number of carbon} \times \text{atomic weight of carbon}}{\text{Molecular weight of TAA}} \times 100$$

$$= \frac{10 \times 12.011}{234.28} \times 100$$

$$= 51.28 \, \%$$

Percentage of hydrogen

$$= \frac{\text{number of hydrogen} \times \text{atomic weight of hydrogen}}{\text{Molecular weight of TAA}} \times 100$$

$$= \frac{10 \times 1.008}{234.28} \times 100$$

$$= 4.29\%$$

Percentage of nitrogen

$$= \frac{\text{number of nitrogen} \times \text{atomic weight of nitrogen}}{\text{Molecular weight of TAA}} \times 100$$

$$= \frac{4 \times 14.007}{234.28} \times 100$$

$$= 23.91\%$$

Percentage of sulfur

$$= \frac{\text{number of sulfur} \times \text{atomic weight of sulfur}}{\text{Molecular weight of TAA}} \times 100$$

$$= \frac{1 \times 32.066}{234.28} \times 100$$

$$= 13.69\%$$

Percentage of oxygen $= \dfrac{\text{number of oxygen} \times \text{atomic weight of oxygen} \times 100}{\text{Molecular weight of TAA}}$

$= \dfrac{1 \times 15.999 \times 100}{234.28}$

$= 6.83\%$

APPENDIX B

Determination of the acid dissociation constants by Half Height Method

At a constant wavelength, the pK value of the compound can be evaluated (where half of the compound exists in the ionized form and the other half in the nonionized form). It is known that:

$$pH = pK + \log \gamma + \log \frac{As}{As_{max} - As}$$

(γ = activity coefficient term and controlled by ionic strength of a supporting electrolyte)

Where As is the absorbance of the solution at given pH; As_{max} the absorbance of the solution when the total amount of reagent is in form H_nA.

The relationship between pH (x-axis) and $\log \dfrac{As}{As_{max} - As}$ (y-axis) were plotted at various wavelengths which selected from the range of wavelength that showed the maximum difference of absorption between low pH and high pH, in the range of 510-530 nm for both p-amino TAA and o-amino TAA. The absorption at pH 2.0 is assigned for the absorbance of H_nA (As_{max}). All absorbances and log $\dfrac{As}{As_{max} - As}$ values at given pH in each wavelength are shown in Appendix Table B1 to Appendix Table B10. The pK_a was obtained from the interception of lines on pH value as shown in Figure 29 and Figure 30 of results and discussion part.

_p_-amino TAA;

Appendix Table B1 The log $\dfrac{As}{As_{max}-As}$ values at $\lambda = 510$ nm with $As_{max} = 1.5972$

pH	Absorbance	
	As	$\log \dfrac{As}{As_{max}-As}$
2.3	1.5418	1.4440
2.6	1.5468	1.4868
3.0	1.5345	1.3887
3.3	1.5091	1.2333
3.6	1.5079	1.2274
4.0	1.4347	0.9458

Appendix Table B2 The log $\dfrac{As}{As_{max}-As}$ values at $\lambda = 515$ nm with $As_{max} = 1.5801$

pH	Absorbance	
	As	$\log \dfrac{As}{As_{max}-As}$
2.3	1.5301	1.4853
2.6	1.5321	1.5034
3.0	1.5173	1.3826
3.3	1.4952	1.2455
3.6	1.4877	1.2068
4.0	1.4221	0.9541

Appendix Table B3 The log $\dfrac{As}{As_{max} - As}$ values at $\lambda = 520$ nm with $As_{max} = 1.5509$

pH	Absorbance	
	As	$\log \dfrac{As}{As_{max} - As}$
2.3	1.5055	1.5202
2.6	1.5097	1.5643
3.0	1.4913	1.3981
3.3	1.4667	1.2411
3.6	1.4587	1.1990
4.0	1.3941	0.9490

Appendix Table B4 The log $\dfrac{As}{As_{max} - As}$ values at $\lambda = 525$ nm with $As_{max} = 1.5147$

pH	Absorbance	
	As	$\log \dfrac{As}{As_{max} - As}$
2.3	1.4728	1.5461
2.6	1.4739	1.5582
3.0	1.4567	1.4003
3.3	1.4286	1.2199
3.6	1.4195	1.1735
4.0	1.3555	0.9303

Appendix Table B5 The log $\dfrac{As}{As_{max} - As}$ values at $\lambda = 530$ nm with $As_{max} = 1.4742$

pH	Absorbance	
	As	$\log \dfrac{As}{As_{max} - As}$
2.3	1.4348	1.5609
2.6	1.4324	1.5340
3.0	1.4163	1.3880
3.3	1.3832	1.1816
3.6	1.3725	1.1300
4.0	1.3088	0.8982

o-amino TAA;

Appendix Table B6 The log $\dfrac{As}{As_{max} - As}$ values at $\lambda = 510$ nm with $As_{max} = 3.5505$

pH	Absorbance	
	As	$\log \dfrac{As}{As_{max} - As}$
2.3	3.5403	2.5412
2.6	3.5433	2.6934
3.0	3.5437	2.7197
3.3	3.5469	2.9908
3.6	3.5474	3.0613
4.0	3.5473	3.0501

Appendix Table B7 The log $\dfrac{As}{As_{max} - As}$ values at $\lambda = 515$ nm with $As_{max} = 3.6648$

pH	Absorbance	
	As	$\log \dfrac{As}{As_{max} - As}$
2.3	3.6580	2.7337
2.6	3.6595	2.8386
3.0	3.6594	2.8297
3.3	3.6615	3.0401
3.6	3.6618	3.0898
4.0	3.6617	3.0668

Appendix Table B8 The log $\dfrac{As}{As_{max} - As}$ values at $\lambda = 520$ nm with $As_{max} = 3.7618$

pH	Absorbance	
	As	$\log \dfrac{As}{As_{max} - As}$
2.3	3.7574	2.9246
2.6	3.7578	2.9662
3.0	3.7572	2.9067
3.3	3.7585	3.0458
3.6	3.7587	3.0732
4.0	3.7583	3.0304

Appendix Table B9 The log $\dfrac{As}{As_{max} - As}$ values at $\lambda = 525$ nm with $As_{max} = 3.8199$

pH	Absorbance	
	As	$\log \dfrac{As}{As_{max} - As}$
2.3	3.8170	3.1112
2.6	3.8169	3.0975
3.0	3.8160	2.9863
3.3	3.8164	3.0359
3.6	3.8164	3.0363
4.0	3.8159	2.9741

Appendix Table B10 The log $\dfrac{As}{As_{max} - As}$ values at $\lambda = 530$ nm with $As_{max} = 3.8520$

pH	Absorbance	
	As	$\log \dfrac{As}{As_{max} - As}$
2.3	3.8500	3.2816
2.6	3.8496	3.1963
3.0	3.8485	3.0349
3.3	3.8481	2.9880
3.6	3.8477	2.9450
4.0	3.8468	2.8654

APPENDIX C

Determination of the acid dissociation constants by Limiting Absorbance Method

For an organic compound of formula H_nA, the first ionization for the ligand takes place as follows:
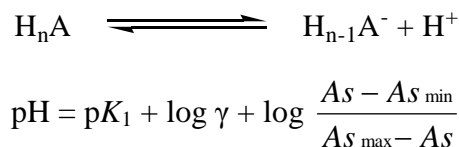
$$H_nA \rightleftharpoons H_{n-1}A^- + H^+$$

$$pH = pK_1 + \log \gamma + \log \frac{As - As_{min}}{As_{max} - As}$$

Where As is the absorbance of the solution at given pH; As_{min} is the absorbance of solution when total amount of solution is in the form H_nA and As_{max} is the absorbance of solution when total amount of solution is in the form $H_{n-1}A^-$

The relationship between pH (x-axis) and $\log \frac{As - As_{min}}{As_{max} - As}$ (y-axis) were plotted at various wavelengths which selected from the range of wavelengths that showed the highest difference of absorption between low and high pH, in the range of 505-530 nm for both *p*-amino TAA *o*-amino TAA. The absorption at pH 5.0 is assigned for the absorbance of $H_{n-1}A^-$ (As_{max}) and at pH 2.0 is assigned for the absorbance of H_nA (As_{min}) at each wavelength. All absorbance and $\log \frac{As - As_{min}}{As_{max} - As}$ values at given pH are shown in Appendix Table C1 to Appendix Table C12. The pK_a was obtained from the interception of lines on pH value as shown in Figure 31 and Figure 32 of results and discussion part.

p-amino TAA;

Appendix Table C1 The log $\dfrac{As - As_{\min}}{As_{\max} - As}$ values at $\lambda = 505$ nm with $As_{\max} = 0.9900$

and $As_{\min} = 1.5970$

pH	Absorbance	
	As	$\log \dfrac{As - As_{\min}}{As_{\max} - As}$
2.3	1.3920	-0.2924
2.6	1.2057	0.2588
3.0	1.1515	0.4407
3.3	1.0737	0.7961
3.6	1.0100	1.4678
4.0	0.9982	1.8645

Appendix Table C2 The log $\dfrac{As - As_{\min}}{As_{\max} - As}$ values at $\lambda = 510$ nm with $As_{\max} = 0.8956$

and $As_{\min} = 1.5972$

pH	Absorbance	
	As	$\log \dfrac{As - As_{\min}}{As_{\max} - As}$
2.3	1.3744	-0.3322
2.6	1.2023	0.1097
3.0	1.0757	0.4617
3.3	1.0130	0.6970
3.6	0.9280	1.3147
4.0	0.9095	1.6933

Appendix Table C3 The log $\dfrac{As - As_{\min}}{As_{\max} - As}$ values at $\lambda = 515$ nm with $As_{\max} = 0.7931$

and $As_{\min} = 1.5801$

pH	Absorbance	
	As	$\log \dfrac{As - As_{\min}}{As_{\max} - As}$
2.3	1.3560	-0.4000
2.6	1.1874	-0.0018
3.0	1.0010	0.4451
3.3	0.9209	0.7127
3.6	0.8346	1.2543
4.0	0.8146	1.5523

Appendix Table C4 The log $\dfrac{As - As_{\min}}{As_{\max} - As}$ values at $\lambda = 520$ nm with $As_{\max} = 0.6901$

and $As_{\min} = 1.5509$

pH	Absorbance	
	As	$\log \dfrac{As - As_{\min}}{As_{\max} - As}$
2.3	1.3250	-0.4488
2.6	1.1442	-0.0479
3.0	0.9224	0.4323
3.3	0.8267	0.7246
3.6	0.7396	1.2149
4.0	0.7129	1.5649

Appendix Table C5 The log $\dfrac{As - As_{min}}{As_{max} - As}$ values at $\lambda = 525$ nm with $As_{max} = 0.5903$

and $As_{min} = 1.5146$

pH	Absorbance	
	As	$\log \dfrac{As - As_{min}}{As_{max} - As}$
2.3	1.2826	-0.4748
2.6	1.1040	-0.0972
3.0	0.8409	0.4295
3.3	0.7354	0.7299
3.6	0.6467	1.1873
4.0	0.6207	1.4679

Appendix Table C6 The log $\dfrac{As - As_{min}}{As_{max} - As}$ values at $\lambda = 530$ nm with $As_{max} = 0.4975$

and $As_{min} = 1.4742$

pH	Absorbance	
	As	$\log \dfrac{As - As_{min}}{As_{max} - As}$
2.3	1.2380	-0.4963
2.6	1.0523	-0.1189
3.0	0.7614	0.4315
3.3	0.6488	0.7368
3.6	0.5589	1.1733
4.0	0.5300	1.4623

***o*-amino TAA;**

Appendix Table C7 The $\log \dfrac{As - As_{min}}{As_{max} - As}$ values at $\lambda = 505$ nm with $As_{max} = 2.8481$

and $As_{min} = 3.3739$

pH	Absorbance	
	As	$\log \dfrac{As - As_{min}}{As_{max} - As}$
2.3	3.2816	-0.6716
2.6	3.1963	-0.2924
3.0	3.0349	0.2588
3.3	2.9880	0.4407
3.6	2.9450	0.6461
4.0	2.8654	1.4678

Appendix Table C8 The $\log \dfrac{As - As_{min}}{As_{max} - As}$ values at $\lambda = 510$ nm with $As_{max} = 2.6625$

and $As_{min} = 3.5505$

pH	Absorbance	
	As	$\log \dfrac{As - As_{min}}{As_{max} - As}$
2.3	3.4191	-0.7602
2.6	3.2685	-0.3322
3.0	3.0507	0.1097
3.3	2.8905	0.4617
3.6	2.8111	0.6970
4.0	2.7036	1.3147

Appendix Table C9 The log $\dfrac{As - As_{\min}}{As_{\max} - As}$ values at $\lambda = 515$ nm with $As_{\max} = 2.4345$

and $As_{\min} = 3.66480$

pH	Absorbance	
	As	$\log \dfrac{As - As_{\min}}{As_{\max} - As}$
2.3	3.5320	-0.9172
2.6	3.3145	-0.4000
3.0	3.0509	-0.0018
3.3	2.7594	0.4451
3.6	2.6342	0.7127
4.0	2.4994	1.2543

Appendix Table C10 The log $\dfrac{As - As_{\min}}{As_{\max} - As}$ values at $\lambda = 520$ nm with $As_{\max} = 2.1717$

and $As_{\min} = 3.7618$

pH	Absorbance	
	As	$\log \dfrac{As - As_{\min}}{As_{\max} - As}$
2.3	3.6018	-0.9512
2.6	3.3445	-0.4488
3.0	3.0106	-0.0479
3.3	2.6008	0.4323
3.6	2.4239	0.7246
4.0	2.2631	1.2149

Appendix Table C11 The log $\dfrac{As - As_{\min}}{As_{\max} - As}$ values at $\lambda = 525$ nm with $As_{\max} = 1.8856$

and $As_{\min} = 3.8199$

pH	Absorbance	
	As	$\log \dfrac{As - As_{\min}}{As_{\max} - As}$
2.3	3.6415	-0.9931
2.6	3.3344	-0.4748
3.0	2.9606	-0.0972
3.3	2.4100	0.4295
3.6	2.1893	0.7299
4.0	2.0036	1.1873

Appendix Table C12 The log $\dfrac{As - As_{\min}}{As_{\max} - As}$ values at $\lambda = 530$ nm with $As_{\max} = 1.5902$

and $As_{\min} = 3.8520$

pH	Absorbance	
	As	$\log \dfrac{As - As_{\min}}{As_{\max} - As}$
2.3	3.6628	-1.0395
2.6	3.3051	-0.4963
3.0	2.8749	-0.1189
3.3	2.2014	0.4315
3.6	1.9406	0.7368
4.0	1.7325	1.1733

APPENDIX D

Calculation of stability constant by Benesi-Hildebrand's equation

1. The stoichiometric ratio between metal and ligands is 1:2

The determination of equilibrium constant, K, the Benesi-Hildebrand's equation (Benesi, 1949) was applied from equilibrium reaction of complex.

$$M + 2L \underset{\longleftarrow}{\overset{K}{\longrightarrow}} ML_2 \qquad ------ (1)$$

The equilibrium constant for the above reaction is defined by the equation

$$K = \frac{[ML_2]}{([M]-[ML_2])([L]-[ML_2])^2} \qquad ------ (2)$$

Where $[ML_2]$ is molar concentration of the complex, $[M]-[ML_2]$ is molar concentration of free metal ion and $[L]-[ML_2]$ is molar concentration of free ligand.

From Beer's law, the true molar extinction coefficient, ε_0, of the complex at the wavelength of maximum absorption will then be given by the equation

$$\varepsilon_0 = \frac{A}{cb} = \frac{A}{[ML_2]b}$$

$$[ML_2] = \frac{A}{\varepsilon_0 b} \qquad ------ (3)$$

In this reaction, ligand is added in excess. Therefore, [L] is much more than $[ML_2]$. The $[ML_2]$ can be eliminated and the equation (2) can be rearranged and obtained as the relationship;

$$K = \frac{[ML_2]}{([M]-[ML_2])([L]-[M\cancel{L_2}])^2}$$

$$K = \frac{A/\varepsilon_0 b}{([M]-A/\varepsilon_0 b)[L]^2}$$

$$K = \frac{A}{\varepsilon_0 b[M][L]^2-[L]^2 A}$$

$$A = K\varepsilon_0 b[M][L]^2 - K[L]^2 A$$

$$K\varepsilon_0 b[M][L]^2 = A + K[L]^2 A$$

$$K\varepsilon_0 b[M][L]^2 = A(1 + K[L]^2)$$

$$\frac{[M]b}{A} = \frac{1}{K\,\varepsilon_0\,[L]^2} + \frac{1}{\varepsilon_0} \qquad \text{------ (4)}$$

The equation (4) is "Benesi-Hildebrand's equation" which is in the form of the linear equation, $y = mx + c$.

2. The stoichiometric ratio between metal and ligand is 1:1

The determination of equilibrium constant, K, the Benesi-Hildebrand's equation was applied from equilibrium reaction of complex.

$$M + L \overset{K}{\rightleftharpoons} ML \qquad \text{------ (5)}$$

The equilibrium constant for the above reaction is defined by the equation

$$K = \frac{[ML]}{([M]-[ML])([L]-[ML])} \qquad \text{------ (6)}$$

Where [ML] is molar concentration of the complex, [M]-[ML] is molar concentration of free metal ion and [L]-[ML] is molar concentration of free ligand.

From Beer's law, the true molar extinction coefficient, ε_0, of the complex at the wavelength of maximum absorption will then be given by the equation

$$\varepsilon_0 = \frac{A}{cb} = \frac{A}{[ML]b}$$

$$[ML] = \frac{A}{\varepsilon_0 b} \qquad \text{------ (7)}$$

In this reaction, ligand is added in excess. Therefore, [L] is much more than [ML]. The [ML] can be eliminated and the equation (6) can be rearranged and obtained as the relationship;

$$K = \frac{[ML]}{([M]-[ML])([L]-[ML])}$$

$$K = \frac{A/\varepsilon_0 b}{([M]-A/\varepsilon_0 b)[L]}$$

$$K = \frac{A}{\varepsilon_0 b[M][L]-[L]A}$$

$$A = K\varepsilon_0 b[M][L] - K[L]A$$

$$K\varepsilon_0 b[M][L] = A + K[L]A$$

$$K\varepsilon_0 b[M][L] = A(1 + K[L])$$

$$\frac{[M]b}{A} = \frac{1}{K\,\varepsilon_0\,[L]} + \frac{1}{\varepsilon_0} \qquad \text{------ (8)}$$

The equation (8) is "Benesi-Hildebrand's equation" which is in the form of the linear equation, $y = mx + c$.

For the experiment, the concentration of rhodium(III) and platinum(IV) are fixed while the concentrations of ligands are varied. The plots from Benesi-Hildebrand's equation are shown in Appendix Figure D1 to Appendix Figure D4.

[Rh(*p*-amino TAA)$_2$] $^{3+}$;

The stoichiometric ratio between metal and ligands is 1: 2.
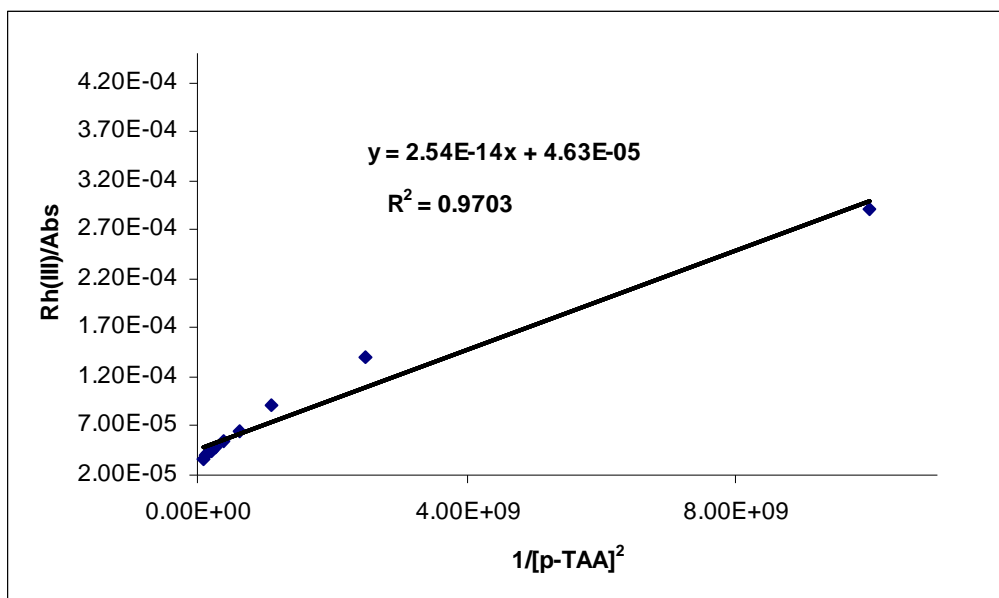
Appendix Figure D1 The relationship between [Rh(III)]/A and 1/ [*p*-TAA]^2.

The stability constant was obtained from the slope and *y*-intercept.

$$\text{Slope} = 1/K\varepsilon_0 = 2.54 \times 10^{-14}$$

$$y\text{-intercept} = 1/\varepsilon_0 = 4.63 \times 10^{-5}$$

$$\text{Stability constant } (K_{stab}) = y\text{-intercept/slope} = 1.82 \times 10^9$$

[Rh(*o*-amino TAA)$_2$]$^{3+}$;

The stoichiometric ratio between metal and ligands is 1: 2.

Appendix Figure D2 The relationship between [Rh(III)]/A and 1/ [*o*-TAA]^2.

The stability constant was obtained from the slope and *y*-intercept.

$$\text{Slope} \ = \ 1/K\varepsilon_0 \ = \ 1.77 \times 10^{-14}$$

$$y\text{-intercept} \ = \ 1/\varepsilon_0 \ = \ 2.23 \times 10^{-5}$$

$$\text{Stability constant } (K_{stab}) = \ y\text{-intercept/slope} = 1.26 \times 10^9$$

[Pt(*p*-amino TAA)] $^{4+}$;

The stoichiometric ratio between metal and ligand is 1:1.

Appendix Figure D3 The relationship between [Pt(IV)]/A and 1/ [*p*-TAA].

The stability constant was obtained from the slope and *y*-intercept.

$$\text{Slope} = 1/K\varepsilon_0 = 6.90 \times 10^{-10}$$

$$y\text{-intercept} = 1/\varepsilon_0 = 1.12 \times 10^{-4}$$

$$\text{Stability constant (K}_{stab}) = y\text{-intercept/slope} = 1.62 \times 10^5$$

[Pt(*o*-amino TAA)$_2$]$^{4+}$;

The stoichiometric ratio between metal and ligands is 1:2.
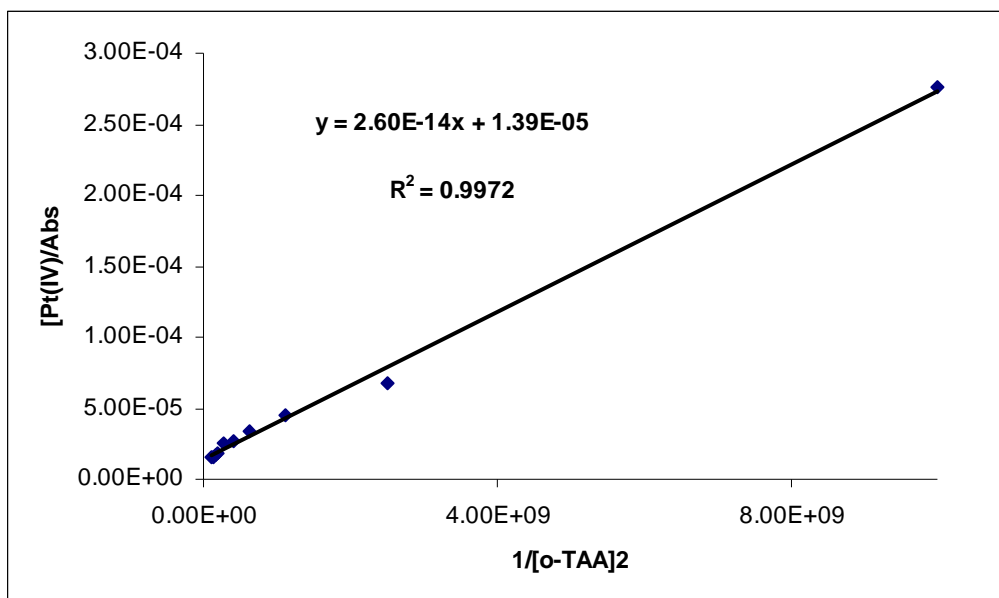
Appendix Figure D4 The relationship between [Pt(IV)]/A and 1/ [*o*-TAA]^2.

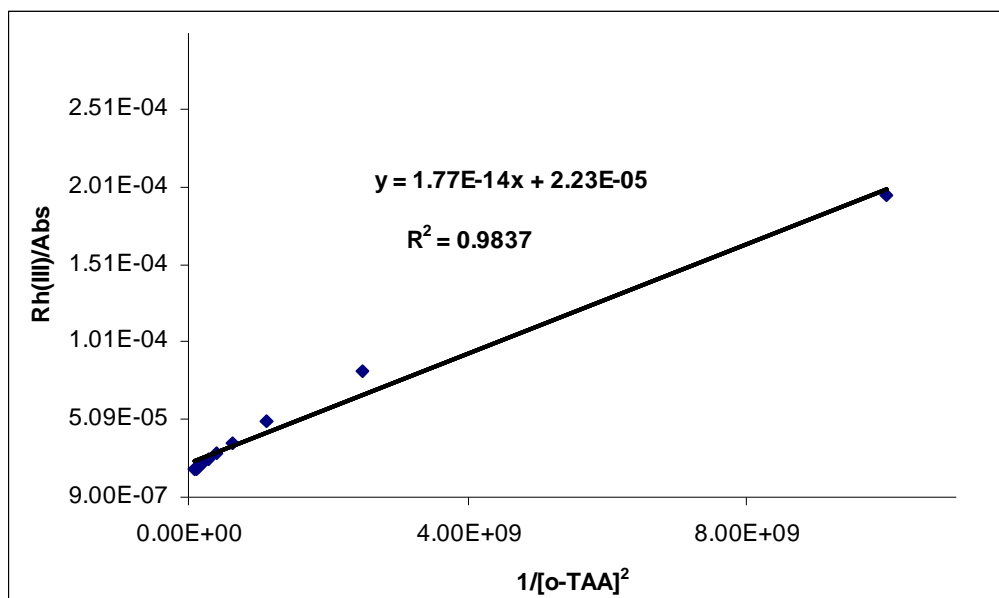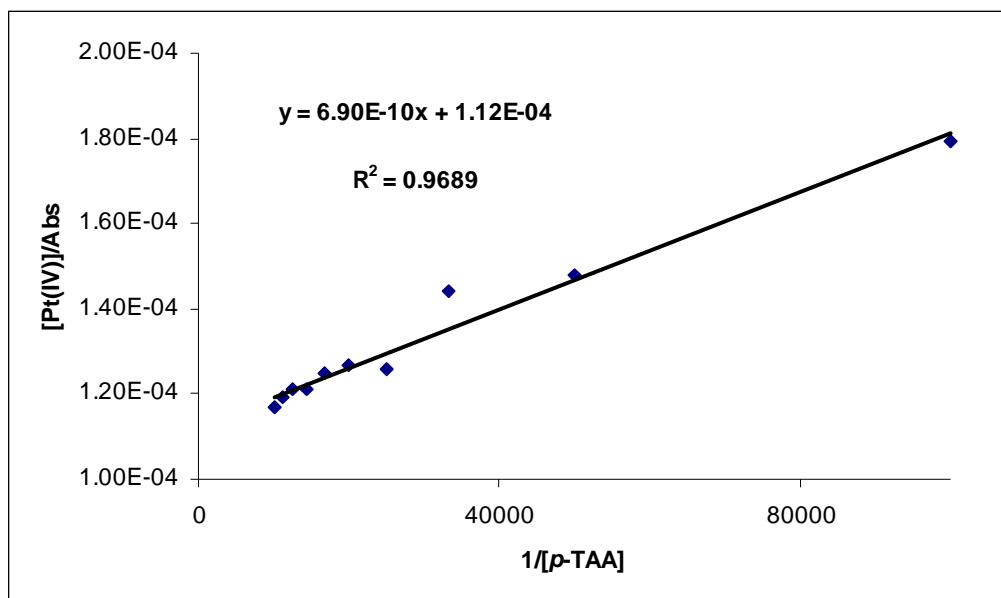The stability constant was obtained from the slope and *y*-intercept.

$$\text{Slope} = 1/K\varepsilon_0 = 2.60 \times 10^{-14}$$

$$y\text{-intercept} = 1/\varepsilon_0 = 1.39 \times 10^{-5}$$

$$\text{Stability constant (K}_{stab}) = y\text{-intercept/slope} = 5.35 \times 10^8$$

APPENDIX E

Calculation of stability constant by continuous variation method

For the continuous variation method (Connors, 1987), stability constant (K_{stab}) of the complex can be evaluated from measurements of the deviations from the theoretical straight line, which represent the curve that would result if the reaction between the ligand and the metal produced to completion.

Rhodium complexes

$$Rh^{3+} + 2TAA \xrightleftharpoons{K_{stab}} [Rh(TAA)_2]^{3+}$$

$$K_{stab} = \frac{[Rh(TAA)_2]^{3+}}{[Rh^{3+}][TAA]^2}$$

$$C_{Rh} = [Rh^{3+}] + [Rh(TAA)_2^{3+}]$$

$$[Rh^{3+}] = C_{Rh} - [Rh(TAA)_2^{3+}]$$

$$C_{TAA} = [TAA] + [Rh(TAA)_2^{3+}]$$

$$[TAA] = C_{TAA} - [Rh(TAA)_2^{3+}]$$

When C_{Rh} = total concentration of rhodium(III) ion

C_{TAA} = total concentration of *p*-amino TAA or *o*-amino TAA

[Rh(*p*-amino TAA)$_2$] $^{3+}$;

[Rh(*p*-amino TAA)$_2$] $^{3+}$ was prepared by mixing of RhCl$_3$·xH$_2$O 1.0×10^{-3} M with *p*-amino TAA 1.0×10^{-3} M.

When $V_{Rh^{3+}} = 0.400$ ml and $V_{p\text{-}TAA} = 0.600$ ml

So, initial concentration of C_{Rh} and $C_{p\text{-}TAA}$ are

$$C_{Rh} = \frac{(0.400 \text{ ml})(1.0 \times 10^{-3} \text{ M})}{10.0 \text{ ml}} = 4.0 \times 10^{-5} \text{ M}$$

$$C_{p\text{-TAA}} = \frac{(0.600 \text{ ml})(1.0 \times 10^{-3} \text{ M})}{10.0 \text{ ml}} = 6.0 \times 10^{-5} \text{ M}$$

If the complex is stable, two straight lines are intercepted and thus the complex concentration is equal to the original concentration of metal ion.

When $[ML_2] = [Rh(p\text{-TAA})_2^{3+}]$

$$[Rh(p\text{-TAA})_2^{3+}]_{ex} = [ML_2]_{ex} = C_{Rh}$$
$$A_{ex} = \varepsilon b[ML_2]_{ex} = \varepsilon b C_{Rh}$$

When A = The highest absorbance from the curvature of the experiment

A_{ex} = The highest absorbance from the theoretical straight line

but $$A = \varepsilon b[ML_2]$$

$$\frac{A}{A_{ex}} = \frac{\varepsilon b[ML_2]}{\varepsilon b C_{Rh}}$$

So, $$[ML_2] = \frac{A}{A_{ex}} C_{Rh}$$

Thus, $$K_{stab} = \frac{[Rh(p\text{-TAA})_2^{3+}]}{[Rh^{3+}][p\text{-TAA}]^2} = \frac{[ML_2]}{[Rh^{3+}][p\text{-TAA}]^2}$$

$$= \frac{[ML_2]}{[C_{Rh} - ML_2][C_{p\text{-TAA}} - ML_2]^2}$$

$$K_{stab} = \frac{\dfrac{A}{A_{ex}} C_{Rh}}{\left(C_{Rh} - \dfrac{A}{A_{ex}} C_{Rh}\right)\left(C_{p\text{-TAA}} - \dfrac{A}{A_{ex}} C_{Rh}\right)^2}$$

$$K_{stab} = \frac{\dfrac{A}{A_{ex}}}{\left(1 - \dfrac{A}{A_{ex}}\right)\left(C_{p\text{-}TAA} - \dfrac{A}{A_{ex}}C_{Rh}\right)^2}$$

When $A = 0.390$ and $A_{ex} = 0.435$

So, $\qquad K_{stab} = \dfrac{0.390/0.435}{[1 - (0.390/0.435)][6.0 \times 10^{-5} - (0.390/0.435)(4.0 \times 10^{-5})]^2}$

$\qquad\qquad K_{stab} = \qquad 3.59 \times 10^{10}$

[Rh(*o*-amino TAA)$_2$]$^{3+}$;

[Rh(*o*-amino TAA)$_2{}^{3+}$] was prepared by mixing of $RhCl_3.xH_2O$ 1.0×10^{-3} M with *o*-amino TAA 1.0×10^{-3} M.

When $V_{Rh^{3+}} = 0.400$ ml and $V_{o\text{-}TAA} = 0.600$ ml

So, initial concentration of C_{Rh} and $C_{o\text{-}TAA}$ are

$$C_{Rh} = \frac{(0.400\ ml)(1.0 \times 10^{-3}\ M)}{10.0\ ml} = 4.0 \times 10^{-5}\ M$$

$$C_{o\text{-}TAA} = \frac{(0.600\ ml)(1.0 \times 10^{-3}\ M)}{10.0\ ml} = 6.0 \times 10^{-5}\ M$$

If the complex is stable, two straight lines are intercepted and thus the complex concentration is equal to the original concentration of metal ion.

When $[ML_2] = [Rh(o\text{-}TAA)_2{}^{3+}]$

$$[\text{Rh}(o\text{-TAA})_2{}^{3+}]_{ex} = [\text{ML}_2]_{ex} = C_{Rh}$$

$$A_{ex} = \varepsilon b[\text{ML}_2]_{ex} = \varepsilon b C_{Rh}$$

but

$$A = \varepsilon b[\text{ML}_2]$$

$$\frac{A}{A_{ex}} = \frac{\varepsilon b[\text{ML}_2]}{\varepsilon b C_{Rh}}$$

So,

$$[\text{ML}_2] = \frac{A}{A_{ex}} C_{Rh}$$

Thus,

$$K_{stab} = \frac{[\text{Rh}(o\text{-TAA})_2{}^{3+}]}{[\text{Rh}^{3+}][o\text{-TAA}]^2} = \frac{[\text{ML}_2]}{[\text{Rh}^{3+}][o\text{-TAA}]^2}$$

$$= \frac{[\text{ML}_2]}{[C_{Rh}- \text{ML}_2][C_{o\text{-TAA}}- \text{ML}_2]^2}$$

$$K_{stab} = \frac{\dfrac{A}{A_{ex}} C_{Rh}}{(C_{Rh} - \dfrac{A}{A_{ex}} C_{Rh})(C_{o\text{-TAA}} - \dfrac{A}{A_{ex}} C_{Rh})^2}$$

$$K_{stab} = \frac{\dfrac{A}{A_{ex}}}{(1 - \dfrac{A}{A_{ex}})(C_{o\text{-TAA}} - \dfrac{A}{A_{ex}} C_{Rh})^2}$$

When $A = 0.440$ and $A_{ex} = 0.505$

So,

$$K_{stab} = \frac{0.440/0.505}{[1 - (0.440/0.505)][6.0 \times 10^{-5} - (0.440/0.505)(4.0 \times 10^{-5})]^2}$$

$$K_{stab} = 2.69 \times 10^{10}$$

Platinum complexes

[Pt(*p*-amino TAA)] $^{4+}$;

$$Pt^{4+} + p\text{-TAA} \xrightleftharpoons{K_{stab}} [Pt(p\text{-TAA})]^{4+}$$

$$K_{stab} = \frac{[Pt(p\text{-TAA})]^{4+}}{[Pt^{4+}][p\text{-TAA}]}$$
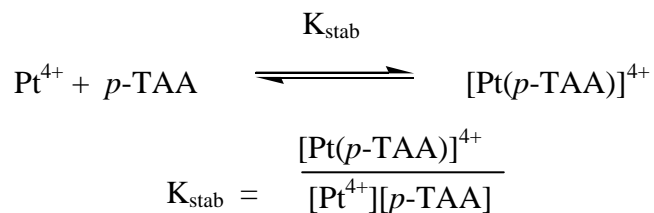
$$C_{Pt} = [Pt^{4+}] + [Pt(p\text{-TAA})^{4+}]$$

$$[Pt^{4+}] = C_{Pt} - [Pt(p\text{-TAA})^{4+}]$$

$$C_{p\text{-TAA}} = [p\text{-TAA}] + [Pt(p\text{-TAA})^{4+}]$$

$$[p\text{-TAA}] = C_{p\text{-TAA}} - [Pt(p\text{-TAA})^{4+}]$$

[Pt(*p*-amino TAA)$^{4+}$] was prepared by mixing of K_2PtCl_6 1.0×10^{-3} M with *p*-amino TAA 1.0×10^{-3} M.

When $V_{Pt}{}^{4+} = 0.500$ ml and $V_{p\text{-TAA}} = 0.500$ ml
So, initial concentration of C_{Pt} and $C_{p\text{-TAA}}$ are

$$C_{Pt} = \frac{(0.500 \text{ ml})(1.0 \times 10^{-3} \text{ M})}{10.0 \text{ ml}} = 5.0 \times 10^{-5} \text{ M}$$

$$C_{p\text{-TAA}} = \frac{(0.500 \text{ ml})(1.0 \times 10^{-3} \text{ M})}{10.0 \text{ ml}} = 5.0 \times 10^{-5} \text{ M}$$

If the complex is stable, two straight lines are intercepted and thus the complex concentration is equal to the original concentration of metal ion.

When $[ML] = [Pt(p\text{-TAA})^{4+}]$

$$[Pt(p\text{-}TAA)^{4+}]_{ex} = [ML]_{ex} = C_{Pt}$$

$$A_{ex} = \varepsilon b[ML]_{ex} = \varepsilon b C_{Pt}$$

but
$$A = \varepsilon b[ML]$$

$$\frac{A}{A_{ex}} = \frac{\varepsilon b[ML]}{\varepsilon b C_{Pt}}$$

So,
$$[ML] = \frac{A}{A_{ex}}C_{Pt}$$

Thus,
$$K_{stab} = \frac{[Pt(p\text{-}TAA)^{4+}]}{[Pt^{4+}][p\text{-}TAA]} = \frac{[ML]}{[Pt^{4+}][p\text{-}TAA]}$$

$$= \frac{[ML]}{[C_{Pt}- ML][C_{p\text{-}TAA}- ML]}$$

$$K_{stab} = \frac{\dfrac{A}{A_{ex}}C_{Pt}}{(C_{Pt} - \dfrac{A}{A_{ex}}C_{Pt})(C_{p\text{-}TAA} - \dfrac{A}{A_{ex}}C_{Pt})}$$

$$K_{stab} = \frac{\dfrac{A}{A_{ex}}}{(1 - \dfrac{A}{A_{ex}})(C_{p\text{-}TAA} - \dfrac{A}{A_{ex}}C_{Pt})}$$

When   A = 0.298 and A_{ex} = 0.349

So,
$$K_{stab} = \frac{0.298/0.349}{[1 - (0.298/0.349)][5.0 \times 10^{-5} - (0.298/0.349)(5.0 \times 10^{-5})]}$$

$$K_{stab} = 8.00 \times 10^{5}$$

[Pt(*o*-amino TAA)₂] $^{4+}$;

[Pt(*o*-amino TAA)₂] $^{4+}$ was prepared by mixing of K_2PtCl_6 1.0×10^{-3} M with *o*-amino TAA 1.0×10^{-3} M.

When $V_{Pt}{}^{4+} = 0.400$ ml and $V_{o\text{-TAA}} = 0.600$ ml

So, initial concentration of C_{Pt} and $C_{o\text{-TAA}}$ are

$$C_{Pt} = \frac{(0.400 \text{ ml})(1.0 \times 10^{-3} \text{ M})}{10.0 \text{ ml}} = 4.0 \times 10^{-5} \text{ M}$$

$$C_{o\text{-TAA}} = \frac{(0.600 \text{ ml})(1.0 \times 10^{-3} \text{ M})}{10.0 \text{ ml}} = 6.0 \times 10^{-5} \text{ M}$$

If the complex is stable, two straight lines are intercepted and thus the complex concentration is equal to the original concentration of metal ion.

When $[ML_2] =$

$$[Pt(o\text{-TAA})_2{}^{4+}]_{ex} = [ML_2]_{ex} = C_{Pt}$$
$$A_{ex} = \varepsilon b[ML_2]_{ex} = \varepsilon b C_{Pt}$$

but
$$A = \varepsilon b[ML_2]$$

$$\frac{A}{A_{ex}} = \frac{\varepsilon b[ML_2]}{\varepsilon b C_{Pt}}$$

So,
$$[ML_2] = \frac{A}{A_{ex}} C_{Pt}$$

Thus, $\quad K_{stab} = \dfrac{[Pt(o\text{-}TAA)_2{}^{4+}]}{[Pt^{4+}][o\text{-}TAA]^2} \doteq \dfrac{[ML_2]}{[Pt^{4+}][o\text{-}TAA]^2}$

$$= \dfrac{[ML_2]}{[C_{Pt}\text{-} ML_2][C_{o\text{-}TAA}\text{-} ML_2]^2}$$

$$K_{stab} = \dfrac{\dfrac{A}{A_{ex}}C_{Pt}}{(C_{Pt} - \dfrac{A}{A_{ex}}C_{Pt})(C_{o\text{-}TAA} - \dfrac{A}{A_{ex}}C_{Pt})^2}$$

$$K_{stab} = \dfrac{\dfrac{A}{A_{ex}}}{(1 - \dfrac{A}{A_{ex}})(C_{o\text{-}TAA} - \dfrac{A}{A_{ex}}C_{Pt})^2}$$

When $A = 0.502$ and $A_{ex} = 0.586$

So, $\quad K_{stab} = \dfrac{0.502/0.586}{[1 - (0.502/0.586)][6.0 \times 10^{-5} - (0.502/0.586)(4.0 \times 10^{-5})]^2}$

$$K_{stab} = 9.02 \times 10^9$$

APPENDIX F

Nucleic Acid Purity Assessment Using A260/A280 Ratios

A common practice in molecular biology is to perform a quick assessment of the purity of nucleic acid samples by determining the ratio of spectrophotometric absorbance of the sample at 260 nm to that of 280 nm. The basis of this test rests on the Beer-Lambert Law:

$$A = \varepsilon Cb \qquad \text{----- (1)}$$

The absorbance (A) is the product of the extinction coefficient (ε), the concentration of the sample (C), and the optical pathlength (b). With an optical pathlength of 1 cm, which is commonly used in spectrophotometers, the pathlength can be ignored and extinction coefficients can be explained as an absorbance value at a specific concentration as seen in the equation below.

$$\varepsilon = A/C \qquad \text{----- (2)}$$

The commonly accepted average extinction coefficients for 1 mg/ml nucleic acid solutions at 260 nm and 280 nm are 20 and 10 respectively. Similarly the extinction coefficient values at 260 nm and 280 nm at a concentration of 1 mg/ml are 0.57 and 1.00 respectively for proteins. Thus in relative terms, nucleic acid samples would be expected to have a higher absorbance at 260 nm than at 280 nm, while with a protein sample, the inverse would be true. Using these extinction coefficients, pure nucleic acid samples would have an A_{260}/A_{280} ratio of 2.0, while protein would be 0.57. Samples that contain a mixture of protein and DNA would of course be influenced by both macromolecules. The theoretical A_{260}/A_{280} ratio for samples that contain a mixture of protein and nucleic acid can be estimated by using the following formula:

$$A_{260}/A_{280} = \frac{(\varepsilon_{260}p \times (\%P) + \varepsilon_{260}n \times (\%N))}{(\varepsilon_{280}p \times (\%P) + \varepsilon_{280}n \times (\%N))} \qquad \text{----- (3)}$$
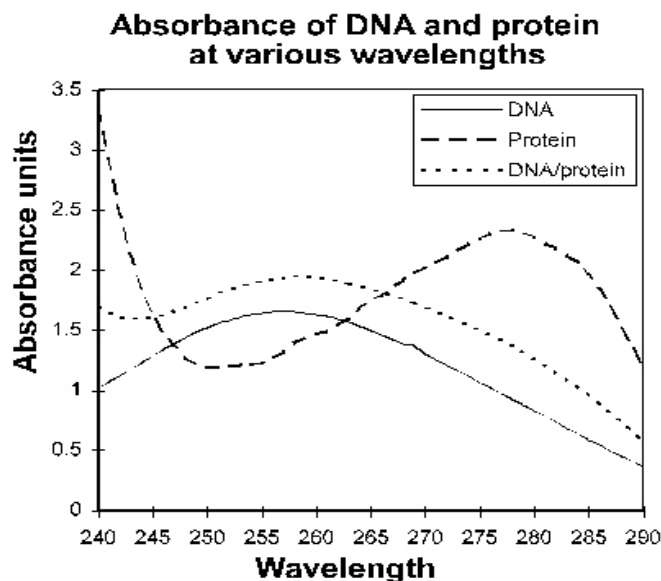
Appendix Figure F1 Absorbance profiles of DNA and protein samples from 240 to 290 nm.

The data depicted in Appendix Figure F1 demonstrates the positioning of peak absorbance of pure DNA and protein solutions, as well as a mixture of the two macromolecules. The peak in absorbance for DNA was at 257 nm and for protein was at 277 nm. A 10:1(w/w) mixture DNA/protein results in a peak absorbance at 259 nm and an absorbance profile very similar in shape as that demonstrated by pure DNA with a small increase at wavelength below 240 nm and represents a sum of the two absorbance patterns of the macromolecules.

A_{280} ratio measurements were then calculated by dividing the absorbance determination at each wavelength by the A_{280} determination for that sample as shown in Appendix Figure F2. It was found that samples containing only protein demonstrate a peak at 280 nm, reflecting the maximal absorbance of proteins at this wavelength. The sample containing a mixture of DNA and protein demonstrates a profile very similar to that of pure DNA in shape, but with values that are much lower, despite having equivalent amounts of nucleic acid in both samples.
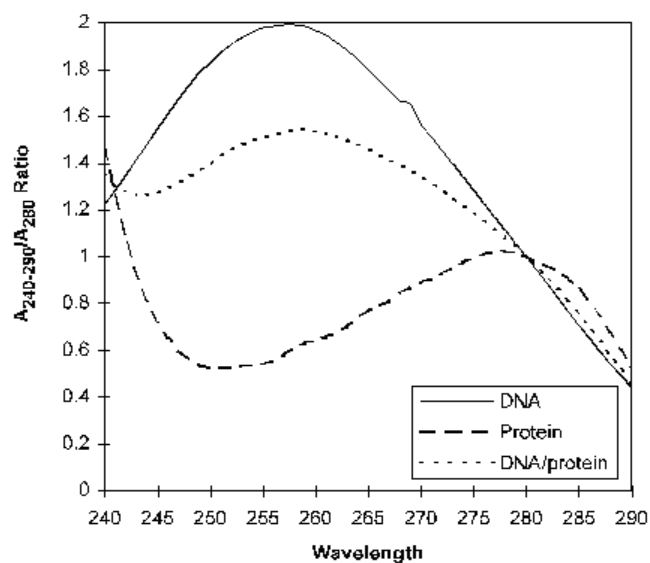
Appendix Figure F2 A280 ratio of samples containing DNA and/or protein at
wavelengths from 240 nm to 290 nm.
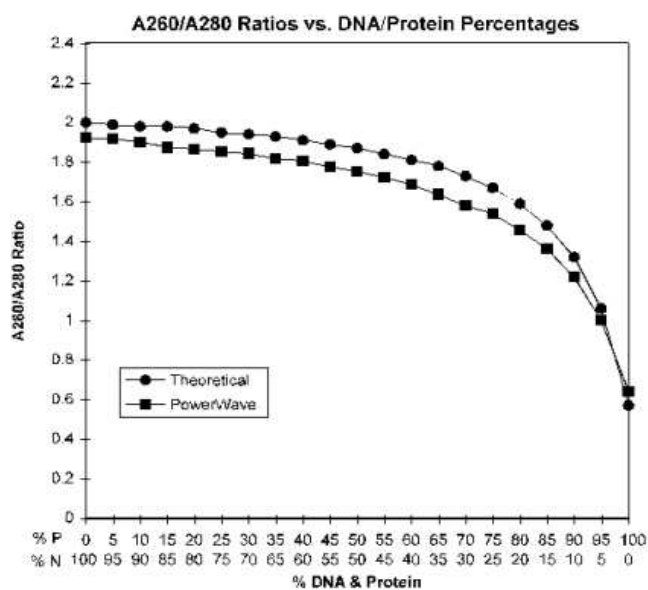
Appendix Figure F3 Comparison of theoretical A_{260}/A_{280} ratios with those determined
using the PowerWave 200 scanning microplate spectrophotometer.

The absorbance of various mixtures of DNA and protein were determined at 260 nm and 280 nm. Subsequently the A_{260}/A_{280} ratios were determined for each mixture and compared to the theoretical value calculated from the extinction coefficients. Filled circles indicate theoretical ratios while filled boxed denote experimentally determined ratios. When the A_{260}/A_{280} ratio is determined for a range of different DNA/protein mixtures one finds that the ratio is relatively insensitive to the addition of protein to pure nucleic acid. As demonstrated in Appendix Figure F3 as increasing percentages of protein are measured little change is seen in the A_{260}/A_{280} ratio until the percentage of protein is approximately 75%. Interestingly, even when equal amounts of nucleic acid and protein by weight are determined a ratio of 1.75, is still returned. DNA or protein only samples were found to have A_{260}/A_{280} ratios of 1.92 and 0.64 respectively.

It is important to note that the A_{260}/A_{280} ratio is only an indication of purity rather than a precise answer. Pure DNA and RNA preparations have expected A_{260}/A_{280} ratios of ≥ 1.8 and ≥ 2.0 respectively and are based on the extinction coefficients of nucleic acids at 260 nm and 280 nm. There are several factors that may affect A_{260}/A_{280} ratios. The 260 nm measurements are made very near the peak of the absorbance spectrum for nucleic acids, while the 280 nm measurement is located in a portion of the spectrum that has a very steep slope. As a result, very small differences in the wavelength in and around 280 nm will effect greater changes in the A_{260}/A_{280} ratio than small differences at 260 nm. Consequently, different instruments will result in slightly different A_{260}/A_{280} ratios on the same solution due to the variability of wavelength accuracy between instruments. Individual instruments, however, should give consistent results. Concentration can also affect the results, as dilute samples will have very little difference between the absorbance at 260 nm and that at 280 nm. With very small differences, the detection limit and resolution of the instrument measurements begin to become much more significant. The type(s) of protein present in a mixture of DNA and protein can also affect the A_{260}/A_{280} ratio determination. Absorbance in the UV range of proteins is primarily the result of aromatic ring structures. Proteins are composed of 22 different amino acids of which only three contain aromatic side chains. Thus the amino acid sequence of proteins would be

expected to have a tremendous influence on the ability of a protein to absorb light at 280 nm.

APPENDIX G

Determination of stabilization energies by quantum chemical calculations

The formation of complex between rhodium(III) and *p*-amino TAA should be as followed:

$$Rh^{3+} \;+\; 2p\text{-amino TAA} \rightleftharpoons [Rh(p\text{-amino TAA})_2]^{3+}$$
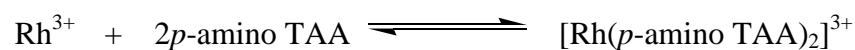
The molecular structures of reactants and products were created on GaussView version 3.0 and their cartesian coordinates were used as input structures on Gaussian03. The quantum chemical calculations were carried out at B3LYP (Lee, Yang and Parr correlation functional) level with 6-31G* basis set for all atoms and SDD (Stuttgart/Dresden) basis set for rhodium atom. The stabilization energy, E, of $[Rh(p\text{-amino TAA})_2]^{3+}$ complex was calculated as followed:

$$E \;=\; (E_{products}) - (E_{reactants})$$

$$=\; [(E_{complex})] - [(E_{Rh}) + 2(E_{p\text{-TAA}})]$$

$$=\; [(-2268.63477)] - [(-108.26190) + 2(-1079.43408)]$$

$$E \;=\; -1.50471 \text{ atomic unit}$$

$$=\; -1.2464812 \times 627.51$$

$$=\; -944.22057 \text{ kcal/mol}$$

1. The example of input data

_p_-amino TAA;

%chk=_p_-aminoTAA.chk

%mem=6MW

%nproc=1

opt b3lyp/6-31g*

Title Card Required

```
0  1
C          0.000000   0.000000   0.000000
C          1.395160   0.000000   0.000000
C          2.092698   1.207751   0.000000
C          1.395044   2.416260  -0.001199
C          0.000219   2.416182  -0.001678
C         -0.697382   1.207976  -0.000682
H         -0.549759  -0.952317   0.000450
H          1.944668  -0.952513   0.001315
H         -0.549903   3.368463  -0.002623
O          2.110512   3.654406  -0.001276
N         -2.167382   1.208221  -0.000923
N          3.562698   1.207858   0.000848
N          4.172772   0.139286   0.062399
C          5.642749   0.131197   0.063716
N          6.452183   1.243662   0.000552
C          7.838844   0.886383   0.022566
C          8.007878  -0.478177   0.100452
S          6.539814  -1.277642   0.144922
H          8.644774   1.621340  -0.018306
H          8.962977  -0.998803   0.130764
C          1.766777   4.403490  -1.169873
H          1.829955   5.449645  -0.954308
H          2.444760   4.160825  -1.961297
H          0.768414   4.160502  -1.468418
H         -2.500626   2.085498   0.344523
H         -2.500934   0.470500   0.586029
```

Rh(*p*-aminoTAA-n)₂ complex;

%chk=Rh(*p*-aminoTAA-n)₂.chk

%mem=6MW

%nproc=1

#b3lyp/gen pseudo=read opt

Title Card Required

3 1

C	5.370919	-0.845290	0.455592
C	4.192427	-0.342650	0.920814
C	2.933830	-0.637686	0.291863
C	2.965730	-1.518074	-0.849687
C	4.143790	-2.044625	-1.309288
C	5.387317	-1.722873	-0.679094
H	6.305468	-0.580772	0.941152
H	4.188030	0.316120	1.780513
H	4.114174	-2.749062	-2.134532
N	1.767653	-0.142011	0.808329
N	1.826369	0.367935	2.014695
O	1.805823	-2.004548	-1.426840
N	6.532712	-2.228248	-1.132177
H	6.569639	-2.852767	-1.930629
H	7.418695	-2.024268	-0.681238
C	0.658338	0.889013	2.434408
C	-1.265467	1.815456	3.624191
C	-1.545187	1.463622	2.335201
H	-1.936265	2.264049	4.346029
H	-2.487373	1.601065	1.822098
H	-5.482216	-4.283300	0.444199
N	-5.706402	-3.421753	-0.041657
C	-4.806049	-2.463473	-0.251694
H	-6.662696	-3.330659	-0.369617
C	-5.181663	-1.264174	-0.948655
C	-3.456396	-2.624676	0.210824
C	-4.264883	-0.278922	-1.166362
H	-6.202873	-1.150643	-1.299109
C	-2.542612	-1.631595	-0.020110
H	-3.186990	-3.540089	0.723161
C	-2.921194	-0.423425	-0.702846
H	-4.536878	-0.631349	1.689463
O	-1.203975	-1.719206	0.359554
N	-1.964309	0.525247	-0.863736
C	-0.738820	-2.911962	1.073367
N	-2.161003	1.659838	-1.460060

H	-0.918450	-3.790325	0.451072
H	0.329296	-2.768744	1.216483
H	-1.254258	-2.981497	2.033308
C	-1.016010	2.388023	-1.496927
C	1.182930	2.832253	-1.159031
C	0.828424	3.928950	-1.891650
H	2.156044	2.638136	-0.726358
H	1.452913	4.764607	-2.180979
Rh	-0.134287	0.132935	-0.125091
C	1.110408	-1.195989	-2.314504
H	0.516981	-1.825043	-2.981315
H	0.306990	-0.564555	-1.778751
H	1.736765	-0.483705	-2.859437
N	0.138021	1.970583	-0.928705
N	-0.452411	0.951808	1.670936
S	-0.848229	3.886592	-2.325257
S	0.393338	1.504835	4.027066

C H N S O 0
6-31G*
****
Rh 0
SDD
****

Rh 0
SDD

CIRRICULUM VITAE

BIRTH DATE   : June 4, 1985

BIRTH PLACE   : Chonburi, Thailand

EDUCATION : **YEAR**	**INSTITUTE**	**DEGREE/DIPLOMA**
2007	Kasetsart Univ.	B.Sc. (Chemistry)

POSITION/TITLE   :   Postgraduated student

WORKPLACE   :   Faculty of Science, Kasetsart University

SCHOLARSHIP/AWARDS :   - Development and Promotion of Science and
Technology Talents Project (DPST)
- Center for Innovation in Chemistry:
Postgraduate Education and Research Program
in Chemistry (PERCH-CIC)